EXTRACELLULAR METABOLIC PROFILING: MEASUREMENT OF SURFACE CONCENTRATIONS AND FLUXES TO DETERMINE CELLULAR KINETICS FROM 2D CULTURES USING ELECTROCHEMICAL MICROELECTRODE ARRAYS

A Dissertation

Submitted to the Faculty

of

Purdue University

by

Siddarth V. Sridharan

In Partial Fulfillment of the

Requirements for the Degree

of

Doctor of Philosophy

August 2019

Purdue University

West Lafayette, Indiana

THE PURDUE UNIVERSITY GRADUATE SCHOOL
STATEMENT OF DISSERTATION APPROVAL

Dr. David B. Janes, Chair

School of Electrical and Computer Engineering

Dr. Jenna L. Rickus

School of Agricultural and Biological Engineering

Dr. Muhammad A. Alam

School of Electrical and Computer Engineering

Dr. Babak Ziaie

School of Electrical and Computer Engineering

Approved by:

Dr. Dimitrios Peroulis

Head of the School of Electrical and Computer Engineering

To my parents for their support and advice

And

To my fiancee for her help and encouragement

ACKNOWLEDGMENTS

I would like to thank my advisor, Professor David Janes, for giving me the opportunity and support to work on this topic. Dr. Janes's guidance and enthusiasm for research has always inspired me to be more confident and passionate about our work. I am extremely grateful to him for his patience and understanding, as I navigated through a field of research relatively new to me. I would like to express my gratitude to my doctoral committee, Dr. Jenna Rickus, Dr. Muhammad Alam and Dr. Babak Ziaie, who have been incredibly supportive and helpful. Especially, I would like to thank Dr. Rickus for all her support in guiding us through the various biological aspects of our project. I would like to thank the staff of Birck Nanotechnology Center at Purdue University for their help and assistance.

Many thanks to my fellow researcher, Jose Rivera for the immense motivation and the sheer number of hours we spent in the lab discussing every experiment and result. The results we achieved while working on this project would not have been possible without your contribution and support. I would like to thank my fellow graduate students Stephen Miloro, James Nolan and Hye-Ran Moon, for their help with the cellular experiments. I would like to express my gratitude to the National Science Foundation (NSF Nano-biosensing Program Grant #1403582) for providing the financial support for the project.

Finally, I would first like to thank my parents, for instilling in me a strong sense of curiosity and a keen desire to learn as much as possible.

TABLE OF CONTENTS

Page

Page

Page

LIST OF TABLES

LIST OF FIGURES

Figure Page

Figure Page

Figure Page

Figure Page

Figure Page

Figure Page

Figure Page

Figure Page

Figure Page

Figure Page

Figure Page

Figure Page

Figure Page

ABSTRACT

Sridharan, Siddarth V. Ph.D., Purdue University, August 2019. Extracellular Metabolic Profiling: Measurement of Surface Concentrations and Fluxes to Determine Cellular Kinetics from 2D Cultures using Electrochemical Microelectrode Arrays. Major Professor: David B. Janes.

In 2D cell cultures uptake/release of various metabolic analytes such as glucose, lactate or metabolic by-products like hydrogen peroxide from/to the extracellular environment results in concentration gradients. The magnitude, direction, and time scales of these gradients carries information that is essential for internal cellular processes and/or for communication with neighboring cells. This PhD research work focusses on the design, fabrication and characterization of electrochemical microelectrode arrays (MEAs) optimized to be positioned in commonly used 2D cell culture setups. Importantly, by simultaneously measuring accurate concentration transients and associated gradients/fluxes near the cell surface (surface concentration) the capability of the device to quantify kinetic rates and distinguish mechanisms involved in various cellular processes is demonstrated. An in-situ transient calibration technique suitable for amperometric MEAs is developed and the technique is validated by quantitatively measuring dynamic concentration profiles with varying spatial (100-800 μm) and time (s to hrs.) scales set up from an electrically controlled diffusion reaction system. With the proposed MEA design and technique three physiological applications are demonstrated. Firstly, the position able 1D MEA was employed real time to quantitatively measure the hydrogen peroxide scavenging rates from astrocyte vs glioblastoma cell cultures. With the ability to extract to dynamic surface concentration and fluxes, the cell lines were shown to have hydrogen peroxide uptake rates dependent on local surface concentrations. Moreover, the cancerous glioblastoma cells demonstrated an upregulated linear peroxide scavenging mechanism as compared to

astrocytes. For the next phase, spatial scales of 1D MEA device along the size and functionalization scheme of the electrodes in the MEA was further modified to selectively sense glucose and lactate to enable extracellular metabolic profiling of cancer vs normal cell lines. Secondly, measurement of glucose concentration profiles demonstrated an increased glucose uptake rate in glioblastoma as compared to astrocytes. Additionally, sigmoidal (allosteric) vs Michaelis - Menten glucose uptake kinetics was observed in glioblastoma vs astrocytes. Moreover, the presence of a glucose sensing mechanism was observed in glioblastoma cells due to the dependence of the glucose uptake rate on initial exposed concentration rather than surface concentration. Finally, simultaneous multi-analyte (glucose and lactate) gradient measurements were performed on genetically modified mouse pancreatic cancer cell lines. While glucose uptake rate was shown to increase with increasing extracellular glucose concentration for one of the cell lines, the lactate release rate was observed to be independent of the initial extracellular glucose dose.

1. INTRODUCTION

1.1 Motivation and Problem Statement

In recent years, altered and reprogrammed metabolism has been linked to survival, proliferation and metastasis of cancerous tumors and development of several diseases [1–5]. Especially in regards to cancer cells, metabolic characteristics such as Warburg dependent glucose metabolism [6], glutaminolysis [7] and fatty acid synthesis [8] have been attributed to drug/therapy resistance in treatment. Critically, tumor metabolic activity has also been linked to poor patient outcomes in cancer patients [9–11]. Therefore, targeting cellular metabolism by providing mechanistic insight into the differences in the metabolic pathway of malignant versus normal cells is considered key to the identification of more effective therapeutic strategies and cancer drugs [1, 12, 13]. In this context, determination of kinetic information is vital to move from phenomenological descriptions to mechanistic insight on fundamental cellular processes like signalling and metabolism [14–21].

Broadly, the metabolic pathway in mammalian cells can be categorized into three kinetic stages,

- Firstly, in combination with diffusion, cells act as sources and sinks setting up the release and uptake of various metabolites (such as glucose and lactate) and their metabolic by products (like reactive oxygen species (ROS)) from/to surrounding extracellular environment.

- Secondly, in addition to passive diffusion across membranes, cells can regulate uptake/release via facilitated diffusion transporters such as Gluts [22, 23] for glucose, monocarboxylate transporters (MCTs) for lactate [24] and membrane proteins such aquaporins for small ROS molecules like hydrogen peroxide

(H_2O_2) [25–27]. Fig. 1.1 shows some common cell flux archetypes which represent common spatial organization of transporters that are observed in living cells.

- Finally, cells contain oxidative/redox centers regulated by multiple enzymes at various stages, which organize biochemical breakdown of metabolites into energy or for production of new cell components.
- While any of these stages could be the rate limiting step, collectively they give rise to the kinetic phenotypic of the cell.

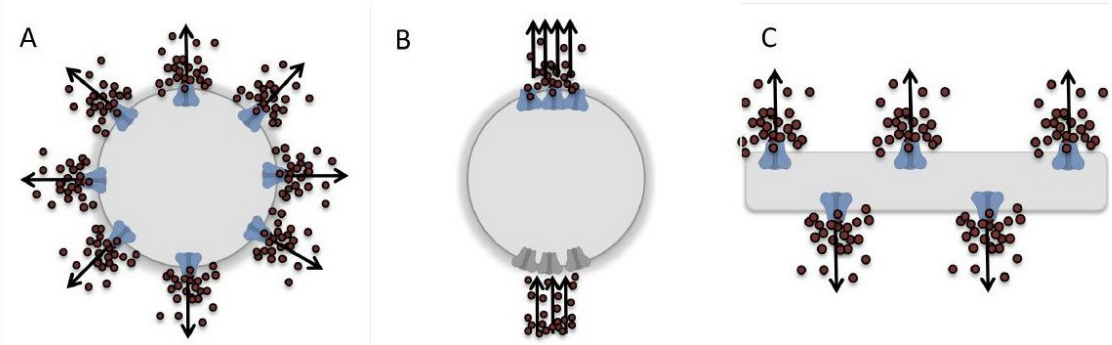

Fig. 1.1. (A) Uniform cellular flux is the most common form whereby there is a continuous release or uptake of the molecule of interest. (B) Bidirectional flux archetype, i.e. release from the apical and uptake from the basal sides of the cell can occur during different stages of cell development and differentiation. Cells can also transition between archetype A and B as they grow. (C)Linear Cable Model represents a linear portion of a single cell or multicellular structure (e.g. a neuronal axon).

The above mentioned sequence of kinetic stages in the metabolic pathways are well encapsulated by a model cell system shown in Fig. 1.2B. The fate of glucose, uptaken via facilitated diffusion, can be categorized into two pathways. Catabolic pathways help in the production of energy via production of ATP in the redox center (mitochondria) of the cell. Energy production also leads to the formation of

other metabolites like lactate (for e.g.via glycolysis). Anabolic pathways pertain to the production of new cell components or biosynthesis. In addition, anabolic pathways are usually dependent on processes that require energy produced from nutrient catabolism. Both these major pathways are tightly regulated via enzymes at various stages. Finally, ROS generated during metabolism or transported from extracellular environment can be scavenged by enzymes present in the redox center. An example of such a system is the the astrocyte-neuron bioenergetic transport cycle in the brain shown in Fig. 1.2A [28–34].

For the understanding overall kinetics of cellular system as seen in Fig. 1.2B, the important cellular parameters are the **uptake rates ($\mathbf{U_R}$), release rate ($\mathbf{R_R}$) and the local or surface concentration ($\mathbf{C_S}$)**. While intracellular components of the metabolic system (e.g., enzyme kinetics, detection of transporters etc.) have been studied individually using biochemical assays, this PhD dissertation describes the development of a tool for real time extracellular metabolite monitoring with the aim of quantifying the overall kinetics of cellular metabolism (**i.e, uptake rate ($\mathbf{U_R}$), release rate $\mathbf{R_R}$ dependence on the local or surface concentration ($\mathbf{C_S}$)** which when combined with study of intracellular biochemical networks provides a holistic image of metabolism.

1.2 2D Cell Cultures

In-vitro tools like 2D cell assemblies are ubiquitously used for the culturing of cells to improve our understanding of cell biology, progression of cancer and diseases, drug discovery etc. [35]. In fact, 2D cell culture provide ease of observation and measurement which has resulted in majority of the studies in cancer research being conducted on 2D cell cultures. Hence an important aspect of a metabolic characterization tool is the adaptability to standard 2D cell cultures. Simultaneous measurement of uptake/release rates and concentrations has generally involved suspended cells or adherent cell cultures in stirred media. While these configurations can be charac-

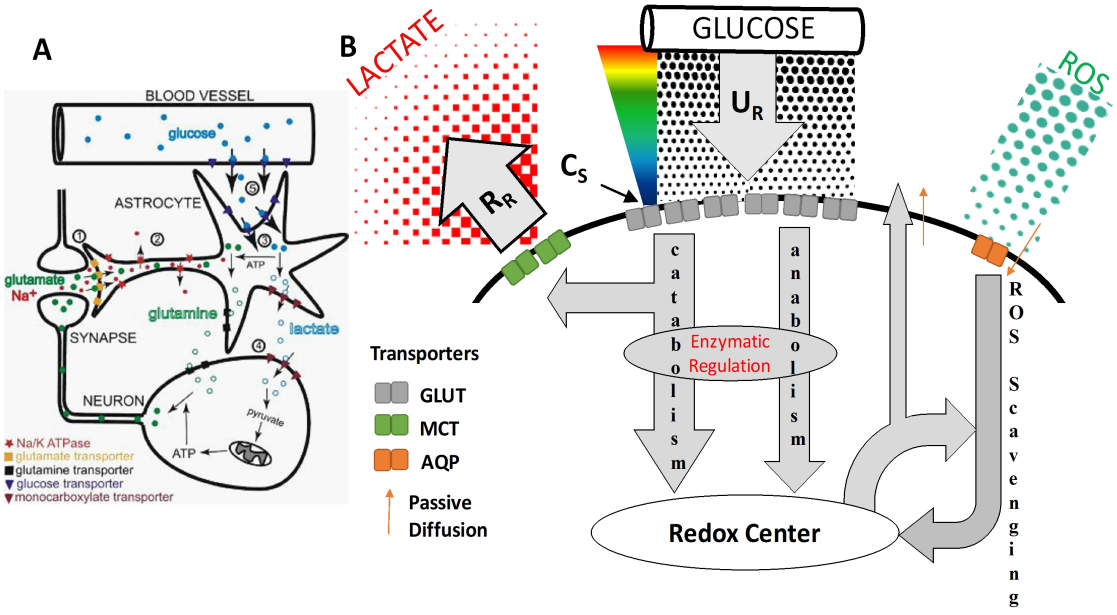

Fig. 1.2. (A) Astrocyte-neuron bioenergetic transport cycle [29]. Astrocytes are a type glial cell, which support neurons in the brain. Due to their close proximity to the interstitial blood vessel, they uptake of glucose via extracellular space from the blood brain barrier. Astrocytes acts as an energy source for neurons by converting the consumed glucose to lactate via glycolysis is transported to neurons. As a consequence of these large glucose uptake in both brain cells [31], large amount ROS is generated which is scavenged primarily by astrocytes. (B) Broad description of metabolic pathway in cells. Estimation of kinetic parameters uptake rate (U_R) or release rate (R_R) and their dependence on the local or surface concentration (C_S) is required to provide a holistic image of metabolism.

terized using volumetric sampling, the chemical microenvironment, which includes natural diffusion of chemical species, local depletion of consumed analytes, build-up of byproducts, and availability of cell-secreted soluble factors, [36–38] is altered by the stirring or the distributed nature of cells in suspension. [39] Adherent 2D cell cultures in static media maintain the natural diffusion processes within the microenvironment and thereby in principle can account for the influence of the chemical microenviroment on cell behaviour. Fig. 1.3 shows the two commonly cell culture setups used in vitro

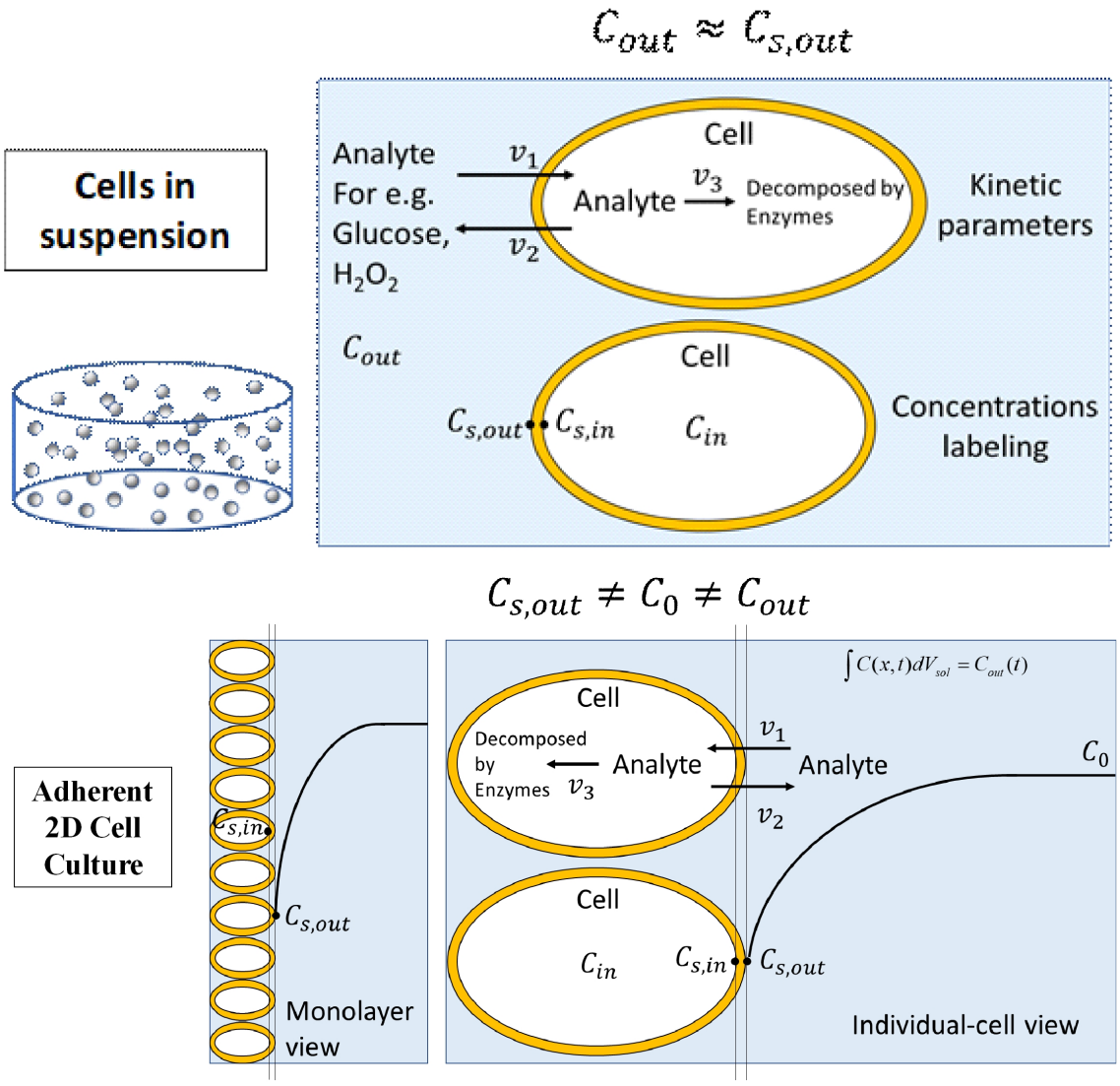

Fig. 1.3. Comparison of the typical cell culture setups used in physiology. The surface concentration varies from the bulk/background concentration in the case of adherent cell cultures.

physiological experiments. For cells cultured in suspension (Fig. 1.3A), volumetric sampling via fluorometric or colorimetric assays provides the transient C_{out}, which is sufficient to provide relevant information to understand the kinetics of the uptake process since the C_{out} (average volumetric concentration) $\approx$ $C_{s,out}$ (surface concentration). However, volumetric sampling cannot provide the relevant dynamic surface

concentration and kinetic information from adherent 2D cell cultures (Fig. 1.3B) which closely resemble in vivo chemical environments. In such 2D configurations, uptake/release of various metabolites and metabolic byproducts from/to surrounding extracellular environment [40–44] results in concentration gradients exhibiting spatial scales of hundreds to thousands of microns with time scales ranging from steady-state to millisecond regimes and local concentration changes going up to a few hundreds of μM. Due to the depletion field of such gradients (Fig. 1.3B) $C_{out} \neq C_0$ (background concentration) $\neq C_{s,out}$ and thereby measuring the transient (C_{out}) is not enough to quantify $C_{s,out}$ and the kinetics.

In situ or real time determination of the total analyte uptake rates (U_R) along with the dependence on the surface concentration requires the accurate measurement of transient concentration gradients in adherant 2D/quasi-3D cell cultures.

1.2.1 Role of Concentration Gradients

Concentration gradients are crucial in many biological processes at the single-cell, tissue, and organ levels. Presence of concentration gradients influences processes such as bacterial communication [45], quorum sensing [46], chemotaxis [47] and the cell signaling mechanisms involved in growth, migration, and differentiation, including the development of fertilized eggs, tissue inflammation, wound healing, and cancer metastasis [48,49]. As mentioned above, in 2D cell cultures via the release and uptake of molecules, cells serve as sources and sinks that combined with diffusion, result in concentration gradients in the extracellular space. A concentration gradient is generated adjacent to any active surface that secretes molecules into the surrounding medium or consumes molecules from the medium. An active surface can be anything ranging from tiny pores in the membranes of cell clusters or facilitative transporters like GLUTs. The magnitude, direction, and time scales of the gradients from the cell surface carry information that that is essential for internal cellular processes and/or

for communication with neighboring cells. Table. 1.1 shows the typical release/uptake observed at the cell surface and the resulting concentration and time scales associated with the resultant gradient.

Quantitatively mapping the extracellular concentration profile is one method by which we can extract the relevant cellular parameters from adherent 2D cell cultures.

Table 1.1.
Typical time scales and release/uptake dynamics commonly observed in physiology. $C_S(t)$ represents the instantaneous the local or surface concentration, $C_S(\mathrm{t}^-)$ represents the local or surface concentration at an earlier time, $J_S(t)$ indicates the surface flux, K_F represents a rate constant which may or may not be dependent on $C_S(t)$

Dynamics at cell surface		**Biological Example**	**Timescale**	**Concentration scale**
Instantaneous quantal release	$C_S = \pm \mathrm{M}\delta(\mathrm{t})$	Neurotransmitter or ROS release	ms	μM
Finite time quantal release	$C_S = \pm \mathrm{M}e^{-kt}$	Neurotransmitter or ROS release	ms-s	μM - mM
Constant Flux	$J_S = \pm \mathrm{M}$	Glucose uptake	min-hrs	mM
Surface Concentration Dependent Flux	$J_S = \pm K_F C_S(t)$	ROS (Hydrogen Peroxide) Uptake	min-hrs	mM
Concentration Dependent Flux	$J_S = \pm K_F C_S(\mathrm{t}^-)$	Glucose Uptake	min-hrs-days	mM
Oscillatory Flux	$J_S = \pm \mathrm{M}sin(kt)$	Glucose uptake	min	μM

1.3 Existing Tools and Techniques

1.3.1 Commercial Tools

As mentioned in section 1.2, while commercially available and widely used volumetric approaches such as flurometric or colorimetric assays although not ideal for quantifying overall kinetics and providing mechanistic insight in adherent 2D cell

cultures in static media, they do play a critical role in delivering phenomenological descriptions. Table. 1.2 shows some commercially available kits and tools used to measure metabolite uptake/release. More importantly, most of the commercial tools are focused on providing information about specific intracellular metabolic pathways. Commercially available real-time monitoring systems like the Seahorse XF analyzer measure extracellular acidification rates (pH) and oxygen consumption rates (OCR) with/without metabolic inhibitors to provide indirect estimates of glucose flux used for glycolysis and respiration. Similarly, end point measurement of glucose analogs and radiolabels provide an indirect estimate of glucose uptake by quantifying the fluorescence or radioactivity of accumulated analog which cannot be broken down at specific stages in the enzyme regulated pathways. This highlights the need for a comprehensive extracellular metabolite monitoring tool capable of quantifying mechanistic behavior, which in combination with some of the tools mentioned in Table 1.2 can provide a coherent picture of the fate of metabolites as it breaks down via multiple catabolic (energy) and anabolic (biosynthesis) pathways.

1.3.2 Techniques for Mapping Concentration Profiles

Gradient measurements require accurate absolute concentration values at various spatial positions to allow for quantitative determination of critical physiological information such as diffusive fluxes [59–62], uptake/release kinetics [63–65], influence radii [47, 66] and local concentration dependencies [41, 59]. Obtaining information about the sink/source dictates that the sensing positions must be within the transient spatial scale (also known as depletion/accumulation width) of the dynamic gradient. In the context of gradient measurements, the relevant spatial and temporal quantities are the spatial range, defined as the distance between the nearest and farthest measurement positions with respect to the source/sink; the spatial resolution, defined as the distance between each measurement position; the sampling time, defined as the time interval between data points; and the measurement time, defined as the time it

Table 1.2.
Commonly used extracellular measurement tools

Method	**Comments**
Glucose/lactate/ROS assay	Volumetric technique, $C_{out} \neq C_{s,out}$ Fluorometric or Colorimetric Poor temporal resolution.
BioProfile Analyzers (Nova Biomedical) [50, 51] Glutamine, Glutamate, Glucose, Lactate	Amperometric, potentiometric, and photometric Integrated bioreactor systems Expensive Volumetric technique, $C_{out} \neq C_{s,out}$ Temporal resolution- 4.5 min
Seahorse XF analyzer [2, 52–56] pH and Oxygen	Optical sensor Integrated metabolite monitoring system Expensive Glycolysis and Respiration rates only; not U_R Temporal resolution- 3 min
Glucose analogs and radiolabels	Optical technique Indirect estimation of glucose uptake based on intracellular accumulation of analog. Can be cell destructive Provides information on a specific pathway rather than overall kinetics End point measurement

takes to obtain quantitative concentration information over the entire spatial range. In general, the shortest transient gradient that can be measured is limited by the measurement time.

Techniques such as the vibrating probe self-referencing technique (SRT) [58, 61, 62, 67–70] have been employed to measure biomolecule gradient/flux from cell surfaces using a single biosensor oscillating between two sensing positions separated by a fixed distance (Fig. 1.3). While SRT techniques can obtain data over reasonably

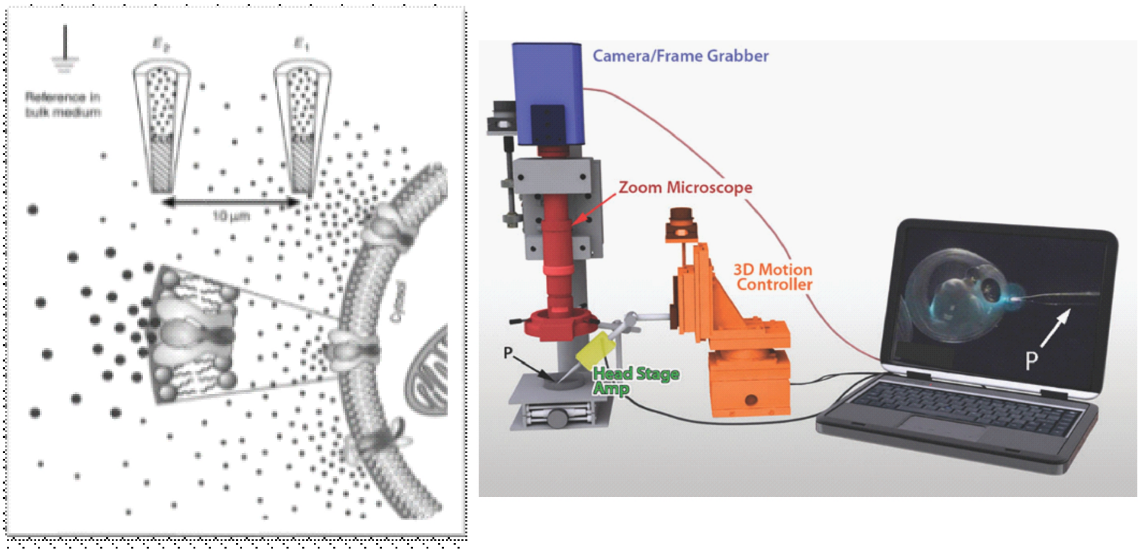

Fig. 1.4. (Left) Illustration of SRT [57] (Right) Typical SRT Setup [58]

large spatial ranges, the measurement time is much longer than the sampling time due to the restrictions on tip velocity to avoid stirring and the required number of oscillations for lock-in detection [58,61,62,69,70]. Acquisition of gradient information at multiple spatial locations requires multiple measurements, typically over tens of seconds, even with rapid sampling times (μs or ms scale) and high spatial resolution (nm scale). As summarized in Table 1.3, techniques such as scanning electrochemical microscopy (SECM) also have high spatial resolution (nm scale) and short sampling times (μs or ms scale) [71–75]; however, in the context of gradient measurements, the multi-point measurements also result in relatively large measurement times due to the restrictions on scan rate (typically 8-25 μm s^{-1}) [41,71] in order to avoid disruption of the gradient via induced convection [71,76]. Moreover, optical techniques involving a fluorescent dye that binds to the analyte of interest have been employed to make concentration sampling over the entire reaction volume. While optical techniques have been used to image a concentration gradient of an electroactive fluorescent molecule near a 2D sink electrode [77], such techniques have not been extended to

Table 1.3.
Spatial and temporal resolution reported for concentration gradient measurements using various electrochemical and optical techniques.

Technique	**Temporal resolution**	**Spatial resolution**	**Measurement time**	**Comments**
SRT [61, 62, 67, 68]	3-10 s per spatial location	1-4 μm	>> 3s	Gradient vs. position requires multiple measurements.
Amperometric microprobe at fixed positions. [79–81]	40 ms - 0.2 s (single spatial point)	2-5 μm	Not real time	Concentration vs. position requires multiple measurements
SECM [41,71]	0.5 s per spatial location	1-25 μm s^{-1} (typical scan rate)	>> 5s	Limited by scan rate.
Fluorescence microscopy [82]	2 min	< 1 μm	> 120s	Dynamic gradient extending over 200 μm was sampled every 2 min

analytes of biological interest. The lack of reversible optical probes for analytes of biological significance like hydrogen peroxide has been identified as a limiting factor in extracellular measurements [78].

1.4 Ultra-Microelectrode Arrays

Within the electrochemical techniques, individually addressed microelectrode arrays (MEAs) provide customizable spatial range and short measurement times by simultaneously measuring at multiple sensor electrodes. Amperometric MEAs have been used to demonstrate real time imaging of various non-physiological transient gradients that were set up by injecting or flowing highly-concentrated solutions (10-1000 mM) within or near a 2D MEA [83–87]. Amperometric MEAs have also been used for purposes other than gradient measurements, e.g., detection of exocytotic release from both single cells [88, 89] and clusters of cells scattered on the MEA surface [90–95].

To date, MEAs have not been widely used to study concentration profiles/gradients in the vicinity of 2D cell cultures or other common culture geometries. Even in measurements involving artificial (non-physiological) gradients, many reports present raw current data or rise times rather than absolute concentration values, thereby preventing the quantification of gradients. Several factors are believed to limit the ability to quantify gradient information.

- Firstly, the MEA substrate geometry and packaging typically are not optimized for positioning the electrodes along a gradient field in proximity to a 2D cell culture or artificial analog thereof.

- Secondly, sensitivity variability hinders the determination of absolute concentrations at multiple electrodes with sufficient accuracy. Many reports present raw current data or rise times rather than concentration values. [83–93,96] Three types of sensitivity variabilities are discussed here:

    a "Response variability" is when sensitivity changes from experiment to experiment are inherent to amperometric sensing in both single-electrode [97–100] and MEA approaches. [91, 93]. The "response variability" (typically 10-20%) [85, 96, 101] is also reported as a standard deviation of the mean value of sensitivity of the total number of replicated experiments.

b "Sensitivity drift" is when sensitivity changes during the time course of an experiment. The issue of "sensitivity drift" has received more attention in the literature of single electrodes [97–99] than in that of MEAs, although the data in MEA reports [90,91,93] show clear evidence of sensitivity drift.

c A third type, "Electrode variability" (when sensitivity changes from electrode to electrode), arises in multi-electrode approaches, as in MEAs. The "electrode variability" (typically 10-20%) [84–87, 90–92] is commonly reported in MEA literature and is calculated as the standard deviation of the mean value of sensitivity of all the electrodes in the MEA.

Taken together, the three categories of sensitivity variability make it difficult to determine concentrations at multiple electrodes with sufficient accuracy to calculate gradients based on concentration differences (ΔC) between pairs of adjacent electrodes. Previous MEA reports [83–85, 87, 91] showed maps of current at various electrode locations corresponding to a spatially-localized source of highly-concentrated solution (10-1000 mM) and more importantly, utilized an inter-electrode spacing such that ΔC was sufficiently large to not be affected by the reported sensitivity variabilities (10-20%) over the time regime interrogated. Accurate resolution of ΔC is crucial while mapping transient gradients and is essential in cases where ΔC between pairs of adjacent electrodes is small in comparison to the background concentrations. For e.g., the uptake of glucose in cells is small in comparison to level of extracellular glucose availability (typically 5-25mM in standard culture mediums).

1.5 Conclusions

To determine surface concentration, gradients and kinetics from 2D/Quasi 3D cell culture setups, quantitative mapping of the extracellular concentration profiles is required. Towards this goal, the following objectives are proposed:

- Development and fabrication of an on chip MEA to address 2D/Quasi 3D cell culture setups. The MEA design must consider the appropriate inter-electrode

spacing and electrode sizes to be able address the transient spatial scale of the relevant concentration gradient.

- A "positionable MEA approach will be required to allow for off chip culture of the cells to maintain appropriate physiological conditions which are important for proper growth and development. Moreover, positioning will also allow us to address spatial scales of multifarious gradients.

- Individual tuning of sensitivity of each electrode in the array will be required to address concentration scales which can vary in the order of μM-mM locally.

- Measurement of quantitative gradients requires the development of a calibration technique which can minimize the various sensitivity variability issues associated with amperometric sensing and provide accurate concentration transients at each spatially distributed micro-electrodes.

- Measurement of concentration transients and their associated gradients with characteristic time scales ranging from intervals as short as few seconds to longer intervals upto few hours.

- The mapping of the extracellular profile must enable quantitative determination of dynamic surface concentration, surface gradients and fluxes and hence the surface kinetic rates. For this two approaches can be adopted,

  - Extrapolation of surface concentration and gradient from the measured profile. For e.g., in case of a 1D gradient a linear extrapolation technique can be used in case surface concentration dependent flux.

  - A reaction-diffusion based simulation methodology to extract relevant surface kinetic information from the measured concentration profile.

- Real time determination of the key cellular parameters i.e, uptake rate (U_R), release rate R_R and their dependence on the local or surface concentration (C_S)

in order to quantify the overall kinetics and provide mechanistic insights of cellular metabolism.

- Simultaneous multi-analyte gradient measurements via individually addressed MEAs for the measurement of ROS (like hydrogen peroxide), glucose and lactate.

- Quantifying the metabolite uptake kinetics of normal vs cancer cells using the MEA and measurement technique to provide mechanistic insights with potential for therapeutic targeting. For this purpose two cellular systems were considered.

    a Human astrocytes versus Glioblastoma.

    b Genetically Engineered Mouse Models of Pancreatic Cancer

2. MEASUREMENT OF TRANSIENT CONCENTRATION GRADIENTS FROM ANALOGS

2.1 Introduction

Amperometric microelectrode arrays (MEAs) interrogate the concentration at multiple positions simultaneously and with sufficient sampling rates, thus being able to capture fast transient gradients. However, sensitivity variability issues in amperometric MEAs degrade the reliability of the measurements, particularly at the small concentration scales found in physiological studies. This chapter describes the development of on-chip platinum amperometric MEAs and in-situ transient calibration for reliable measurement of physiological transient concentration gradients. The MEAs were designed in a geometry suitable for measurements of gradients in conventional 2D cell culture setups. The proposed in-situ transient calibration minimizes the aforementioned effects of sensitivity variability via the in-situ acquisition of sensitivity factors for each electrode in the array just prior to capturing the transient of interest. This approach to measuring gradients could be considered a hybrid between SRT and traditional 2D MEAs, allowing acquisition of quantitative gradient information at multiple locations with measurement times significantly faster than typical SRT approaches. A planar large sink electrode (LSE, electrical analog) is used to controllably induce dynamic gradients of hydrogen peroxide (H_2O_2) by consuming H_2O_2 upon excitation (Fig. 2.7). This LSE geometry mimics a 2D cell assembly, e.g., a monolayer of astrocytes [40, 42], endothelial cells [43] or bacteria [41], consuming H_2O_2 from the surroundings. Transients/gradients generated by the LSE were characterized experimentally, and the reliability of the measurements was assessed by comparing experimental and numerical data via normalized time analysis. In contrast to previous MEA reports, the current study focuses on gradients that are

characterized by smaller background concentration scales (20 μM to 1 mM), short to long transients (150 ms-1000 s), and most importantly, small local concentration differences (ΔC down to sub-μM scale). Finally, the application of the approach to a physiological system is demonstrated by measuring H_2O_2 concentration transients near a 2D cell culture of human astrocytes and determining the associated gradients.

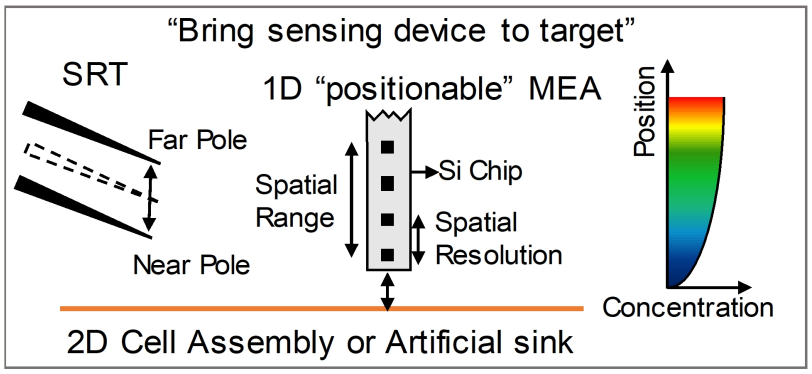

Fig. 2.1. Analyte sink induces a concentration profile (rainbow colored) where concentration increases with position with respect to the sink. A positionable MEA (1D in this work) interrogates simultaneously all the electrodes within a desired spatial range every 10 ms, thus yielding a measurement time suitable for quantifying gradients induced by sub-second events in a "single-shot" measurement. Vibrating probe techniques like SRT (left) acquire gradient information at a single spatial location by oscillating the probe tip between near and far poles. Even at a single spatial location, measurement times are typically much greater than sampling time due to restricted oscillation frequency (typically less than 1 Hz), required to keep the tip velocity below the level that disrupts the gradient of interest, and due to the need for measurements over multiple oscillation periods. The use of an MEA with appropriate electrode size and spatial range, along with in-situ calibration approach, allows measurements of concentration transients at various electrode locations, and determination of local gradients/fluxes near artificial or physiological (e.g. common 2D cell/tissue culture geometries) planar sinks of analytes.

2.2 Materials and Methods

2.2.1 Reagents

Hydrogen peroxide 30% (w/w) was purchased from Alfa Aesar (Ward Hill, MA) and phosphate buffer saline (PBS) pH 7.4 was purchased from Sigma-Aldrich (St. Louis, MO). All H_2O_2 solutions were prepared with 0.01 M PBS in ultrapure water. Human cerebral cortex astrocytes, astrocyte medium, cell freezing medium and 10 mg/ml poly-L-lysine were purchased from ScienCell Research Laboratories (Carlsbad, CA). Astrocyte medium contained 500 ml of basal medium, 10 ml of fetal bovine serum (FBS, Cat. No. 0010), 5 ml of astrocyte growth supplement (AGS, Cat. No. 1852) and 5 ml of penicillin/streptomycin solution (P/S, Cat. No. 0503). Glucose solution (50 ml of 200 g/L) and 4-well chambered cover glass systems with 1.0 borosilicate glass were purchased from Thermo Fisher Scientific (Waltham, MA).

2.2.2 MEA Design and Fabrication

Fig. 2.2A shows the details of the MEA design and fabrication process. To start with a silicon substrate was passivated by LPCVD deposition of 300 nm silicon nitride. The electrode material, titanium/platinum (10nm/100nm), was deposited by PVD (e- beam evaporation), photo-lithographically patterned, and processed by lift-off. Photo-lithographically defined SU-8 photoresist (0.5 μm, 2 μm, 0.5 μm thick) was used to selectively passivate the lead traces. The silicon wafer was diced such that each die was either a rectangle (L:10mm x W: 6mm) or a tapered rectangle with a base width of 1 mm (See Fig. 2.2B). Electrodes are located very close (30 μm) to the bottom edge of the silicon die, and were assigned the names E1, E2, E3 and so on, where E1 is the electrode closest to the edge. Each die was wire-bonded to a printed circuit board (PCB). The wired bonds were covered with either apiezon wax or epoxy resin to prevent exposure to the solution. Microelectrode arrays with varying electrode

Table 2.1.
Sizes and shapes of electrodes of various MEA

Electrode Shape	**Length of electrodes**	**Width of electrodes**	**Spacing b/w electrodes**	**No. of working electrodes**	**Spatial scale of electrode array**
Microband	50 µm	3 µm	15 µm	5	50 µm x 75 µm
	50 µm	3 µm	30 µm	5	50 µm x 135 µm
	50 µm	4 µm	15 µm	5	50 µm x 80 µm
	50 µm	4 µm	30 µm	5	50 µm x 140 µm
Square	3 µm	3 µm	15 µm	10	3 µm x 165 µm
	5 µm	5 µm	15 µm	3	5 µm x 45 µm
	5 µm	5 µm	30 µm	10	5 µm x 320 µm
	5 µm	5 µm	15 µm	10	5 µm x 235 µm
	10 µm	10 µm	30 µm	3	10 µm x 90 µm
	10 µm	10 µm	30 µm	10	10 µm x 370 µm
	10 µm	10 µm	60 µm	10	10 µm x 640 µm
	20 µm	20 µm	60 µm	10	20 µm x 740 µm

sizes and inter-electrode spacing were fabricated on a silicon substrate. Table 2.1 illustrates the specific dimensions.

In this chapter, for the non-physiological measurements, the MEA consists of a 1D array of three electrodes (5 μm $\times$ 5 μm) with inter-electrode separation of 35 μm center-to-center (or 30 μm edge-to-edge). Electrodes are located very close (30 μm) to the bottom edge of the silicon die, and designated E1, E2 and E3, where E1 is the electrode closest to the edge. For the physiological measurements, the MEA consists of a 1D array of five electrodes (10 μm $\times$ 10 μm) with inter-electrode separation of

140 μm center-to-center, which allows for measurements over a larger spatial range of the concentration profile (~600 μm).

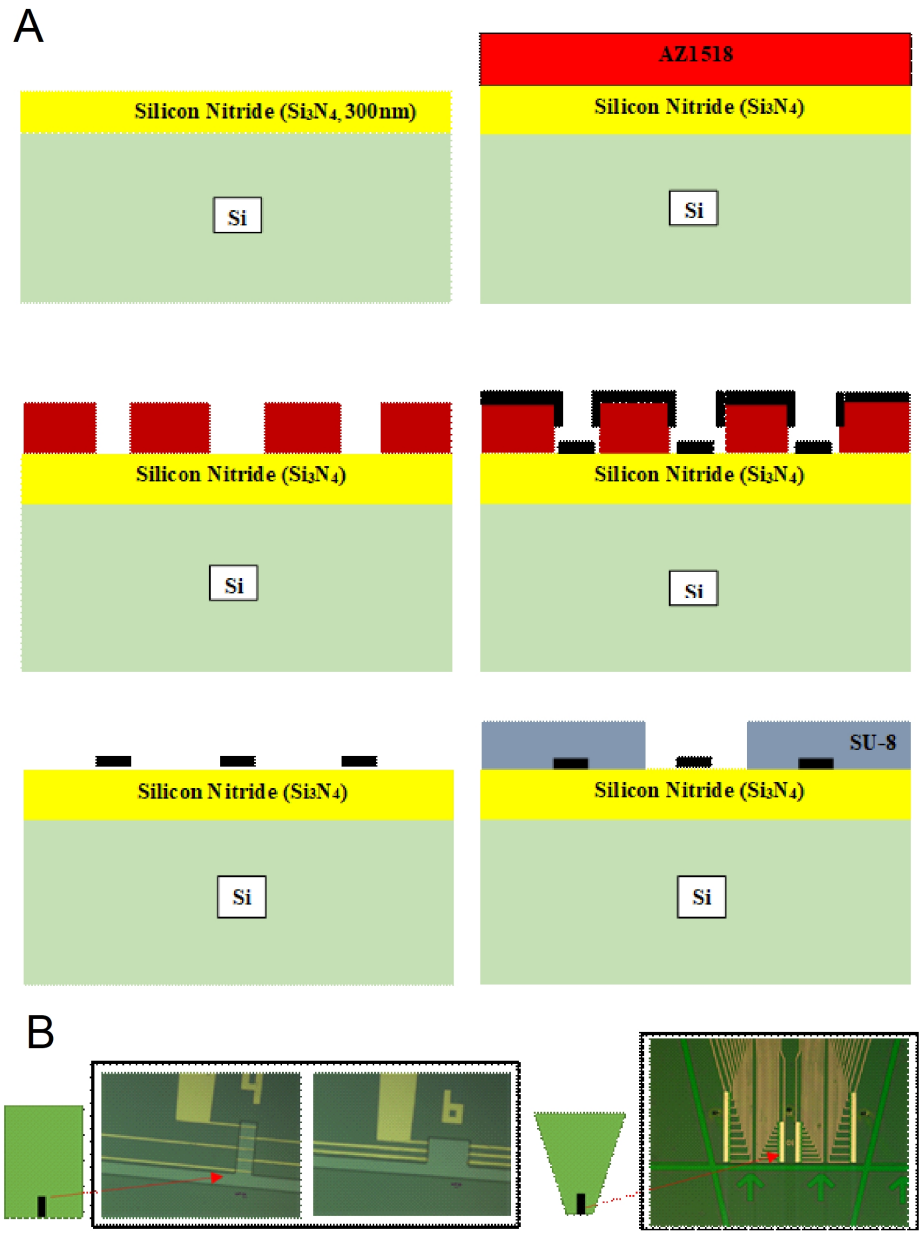

Fig. 2.2. (A) Schematic representation of the fabrication process flow. (B) (Left) MEA on a rectangular silicon chip. (Length 6mm x Width 10 mm). (Right) MEA on a tapered rectangular silicon chip (Length 20mm x Base Width 1mm)

2.2.3 Apparatus

Multiple potentiostats (Reference 600, Gamry Instruments Inc., Warminster, PA) were employed to individually bias the electrodes in the array and the LSE; the latter consisted of a platinum disk electrode (1.6 mm diameter). Platinum wire and disk (0.5 mm and 1.6 mm diameter, respectively) were used as counter electrodes; the wire was shared among the sensing electrodes in the array, while the disk was the auxiliary for the LSE. Two Ag/AgCl (sat'd 3M NaCl) reference electrodes were used; the sensing electrodes in the array shared a single reference electrode. Both the counter electrodes, LSE and reference electrodes were purchased from BASI Inc. (West Lafayette, IN). For the measurements with cultured human astrocytes, only the sensing electrodes in the MEA were used. Unless stated otherwise, all potentials are referred to the Ag/AgCl (sat'd 3M NaCl) reference electrode (See Fig. 2.3), and all experiments were performed at room temperature.

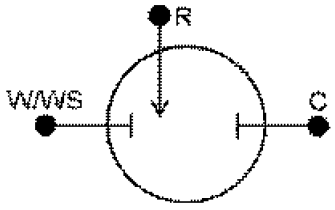

Fig. 2.3. Typical 3-electrode setup for a single sensor.Adopted from [102]

2.2.4 MEA Characterization

Cyclic voltammetry of 0.5 mM H_2O_2 in 0.01 M phosphate buffered saline was used to characterize the oxidation peak of H_2O_2 at Pt surface, which was found to be 0.5 V. For initial characterization, the amperometric response of the electrodes to concentrations ranging from 0 to 1.2 mM H_2O_2 were recorded by immersing the MEA chip in various unstirred H_2O_2 solutions (6 mL) followed by biasing the electrodes at

0.5 V. The obtained data were used to evaluate linearity, transient sensitivities, and electrode-to-electrode variabilities. For all concentration transient/gradient measurements, the electrodes were calibrated via in situ transient calibration procedure, as described in Section 2.2.6.

Hydrogen Peroxide Sensing

Hydrogen peroxide (H_2O_2) is a representative analyte for amperometric sensing, both in terms of direct redox processes at platinum (Pt) electrodes and as the intermediate species in several enzyme-based approaches. Direct oxidation of H_2O_2 at platinum occurs when the working Pt electrode is biased at 0.5V vs Ag/AgCl. The oxidation reaction which occurs generates 2 electrons per molecule of H_2O_2 oxidized at the surface. See Fig. 2.4

Tuning Hydrogen Peroxide Sensitivity

Nano structuring of the bare platinum surfaces via controlled electrochemical deposition of amorphous Platinum Black (Pt-B) was used to enhance the sensitivity towards (H_2O_2). [103] Fig. 2.6 demonstrated a charge controlled deposition of Pt-B. By maintaining consistent charge across all the electrodes in the MEA we can reduce the variability in sensitivity. However, as will be mentioned later, not only does variability still exists in other forms (such as response variability) but sensitivity also inherently depends on the position of the electrodes in the array and the geometry used for calibrations. This functionalization not only leads to an increase effective surface area while maintaining small sensing footprint but more importantly Pt-B enhances the surface reaction rate (See Fig. 2.5) and (H_2O_2) sensitivity. Electrodes were subjected to pulsed voltage injection (square wave, 10ms ON, 3s OFF) in a standard three-electrode setup while immersed in a platinizing solution composed of 17.5mM Hexachloroplatinic acid and 0.03mM Lead Acetate. The charge deposited

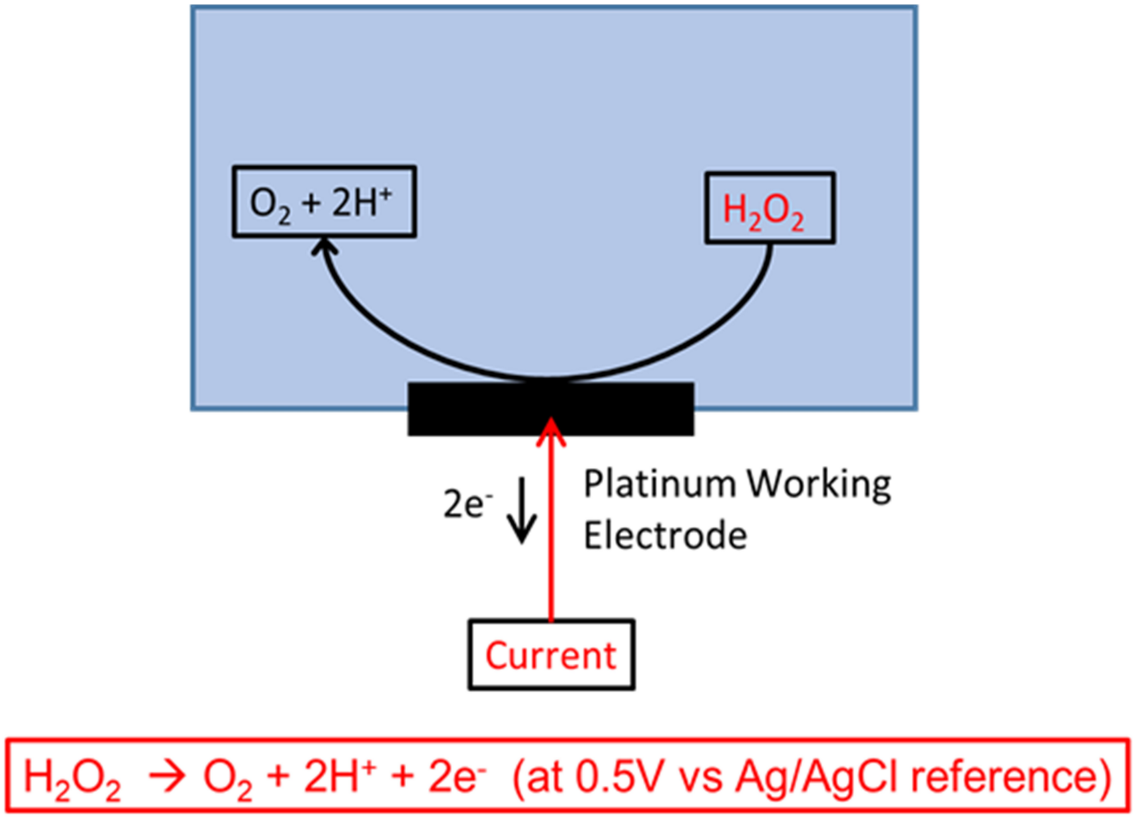

Fig. 2.4. Schematic representation of Hydrogen Peroxide oxidation at Pt electrodes

per cycle was monitored and maintained at a constant value for each electrode in the array.

2.2.5 Geometry for Transient and Gradient Measurements with LSE

The silicon chip with the MEA was manually brought into proximity to the LSE surface (Fig. 2.7) such that the three sensor electrodes were aligned perpendicular to the surface of the LSE and centered within the area of the LSE. Using optical microscopy, the distances z_i between the LSE surface and the center of each electrode E_i (i = 1, 2, 3) were found to be $z_1 \approx 165$ μm, $z_2 \approx 200$ μm and $z_3 \approx 235$ μm (Fig. 2.7). Once the chip was placed in position, all the experiments were run in sequence

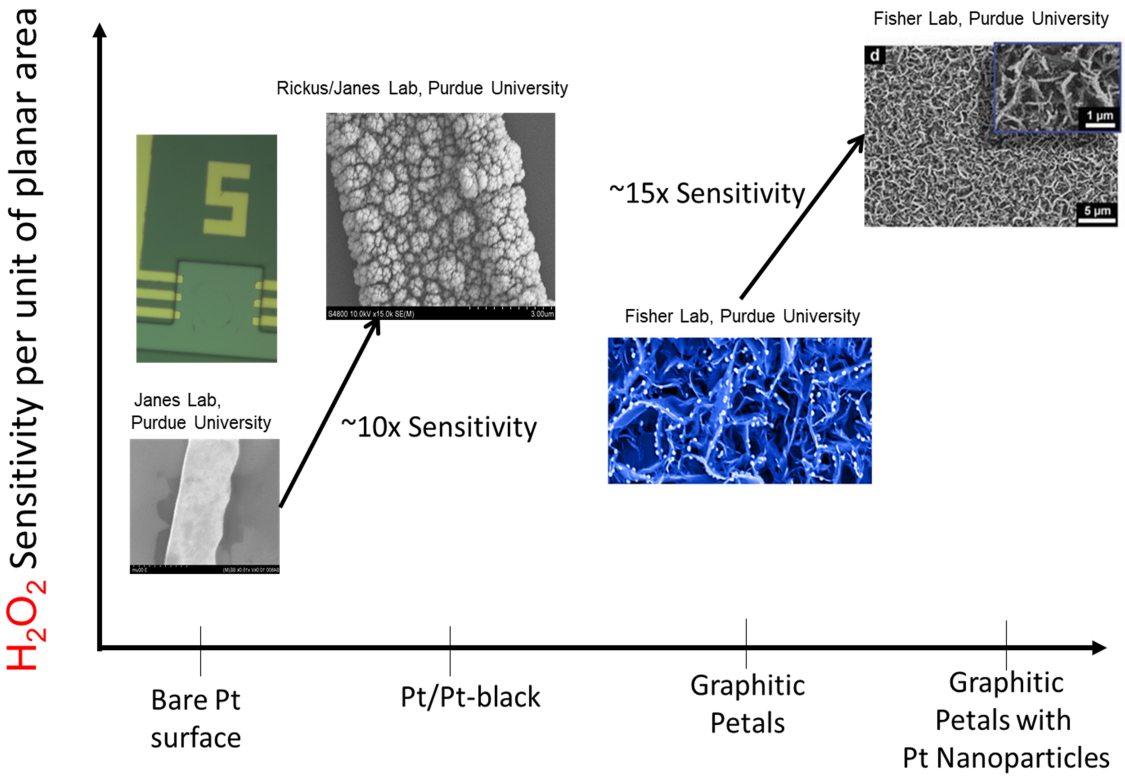

Fig. 2.5. Functionalization schemes used to enhance hydrogen peroxide sensitivity. Pt to Pt-B was employed in this work

without movement of the chip with respect to the LSE. A Petri dish containing 6 mL 0.01M phosphate buffer saline with uniform concentration of 1 mM H_2O_2 was used throughout the measurements.

2.2.6 In situ Transient Calibration and Measurement of Transient Concentrations and their Gradients

With the MEA chip positioned as described in Section 2.2.5, the three MEA electrodes were biased at 0.5 V starting from t = 0 s and throughout the course of an experiment. Every electrode i in the array provides a current $I_i(t)$ due to the time-dependent local concentration at the position z_i perpendicular to the LSE surface.

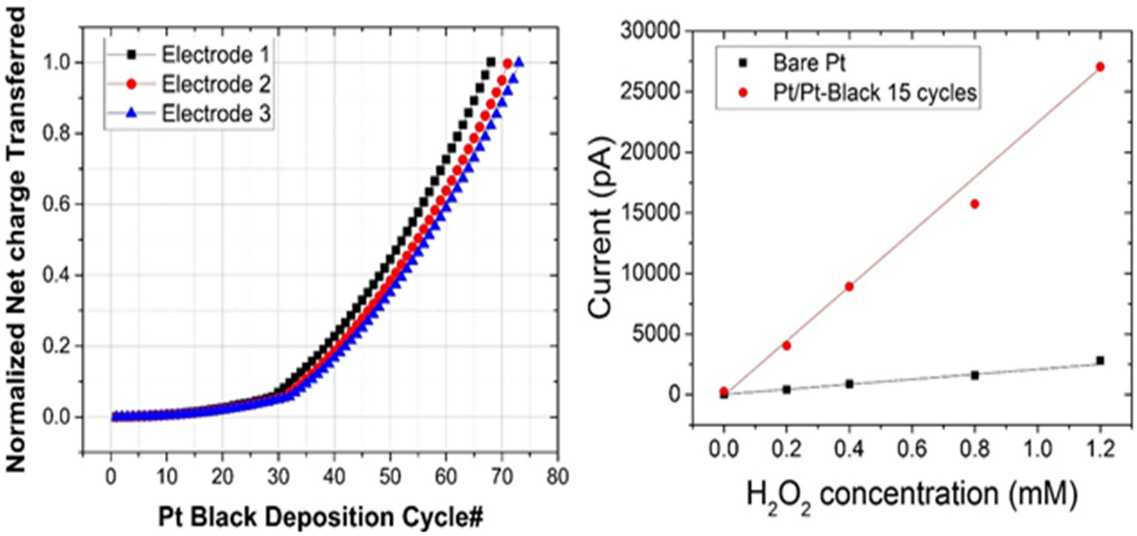

Fig. 2.6. (Left) Charge-controlled deposition of Pt-B reduces variability. (Right) Enhanced sensitivity to hydrogen peroxide (H_2O_2) achieved by nano- structuring the bare Pt electrode with Pt Black.

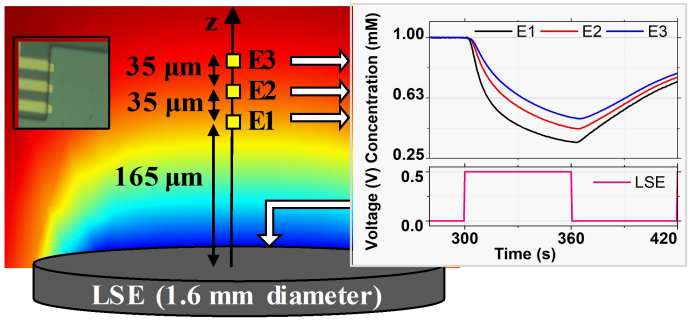

Fig. 2.7. **Schematic of experimental setup, not drawn to scale. Large sink electrode (LSE) controllably generates a concentration field (indicated by color scale) with associated gradients as a function of time and position, and in response to a potential of 0.5 V applied between 300-360 s (see inset). This diffusion-reaction system emulates a 2D assembly of cells consuming analyte from the surroundings, and constitutes the benchmark to evaluate the performance of the microelectrode array (MEA) as a reliable tool for measurement of physiological gradients.** Platinum microelectrodes E1, E2 and E3 (5 μm $\times$ 5 μm each) in the MEA are one-dimensionally arranged with inter-electrode separation of 35 μm (center-to-center). MEA packaging allowed positioning of E1 at 165 μm from the LSE. These microelectrodes record changes in local concentration at positions 165, 200, and 235 μm with respect to the LSE via amperometric signals, which are later converted into concentration data. The spatial dependence of the concentration field dictates that concentration increases with distance from LSE. Left inset shows photograph of the three microelectrodes in the MEA. Right inset shows concentration transients obtained simultaneously from the three microelectrodes in response to a potential of 0.5 V applied to the LSE between 300-360 s followed by a recovery interval from 360-420 s. The concentration was uniform and constant at 1 mM before 300 s. The spatial dependence of the concentration field dictates that concentration increases with distance from LSE, as indicated by the order E1 $<$ E2 $<$ E3 in the concentration amplitudes. This systematic behavior indicates that each microelectrode records the concentration transient locally.

No bias was applied to the LSE during the first 300 s, such that the amperometric data corresponded to the electrode responses to the uniform concentration of 1 mM H_2O_2. Taken together, the known H_2O_2 concentration ($C_0 = 1$ mM) and the electrode

currents at t = 300 s (called I_{300}) were subsequently used to convert $I_i(t)$ from each electrode into a spatially-resolved concentration vs. time, namely $C_i = C\ (z_i,\ t) = (C_0/I_{300})_i \times I_i(t)$, where $(C_0/I_{300})_i$ is the sensitivity factor for electrode i. This procedure is denoted in situ transient calibration. The settling time of 300 seconds was chosen to reduce the sensitivity drift to a level (1.7% min^{-1}) that allows measurement of transient response over several minutes, as determined by a separate experiment involving monitoring of the electrode sensitivities over approximately 2000 seconds.

Immediately after, starting at t = 300 s, time-dependent gradients were generated electrochemically by applying a sequence of four potential pulses to the LSE, consisting of voltages of 0.5 V during the interval t_{uptake} and open circuit potential during the interval $t_{recovery}$; hence, the pulse period was $t_{pulse} = t_{uptake} + t_{recovery}$. The interval t_{uptake} was set at 0.15, 1, 10 or 60 s for a given experiment, and the time $t_{recovery}$ was kept constant at 60 s for all the experiments. The local time-dependent gradient was calculated as $G_{i+1,i} = (C_{i+1} - C_i)/\Delta z$, where Δz is the distance between z_i and z_{i+1} in the direction perpendicular to the LSE surface. The $G_{i+1,i}$ is associated with the position at half the distance between z_i and z_{i+1}. From this result, the diffusive flux $J_{i+1,i}$ is calculated by invoking Fick's second law as $J_{i+1,i}$ = -D $G_{i+1,i}$, assuming that the H_2O_2 diffusion coefficient D is 1.71×10^{-5} cm^2 s^{-1} [104]. This methodology is a logical extension of the self-referencing technique (SRT), which has shown that the numerical value of $G_{i+1,i}$ is a good approximation to the actual local gradient as long as Δz is small enough to ensure the linearity of the gradient between z_i and z_{i+1} [62, 67]. Typically, gradient measurements using SRT have been performed with $\Delta z \sim 30$ μm [58, 61, 62, 69, 70].

2.2.7 Numerical Model

Numerical solution of a diffusion-reaction model was performed using Comsol Multiphysics to resolve the spatio-temporal changes in the concentration profile as a function of the potential pulses applied to the LSE. Due to the cylindrical symmetry

of the problem, the geometry of the Petri dish corresponds to the volume enclosed by r = 20 mm and $0 \leq z \leq 10$ mm, and the geometry of the circular LSE corresponds to the surface enclosed by r = 0.8 mm at z = 0. Therefore, a two-dimensional solution of the diffusion equation in cylindrical coordinates with surface reactions occurring at both the LSE and the sensing electrodes was sufficient to resolve the physics of the problem. The diffusion coefficient of H_2O_2, 1.71×10^{-5} cm^2 s^{-1}, was obtained from the literature [104], and the heterogeneous reaction rate constant (k_F) of the LSE was adjusted to fit the experimental data. See Fig. 2.8 and corresponding equations.

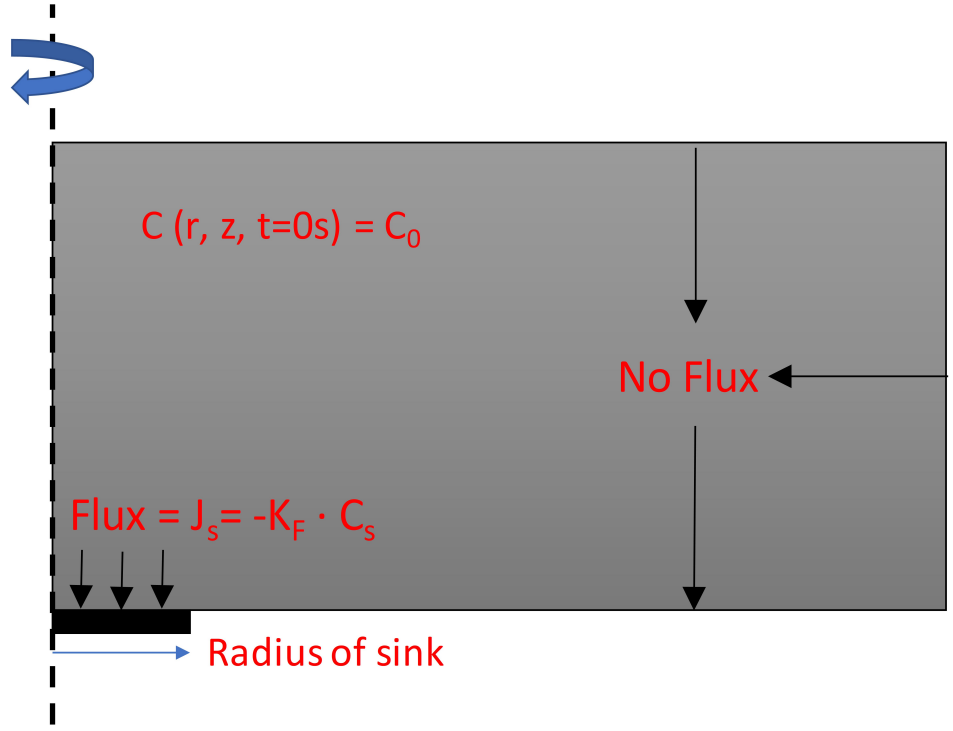

$$\frac{\partial C(r,z,t)}{\partial t} = D\left[\frac{\partial^2 C(r,z,t)}{\partial r^2} + \frac{1}{r}\frac{\partial C(r,z,t)}{\partial r} + \frac{\partial^2 C(r,z,t)}{\partial z^2}\right]$$

Fig. 2.8. Boundary conditions for solving the diffusion equation in cylindrical coordinates.

2.2.8 Cell Culture

Human cerebral cortex astrocytes were obtained from Sciencell (Carlsbad, CA) cryopreserved at passage one. Astrocytes were expanded and maintained per the company's protocol. For each experiment, passage three astrocytes (5.0×10^4 cells cm^{-2}) were seeded onto poly-L-lysine-coated chambered cover glass system wells and incubated for two days in a humidified atmosphere containing 5% CO_2 at 37°C. Medium was replaced with fresh astrocyte medium one day after seeding. Cells were used for gradient measurements after two days of incubation. Prior to the gradient measurements, the cultures were washed twice with PBS (pH 7.4), and then 0.3 mL of 5.5 mM glucose in PBS was added to culture well.

2.2.9 Geometry and Timeline for Transient and Gradient Measurements with Cultured Human Astrocytes

For the physiological experiments, a MEA with different dimensions (10 μm $\times$ 10 μm electrodes with a 140 μm pitch) was used to enable measurements over the temporal and spatial ranges of interest for H_2O_2 consumption by the cells. In addition, an alternative approach for establishing the starting time for H_2O_2 consumption and performing in-situ transient calibration was developed, as follows. The MEA was initially positioned over the cell culture, such that the bottom of the chip was 5 mm from the cell surface. Initially, the cell culture contained 0.3 mL of 5.5 mM glucose in PBS. At t = 0 s, 1.2 mL of solution containing 25 μM H_2O_2 and 5.5 mM glucose in PBS was added to obtain 1.5 mL of solution with final concentrations of 20 μM H_2O_2 and 5.5 mM glucose in PBS. At t = 30 s, the five electrodes in the MEA were simultaneously biased at 0.5 V; this bias was maintained throughout the course of the experiment. The amperometric response was allowed to settle for 300 s; then the current at each electrode at t = 330 s was used to determine the in-situ sensitivity factor for that electrode. Based on modeling of the diffusion profile using the inferred consumption rate of peroxide (and confirmed by the experimental results), the diffusion profile has

not yet reached the position of the MEA electrodes at t = 330 s, so the concentration at the location of the MEA is the background concentration of 20 μM. Just after the measurement at t = 330 s, the MEA was moved using a XYZ micro-positioner to a position such that the distances z_i between the cell culture surface and the center of each electrode E_i (i = 1, 2, 3, 4, 5) were $z_1 \approx 60$ μm, $z_2 \approx 200$ μm, $z_3 \approx 340$ μm, $z_4 \approx 480$ μm and $z_5 \approx 620$ μm. The transient measurements started immediately thereafter, and the current at each electrode was converted into a concentration using the corresponding in-situ sensitivity factor. Concentration measurements at all five electrodes were obtained in a single measurement run, and gradients were calculated at each time point from the corresponding concentration values, without smoothing or multi-point averaging.

2.3 Results and Discussion

2.3.1 MEA Device Characterization

Amperograms of ultramicroelectrodes typically exhibit an initial transient response (settling time) before achieving steady state, and conventional calibration methods use the values of steady state current to extract sensitivities. Electrodes with high heterogeneous rate constant k_F, such as the MEA electrodes biased at 0.5 V, form a significant depletion well in the solution volume adjacent to the electrode and therefore require a certain amount of time to achieve a steady state response, even in a uniform concentration solution. Hence, a settling time of 2000 s was allowed in anticipation of a response close to steady state. In our experiments, the amperograms of the electrodes biased at 0.5 V were monitored for 2000 s without observing steady state currents (Fig. 2.9). This effect, interpreted as a drift in sensitivity and observed in other MEA [91, 93, 105, 106] and single-electrode [97–99] studies, precluded the extraction of conventional steady state sensitivities. Experimental results in Fig. 2.9 show signals that drop from 625 pA (t = 300 s) to 500 pA (t = 1000 s), corresponding to an average signal drift rate of 1.7% min^{-1}. Since the concentration is uniform and

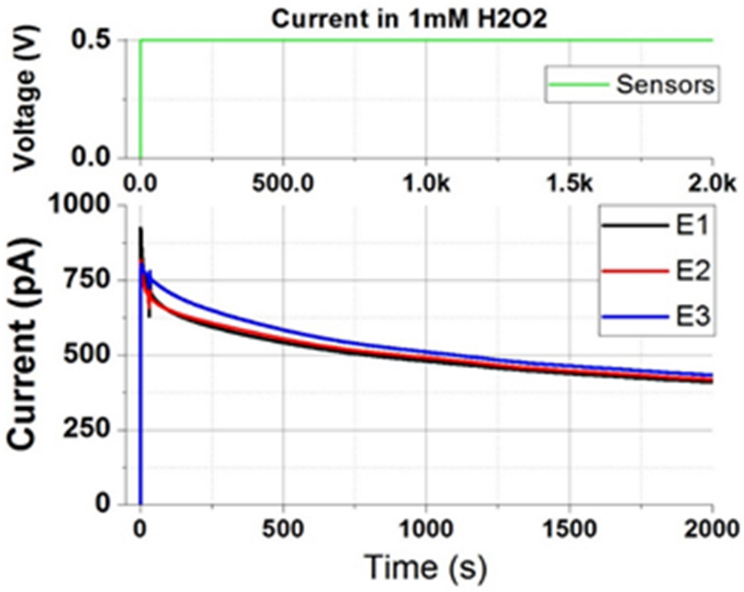

Fig. 2.9. Chronoamperometric signals show a lack of steady state response for each electrode in the microelectrode array (MEA) in a solution with uniform constant concentration of 1 mM hydrogen peroxide (H_2O_2) in 0.01 M phosphate buffer saline.

constant, the signal drift can be interpreted as sensitivity drift whose average rate is 1.7% min^{-1}. This drift rate in the signal points to the transient nature of sensitivity factor (I_0/C_0). Hence, for all the experiments the in situ transient calibration was performed at a fixed time (300 s). The in-situ calibration is the common practice when the sensor response is known to change between identical experiments, and between calibration setup and actual experimental setup. Moreover, since the transient calibration is done with the three electrodes simultaneously biased, the overlap between the diffusion fields of adjacent electrodes is already accounted for, thus providing more accurate values of sensitivity factors (I_0/C_0). The drift in sensitivity could not be eliminated by any reasonable attempt, and further investigation on the causes of sensitivity drift was not in the scope of this study; however, the effects of such drift were only important during the time periods when the gradient was either absent or sluggish with respect to the sensitivity drift rate. For instance, biasing the LSE for

60 s induces a drop of 62.5% in local concentration at electrode E1, corresponding to a rate of change of 62.5% min^{-1}, which is much larger than the sensitivity drift (1.7% min^{-1}). In comparison, the simulated results (Fig. 2.10) for the current response in 1 mM H_2O_2 for an MEA with three individually addressable 5 x 5 μm electrodes operated at a high heterogeneous rate constant of 10^{-2} cm s^{-1} demonstrate a steady state response within 1 s of biasing the electrodes. The short time to reach a steady state observed in the numerical results is consistent with literature. [107, 108]

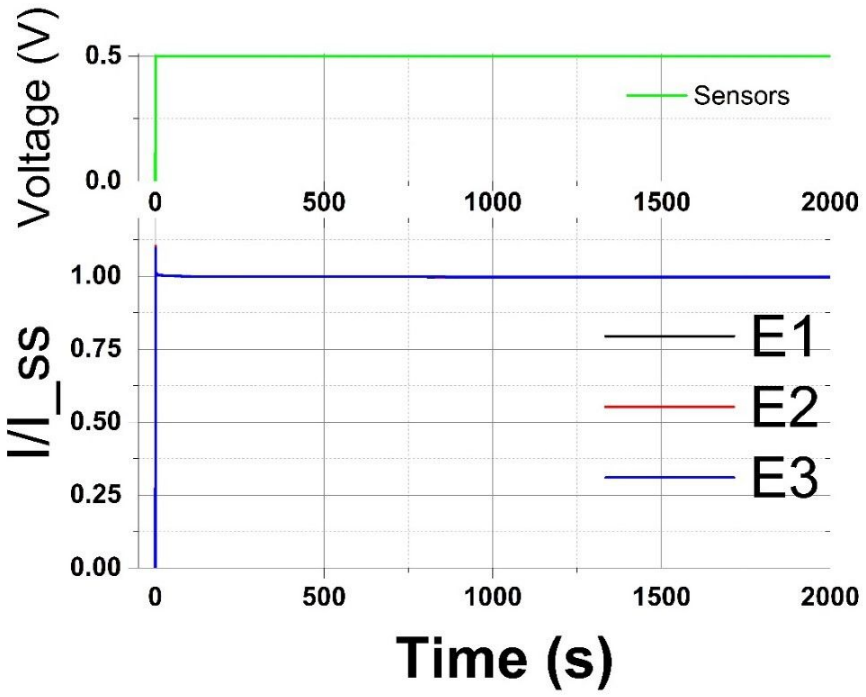

Fig. 2.10. Numerical simulations predict a steady state response for each electrode in the MEA in a solution with uniform constant analyte concentration of 1 mM. Simulated signals were normalized to the steady state current magnitude I_{SS}

Alternatively, sensitivity was obtained by plotting the current measured at t = 300 s (called I_{300}) vs. the concentration present in the solution (0, 0.2, 0.4, 0.8 and 1.2 mM H_2O_2), for each electrode in the array (Fig. 2.11). This time point (t = 300 s) was chosen to provide a good trade-off between settling time and average rate of

sensitivity drift (1.7% min^{-1}). The data of I_{300} vs. concentration (shown in Fig. 2.11) were used to assess linearity and to determine sensitivity (called S_{300} as it is associated to I_{300}) and limit of detection for each electrode. Linear fitting provided S_{300} values of 2.07 ± 0.11, 1.44 ± 0.05 and 1.47 ± 0.06 nA mM^{-1} (mean ± standard error, n = 3) for E1, E2 and E3, respectively, and the corresponding R-square values were always above 0.99, indicating that the three electrodes in the array are linear over the range of interest (0-1.2 mM). The average sensitivity ± standard deviation was 1.65 ± 0.36 nA mM^{-1}, yielding electrode variability of 21.8%, whereas the response variability from triplicate experiments was found to be 2.5%. In order to avoid the need for selectivity, the experiments were performed with media containing only H_2O_2 and buffered inert electrolyte (phosphate buffer saline), as has been common in prior reports [42, 44, 59, 109–113]. However, our approach can be applied to the sensing of other analytes and can incorporate typical approaches for achieving selectivity through enzymatic and nanostructured functionalizations [58, 61, 62, 69, 70, 100, 103, 114–116].

2.3.2 In situ Transient Calibration

Characterization of the MEA indicates that the electrode variability (21.8%) and the response variability (2.5%) are large enough to prevent accurate determination of dynamic gradients based on concentrations quantified by the traditional MEA calibration. Therefore, in situ transient calibrations were performed, as described in Section 2.2.6, to obtain calibration factors immediately prior to applying a potential pulse waveform or prior to approaching the chip to the cell surface. The in situ transient calibration minimizes both response variability and sensitivity drift by obtaining a calibration factor for every experiment "in situ" just prior to the generation of the gradient of interest, and minimizes electrode variability by performing an individual calibration of each electrode in the MEA. This approach could be viewed as a multi-electrode version of in situ calibration approaches previously used to interpret single electrode experiments [59, 71]. Like the conventional single point calibration,

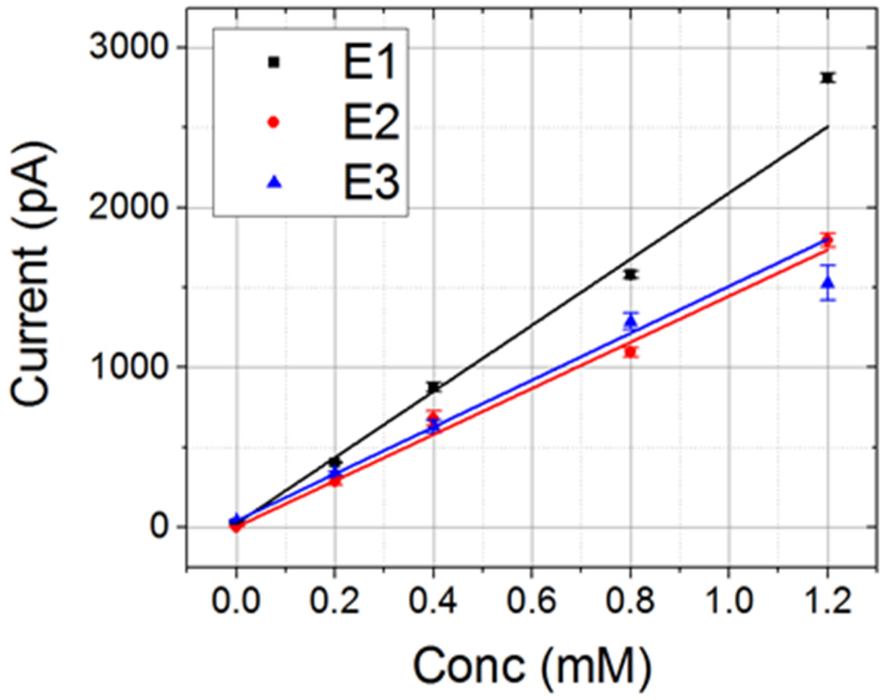

Fig. 2.11. Calibration plot indicates that concentration range utilized in the experiments (0-1 mM) lies within the linear range of each electrode (at least 0-1.2mM). The data points are mean values calculated from three identical experiments using the same array, and the error bars represent standard deviation of the mean value (n = 3). Maximum coefficient of variation of ±8% was observed.

the in situ transient calibration relies on response linearity and negligible offset, as established by the data of I_{300} vs. concentration, and works well for concentration transients that change more rapidly than the sensitivity drift rate (see discussion in Section. 2.3.1).

The approach involves placing the MEA chip in the same position to be used for the transient gradient measurements, in a known background concentration of the analyte. All electrodes in the MEA are biased simultaneously and the response of each electrode is monitored for a time interval sufficient to reduce the sensitivity drift of the electrode to an acceptably low value to allow quantitative measurements over the desired time interval. A calibration factor for each electrode is extracted based on the current at the end of this settling time, and the transient of interest is triggered immediately thereafter. Hence, the pre-requisites for performing a an in-situ transient calibration are,

- A known concentration solution prior to the generation of the gradient.
- A controllable trigger to generate the gradient. It is worth noting that these quantitative curves are possible if both the concentration C_0 is known at the instant when the gradient is triggered, and stimuli that promote/inhibit analyte consumption/release are controllably applied. In physiological experiments, stimuli of interest include shining light [117], pricking [77] or stretching cells [118], wounding a tissue [82], injecting promoter/inhibitors [61,119,120] or drugs [63], applying electrical pulses [63,65,121], and exposing a cell assembly to a step change in concentration [41].
- In case an optical or chemical trigger is not available, the MEA chip can be positioned outside the spatial scale of the gradient in the presence of the known background concentration and then lowered near the active after the sensitivity factor is obtained. Please note that although this positionable approach limits the temporal spectrum of data which can be captured, it is a work around for relatively slow gradients and fluxes (min-hrs).

2.3.3 Spatio-Temporal Resolution of Transient Concentrations Using the MEA

Fig. 2.7 shows the schematic diagram of a diffusion-reaction system constituted by an LSE surrounded by H_2O_2 solution. This system was used to controllably generate transient gradients by applying potential pulse waveforms to the LSE, and the generated gradients were measured by the MEA. A potential pulse waveform comprises four pulses, and each pulse consists of an interval (t_{uptake}) with potential at 0.5 V followed by an interval ($t_{recovery}$) at open circuit potential. During the interval t_{uptake}, the LSE electro-oxidizes (i.e., consumes) H_2O_2 causing a depletion in concentration. During the interval $t_{recovery}$, the depleted solution adjacent to the LSE recovers progressively toward the initial concentration due to diffusion from the bulk solution. Fig. 2.7 (right inset) shows the processes of depletion and recovery of the concentration near the LSE in response to a single pulse applied to the LSE. In this case, the background concentration is 1 mM, the pulse starts at t = 300 s and has t_{uptake} and $t_{recovery}$ equal to 60 s, and the concentrations at the positions of the electrodes display transient behaviors consistent with depletion and recovery. Similar results for a single pulse having t_{uptake} = 1 s and $t_{recovery}$ = 60 s in 20 μM background concentration are shown in Fig. 2.12. Note that other reports on gradient measurements using amperometric MEAs have worked with concentrations in the range of 10-1000 mM [83–87] whereas the expected physiological concentrations of H_2O_2 are below 1 mM [122]. Since sensitivity variability is more detrimental at small concentrations, the above results indicate that MEA and in situ transient calibration, altogether, are effective at physiological concentrations.

Fig. 2.13A and 2.13C show the transient concentrations for potential pulse waves with t_{uptake} of 0.15 and 60 s. Corresponding results for pulse waves with t_{uptake} of 1 and 10 s are shown in Fig. 2.14. In these four cases, $t_{recovery}$ is 60 s and the positions of the sensors with respect to the LSE are 165, 200, and 235 μm, as illustrated in Fig. 2.7. The systematic change in signal waveforms at various electrodes, and the

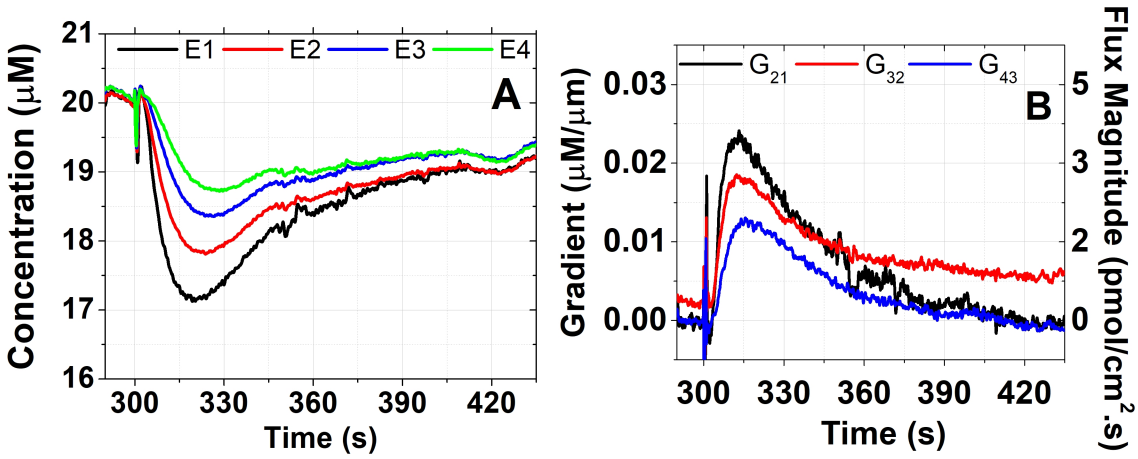

Fig. 2.12. (A) Microelectrode array (MEA) with four electrodes quantifies and resolves simultaneously in space and time the concentration profile generated by the LSE for a single pulse with t_{uptake} = 1 s and a small initial background concentration of 20 μM. The MEA is placed within 100 μm from the LSE demonstrating the utility for physiological scenarios wherein small scale gradients with fast transients and small diffusional delay times need to measured. (B) MEA measures dynamic gradients via concentration differences between pairs of adjacent electrodes. G_{21} is the gradient obtained from concentration difference between E1 and E2; G_{32} is that obtained from difference between E2 and E3 and G_{43} is that obtained from difference between E4 and E3. Diffusive fluxes associated to these gradients exhibit peaks in a physiologically relevant range of 2-5 pmol cm^{-2} s^{-1}. Diffusion coefficient of hydrogen peroxide (H_2O_2) was 1.71 $\times$ 10^{-5} cm^{-2} s^{-1}.

order in the signal amplitudes (E1 < E2 < E3), indicate that each sensor captures the concentration dynamics locally, with spatial resolution given by the inter-electrode separation (35 μm).

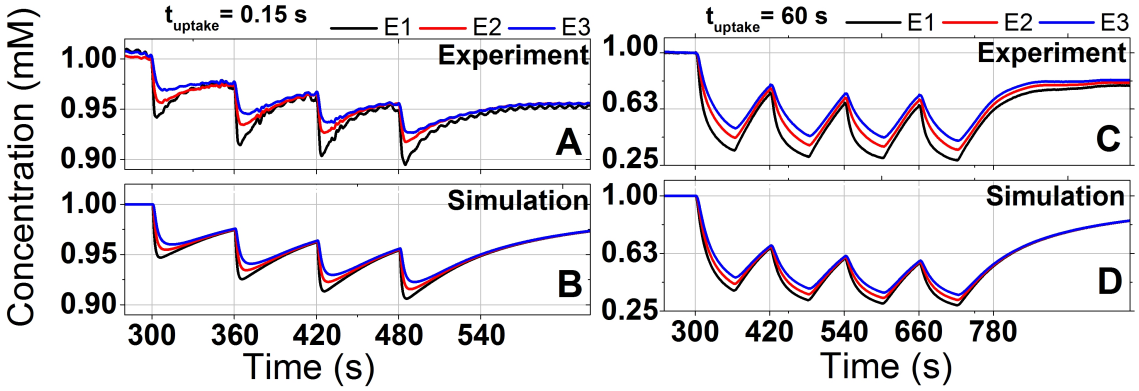

Fig. 2.13. Simultaneous concentration measurements were obtained at multiple electrodes, thus capturing transients induced by the LSE in response to uptake intervals as short as 0.15 s (left). Experimental curves (A, C) agree well with corresponding numerical simulation results (B, D) over most of the temporal scale of the experiments. The plotted curves indicate concentrations measured at electrodes E1 (165 μm), E2 (200 μm) and E3 (235 μm) in response to potential pulse waves applied to the LSE, starting at t = 300 s. Each wave comprises four pulses, and each pulse has duration $t_{pulse} = t_{uptake} + t_{recovery}$, with $t_{recovery}$ = 60 s for all the pulse waves. (A, B) t_{uptake} = 0.15 s, (C, D) t_{uptake} = 60 s. The concentration was uniform and constant at 1 mM before 300 s.

Experimental curves in Fig. 2.13A and 2.13C agree well with the simulated curves shown in Fig. 2.13B and 2.13D, respectively. These results indicate that the intrinsic response time of each individual electrode is fast enough to resolve the transient concentrations arising from uptake events as short as 0.15 s. This ability to measure gradients caused by rapid (e.g., sub-second) uptake events in stagnant solution is a major advantage of MEAs over scanning probe techniques. The good agreement between experimental and numerical results also indicates that accurate quantification of concentration is possible via the in situ transient calibration, wherein the currents corresponding to a known background concentration (in this case, 1 mM) are mea-

sured for each electrode just prior to the onset of the uptake event. In contrast, the concentrations quantified via the conventional MEA calibration do not agree with the numerical predictions neither qualitatively nor quantitatively, as shown in Fig. 2.15 (B and E). Conventional MEA calibration provides a value of sensitivity (S_{MEA}) that is obtained by averaging the sensitivities of all the electrodes in the MEA, and is usually reported along with the corresponding standard deviation (i.e., electrode variability). The usual procedure to obtain a change in concentration from the measurement of a change in raw current is:

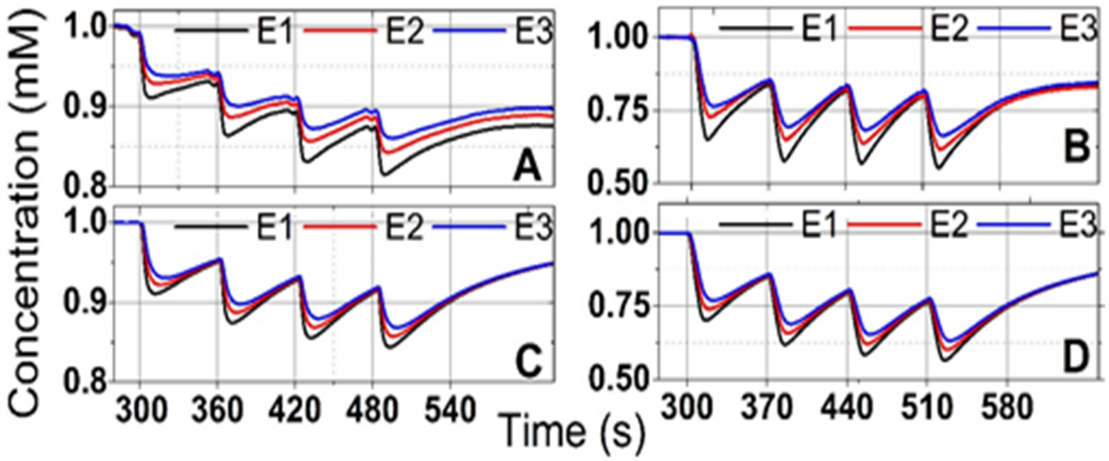

Fig. 2.14. Microelectrode array (MEA) quantifies and resolves simultaneously in space and time the concentration profile generated by the LSE via recording of transient concentrations at each electrode. Sequences of four pulses with different values of $t_{PULSE} = t_{uptake} + t_{recovery}$, with $t_{recovery}$ = 60 s for all the pulse waves. (A, C) t_{uptake} = 1 s, (B, D) t_{uptake} = 10 s. The concentration was uniform and constant at 1 mM before 300 s. Experimental curves (A, B) are in good agreement with corresponding numerical simulation results (C, D) for the transient concentrations at E1 (165 μm), E2 (200 μm) and E3 (235 μm).

$$\Delta C(t) = C(t) - C_0 = \frac{\Delta i(t)}{S_{MEA}} = \frac{i(t) - i_{REF}}{S_{MEA}}$$

where, ΔC(t): change in concentration with respect to a change in time; $C(t)$: concentration; C_0 : uniform, constant background concentration; Δi(t) : change in raw current with respect to a change in time; S_{MEA} : mean value of sensitivity of all the electrodes in the MEA; i_{REF} : reference current that is measured just prior to the measurement of the event of interest; $i(t)$: raw current resulting from the amperometric measurements

Altogether, the above results differ from other amperometric MEA reports in various aspects. First, all the measured transients are due to diffusion, as the solution is stagnant, whereas in other reports the transients are due to flow or injection of analyte [83–86]. Second, all the measurements are performed in the direction perpendicular to the active surface. This geometry is consistent with the direction of mass transport in 2D adherent cell cultures [61]. Third, the signals are quantified in absolute concentration scale. Absolute concentration values allow for quantitative determination of critical physiological information such as diffusive fluxes [59–62], uptake/release kinetics [63–65], influence radii [47,66] and local concentration dependencies [41,59]. Fourth, the experiments addressed measurements of uptake intervals as short as 150 ms, thus paving the way toward the study of rapid transient gradients in, for instance, in vitro cell networks [61].

2.3.4 Dynamic gradients and fluxes of hydrogen peroxide

Transient gradients were obtained by calculating the difference in the measured transient concentrations between pairs of adjacent electrodes, as described in Section 2.3.3 Fig. 2.16 shows the transient gradients for potential pulse waves with t_{uptake} of 0.15 and 60 s. Corresponding results for pulse waves with t_{uptake} of 1 and 10 s are shown in Fig. 2.17. The peak of the gradient inferred from the concentration difference between E1 and E2 is larger than that inferred from E2 and E3, as expected from the relative positions with respect to the LSE.

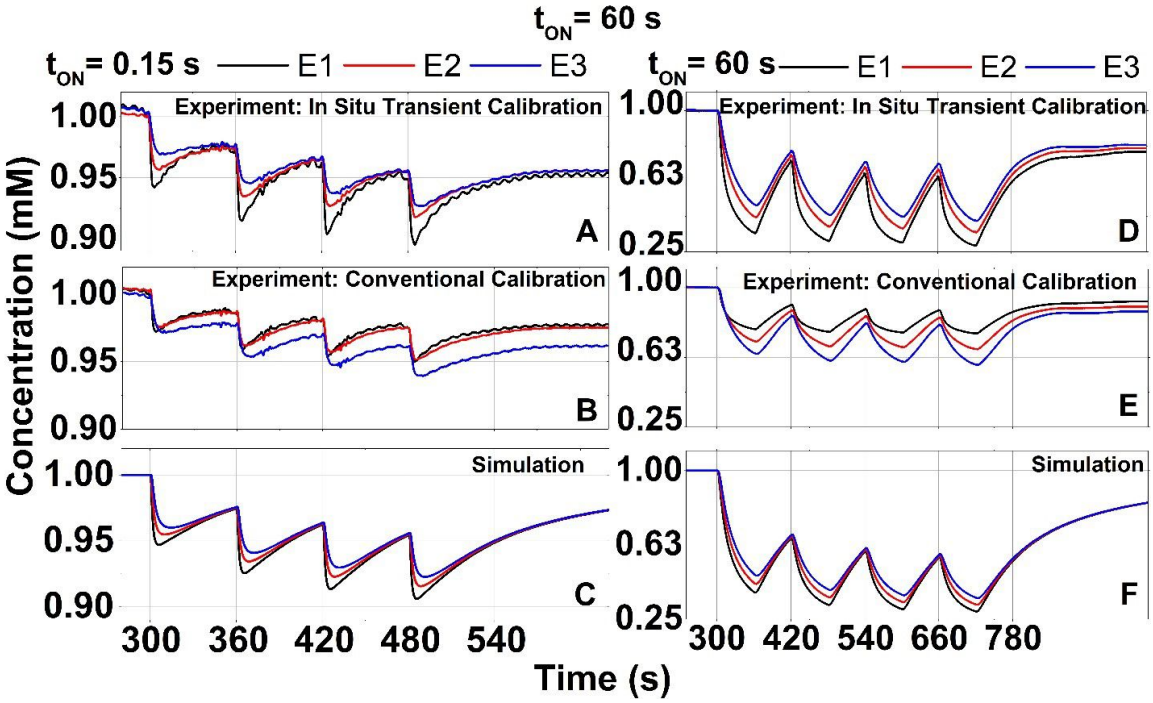

Fig. 2.15. The plotted curves indicate concentrations measured at electrodes E1 (165 μm), E2 (200 μm) and E3 (235 μm) in response to sequences of four potential pulses ($t_{PULSE} = t_{ON} + t_{OFF}$) applied to the LSE. (A, B, C) $t_{ON} = 0.15$ s, (D, E, F) $t_{ON} = 60$ s. For all sequences $t_{OFF} = 60$ s. Curves A and B are experimental and must be compared to simulated curve C. Curves D and E are experimental and must be compared to simulated curve F. Curves A and D, obtained via in situ transient calibration, are in good agreement with corresponding numerical simulation results (C and F) over most of the temporal scale of the experiments. In contrast, the experimental curves B and E, obtained via conventional MEA calibration, do not agree neither qualitatively nor quantitatively with corresponding numerical results (C and F).

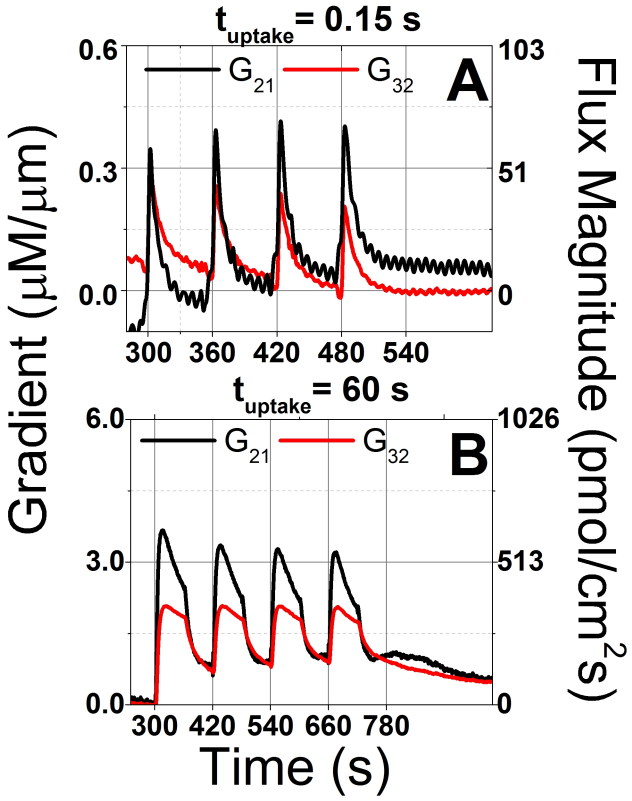

Fig. 2.16. Reliable concentration data from multiple electrodes allow for determination of transient gradients based on the concentration differences between pairs of adjacent electrodes. In situ transient calibration provides the required reliability by reducing the effects of sensitivity variability. The plotted curves indicate the gradients obtained from computation of the concentration difference between E1−E2 (G_{21}), and E2−E3 (G_{32}) in response to potential pulse waves applied to the LSE. (A) t_{uptake} = 0.15 s, (B) t_{uptake} = 60 s. For all pulse waves, $t_{recovery}$ = 60 s. Corresponding diffusive flux magnitudes can be read from the right scale axis. Peak diffusive flux magnitudes are in the range of 34-625 pmol cm^{-2} s^{-1}. These experimental results are in the same order of magnitude as reported physiological measurements.

The gradients are presented here in units of μM μm^{-1}, which are particularly useful for intuitive understanding of physiological scenarios; other relevant units such as mol cm^{-4} can be obtained using appropriate conversion factors. Using diffusion coefficients from the literature, the calculated gradients can be converted to diffusive fluxes, with peak amplitudes in the range of 34-625 pmol cm^{-2} s^{-1}. Fluxes exhibiting peak amplitudes in the range of 2-5 pmol cm^{-2} s^{-1} were also measured for background concentration of 20 μM (Fig. 2.12). These experimental results are in the same order of magnitude as reported physiological measurements. For instance, data from literature allows to calculate an average H_2O_2 influx of 29 pmol cm^{-2} s^{-1} for a monolayer of human breast cancer cells (MDA-MB-231, 2.1 $\times$ 10^5 cells distributed on a circular surface of 6.35 mm diameter) [42], and other report quoted H_2O_2 influx of 10 pmol cm^{-2} s^{-1} for bacteria biofilm. [41] These gradient measurements illustrate the potential of the MEA as an analytical tool for physiological studies.

2.3.5 Numerical Simulation

Calculation of transient gradients requires reliable measurements of transient concentrations. The reliability of the measurements was assessed via predictions based on the well-known diffusion-reaction model [99, 108, 123–126], which allows for computation of the local concentration profile as well as the corresponding transient concentrations at the positions of the sensor electrodes. The diffusion-reaction model sets the reaction flux occurring at the active surface (in this case, the LSE surface) to be proportional to the local concentration, with proportionality constant k_F (also known as heterogeneous reaction rate constant). As previously shown in Fig. 2.13, the simulated curves (panels B and D) agree qualitatively and quantitatively with the corresponding experimental curves (panels A and C) when k_F is set at 10^{-2} cm s^{-1}, thus indicating that explicit information about the active surface can be obtained by fitting the simulation to the experimental data. This strategy to obtain information about the active surface has been discussed theoretically [60].

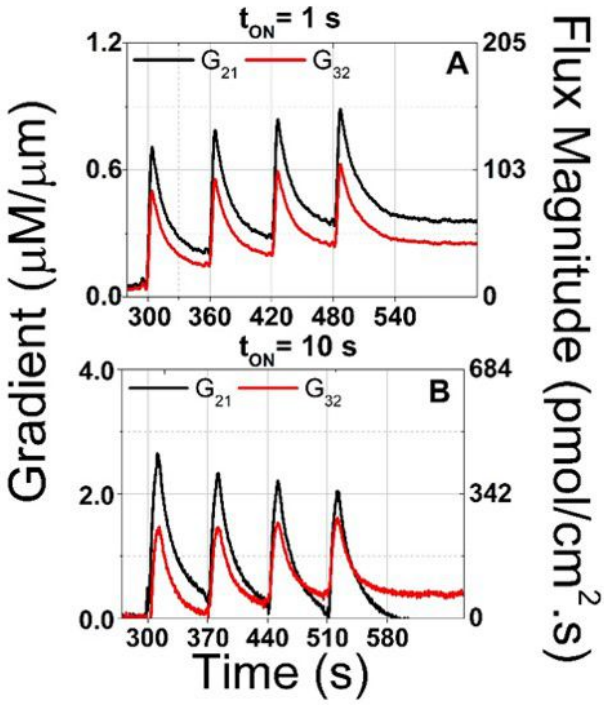

Fig. 2.17. Microelectrode array (MEA) measures dynamic gradients via concentration differences between pairs of adjacent electrodes. (A) t_{uptake} = 1 s, (B) t_{uptake} = 10 s. G_{21} is the gradient obtained from concentration difference between E1 and E2, and G32 is that obtained from difference between E2 and E3.

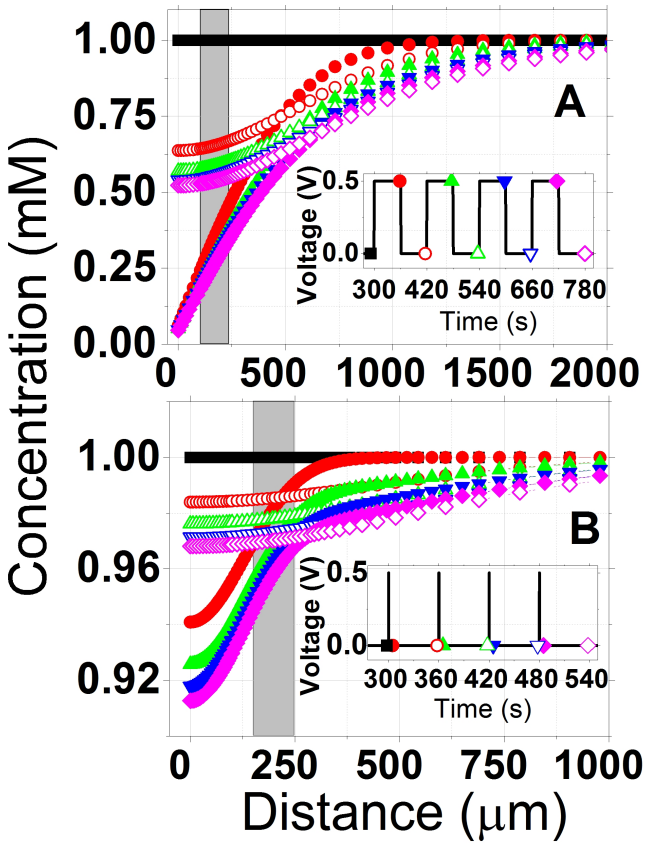

Fig. 2.18. **Simulated concentration profiles were obtained for various time points during the potential pulse waves applied to the LSE. Each pulse wave comprises four pulses. Despite being identical, the pulses yield concentration profiles that differ quantitatively from one pulse to another, due to partial recovery of the concentration profile before starting a new pulse.** Plotted curves indicate simulated concentration profiles as functions of distance along the z-axis (LSE is at z = 0) and for various time points indicated by symbols in the insets. Curves in the insets indicate potential pulse waves ($t_{pulse} = t_{uptake} + t_{recovery}$) applied to the LSE with (A) $t_{uptake} = 60$ s and (B) $t_{uptake} = 0.15$ s. In both cases $t_{recovery} = 60$ s. Shaded bands (150 μm $< z <$ 250 μm) indicate the regions occupied by the electrodes during the experiments. Since $t_{recovery}$ is the same for all pulse waves, the numerical results indicate that t_{uptake} is responsible for the magnitude of concentration change at the electrode positions during each uptake interval, and is also responsible for the transient spatial scale of the corresponding concentration fields.

The overall behavior within a pulse wave can be understood by considering Fig. 2.18, which presents simulated concentration profiles for t_{uptake} of 60 and 0.15 s. Each curve corresponds to a specific time point within the pulse waveform, as indicated by symbols in the corresponding insets, and the shaded bands represent the distance range (150-250 μm) wherein the electrodes were located during the experiments. When the LSE is biased at 0.5 V (uptake intervals), the electro-oxidation of H_2O_2 takes place at the LSE surface with a high rate constant k_F, so the concentration near the LSE becomes depleted. When the LSE is left at open circuit potential (recovery intervals), negligible electro-oxidation reaction occurs at the LSE surface, and the concentration near the LSE recovers progressively toward initial concentration due to diffusion from the bulk solution. The profile recovery is only partial for all the recovery intervals, i.e., the concentration profile never recovers the initial functional form (indicated by curves in black-filled symbols). Consequently, deeper diffusion profiles are induced pulse after pulse. This behavior indicates that, for the diffusion-reaction system studied here, each potential pulse within the studied pulse waves yields a unique concentration profile. Accordingly, the concentrations at the positions of the electrodes (i.e., within the shaded bands in Fig. 2.18) exhibit a decreasing trend from one pulse to another. This trend is captured quantitatively by the MEA, as shown in Section 2.3.3. To better assist the comprehension of spatiotemporal propagation of uptake events occurring at the LSE surface, simulated 3D plots of concentration as a function of time and distance from the LSE, and in response to single pulses with t_{uptake} of 60 and 0.15 s, are shown in Fig. 2.19.

2.3.6 Diffusional Distortion and Normalized Time Analysis of Spatial and Temporal Response

Although consumption of H_2O_2 at the LSE starts immediately after the voltage pulse is applied, the corresponding depletion of analyte at the location of the MEA electrodes does not happen instantaneously. Therefore, extracting information about

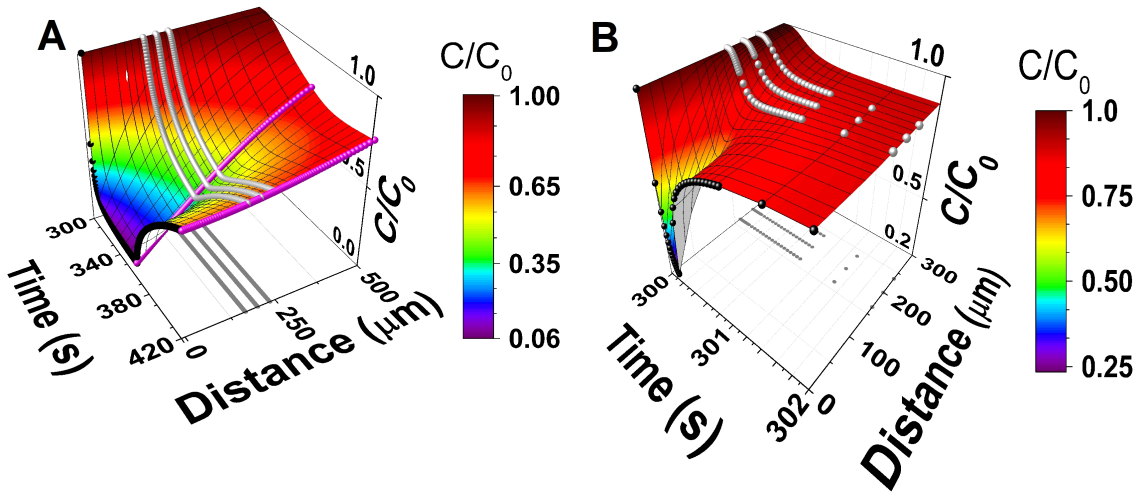

Fig. 2.19. Simulation results from reaction-diffusion model illustrate transients in concentration at the surface of the LSE (simulated black dotted curves) and time-evolution of concentration versus distance (color scale). At locations of three electrodes (simulated gray dotted curves), diffusional distortion is such that a long pulse (A) is detected while the LSE is still active whereas a short pulse (B) is detected after the LSE becomes inactive. Reconstruction of the transients at a planar source/sink is therefore possible by fitting measured transient concentration data to a reaction-diffusion model.

the events occurring at the active surface requires an approach to account for the delay time t_0 caused by diffusion between the LSE surface and the electrode locations. This phenomenon, known as diffusional distortion [81], is used here to interpret the time-dependent measurements obtained at known distances from the LSE. Note that the delay time t_0 is a position-dependent quantity and is an inherent characteristic of diffusion-reaction systems. It should not be mistaken for the response time of the electrodes in the MEA.

The analytical expression for the measured transient concentrations has the general functional form $C/C_0 = f(t_{uptake}, t_{recovery}, D, z, t)$, where C_0 is the initial background concentration, D is the diffusion coefficient, z is the position with respect to the active surface, t is the time, and t_{uptake} and $t_{recovery}$ are the uptake and recovery intervals, as defined previously. t_{uptake} and $t_{recovery}$ are controllable parameters for excitation of the active surface. Fickian diffusion is such that, for an infinitely long uptake interval (i.e., $t_{uptake} \to \infty$, $t_{recovery} \to 0$), the general functional form boils down to $C/C_0 = f(D, z, t)$. This expression can be written in terms of the delay time t_0 as $C/C_0 = f(t/t_0)$ because D, z and t are interrelated when the mass transport is due to Fickian diffusion. Therefore, for a given D, t_0 is the time required for the ratio C/C_0 at position z to reach a given value. For instance, in the present analysis t_0 is the time at which $C/C_0 = 0.7$ at the sensor positions, where the value of 0.7 corresponds approximately to the condition at which $t_0 = z_i^2/2D$, with z_i being the position of electrode i.

Derivation of Diffusional Distortion

To analyze data obtained at various electrode positions and for various values of t_{uptake}, the time scales in the experimental and numerical results can be normalized to a position-dependent delay time, t_0. When the mass transport is due to Fickian diffusion, as is the case in the experiments presented here, the general functional form of the analytical expressions describing the concentration as a function of time

and position can be written as $C/C_0 = f(t_0/t)$, where t_0 depends on both D and the position z from the source/sink of analyte, i.e., $t_0 = f(z , D)$. Specifically, given D, t_0 is the time required for the ratio C/C_0 at position z to reach a particular value.

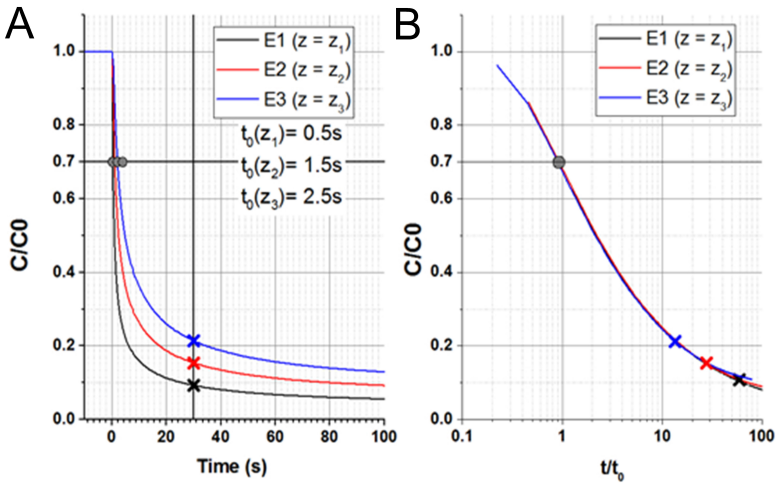

Fig. 2.20. Accounting for the diffusional delay t_0 for each electrode allows us to verify that all data points satisfy the general function $C/C_0 = \mathrm{erf}(t_0/t) = 0.7$ that describes 1D diffusion near a sink electrode. (A) measured local transient concentrations at three electrode positions for an interval $t_{uptake} = 100$ s. (B) same data as in (A) but plotted with time scale normalized to the value of t_0 for each electrode. Data points marked with "×" represent the same measurement time as in (A), but are spread in normalized time t/t_0 due to diffusional delay.

For example, Fig. 2.20A shows the concentration transients for a single t_{uptake} interval of 100 s measured by the MEA with the chip edge located roughly at 15 μm from the LSE (electrodes located at distances $z_1 \approx 40$ μm, $z_2 \approx 70$ μm and $z_3 \approx 100$ μm) using the same setup as shown in Fig. 2.7. As indicated in the main text, t_0 was chosen as the time at which $C/C_0 = 0.7$, which is approximately equal to the condition at which $t = t_0 = z_i^2/2D$ in the case of 1D diffusion near a large sink electrode, which is described by . From Fig. 2.20A, the values of t_0 are found to be 0.5, 1.5 and 2.5 s for the electrodes positioned at z_1, z_2 and z_3, respectively. When the time scale of each curve in Fig. 2.20A is normalized to the respective t_0 for

each electrode, the three curves merge together into the form of the function stated below,as shown in Fig. 2.20B.

$$C(z,t) = C_0 \left[erf \sqrt{\left(\frac{t_0}{2t} \right)} \right]$$

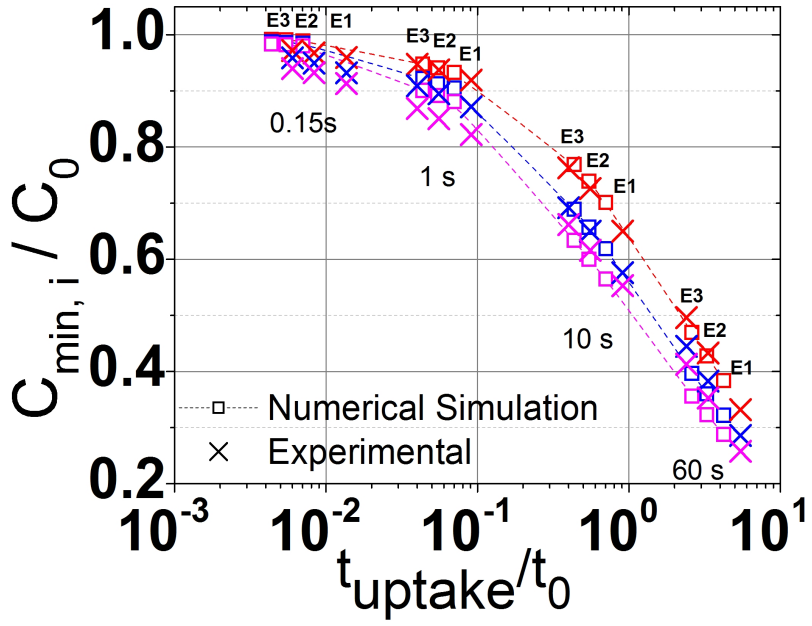

Fig. 2.21. Concentration minima (normalized to C_0) associated to the i-th pulse within a pulse wave are plotted as a function of t_{uptake}/t_0, for the four studied pulse waves, and from both experimental and simulated data. Normalization of the uptake interval t_{uptake} by the characteristic delay time t_0 associated to each electrode position allows for direct comparison between experimental and simulated data independently of diffusion coefficient and electrode positions. Experimental and simulated data agree quantitatively within a maximum difference of 7% relative to full concentration scale. C_0 is the initial background concentration, and pulse i = 3 has been omitted for clarity. Each group of points corresponds to data for the three electrodes (E1, E2, and E3) and for the indicated t_{uptake} values (0.15, 1, 10 and 60 s). Normalization of t_{uptake} by t_0 spreads and arrange the data points in the order E3, E2 and E1 from left to right in each group, consistent with t_{uptake}/t_0 being smaller for electrodes located farther from the LSE. Line connecting numerical simulation points is a guide to the eye.

As illustrated by the data points marked with "×" (corresponding to same data points in Fig. 2.20A and Fig. 2.20B), the normalization to t_0 spreads out the time axis per the position of the sensing electrode. The ability to measure t_0 directly from experiment eliminates the need to determine both the exact sensor positions and the diffusion coefficient. It should be noted that the t_0 values inferred from Fig. 2.20A are smaller than the corresponding values for the gradient experiments in Fig. 2.13 - Fig. 2.14 because the electrodes were closer to the LSE surface in the former.

The delay time t_0 allows to write the general above mentioned expression for the measured transient concentrations in terms of normalized times, i.e., $C/C_0 = f(t_{uptake}/t_0,\ t_{recovery}/t_0,\ t/t_0)$. This normalization allows for direct comparison between concentrations measured experimentally and concentrations obtained from simulations, without requiring experimental determination of the exact values for sensor positions and diffusion coefficient. To perform the reliability assessment, both experimental and simulated data must be normalized to the corresponding values of t_0. Experimental data for t_{uptake} of 60 s provided t_0 values of 12, 18 and 25 s for E1, E2 and E3, respectively. Similarly, t_0 values from simulated data were obtained by simulating the transient concentrations measured by electrodes at positions 165, 200, and 235 μm with respect to the LSE, in response to a pulse with t_{uptake} of 100 s, and then extracting the time at which $C/C_0 = 0.7$. Experimental data in Fig. 2.20 shows that electrode positioned closer to the LSE (40, 65 and 90 μm) result in smaller values of t_0 (0.5, 1.5, and 2.5 s).

Fig. 2.21 shows the concentration minima $C_{min,i}$ (normalized to initial background concentration C_0) as a function of t_{uptake}/t_0, for the four studied pulse waves, and from both experimental and simulated data. $C_{min,i}$ indicates the concentration minimum associated to the i-th pulse within a pulse wave (see naming convention Fig. 2.22). A maximum difference of 7% relative to full concentration scale (i.e., relative to C_0) is observed between experimental and simulated results, thus quantifying the ability of the MEA to resolve the signal minima for successive pulses. Here is important to note that, first, this result was obtained despite the electrode variability (21.8%)

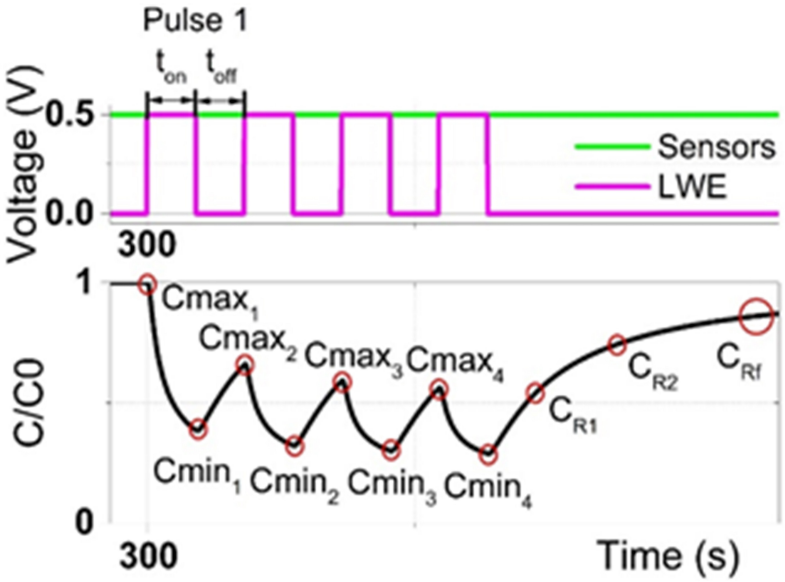

Fig. 2.22. Naming convention for the parameters extracted from the experimental and numerical results.

and response variability (2.5%) observed in our experiments, and second, other works in the literature have reported similar variabilities for MEAs [84–87, 90–92]. These observations indicate that the in situ transient calibration is crucial to minimize the effects of sensitivity variability.

Fig. 2.23 shows the concentrations (normalized to C_0) at various stages of recovery (after the fourth pulse in a pulse wave) as a function of t_{uptake}/t_0, for the four studied pulse waves, and from both experimental and simulated data. The various stages of recovery are denoted by C_{R1}, C_{R2} and C_{Rf} (see Fig. S-10 in Supplementary Material), where C_{R1} is the concentration at the end of the fourth pulse, C_{R2} is the concentration after 60 s from C_{R1}, and C_{Rf} is the concentration after 200 s from C_{R1}. In this case, the difference between the experimental and simulated results is larger, particularly for later stages of the recovery, but without exceeding 15% relative to full concentration scale. For instance, in the case of $t_{uptake} = 60$ s the simulation predicts 90% of recovery, whereas the experiment exhibited 80%. In the initial stages of recovery (C_{R1} and C_{R2}), there is reasonable agreement between the experimental and simulation results. In general, the electrode response becomes saturated as it evolves from C_{R1} to C_{R2}, and finally to C_{Rf}.

This effect is attributed to the signal drift in a uniform constant concentration, which is a phenomenon inherent to amperometric sensing, as observed in other reports [91, 93, 97–99]. It is important to note that this drift dominates only in conditions where the gradient of interest is either absent (i.e., in uniform constant concentration) or sluggish with respect to the signal drift rate (e.g., at later recovery stages). This observation indicates that quantitative measurements can be made with minimal errors in presence of a transient gradient that changes faster than the sensitivity drift rate.

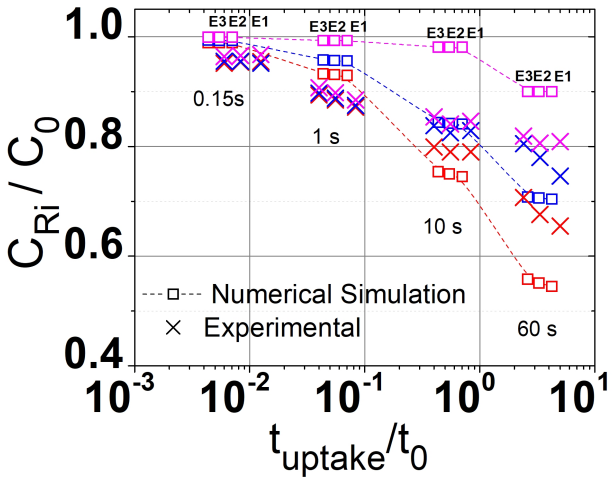

Fig. 2.23. **Concentrations (normalized to C_0) at three time points after the fourth pulse in a pulse wave are plotted as a function of t_{uptake}/t_0, for the four studied pulse waves, and from both experimental and simulated data. Experimental and simulated data agree quantitatively within a maximum difference of 15% (relative to full concentration scale) during the illustrated stages of recovery. This increase in the difference between data sets is explained in the main text in terms of sensitivity drift.** The illustrated stages of recovery are denoted by C_{Ri} (i = 1, 2, f), where C_{R1} (red) is the concentration at the end of the fourth pulse, C_{R2} (blue) is the concentration after 60 s from C_{R1}, and C_{Rf} (pink) is the concentration after 200 s from C_{R1}. These stages quantify the final recovery when the concentrations change from $C_{R1} \rightarrow C_{R2} \rightarrow C_{Rf}$ at the electrode positions. Each group of points corresponds to data for the three electrodes (E1, E2, and E3) and for the indicated t_{uptake} values (0.15, 1, 10 and 60 s). Normalization of t_{uptake} by t_0 spreads and arrange the data points in the order E3, E2 and E1 from left to right in each group, consistent with t_{uptake}/t_0 being smaller for electrodes located farther from the LSE. Line connecting numerical simulation points is a guide to the eye.

2.3.7 Extrapolating Surface Concentrations and Gradients from analogs

The reaction rate at the LSE can be modified by varying the potential vs Ag/AgCl. This was used to map the concentration profile set up two different surface reaction rates at 0.25V and 0.5V vs Ag/AgCl. By mapping the concentration profile and extrapolating back to the surface of the electrode, the dynamic surface concentration for the two cases were determined. Moreover, due to the linear nature of the profile after the initial transient, extraction of surface gradient was possible by linear fitting. For this experiment, the following setup and timeline was used (Fig. 2.24).

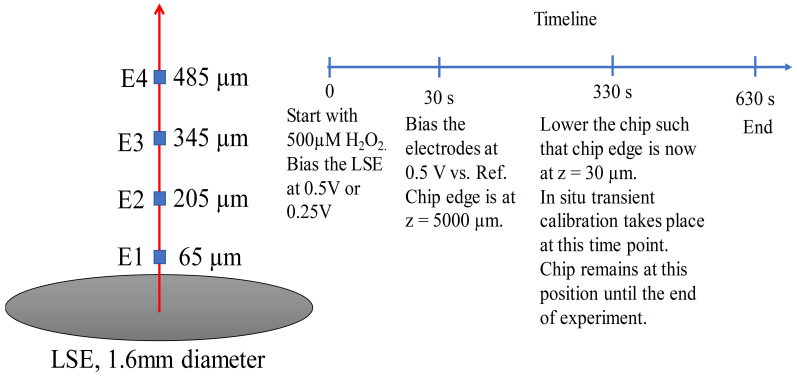

Fig. 2.24. Setup and timeline employed to extract dynamic surface concentration and varying reaction rates at the LSE surface.

Fig. 2.25 shows the concentration transients measured at the electrodes for the two varying reaction rates associated with 0.25V and 0.5V. The figure clearly demonstrates that for the case of the higher reaction rate (0.5V) the concentration at E1 is lower than in the case of lower reaction rate (0.25V). This is further illustrated from the concentration vs distance plot for the two reaction rates in Fig. 2.26. Due to higher rate of hydrogen peroxide consumption at high reaction rate (0.5V) the depletion near the LSE is higher and hence the concentration lower than the low reaction rate case (0.25V).

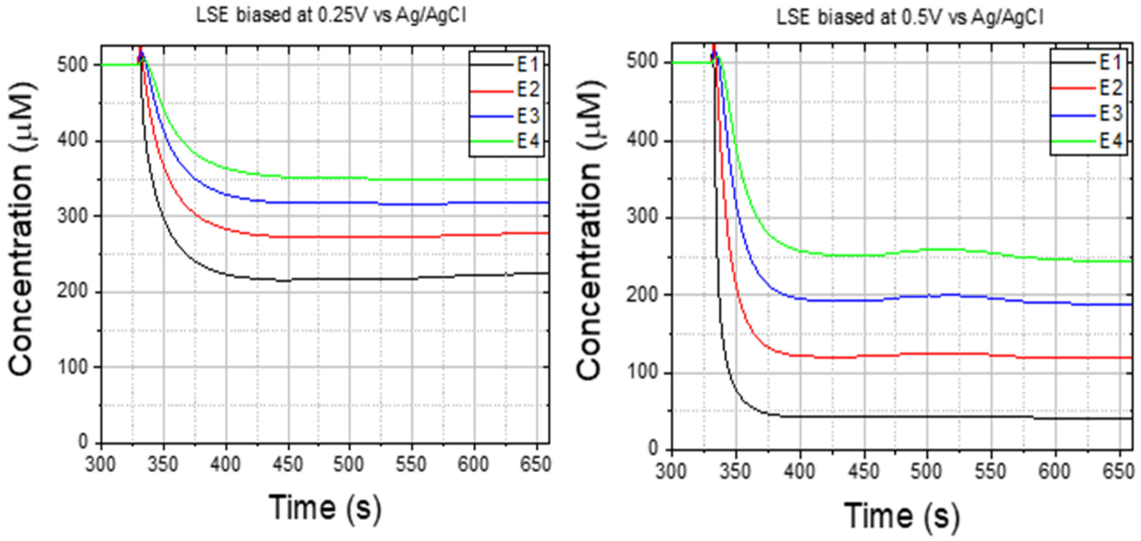

Fig. 2.25. Shows the concentration transients measured at the electrodes for the two varying reaction rates associated with 0.25V and 0.5V.

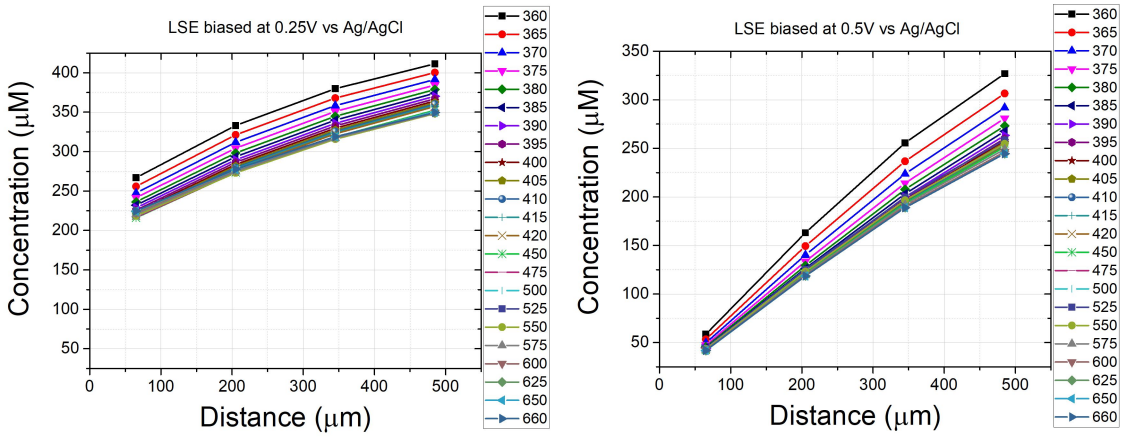

Fig. 2.26. Shows the concentration profile measured at the electrodes for the two varying reaction rates associated with 0.25V and 0.5V.

Linear fitting of the concentration profile was used to extrapolate the concentration back to the surface of the LSE at 0 μm. The linear fitting provided R^2 values greater than 0.95 confirming the linear profile thereby enabling extraction of the surface gradient. Fig. 2.27 illustrates the extrapolated surface concentration for the two different reaction rates. For the higher reaction rate (0.5V) the surface concentration is lower than the lower reaction rate case (0.25V). Fig. 2.28 clearly shows that the higher reaction rate case creates a steeper gradient.

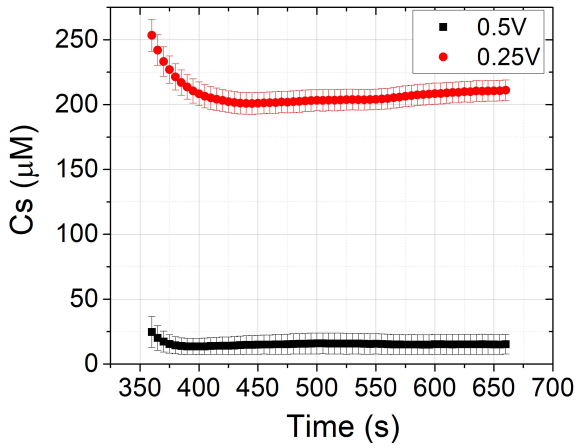

Fig. 2.27. Illustrates the extrapolated surface concentration for the two different reaction rates. The error bars indicate the standard error of the linear fitting at each time point.

By estimating surface concentrations and surface gradients we can estimate the dynamic reaction rate (K_F) Fig. 2.29 . The boundary condition at the surface of the LSE is,

$$D \bullet G_s(t) = K_F \bullet C_S(t)$$

$$K_F = \frac{D \bullet G_s(t)}{C_S(t)}$$

Where, D: Diffusion Coefficient

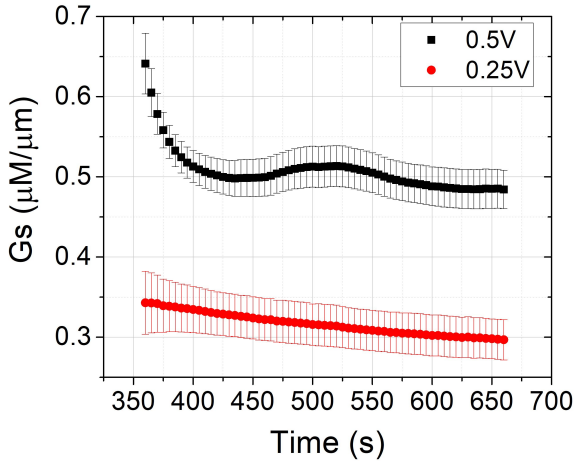

Fig. 2.28. Illustrates the extrapolated surface gradient for the two different reaction rates. The error bars indicate the standard error of the linear fitting at each time point.

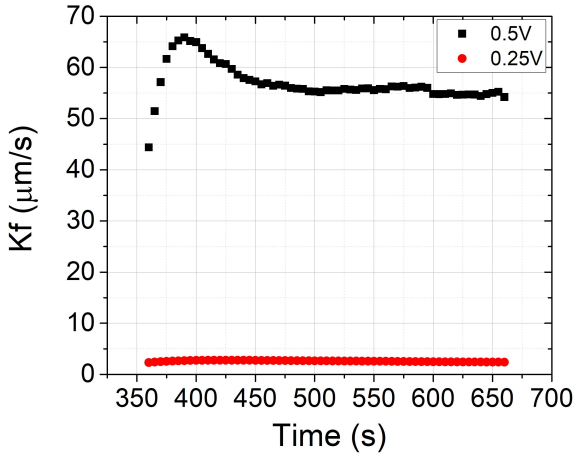

Fig. 2.29. Demonstrates the estimation of surface reaction rate vs time which can be extracted by mapping the concentration profile. The reaction rate at 0.5V is estimated at 55 μm/s and remains constant over time while the reaction rate at 0.25V is estimated at 3 μm/s.

2.3.8 Quantification of physiological gradient in 2D cell culture of human astrocytes

In-vitro demonstration of a physiological gradient takes advantage of the fact that 2D monolayers of astrocytes uptake H_2O_2 from the extracellular space [40, 42], thus setting up a concentration profile with associated gradients. Fig. 2.30 demonstrates the ability of the MEA to be positioned near the 2D cell culture and extract concentration transients at each electrode position when the cells are exposed to 20 μM H_2O_2. Due to the non-availability of a stimulus to start the uptake, a modified in situ transient calibration is employed, consisting in locating the MEA at 5 mm from the cell surface (prior to t = 330 s) to extract the calibration factors of the electrodes, and then positioning the MEA near the cells (at t = 330 s) such that the electrodes end up located at 60, 200, 340, 480 and 620 μm from the cell surface (see Fig. 2.30A). Fig. 2.30C shows the transients extracted beyond 334 s (the motion of the MEA chip takes 4 s) and indicates the presence of a gradient of H_2O_2 set up by cellular uptake, such that the order in the concentration amplitudes is E1 < E2 < E3 < E4 < E5 at any time. Fig. 2.30D shows the gradients and fluxes calculated from the measured transient concentrations. The concentration transients in this figure, and the corresponding gradients, were determined from single measurement runs, without averaging or smoothing.

2.4 Conclusions

Sensitivity variability in amperometric sensing, and particularly in MEAs, has hindered the determination of local absolute concentrations with enough accuracy as to determine gradients based on concentration differences between closely spaced electrodes. This issue becomes worse at the smaller concentration scales found in physiological studies. In this chapter, we demonstrated quantitatively the measurement of transient gradients of H_2O_2 using MEAs and an active surface that controllably induces transient gradients (analog) upon excitation, and we evaluated the reliability

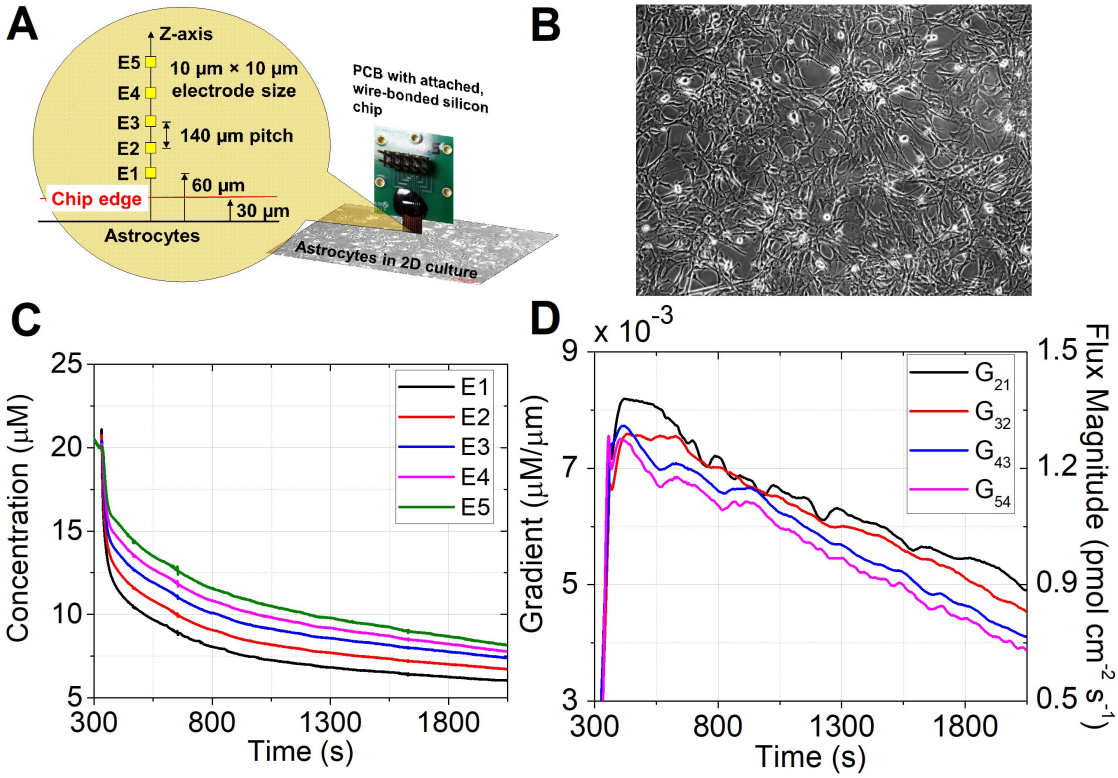

Fig. 2.30. On exposure to 20 μM hydrogen peroxide (H_2O_2), adherent 2D cell culture of human astrocytes continuously consumes H_2O_2, setting up an extracellular concentration gradient which is quantified using on-chip MEA and in situ transient calibration. (A) Setup for the experiment. MEA comprises five platinum electrodes labeled E1 through E5, which are positioned at 60, 200, 340, 480 and 620 μm from the cell surface, respectively, during the transient measurements (t > 330s). (B) Photograph of the 2D culture of astrocytes seeded in a chambered cover glass well prior to H_2O_2 exposure. (C) Concentration transients measured with the five electrodes in the MEA, at the positions illustrated in (A), corresponding to H_2O_2 exposure started at t = 0. The concentration amplitudes follow the order E1 < E2 < E3 < E4 < E5, clearly indicating the presence of a dynamic gradient. (D) Gradients calculated from measured concentrations at adjacent electrodes and corresponding diffusive fluxes, which are in the range of 0.7-1.4 pmol cm^{-2} s^{-1} and decrease with time due to depletion of the local concentration.

of the measurements by comparing experimental and simulated data via normalized time analysis. The results of this analysis indicate that the in situ transient calibration, developed here, minimizes the effects of sensitivity variability to such an extent that accurate determination of local absolute concentrations is possible. Measurements demonstrated here include transient gradients caused by sub-second uptake events (using sampling time and measurement time of 10 ms, spatial range of 70 μm, and spatial resolution of 35 μm), and in vitro gradients caused by continuous H_2O_2 uptake by a 2D cell culture of human astrocytes (using spatial range of 560 μm). The diffusive fluxes associated to the measured gradients exhibited values in the range of 0.7-625 pmol cm^{-2} s^{-1}, being this a range that holds physiological relevance. Taken together, these results demonstrate the design, fabrication and application of amperometric MEAs and in situ transient calibration for the measurement of physiological gradients and fluxes in real time.

3. HYDROGEN PEROXIDE UPTAKE KINETICS OF GLIOBLASTOMAS VS. ASTROCYTES

3.1 Introduction

The focus of this chapter is the cellular uptake of hydrogen peroxide (H_2O_2), a reactive oxygen species (ROS) that plays a vital role in the normal cell functioning when tightly regulated [19, 127–130] and is associated to neurodegenerative diseases [131] and cancer onset [21] when dysregulated. The uptake rate of H_2O_2 (U_R), defined as the number of H_2O_2 molecules transported across the plasma membrane per unit time per cell (or per unit mass of protein), has been widely studied in bacterial, [132] fungal [18, 133] and mammalian cells, [40, 42, 43, 129, 134–143] including brain cells such as neurons, astrocytes and glioma cells. Neurons have the highest glycolytic rate in brain and are a major producer of ROS, including H_2O_2, [144] but the cooperative coupling of neurons with astrocytes neutralizes H_2O_2. [40, 145, 146] Glioblastoma multiforme (GBM) is the most aggressive form of brain cancer, [147] originated from astrocytes [148] and, like astrocytes, express similar mechanisms to scavenge H_2O_2. [149] Maintenance of ROS levels in GBM is pivotal since high oxidative stress aids malignant progression but insufficient regulation results in cytotoxicity. [150] GBM reliance on antioxidant defenses to control metabolically-associated ROS, including H_2O_2, is a vulnerability which could be exploited therapeutically [21,151] and therefore has motivated the recent interest in characterization of H_2O_2 uptake rate of cancer vs. normal cells. [21, 138, 143, 152, 153]

While many studies on H_2O_2 uptake by various cell types have focused on the low concentration range where the uptake rate follows first-order kinetics, i.e., the uptake rate is proportional to the concentration, [40, 42–44, 129, 135–138] other studies have extended the concentration range and found that uptake rate exhibits a non-linear

dependence on concentration for various cell types, including astrocytes and glioma cells. [139–143] Separate determination of enzyme activities allowed this behavior to be ascribed to a combination of linear kinetics due to catalase (CAT) and Michaelis-Menten kinetics due to glutathione peroxidase (GPx1). [139–143] Since these observations were obtained with adherent cell cultures in stirred fluid, it is thus desirable to arrive at the same results but in static media.

Dynamic mapping of the concentration profile near the cell surface allows for determination of surface concentration (C_S) and surface gradient (G_S) by extrapolation to the cell plane. Surface uptake flux (F_S) is derived from G_S using Fick's law. Available fluorometric assays for extracellular H_2O_2 detection (see reviews [154–156]) have not been used to dynamically map concentration profiles. The most popular fluorometric assays, 10-acetyl-3,7-dihydroxyphenoxazine and boronate-based probes, are irreversible and therefore measure cumulative bulk effects rather than real-time local concentrations [154–156]. In contrast, electrochemical techniques like scanning electrochemical microscopy (SECM) [71–75] and self-referencing vibrating probe (SR) [58, 61, 62, 67–70] can map concentration profiles perpendicular to the surface of 2D cell cultures [41, 58, 69] but are generally limited in terms of the overall measurement time required to obtain multi-point concentration measurements over relevant spatial scales, without perturbing the solution around the probe tip. [41, 58, 61, 62, 69–71, 76] Electrochemical techniques based on microelectrode arrays (MEAs) [83–96, 101, 157–159] can provide real-time, customizable (in time and space) measurement capabilities and are more amenable to miniaturization, automation, and lab-on-a-chip integration, [94, 160, 161] which are desirable features for applications like point-of-care, microfluidic cell cultures, high-throughput drug screening, and space missions. MEAs have been generally utilized for 2D imaging of ex-vivo tissue and multi-point detection of cellular exocytotic release. Recently, MEA geometries and measurement approaches suitable for real time measurement of multi-point concentrations/gradients near aerobic granules and 2D cell cultures have been reported. [157, 159]

Table 3.1.

List of symbols and units

Symbols	Definition and Units
$C(z,t)$	Concentration of H_2O_2 as a function of position z and time t (μM)
C_0	Initial concentration (μM)
C_S	Surface concentration (μM)
C_{bulk}	Concentration at the air/solution interface (μM)
G_S	Surface gradient (μM μm^{-1})
F_S	Surface uptake flux (pmol cm^{-2} s^{-1})
U_R	Uptake rate (fmol s^{-1} $cell^{-1}$)
k_F	Uptake rate factor, defined as the ratio U_R/C_S (L s^{-1} $cell^{-1}$)
k_1	Rate constant of the linear kinetic mechanism (L s^{-1} $cell^{-1}$)
J_0	Saturation rate of the Michaelis-Menten mechanism (fmol s^{-1} $cell^{-1}$)
k_2	Concentration at $J_0/2$ (μM)
k_{obs}	Observed rate constant during volumetric sampling (s^{-1})
k_{cell}	k_{obs} normalized by the number of cells
	per unit volume of solution (L s^{-1} $cell^{-1}$)
A	Culture area (cm^2)
N	Number of cells (cell)
V	Volume of solution (L)

In this chapter, we have utilized the MEA-based approach to measure the time-dependent local concentration of H_2O_2 at multiple spatial locations near the surface of adherent 2D cell cultures of human astrocytes and glioblastoma multiforme (GBM43) cells in unstirred solutions. At each time point, the spatial profile is extrapolated to the cell plane to determine the corresponding C_S and G_S. Experiments over a range of initial concentrations (20-500 μM) allow determination of relationships between U_R and C_S. For both cell types, we found that the uptake rate is non-linear with the cell surface concentration, and this behavior is described by a combination of linear and Michaelis-Menten kinetic mechanisms, in agreement with observations from astrocytes and glioma cells from rat. [143] The obtained kinetic parameters describe the concentration dependence of the uptake rate and therefore can be used to refine reaction-diffusion models of antioxidant metabolism. The results point to the need for characterization of U_R over a wider range of C_S whenever H_2O_2 plays a role as a therapeutic agent against cancer. Altogether, the MEA, methodology and experimental results constitute a proof-of-concept of on-chip characterization of H_2O_2 uptake kinetics of cancer vs. normal cells.

3.2 Experimental

3.2.1 Reagents

Human cerebral cortex astrocytes, astrocyte medium, cell freezing medium and 10 mg/ml poly-L-lysine were purchased from ScienCell Research Laboratories (Carlsbad, CA). Dulbecco's Modified Eagle's Medium (DMEM) and EDTA solution were purchased from Life Technologies (Carlsbad, CA). Astrocyte medium contained 500 ml of basal medium, 10 ml of fetal bovine serum (FBS, Cat. No. 0010), 5 ml of astrocyte growth supplement (AGS, Cat. No. 1852) and 5 ml of penicillin/streptomycin solution (P/S, Cat. No. 0503). Glucose solution (50 ml of 200 g/L) and chambered coverglass systems with 1.0 borosilicate glass and 4-wells were purchased from Thermo Fisher Scientific (Waltham, MA). Hydrogen peroxide 30% (w/w) was purchased from

Alfa Aesar (Ward Hill, MA) and phosphate buffer saline (PBS) pH 7.4 was purchased from Sigma-Aldrich (St. Louis, MO).

3.2.2 MEA design, fabrication and characterization

The 1D MEA array consists of five electrodes (10 μm $\times$ 10 μm) with inter-electrode separation of 140 μm center-to-center such that the spatial range of the gradient measurements is 560 μm (Fig. 3.1). Electrodes are located very close to the bottom edge of the silicon die and are designated E1, E2, E3, E4 and E5. Relative to the bottom edge of the die, E1 and E5 are the closest and the farthest electrodes, respectively. Fig. S-3 in Appendix 1 provides details of the microfabrication process. Platinum black was electrodeposited to increase the sensitivity of the electrodes, using reported protocols. [61, 103] Electrodes were characterized for H_2O_2 response by performing cyclic voltammetry and amperometry in unstirred solution, finding sensitivity variations from electrode to electrode (21.8%) and from experiment to experiment (2.5%). The effects of these sensitivity variations are minimized via in situ transient calibrations where calibration factors are acquired immediately prior to the measurements near the cell surface. [159] No additional functionalization was required to achieve selectivity for H_2O_2 in the medium consisting of glucose and buffered inert electrolyte (phosphate buffer saline), a composition commonly found in the literature. [42, 44, 59, 109–113, 143] Control experiments (Fig. S-1 in Appendix 1) showed that background signals measured for astrocytes and GBM43 in PBS/glucose (without H2O2) were smaller than the signal measured during exposure to 20 μM H_2O_2. The relative sensitivities of the electrodes to H_2O_2, glucose and lactate were also characterized (Fig. S-2 in Appendix 1), and the selectivities of H_2O_2 with respect to glucose and lactate were found to be 1130 and 437, respectively. In general, changes in metabolic activity upon exposure to H_2O_2 would change the magnitude of background signals. Reports from the literature can be used to estimate the relative effects. The exposure of rat astrocytes to a sustained concentration of 50 μM H_2O_2

for 2 hours has been reported to reduce both glucose uptake and lactate release. [162] While some types of cancer cells release H_2O_2 due to oxidative stress, [163, 164] no release of H_2O_2 by human glioblastoma cells has been observed upon exposure to H_2O_2. [165] Therefore, for cells in PBS/glucose with or without H_2O_2, the response due to cellular release of interferents (if any) is expected to be below the magnitude of the signals measured for H_2O_2, even for the smallest H_2O_2 concentration in this study.

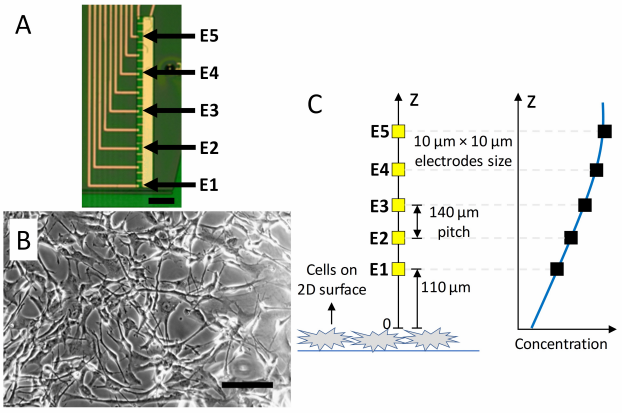

Fig. 3.1. **MEA simultaneously measures concentrations at five positions near the surface of cells in 2D cell culture.** (A) Photograph of a representative MEA. 10 platinum microelectrodes, 10 μm × 10 μm each, are arranged in a one-dimensional array, with the five electrodes indicated by arrows used in experiments, thus yielding a pitch of 140 μm. Scale bar is 100 μm. (B) Photograph of a representative culture of human astrocytes on a 2D surface. Scale bar is 100 μm. (C) Schematic of the experimental setup (not drawn to scale) illustrating how the five MEA electrodes acquire five spatial data points of the concentration profile near the cell surface. The MEA packaging allows positioning of E1 at 110 μm from the cell surface.

3.2.3 Apparatus and method for spatio-temporal resolution of gradients

The schematic diagram in Fig. 3.1(C) illustrates a reaction-diffusion system comprising a 2D cell culture (astrocytes or GBM43) surrounded by H_2O_2 solution and

having five MEA electrodes arranged perpendicularly to the cell culture plane. Each electrode in the MEA operates amperometrically due to the application of a potential that drives the electrooxidation of H_2O_2 at the electrode surface and results in an electrical current proportional to the local concentration of H_2O_2. The MEA electrodes were individually addressed by dedicated potentiostats (Reference 600, Gamry Instruments Inc., Warminster, PA) using shared counter and reference electrodes. The counter electrode was a platinum wire of 0.5 mm diameter and the reference electrode was Ag/AgCl (sat'd 3M NaCl), both purchased from BASI Inc. (West Lafayette, IN). Unless stated otherwise, all potentials are referred to the Ag/AgCl (sat'd 3M NaCl) reference electrode, and all experiments were performed at room temperature. The 1D arrangement of the MEA electrodes allows mapping of the concentration profile over a spatial range of 560 μm. The sampling period of each electrode was set at 0.5 s. The measurements were run in a sequence of steps, as follows. Initially, no intentional H_2O_2 was in the culture medium. Upon exposure to H_2O_2 at t = 0 s, the cells immediately begin uptaking H_2O_2 and this uptake generates a transient concentration gradient in the direction perpendicular to the cell culture plane. As it is usual in amperometric measurements, the signals must be conditioned for some time such that the diffusion field around each electrode is reasonably stable. In the present study the conditioning time is 300 s and begins by biasing the electrodes 30 s after H_2O_2 exposure. During the conditioning time the MEA chip edge is at 5 mm from the cell surface, and just at the end of this conditioning time (i.e., at t = 330 s) the chip edge is positioned at 30 μm from the cell surface using a XYZ motion control system (Applicable Electronics, New Haven, CT). This movement of the MEA chip from 5 mm to 30 μm takes 4 s. The relevant data is thus acquired from t = 334 s onwards and the electrode closest to the cell surface (i.e., electrode E1) is located at 110 μm from the cell surface, as illustrated in Fig. 3.1. The amperometric signals measured at t = 330 s and the bulk initial concentration of H_2O_2 provided the information to compute the calibration factors for the electrodes, as reported elsewhere. [159]

3.2.4 Astrocyte cell culture

Human cerebral cortex astrocytes arrived from ScienCell (Carlsbad, CA) cryopreserved at passage one. Astrocytes were expanded and maintained according to the company's protocol. For each measurement of H_2O_2 consumption, passage-three astrocytes (5.0×10^4 cells cm^{-2}) were seeded onto poly-L-lysine-coated chambered coverglass 4-well systems and incubated for two days in a humidified atmosphere at 37 °C with 5% CO_2. Medium was replaced with fresh astrocyte medium one day after seeding. H_2O_2 uptake rate was measured after two days of incubation. By this time, cultures had grown to approximately 1.2×10^5 cells cm^{-2}. This number was calculated from a growth curve of three human astrocyte cultures (5.0×10^4 cells cm^{-2}) counted each day of incubation for three days. The doubling time was calculated to be 1.547 days. The exponential fit of the cell counts had an R^2 ¿ 0.99. Cells were counted by hemocytometer and viability was determined through Trypan Blue Exclusion. Individual cell counts for each culture were acquired immediately following each measurement.

3.2.5 Glioblastoma cell culture

Primary patient-derived GBM43 cells were provided by Dr. Jann Sarkaria (Mayo Clinic, Rochester, MN) and have been described prior. [166] Cells were maintained in Dulbecco's Modified Eagle's Medium (DMEM) containing 10% fetal bovine serum in humidified atmosphere at 37 °C with 5% CO_2. Cells were propagated in T75 flasks and fed with growth media every other day. Cells were enzymatically dissociated using 0.25% trypsin/0.5 mmol L^{-1} EDTA solution and passaged every 3 days. For each measurement of H_2O_2 uptake rate, propagated GBM43 cells were trypsinized and plated at a density of 10^5 in 1 mL of growth media in 12-well plates (Corning Costar 3515). H_2O_2 uptake rate was measured after the cells had grown to confluency over 3 to 4 days. Cells were counted by hemocytometer and viability was determined

through Trypan Blue Exclusion. Individual cell counts for each culture were acquired immediately following each measurement.

3.2.6 Cell imaging and preparation for MEA measurements

Prior to exposing cultures to H_2O_2 and measuring uptake rate, cultures were imaged at 100X magnification with ToupView then washed twice with 5.5 mM glucose in PBS (pH 7.4). The culture wells were then filled with 0.3 ml (astrocytes) or 1 ml (GBM43) of 5.5 mM glucose in PBS. Next, the culture wells and MEA were put in position for measurement. Finally, 1.2 ml (astrocytes) or 2 ml (GBM43) of PBS with 5.5 mM glucose and H_2O_2 was added, so the resulting H_2O_2 concentrations were 20, 60, 100, 200, 300 or 500 μM in total volumes of 1.5 ml (astrocytes) or 3 ml (GBM43). The corresponding surface area and height of the liquid were 1.8 cm^2 and 0.83 cm (astrocytes), and 3.8 $cm^2$and 0.79 cm (GBM43), respectively. Following each measurement in H_2O_2 solution, cells were imaged again. Fig. S-4 in Appendix 1 shows representative pictures of astrocyte and GBM43 cultures before and after exposure to 500 μM H_2O_2.

3.2.7 Viability assays

Live/dead assay of astrocyte and GBM43 was used to assess viability of cells after 2 hours of H_2O_2 exposure. Cultures were treated in one of four ways: (1) 2 hours in PBS with 5.5 mM glucose, (2) 2 hours in PBS with 5.5 mM glucose and 500 μM H_2O_2, (3) 20 minutes in formalin (negative control), and (4) directly assayed without treatment (positive control). Following treatment, cultures were stained with CellTracker Green (live stain) and propidium iodide (dead stain) (Thermo Fisher Scientific). Images were obtained using confocal fluorescence microscopy with model FV1000 (Olympus). Fig. S-5 in Appendix 1 shows the results. Two hours in 500 μM H_2O_2 had no apparent harmful effect on glioblastoma viability (Fig. S-5(H) in Appendix 1). On the other hand, two hours in H_2O_2 caused a fraction of astrocytes

to lose adherence and thus being washed away during the live/dead assay, which would explain the apparent reduction in cell confluence (Fig. S-5(D) in Appendix 1). However, the astrocytes that remained adhered were viable.

3.2.8 Simulation details and numerical model

Since the concentration field induced by cellular uptake of H_2O_2 is one dimensional, i.e., perpendicular to the plane of cell culture, the simulation geometry consisted of a one-dimensional domain with length L equal to the distance between the cell surface and the solution/air interface, as shown in Fig. S-6 in Appendix 1. The diffusion equation (3.1) is solved numerically using Comsol finite element software,

$$\frac{\partial C(z,t)}{\partial t} = D\frac{\partial^2 C(z,t)}{\partial z^2} \tag{3.1}$$

where $C(z,t)$ is the concentration of H_2O_2 as a function of position z and time t, and $D = 1.71\times\ 10^{-9}$ m^2 s^{-1} is the diffusion coefficient of H_2O_2. [104] The boundary condition at the cell surface, located at $z = 0$, is set by U_R which is a function of C_S, as given by Eq. (3.2),

$$D\frac{A}{N}\left.\frac{\partial C(z,t)}{\partial z}\right|_{z=0} = U_R = k_F(C_S)\cdot C_S \tag{3.2}$$

where A is the culture area and N is the number of cells. The C_S dependent uptake rate factor $k_F(C_S)$ is defined as the ratio U_R/C_S. As discussed in Section 3.3.4, the U_R vs. C_S relationship for each cell type is determined from experiments at multiple initial concentrations C_0, and $k_F(C_S)$ is expressed in units of L s^{-1} cell^{-1}. The boundary condition at the air/solution interface is set to zero flux, as given by Eq. (3.3).

$$D\left.\frac{\partial C(z,t)}{\partial z}\right|_{z=L} = 0 \tag{3.3}$$

For each cell type, simulations were performed at the same values of C_0 used in the experiments, i.e., $C(z,0) = C_0$ where C_0 = 20, 60, 100, 200, 300 or 500 μM.

3.3 Results

3.3.1 Real time acquisition of transient concentrations at multiple positions from the cell surface

Fig. 3.2 shows representative concentration transients measured in real time at the electrode positions during experiments wherein the cell cultures of astrocytes and GBM43 are exposed to C_0 of 100 μM H_2O_2. Electrodes are labeled as E1 through E5, with E1 and E5 denoting the electrodes nearest to and farthest from the cell surface, respectively. These signals were acquired with sampling period of 0.5 s and were neither filtered nor averaged over time. Corresponding results for C_0 of 20, 60, 200, 300 and 500 μM H_2O_2 are included in Fig. S-7 in Appendix 1. The relative values of the concentration amplitudes (E1 < E2 < E3 < E4 < E5) indicates the presence of a gradient in H_2O_2 concentration due to cellular uptake. The recorded concentration transients shown in Fig. 3.2 provide the information required to dynamically map the concentration profile of H_2O_2 and determine the corresponding uptake kinetics.

3.3.2 Mapping of the dynamic concentration profile from experimental data

Fig. 3.3 shows concentration as a function of distance from the cell surface at selected time points for both astrocytes and GBM43 cells exposed to C_0 of 100 μM H_2O_2. Solid symbols are experimental data points obtained from the MEA electrodes (E1-E5) at the indicated time points. The solid red lines represent fits at the corresponding time points, discussed later. Collectively, the data points indicate the evolution of $C(z,t)$ measured over a spatial scale of $\sim$700 μm and for various time points between 360 and 4000 s. Although the concentration at each electrode was sampled every 0.5 s, as shown in Fig. 3.2, $C(z,t)$ is only shown for selected time points for the sake of clarity. Corresponding results for C_0 of 20, 60, 200, 300 and 500 μM H_2O_2 are included in Fig. S-6 in Appendix 1.

The uptake of H_2O_2 at the 2D cell surface depletes the analyte nearby and therefore induces a one-dimensional concentration gradient extending continuously into the bulk solution. Overall, the GBM43 cells exhibit higher H_2O_2 U_R than the astrocytes since the concentrations near the surface of GBM43 cells are smaller than those of astrocytes. While a nonlinear $C(z,t)$ was observed for both cell types at early times (0-500 s), non-linearity is more evident in GBM43 cells due to higher U_R. Beyond 500 s, the $C(z,t)$ over the spatial scale addressed is linear for both cell types.

For each time point, C_S and G_S can be obtained via extrapolation of the concentration to $z = 0$ and calculation of the corresponding gradient, respectively. Considering the nonlinear $C(z,t)$ observed in the experimental points in Fig. 3.3, particularly at earlier time points, a simple linear extrapolation does not provide accurate values for C_S and G_S. In order to provide an expression which better fits the experimental data and can be directly related to physical parameters, a general form of an expression describing a first-order irreversible reaction at a planar electrode in contact with a semi-infinite volume of solution [167] (see discussion and original expression in ESI) was employed,

$$C(z) = A_1 \left[1 + A_2 erfc(A_3 z)\right] \tag{3.4}$$

where A_1, A_2 and A_3 are fitting parameters. Eq. (3.4) was used to fit the experimental concentration versus distance data at time points spaced by 10 s. Fig. 3.3 shows the fitted curves (solid red lines) corresponding to the experimental data sets presented in the figure. In the current study, the depth of the solution is finite and the 2D monolayer of cells is expected to act as H_2O_2 sink exhibiting kinetics beyond first-order; hence the fitting parameters A_1, A_2 and A_3 will have somewhat different but related physical interpretations from the original expression. The fitting was performed at each time point independently, without carrying any information over from prior time points, and the obtained best fits consistently provided R^2 ¿ 0.99 at every time point for all the experiments: 36 experiments in total; 18 experiments for each cell type, comprising triplicates of 6 initial concentrations. The experimental

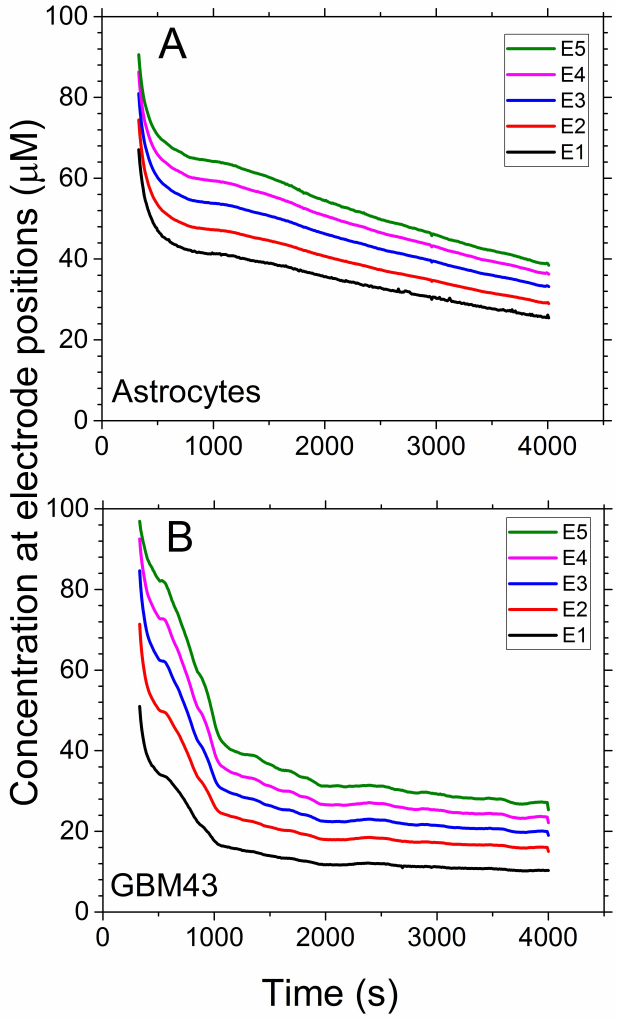

Fig. 3.2. **Curves are representative measurements of local concentrations at the positions of the electrodes E1-E5 (located within 700 μm from the cell surface) for astrocytes (A) and GBM43 (B) exposed to C_0 of 100 μM H_2O_2.** The sampling period is 0.5 s and no filtering nor moving-window averaging is performed on the acquired signals. A 330 s interval between addition of H_2O_2 (t = 0 s) and start of measurement allows stabilization of electrode response, and in-situ calibration technique described in text utilizes the current at each electrode at the end of that interval. The order in the amplitudes of the signals, E1 < E2 < E3 < E4 < E5, indicates the presence of a concentration gradient since E1 and E5 are the closest and farthest electrodes from the cell surface, respectively. Measurements were conducted with astrocytes and GBM43 cells at various initial concentrations, as described in text.

results were also fitted by linear regressions (not shown), resulting in R^2 values within 0.79–0.95 and therefore confirming that fitting to a well-established diffusion-reaction model is better than simple linear regression.

3.3.3 Determination of surface concentration and gradient from experimental data

Once A_1, A_2 and A_3 are determined for a given time, the corresponding $C_S(t)$ and $G_S(t)$ can be obtained using expressions developed from Eq. (3.4), namely

$$C(z,t)|_{z=0} \equiv C_S(t) = A_1 + A_2 \tag{3.5}$$

$$\left.\frac{\partial C(z,t)}{\partial z}\right|_{z=0} \equiv G_S(t) = -\frac{2A_2A_3}{\sqrt{\pi}} \tag{3.6}$$

Curves of C_S and G_S versus time are determined using (3.5) and (3.6), respectively, for all the experiments performed in this study. The triplicate curves of C_S and G_S for each initial concentration are combined into averaged curves, and these averaged curves are indicated by solid lines in Figs. 3.4 and 3.5, respectively, for astrocytes and GBM43 cells exposed to C_0 of 20, 60, 100, 200, 300 and 500 μM H_2O_2. The error bars indicate standard deviation of the averaged curves (n = 3). The dashed lines in Figs. 3.4 and 3.5 represent the results of simulations for the corresponding C_0, discussed later. G_S is presented in units of μM μm^{-1} to facilitate physiological interpretations but other relevant units such as mol cm^{-4} can be obtained using appropriate conversion factors. Using the H_2O_2 diffusion coefficient from the literature, [104] the G_S values are converted into surface fluxes (F_S) as indicated by the corresponding scale in Fig. 3.5. Considering the whole spectrum of C_0 from 20 to 500 μM, astrocytes show less uptake than the GBM43 cells.

Although both astrocytes and GBM43 cells showed changes in morphology after exposure to 300 and 500 μM H_2O_2 (see Fig. S-4 in Appendix 1), the cells kept consuming H_2O_2, highlighting the robust nature of the oxidant scavenging mechanisms

present in both cell types. Separate live/dead stains (see Fig. S-5 in Appendix 1) performed on the cells after exposure to 500 μM H_2O_2 indicated high viability of both cell types. The GBM43 cells exhibited better viability than astrocytes, suggesting that the cancerous cells are more resilient to H_2O_2 than their healthy counterparts.

The dashed lines in Figs. 3.4 and 3.5 are simulated curves obtained from numerical solutions of the reaction-diffusion model (see Section 3.3.4) at the indicated C_0, using the geometry of the 2D cell culture and the kinetic parameters extracted from analysis of U_R as a function of C_S, as discussed in Section 3.3.5. It is important to note that only C_0 is modified from simulation to simulation, indicating that the diffusion model developed here qualitatively captures the physics of cellular uptake of H_2O_2 over the different time regimes and over the whole spectrum of C_0.

3.3.4 Real time determination of uptake kinetics and extraction of kinetic parameters

The transient behavior of C_S and G_S discussed above captures the effects of cellular kinetics in conjunction with the diffusion profile in the given geometry. In order to minimize variability in cell density between multiple experiments and extract the kinetic parameters in the same units as standard volumetric rate constants (see Discussion), the F_S (mol cm^{-2} s^{-1}) presented in Fig. 3.5 is normalized to the cell density (cell cm^{-2}) to obtain U_R on a per cell basis (mol s^{-1} cell^{-1}).

Open symbols in Figs. 3.6 and 3.7 indicate the values of U_R versus C_S extracted from experimental data for astrocytes and GBM43; both figures present the same data but over different ranges of C_S to help visualize some details in the U_R–C_S relationship. For each cell type, data is plotted for the various C_0 values in order to span the whole spectrum of concentrations for both cell types. This yields a series of overlapping segments (e.g. within astrocyte data, segments corresponding to C_0 of 300 and 500 μM correspond to segments covering C_S ranges of $\sim$110-240 μM and $\sim$175-350 μM, respectively). Shaded bands surrounding the open symbols indicate

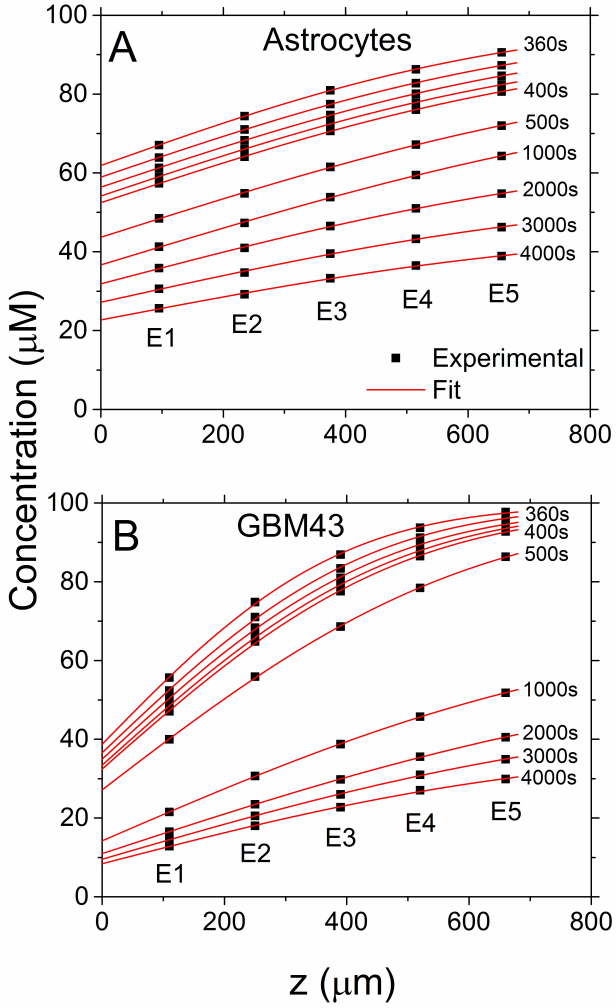

Fig. 3.3. **Representative concentration profiles at the indicated time points, as measured by the electrodes E1-E5 (symbols) and as obtained from the best fits to a reaction-diffusion model (solid lines) for astrocytes (A) and GBM43 (B) exposed to C_0 of 100 μM H_2O_2.** The procedure for the best fits and the reaction-diffusion model are described in the text. For clarity, the profiles are shown at relatively fewer time points as compared to the sampling time of 0.5 s. Concentration profiles within 360 and 400 s are shown in steps of 10 s. The data fits allow determination of surface concentration and surface gradient at each time point by extrapolation to the cell surface.

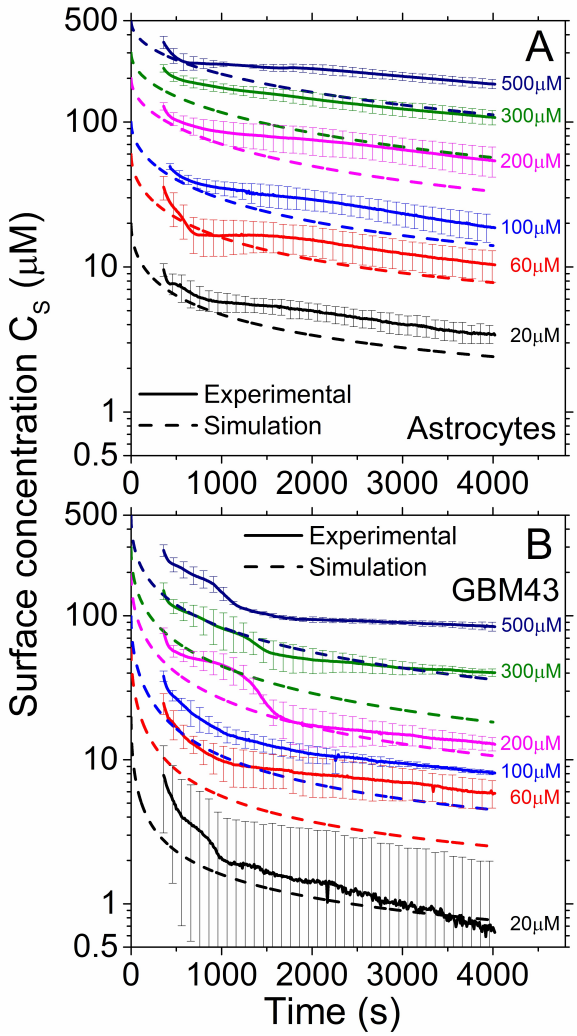

Fig. 3.4. **Transient surface concentrations, C_S, for experiments with the indicated C_0 values for astrocytes (A) and GBM43 (B), as extrapolated from the concentration profiles fitted from experimental data (solid lines) and as obtained from simulations (dashed lines).** Data points in solid lines are spaced by 10 s. Error bars indicate standard deviation of the mean value from triplicate experiments. For the sake of clarity, error bars are plotted every 100 s. The kinetic parameters (see Table 3.2) were kept fixed and only the initial concentrations were changed from simulation to simulation. Other simulation details are described in the text.

standard deviation of the mean value of U_R (n = 3). Overall, the U_R–C_S relationships are observed to be non-linear.

The solid lines passing through the experimental data points (open symbols) in Figs. 3.6 and 3.7 are best fits to Eq. 3.7, which describes the dependence of U_R on C_S using established kinetic mechanisms, namely linear (first term) and Michaelis-Menten (MM) [168, 169] (second term),

$$U_R(C_S) = k_F(C_S) \cdot C_S = \left[k_1 + \frac{J_0}{k_2 + C_S}\right] \cdot C_S \tag{3.7}$$

where k_1 is the rate constant of the linear mechanism, J_0 is the saturation uptake rate of the MM mechanism and k_2 is the MM constant (i.e., concentration at $J_0/2$). Note that the term in the brackets in Eq. (3.7) is the definition of the uptake rate factor $k_F(C_S)$, which clearly demonstrates the deviation from first-order kinetics. Eq. (3.7) was fit to the data in Fig. 3.6 using k_1, k_2 and J_0 as fitting parameters. The data fitting procedure included the overlapping data points (points from multiple C_0 overlapping over portions of their corresponding C_S ranges), along with the standard deviation of U_R (shaded bands in Fig. 3.6). The inclusion of the standard deviation of U_R in the data fitting places stronger weighting on data points having the least uncertainty. R^2 for astrocytes and GBM43 cells are 0.997 and 0.985, respectively. The extracted values of k_1, k_2 and J_0 are presented in Table 3.2 for astrocytes and GBM43 cells.

Table 3.2.
Kinetic parameters extracted from experimental data

	k_1 (10^{-12} L s^{-1} $cell^{-1}$)	k_2 (μM)	J_0 (fmol s^{-1} $cell^{-1}$)
Astrocytes	0.87 ± 0.007	46 ± 0.8	0.09 ± 0.002
GBM43	2.3 ± 0.03	13 ± 1.3	0.06 ± 0.003

Fig. 3.7 magnifies the low C_S range (0-100 μM) of Fig. 3.6 to illustrate more clearly the non-linearity of U_R vs. C_S and the transition from a regime in which

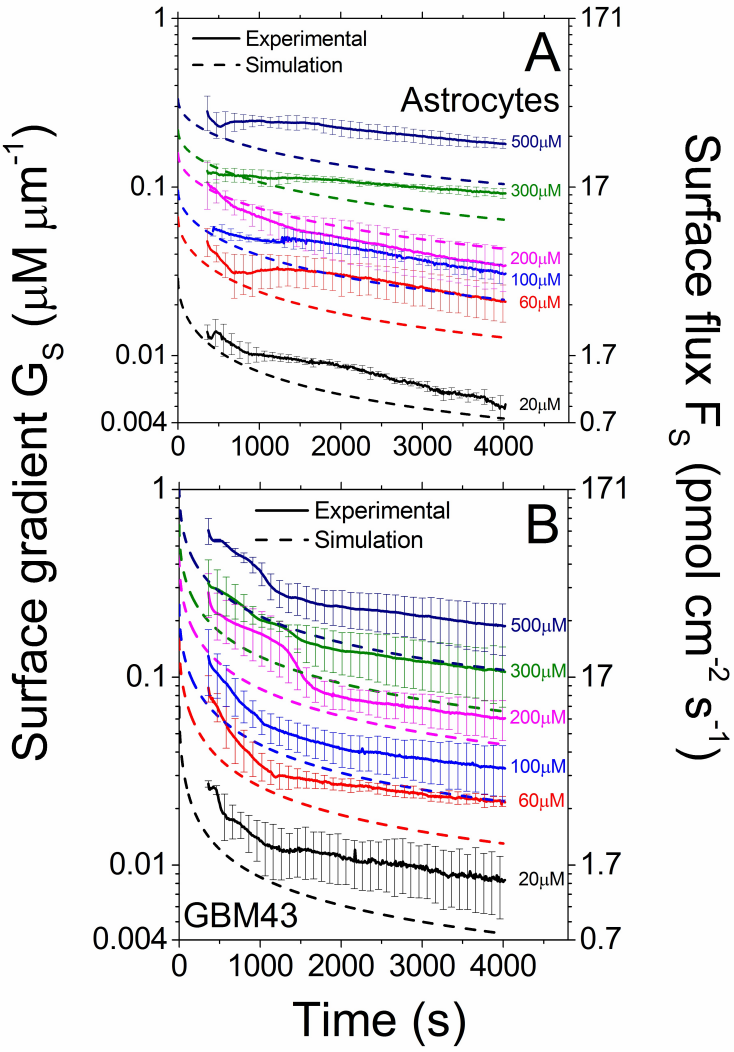

Fig. 3.5. **Transient surface gradients, G_S, for experiments with the indicated C_0 for astrocytes (A) and GBM43 (B), as extrapolated from the concentration profiles fitted from experimental data (solid lines) and as obtained from simulations (dashed lines).** The corresponding surface flux, F_S, (right axis) is computed as the product of G_S and diffusion coefficient of H_2O_2. Data points in solid lines are spaced by 10 s. Error bars indicate standard deviation of the mean value from triplicate experiments. For clarity, error bars are plotted every 100 s. The kinetic parameters (see Table 3.2) were kept fixed and only the initial concentrations were changed from simulation to simulation. Other simulation details are described in the text.

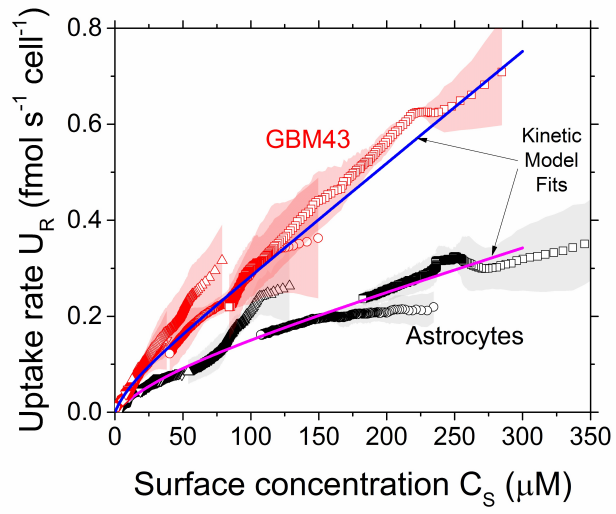

Fig. 3.6. **The uptake rate of H_2O_2, U_R, as a function of surface concentration, C_S**, for astrocytes and GBM43 as measured experimentally (symbols) and as obtained from the best fits to a kinetic model (solid lines) that considers linear and Michaelis-Menten components. U_R is computed as the experimental surface flux, F_S, divided by the cell density. Shaded bands indicate standard deviation of the mean of U_R from triplicate experiments. For each cell type, results are presented for C_0 of 500 (squares), 300 (circles), 200 (up-triangles), 100 (down-triangles), 60 (rhombuses) and 20 μM (pentagons); within each experiment at a given C_0, C_S evolves from high concentration (short time) to low concentration (long time).

both terms contribute strongly to a regime in which the linear term dominates. In Fig. 3.7 , solid lines labeled as 'Kinetic Model Fit' are the same curves shown in Fig. 3.6 , and solid lines labeled as 'linear' and 'MM' represent the linear and MM terms from Eq. (3.7) using the corresponding values from Table 3.2. These linear and MM curves quantify the contribution of each mechanism to the measured U_R at any given C_S. The cross-over point between linear and MM curves indicates the concentration at which both mechanisms contribute equally. The cross-over points occur at 13 and 55 μM for GBM43 and astrocytes, respectively, mainly due to the fact that the linear term (k_1) is 2.5 times larger in GBM43 than in astrocytes (see Table 3.2). In the low concentration range (0–20 μM), which corresponds to the extracellular H_2O_2 concentration associated to the homeostatic level, [**?**, 19] GBM43 and astrocytes exhibit contribution ratios of approximately 1:1 and 2:1 (MM:linear), respectively. As the concentration increases the MM mechanism reaches saturation and the linear mechanism takes over the MM mechanism. The MM saturation value (J_0) in GBM43 is 66.6% of that in astrocytes.

To illustrate how U_R–C_S deviates from first order as C_S increases, dashed lines in Fig. 3.7 show linear extrapolations of the initial slopes in the data curves, obtained from linear regressions of the experimental data of U_R–C_S in the range of 0–20 μM H_2O_2. These linear regressions yielded k_F of $(2.63 \pm 0.005) \times 10^{-12}$ L s^{-1} $cell^{-1}$ for human astrocytes and $(4.2 \pm 0.02) \times 10^{-12}$ L s^{-1} $cell^{-1}$ for GBM43, which are comparable to results from typical volumetric measurements, [138] as discussed in Section 3.4.

3.3.5 Simulation of the 2D cell cultures based on the determined parameters

The kinetic parameters k_1, k_2 and J_0 in Table 3.2 are included in the numerical solution of a diffusion–reaction system representing the same geometry of the 2D cell culture. For a given cell type, simulations are performed at various C_0 while

keeping the values of k_1, k_2 and J_0 fixed. Simulated curves of C_S and G_S versus time are indicated by dashed lines in Figs. 3.4 and 3.5, respectively. The simulation captures the qualitative features of the experimental curves, including decreasing slopes with increasing time, relative changes in C_S and G_S at long times for various values of C_0 and the relative differences between behavior of astrocytes and GBM43. The simulation did not include effects such as natural convection [37] and potential mixing effects due to the MEA chip motion at 300 s, which would result in a better fit to the data but would require assumptions regarding the magnitudes of these effects. Compared to simulations with the constant k_F extracted at low H_2O_2 concentrations (0–20 μM), the simulated curves using the kinetic parameters in Table 3.2 better capture the main features of the uptake mechanisms of astrocytes and GBM43 cells over the investigated range of C_S and over a larger time window (see Fig. S-9 in Appendix 1).

3.4 Discussion

In this study we have demonstrated the analytical capabilities of the MEA approach to measure cellular uptake kinetics in real time. It is informative to compare the results from the current study with those from prior experiments. In typical volumetric experiments, [42, 129, 136, 170–173] a first-order rate coefficient k_{obs} (in units of s^{-1}) is obtained from

$$\frac{dC_{vol}}{dt} = -k_{obs}C_{vol} \tag{3.8}$$

where C_{vol} is the volumetric concentration. As discussed by Wagner et. al., [42] the value of k_{obs} is dependent on both the solution volume (V) and number of cells (N), but normalization by N and V yields a rate constant k_{cell}, in units of L s^{-1} $cell^{-1}$, which can be directly compared for various experiments.

$$k_{cell} = \frac{V}{N}k_{obs} \tag{3.9}$$

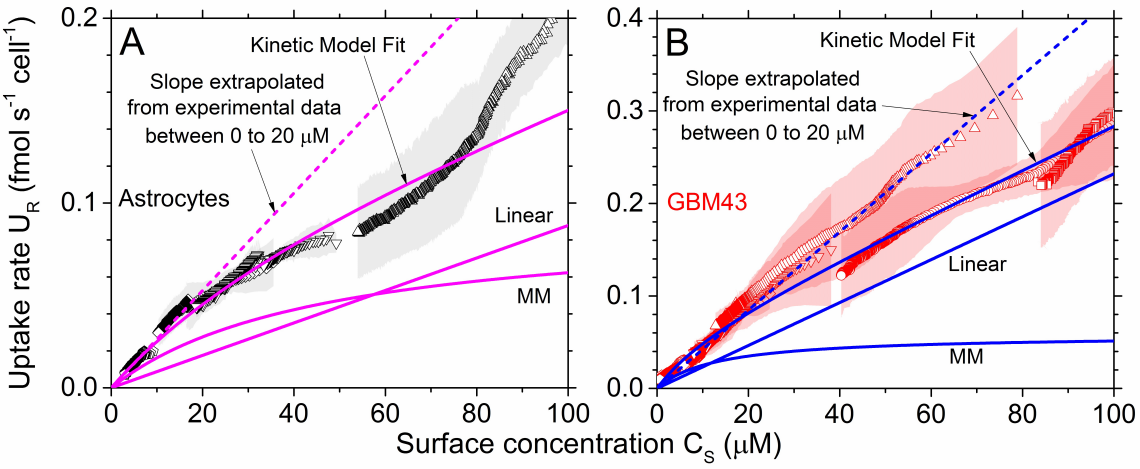

Fig. 3.7. **The uptake rate, U_R, as a function of the surface concentration, C_S, over the low concentration range for astrocytes (A) and GBM43 (B).** Experimental data points (symbols) and solid lines labeled as "Kinetic Model Fit" are the same as in Fig. 3.6, and the same symbols are used to indicate initial concentrations. Shaded bands indicate standard deviation of the mean of U_R from triplicate experiments. Linear and Michaelis-Menten (MM) kinetic components are indicated by solid lines which are labeled accordingly, illustrating the relative magnitudes and the cross-over point of the two terms. Dashed lines extrapolate the slope from experimental data within 0–20 μM in order to predict uptake rates at higher concentration range based on the conventional first-order kinetics approach.

The uptake rate factor k_F, defined earlier as the ratio U_R/C_S, allows quantitative comparison of MEA results to k_{cell} or k_{obs} from volumetric measurements, independent of diffusion geometry and mass transport. Based on Figs. 3.6 and 3.7, it is clear that k_F varies with C_S; the units for U_R and C_S in these figures have been chosen in order to provide k_F in the same units as k_{cell} (L s^{-1} $cell^{-1}$). In addition to this concentration-dependence, differences between k_F values from MEA measurements and k_{cell} values from volumetric measurements are expected due to differences in cell geometry (i.e., adherent versus suspended) and different relationships between C_S and C_{vol} associated with the hydrodynamics (i.e., static versus stirred solution). In experiments involving adherent cells in stirred solutions or suspended cells, $C_S \approx C_{vol}$ and Eq. (3.8) is the governing equation, so volumetric measurements yield k_{cell} values corresponding to C_0, if sampled within a short period after exposing the cells to C_0. By considering a number of C_0 values, such techniques have been used to study the concentration-dependence of k_{cell}. [139–143] In contrast, experiments involving adherent 2D cultures exposed to analyte in unstirred solution for specific intervals, followed by stirring just prior to volumetric sampling, will have $C(z,t)$ (during the uptake period) comparable to that in the current study. In this class of experiments, the C_{vol} observed after an uptake period T_0 can be related to C_0, C_S and k_F via

$$C_{vol}(T_0) = C_0 - \frac{N}{V}\int_0^{T_0} k_F C_S(t)dt \tag{3.10}$$

For small T_0, which is typical in this class of experiments, a semilogarithmic plot of C_{vol} vs. T_0 is approximately linear and k_{cell} is extracted from the slope of this curve. Since C_S is less than the concentration averaged throughout the volume, such experiments will yield k_{cell} values lower than k_F (obtained in this work) or lower than the k_{cell} values inferred from experiments governed by Eq. (3.8). These observations indicate that there are qualitative and quantitative differences between experiments, dictated by cell geometry (adherent or suspended) and hydrodynamics (stirred or unstirred).

In our experiments, values for k_F at low C_S were determined from the average slope of the U_R–C_S relationships in the range of 0 ¡ C_S ¡ 20 μM (dashed curves in Fig. 3.7), yielding $k_F = (2.63 \pm 0.005) \times 10^{-12}$ L s^{-1} $cell^{-1}$ for human astrocytes and (4.2 $\pm$ 0.02) $\times$ 10^{-12} L s^{-1} $cell^{-1}$ for GBM43. Using volumetric approaches with initial concentration of 20 μM, Doskey et. al. measured k_{cell} values (all in units of L s^{-1} $cell^{-1}$) between 4.4 $\times$ 10^{-12} and 7.3 $\times$ 10^{-12} for human astrocytes, 4.8 $\times$ 10^{-12} for GBM U87, and 4.6 $\times$ 10^{-12} for GBM U118. [138] Compared to Doskey et. al., our values of k_F are in the same range, although the smaller value for astrocytes relative to that for GBM43 is in opposition to the general trend of tumor cells having lower k_{cell} than normal cells. [138] Since this trend may invert itself at higher concentrations, as indicated by Makino et. al., [143] characterization over a wider range of surface concentrations is warranted if H_2O_2 is going to be used as a therapeutic agent against cancer.

The concentration dependence of U_R can also be compared to prior volumetric studies. The biphasic behavior in U_R–C_S is comparable to that reported by Makino et. al. in studies on rat astrocytes and C6 glioma using 2D cell cultures in stirred media. [139–143] These studies attributed the linear behavior to catalase (CAT) and the Michaelis-Menten behavior to glutathione peroxidase (GPx1). [143,174–176] Two observations are evident between our results for human cells and those of Makino et. al. for rat cells. First, Makino et. al. observed that C6 glioma cells exhibit a higher U_R compared to astrocytes for concentrations above 20 μM, but a lower rate between 0-20 μM. [143] In contrast, our results show higher U_R in GBM43 than in astrocytes over the entire investigated concentration range (0–350 μM). Second, the ratio of J_0 for cancer to normal cells in Makino et. al. is 1.76 whereas that ratio in our results is 0.67. [143] Based on various issues which have been raised regarding the use of rat C6 glioma as a model for human glioblastoma and comparisons regarding growth, invasion, metastasis and drug response, [177–179] differences are expected between human and rat cells. For human cells, biochemical analyses indicate that glioblastoma contains more CAT but less GPx1 than astrocytes; [180] assuming the correlation by

Makino et. al. [139] wherein the linear and MM mechanisms correspond to CAT and GPx1, respectively, our results are in qualitative agreement with that report.

The U_R–C_S relationships shown in Figs. 3.6 and 3.7 consist of sets of overlapping time trajectories, obtained using various C_0 values. For each cell type, these trajectories can provide insights into the relative effects of cumulative exposure to the analyte, e.g. by comparing the behavior at long exposure times for a large C_0 with that at short time for a smaller C_0. Such time-dependence could be used to quantify the onset of toxicity in prior studies. [129, 181] In the current experiment, the trajectories for GBM43 show a tail-off in U_R after long exposure, i.e., the U_R values fall below those extrapolated from the intermediate-time regime. Such a roll-off could be indicative of H_2O_2 toxicity or reduction in H_2O_2 scavenging ability. In the case of astrocytes, comparable roll-off is not observed. Although clear changes in morphology were observed for both cell types after exposure to 300 and 500 μM H_2O_2 (see Fig. S-4 in Appendix 1), the roll-off in U_R was moderate even for the GBM43 cells. The continuous monitoring of C_S over the course of the experiment allows a more accurate determination of the cumulative exposure of the cells to the analyte, in comparison to experiments in unstirred solutions followed by volumetric sampling.

The MEA approach should be well-suited to assess the chemical impact of one cell type on others when multiple cell types are cultured together (i.e., co-cultured). Studies have shown that the chemical microenvironment differs significantly among 2D cultures containing one, two and three different cell types cultured together, [182] and these observations have been ascribed to paracrine signaling via cell secreted factors. [36–38, 183] Seeding of various cell types on a surface using cell patterning techniques [184] followed by co-culture could be used to measure kinetic parameters under the influence of paracrine signaling. The MEA approach allows measurements in unstirred solution, preserving the natural diffusion environment, and can in principle provide information on spatial heterogeneity, e.g., by localizing at the cell type of interest. Once the kinetic parameters are determined, they can be incorporated into 3D models to study the behavior of cells within tissue.

The MEA approach could be applied for other electroactive species without major adjustments and provides customizable spatial and temporal resolutions. Although the focus of the present study is on H_2O_2, the same MEA and methodology, except for minor adjustment of bias potential, can be used to measure uptake kinetics and C_S of other electroactive species of biological interest including dopamine and serotonin. The current experiment utilized platinum electrodes, which yielded relatively high sensitivity but also a relatively long time for stabilization of the H_2O_2 response. [97, 185–189] The latter dictated a waiting period of 300 s between addition of H_2O_2 and start of concentration measurements. Other materials, e.g., carbon electrodes, could reduce the electrode stabilization time, but trade-offs in sensitivity are expected. [185–189] As shown elsewhere, [159] parameters such as sampling period and spatial resolution can be customized to fit other requirements, e.g., sub-second transient concentrations and gradients have been measured with sampling period of 10 ms and inter-electrode distance of 35 μm.

3.5 Conclusions

In this chapter, we demonstrate the use of a MEA customized for typical 2D culture setups to measure dynamic H_2O_2 concentration profiles from normal (human astrocytes) versus astrocyte derived cancer (GBM43) cells. The MEA provides multi-point concentration data with a sampling period of 0.5 s. At each time point, the concentration data is fit using an analytical expression for a 1D diffusion/reaction system, allowing extrapolation of the surface concentration and surface gradient. Measurements at various initial concentrations allow determination of the uptake rate over a wide range of surface concentrations. Both cell types show surface concentration dependent uptake rates, i.e., non-linear kinetics. The results show that GBM43 cells have increased H_2O_2 uptake rates as compared to astrocytes due primarily to an elevated linear scavenging mechanism, which has previously been attributed to catalase. The Michaelis-Menten components are comparable for the two cell types for H_2O_2

concentrations within the 0–100 μM range. A comparison of the diffusion–reaction models using the non-linear parameters and standard first-order relationships indicates that the overall behavior is better described by the non-linear relationships. As shown in Eq.3.10 and associated discussion, our results can also be used to quantitatively understand the differences between volumetric measurements using stirred versus unstirred media during uptake.

The monitoring of U_R vs C_S can also be used to quantify cumulative exposure effects, e.g., by comparing the uptake rate observed at the same C_S for different initial concentrations and therefore different cumulative exposures to H_2O_2. In the current experiment, a tail-off in uptake rate after long exposure to high concentrations of H_2O_2 is observed for GBM43 cells. The capabilities to quantify cumulative exposure effects and uptake rates over a wide range of cell surface concentrations are relevant for both toxicity studies and evaluation of potential therapeutic approaches based on differential uptake by cancerous versus normal cells.

In addition to shedding light on mechanistic behavior, the resulting kinetic parameters should be well suited for developing reaction–diffusion models that more accurately describe more complex culture/tissue geometries. Key aspects include measurements in a more natural local environment and the ability to obtain U_R vs C_S relationship which are nominally independent of the specific diffusion geometry. The MEA technique can also be extended to mixed cultures and multi-analyte measurements, e.g., monitoring of both uptaken and released analytes. Collectively, these capabilities can provide parameters which, when coupled with a diffusion model representing a realistic geometry for influx/efflux of various analytes, can yield models which more accurately represent the behavior of 3D cultures and tissue microenvironments.

4. GLUCOSE UPTAKE KINETICS OF GLIOBLASTOMAS VS. ASTROCYTES

4.1 Introduction

Glucose is a major source of energy in mammalian cells and plays a critical role in various pathways involved in proliferation, survival, metabolism and signaling [190–201] Cancer cells exhibit reprogrammed glucose metabolism by altering transporter expressions and/or kinetic and regulatory activities of internal enzymes to fulfill their needs in nutrient deficient microenvironments [196, 202–209]. In the context of in-vitro metabolic characterization of cancer/normal cells via adherent 2D cell cultures in static media, the direct quantification of the total glucose uptake rates is a critical piece in deciphering the fate of glucose as it is catabolized for energy (via glycolysis and respiration) and anabolic macromolecule biosynthesis. Standard fluorometric or glucose analog based assays although extremely adept at providing end point estimates of averaged volumetric or intracellular glucose analog concentration [53, 210], do not sufficiently capture real time glucose uptake kinetics in static media as it is mediated by facilitated glucose transporters and diffusive mechanisms driven by the hysteretic availability glucose at the cell surface [22, 199, 211–216]. This chapter builds on previous work [159, 217] and presents the use of transient measurements of glucose gradients and concentrations within few hundred of μm from adherent 2D cell cultures in static media to simultaneously determine glucose uptake rate and correlated instantaneous surface concentrations, which enables development of a comprehensive kinetic model along with the ability to provide mechanistic insights of the glucose sensing and signaling apparatus in cells. The measured total glucose uptake rate when used in conjunction with other pH and oxygen measurement tools has the capability to provide an overall picture of glucose flux (glycolysis

+ respiration + biosynthesis), and can potentially help in the therapeutic targeting of the altered metabolic pathways in cancer cells [1, 12, 204, 213, 218–223].

As the focus of this chapter, we consider the cellular uptake of glucose in glioblastoma multiforme (GBM) and astrocytes. GBM, one of the most aggressive form of brain cancer [147], is known for its increased glucose consumption to support its extensive metabolic demands [204,211,224–230]. Astrocytes on the other hand, are a type of glial cell which act as the primary consumers of glucose in the human brain due to their close proximity to intracerebral blood vessels and have been recently associated to play an active role in 'energy' distribution to neurons. [28–30, 33, 34]. Interestingly, GBMs despite sharing glial lineage with astrocytes [148] have reprogrammed metabolic pathways via overexpressed GLUT transporter expressions [157, 204, 211, 224–228, 230] and/or altered enzymatic regulation [220, 231–234]. The resulting increased glucose uptake enables progression, metastasis and survival of GBM tumor cells in nutrient poor microenviroments [224] and is correlated with poor patient outcomes [235–237]. GBMs over reliance on glucose to survive is a vulnerability which could be exploited therapeutically [211, 221, 227] and therefore has motivated the recent interest in metabolic characterization.

To get a complete picture of the enhanced glucose metabolism in gliomas previous studies have relied on a combination of methods and tools tuned for identifying the specific aspects in the intracellular metabolic pathways [11,213,224,225,228,238–245]. These studies are usually performed with the help of enzymatic assays, specific inhibitors and/or western blotting to elucidate specific biochemical components. In addition, indirect estimation of glucose uptake is done via end point detection of entrapped glucose analogs such as radio-labeled 2-deoxy-d-[1,2-3H]-glucose, 2-deoxy-d-[1-14C]-glucose, 2-deoxy-2-(18F)-fluoro-d-glucose (18FDG) or fluorescent 2-[N-(7-nitrobenz-2-oxa-1,3-diaxol-4-yl)amino]-2-deoxyglucose (2-NBDG) [53, 210, 246]. Similarly, extremely useful tools like the Seahorse XF analyzer can also provide indirect estimates of glycolytic and respiration rates by measuring extracellular pH and oxygen with/without use of specific inhibitors etc. [2, 4, 54, 247, 248]. However, it is desirable

to complement these tools and methods with real time and direct measurement of the total glucose uptake with high temporal resolution over a wide range of concentrations to provide a holistic image of the kinetic pathways involved in glucose uptake. Such flexibility would not only allow researchers to deduce dominant mechanistic effects but also work towards an 'glucose' budget so as to identify new pathways with therapeutic vulnerability.

In order to extract real time kinetic information, dynamic mapping of the concentration profile near the cell surface is required to enable simultaneous determination of surface concentration (C_S) and uptake rates (U_R) by extrapolation to the cell plane [159, 217]. Amperometric glucose biosensors based on immobolized glucose oxidase are an attractive approach for the real-time and continuous monitoring of glucose in 2D cell cultures due to their high sensitivity, selectivity and fast response times [62, 69, 103, 249–256]. Previous works have demonstrated the extension of enzymatic biosensors to ceramic [116, 257–261] or silicon [262–269] based microelectrode arrays (MEAs) for measuring glucose transients in response to in-vivo or in-vitro physiological events. *Meyer et al,.1995* [87] demonstrated real time imaging of various non-physiological transient gradients within a 2D MEA. In contrast, self-referencing vibrating glucose probe (SRT) [58, 61, 62, 69, 70, 270] can map concentration profiles perpendicular to the surface of 2D cell cultures [41, 58, 69] but are generally limited in terms of the overall measurement time required to obtain multi-point concentration measurements over relevant spatial scales, without perturbing the solution around the probe tip. [41, 58, 61, 62, 69–71, 76]. Extension of the enzymatic biosensing strategy to a positionable MEA with customized geometries, discussed previously [159, 217], provides an excellent platform for real time measurement of multi-point concentration transients and associated gradients near 2D cell cultures. Moreover MEA based platforms have the potential for simultaneous multi-analyte sensing (e.g reactive oxygen species, glucose (this work) and lactate [87, 264–266, 271, 272] etc and are more amenable to miniaturization, automation, and lab-on-a-chip integration, [94, 160, 161]

which are desirable features for a high throughput in-vitro metabolic characterization tool.

In this study we have utilized enzymatic glucose MEA with a measurement approach reported previously [159, 217] to acquire the time-dependent local concentration of glucose at multiple spatial locations near the surface of adherent 2D cell cultures of human astrocytes and glioblastoma multiforme (GBM43) cells in unstirred solutions. At each time point, the spatial profile is extrapolated to the cell plane to determine the corresponding C_S and U_R. Experiments over a range of initial concentrations (3-15 mM) allow determination of relationships between $U_R(t)$ and $C_S(t)$. For astrocytes, we found that the uptake rate is well described by a combination of linear (simple diffussion) and a high affinity Michaelis-Menten transport mechanism which is in agreement with observation of GLUT1 transporters expressed in astrocytes. [5, 204, 205, 213, 221, 273]. For GBM43, an increased glucose uptake rate is observed over the entire concentration spectrum (3-15mM) in comparison to astrocytes. Moreover, the kinetics of glucose uptake is well described by a combination of higher affinity Michaelis-Menten transport mechanism dominant at low concentrations (3-5mM) and a sigmoidal (allosteric) mechanism dominant at higher concentrations (8-15mM). The kinetic parameters extracted from measurements are in agreement with the observation of overexpressed levels of GLUT1 and GLUT3 transporters in GBM43 [211, 224–226, 228]. Additionally, the transient evolution of glucose uptake rate in GBM43 is found to be dependent on the initial glucose exposure, pointing to a hysteretic nature of glucose metabolism which is usually associated with the presence of a glucose sensing apparatus in GBM [274, 275]. Finally, the obtained kinetic parameters describe the concentration dependence of the uptake rate and therefore can be used to refine pathway models of glucose metabolism. Altogether, the MEA, methodology and experimental results constitute a proof-of-concept of on-chip characterization of glucose metabolism of cancer vs. normal cells.

4.2 Material and Methods

4.2.1 Reagents

Human cerebral cortex astrocytes, astrocyte medium, cell freezing medium and 10 mg/ml poly-L-lysine were purchased from ScienCell Research Laboratories (Carlsbad, CA). Dulbecco's Modified Eagle's Medium (DMEM) and EDTA solution were purchased from Life Technologies (Carlsbad, CA). Astrocyte medium contained 500 ml of basal medium, 10 ml of fetal bovine serum (FBS, Cat. No. 0010), 5 ml of astrocyte growth supplement (AGS, Cat. No. 1852) and 5 ml of penicillin/streptomycin solution (P/S, Cat. No. 0503). Glucose solution (50 ml of 200 g/L) and chambered coverglass systems with 1.0 borosilicate glass and 4-wells were purchased from Thermo Fisher Scientific (Waltham, MA). Hydrogen peroxide 30% (w/w) was purchased from Alfa Aesar (Ward Hill, MA) and phosphate buffer saline (PBS) pH 7.4 was purchased from Sigma-Aldrich (St. Louis, MO).

4.2.2 MEA Design, Fabrication and Characterization

The 1D MEA array employed for this study has an increased pitch (ΔX) of 280μm and effective size (two 10 μm $\times$ 10 μm electrodes were combined) in comparison to the previous studies performed on the uptake of H_2O_2 [159, 217].Electrodes are located very close to the bottom edge of the silicon die and are designated E1, E2 and E3. Relative to the bottom edge of the die, E1 and E3 are the closest and the farthest electrodes, respectively. Fig. S-3 in Appendix 1 provides details of the microfabrication process. The increased pitch means that the spatial range of the gradient measurements is $\sim$ 700 μm (Fig. 4.1). Concentration of H_2O_2 usually varies from sub μM to hundreds of μM in cellular environments. Coupled with the high scavenging rates of H_2O_2 observed, the concentration gradients generated exhibited large spatial scales and concentration differences (ΔC) between multiple points (ΔX-pitch). In 2D cell cultures, the glucose concentration ranges from 5mM - 25mM

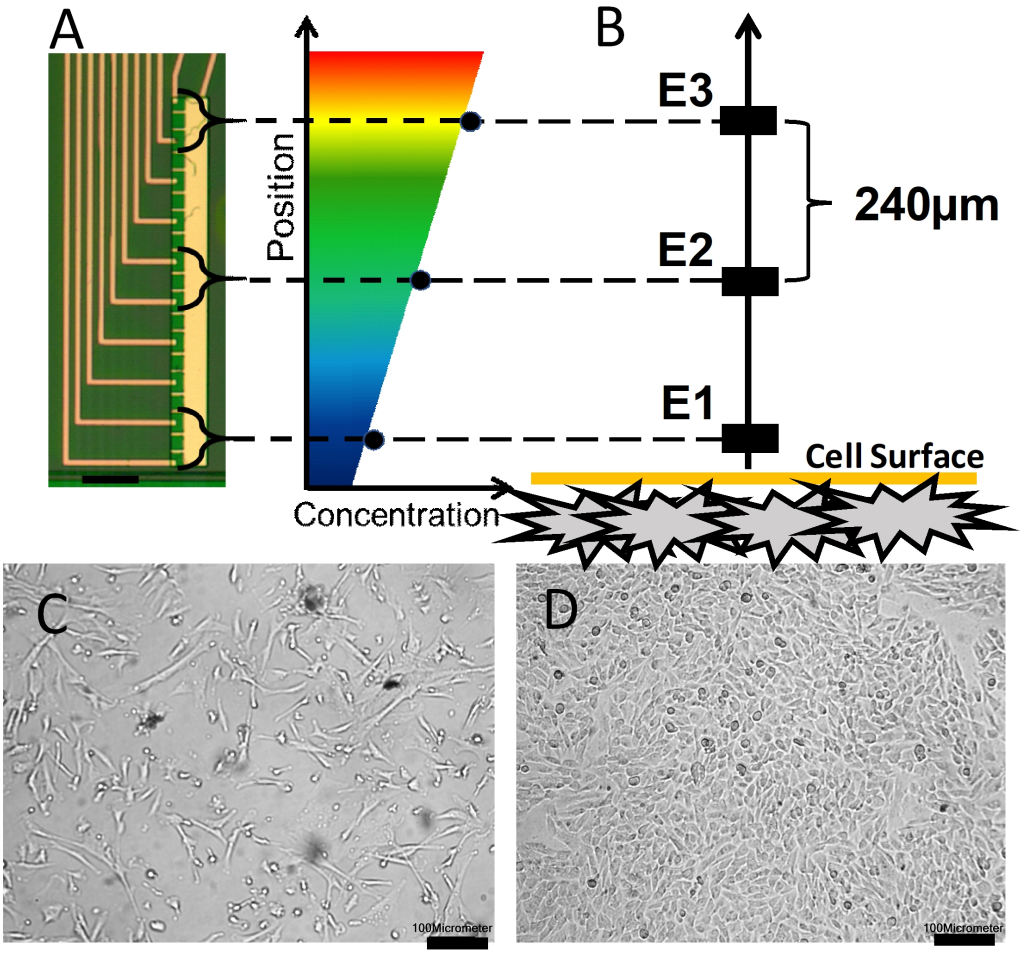

Fig. 4.1. Glucose MEA simultaneously measures transient glucose concentrations at three positions near the surface of cells in 2D cell culture. (A) Photograph of a representative MEA. 10 platinum microelectrodes, 10 μm 10 μm each, are arranged in a one-dimensional array. Sets of two electrodes, as indicated by arrows, are combined and used in experiments, thus yielding a pitch of 280μm. (B) Schematic of the experimental setup (not drawn to scale) illustrating how the glucose MEA electrodes acquire three spatial data points of the concentration profile near the cell surface. (C) Image of astrocytes in 2D culture prior to experiment (D) Image of GBM43 in 2D culture prior to experiment. Scale bar is 100μm.

and the small glucose uptake rates observed in cells (See Table4.2) results in shallow concentration gradients. Hence, the pitch was increased to account for the smaller (ΔC). Using a set of 2 electrodes in combination improves the sensitivity and the signal to noise ratio.

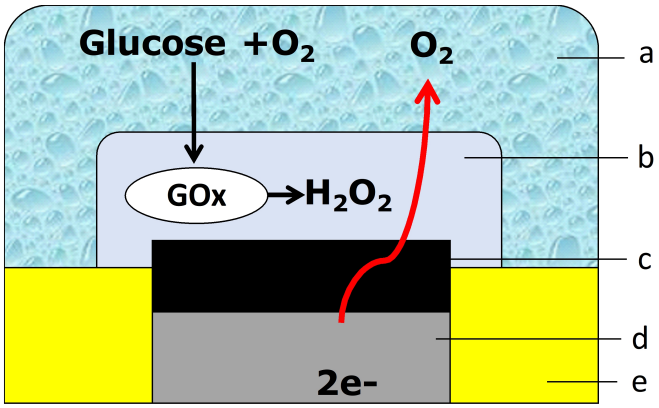

Fig. 4.2. Bio-functionalization scheme employed to fabricate glucose selective electrodes. (a) Bulk Solution (b) Perm selective PoAP with GOx. (c) Platinum-black (d) Pt electrode (e) Passivation layer

A biofunctionalization scheme adopted from [103] was modified to perform amperometric sensing of glucose using an on-chip MEA to achieve selectivity for glucose in the medium consisting of only glucose and buffered inert electrolyte (phosphate buffer saline), a composition commonly found in the literature. [42,44,59,109–113,143]. The basic principle of enzymatic glucose sensing is illustrated in (Fig. 4.2). Glucose oxidase (GOx) is the primary transducer which oxidizes glucose into gluco-lactone and H_2O_2.

D-Glucose + O_2 $\longrightarrow$ D-glucono-1,5-lactone + H_2O_2

Electro-oxidation of the intermediate H_2O_2 produces the current proportional to the glucose concentration. The bare Pt microelectrodes are nanostructured by electrodeposition of platinum black (Pt-B) to enhance the sensitivity to H_2O_2. Glucose oxidase (GOx) is immobilized in a perm-selective layer of poly-O-aminophenol (PoAP) which is electrodeposited on the Pt-B surface. The electroactive polymer layers were

deposited one after another using multiple rounds of potential cycling in aqueous enzyme doped monomer solutions. The perm selective layer acts as a deterrent for interferents such as ascorbic acid commonly found in physiological solution [103] . Tuning of the sensitivity was done by controlling the enzyme loading in the perm selective layer. 8 mg/ml was chosen as the optimum enzyme loading concentration based on maximum sensitivity. The number of voltammetry cycles in the aqueous enzyme doped monomer solution (O- Aminophenol + Glucose Oxidase) is kept constant (N=5). See Appendix for plots and further discussion on Glucose sensor.

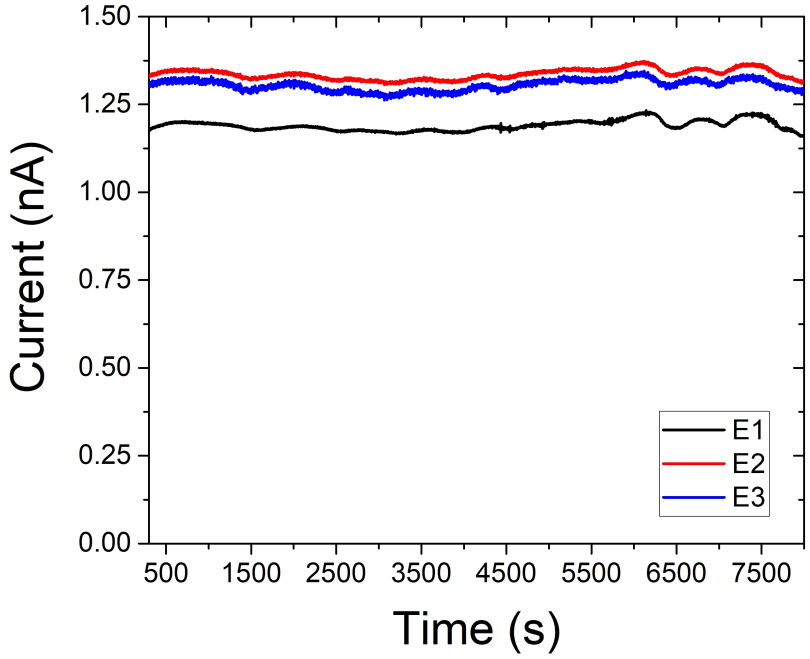

Fig. 4.3. Stable signals are measured from all electrodes in the MEA in response to a uniform concentration of 10 mM glucose upto for 8000s.

A major problem for first generation glucose sensors is the buildup of H_2O_2 caused by non-selective adsorption of GOx on the passivating photoresist layers. The high diffusivity of H_2O_2 ($\sim 10^{-9}$ m^2 s^{-1}) causes local buildup which in turn causes the current signal at glucose electrodes to increase over time and affect the response of neighboring glucose electrodes in the MEA. See appendix for further discussion. Hence, the

modified biofunctionalization scheme was supplemented by pre-surface treatment and post-glucose wash to achieve signal stability. Prior to GOx deposition, the electrodes were were incubated in a solution of 12 mg/ml tris(hydroxymethyl)aminomethane (TRIS) and $\sim$ 1 mg/ml glycine in PBS for 48-60 hours at room temperature. The treatment prevents non-specific adsorption of GOx on the SU8 passivation layer [276]. Post GOx deposition, the glucose wash further removes any loosely attached enzymes to provide a relatively stable signal. As shown in Fig. 4.3 stable signals are measured from all electrodes in the MEA in response to a uniform concentration of 10 mM glucose upto for 8000s.

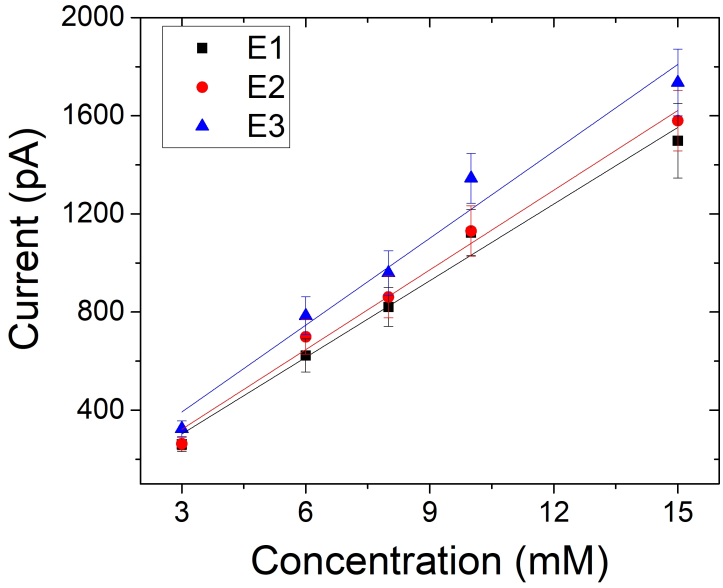

Fig. 4.4. Glucose sensors in the MEA have a linear range and sensitivity of 0-15mM and 110 $\pm$ 19 pA mM^{-1}.

Electrodes were characterized for glucose response by performing amperometry in unstirred solution, as shown in in Fig. 4.4. The sensitivity for E1,E2 and E3 were found to be 104 $\pm$ 8 pA mM^{-1}, 108 $\pm$ 6 pA mM^{-1}, 118 $\pm$ 11 pA mM^{-1}. Moreover, as shown in linear range of the glucose sensor was verified to be at least (0-15mM),

which is within the concentration range of interest for this study. The effects of the sensitivity variations (electrode-electrode ∼17% and experiment to experiment ∼12%) are minimized via in situ transient calibrations where calibration factors are acquired immediately prior to the measurements near the cell surface. [159, 217]

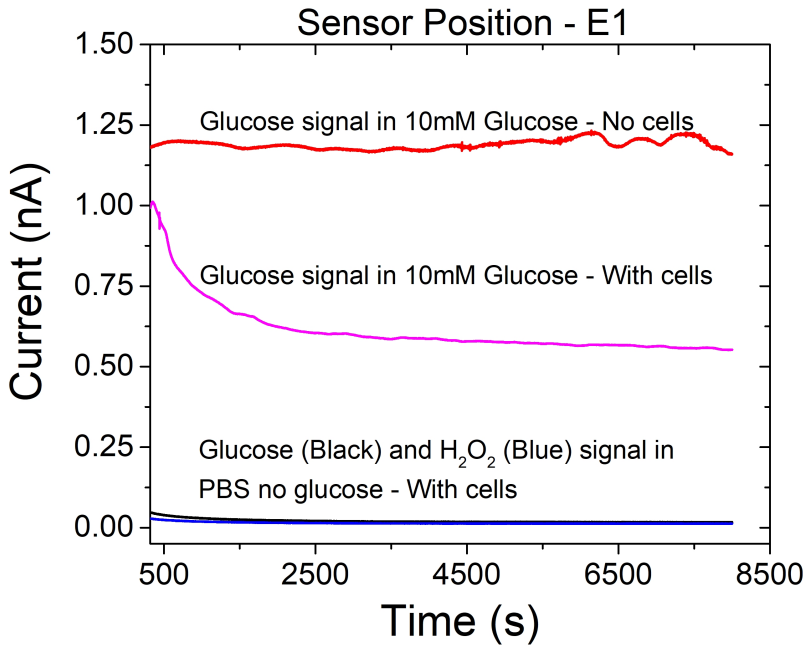

Fig. 4.5. Positive and negative controls performed in the same setup as described in the text.

Further, control experiments Fig. 4.5 showed that glucose signals measured for astrocytes and GBM43 in PBS (without glucose) were much smaller (close to zero) than the signal measured during exposure to 10 mM glucose. The signal measured during exposure to 10 mM glucose without cells is stable for 8000s which is the time duration of the experiments. The relative sensitivities of the electrodes to H_2O_2 [103], glucose and lactate were also characterized, and the selectivity of glucose with respect to lactate were found to be 4000. In addition, no signal was detected from a Pt electrode biased to measure hydrogen peroxide or other ROS species at 0.5V with respect to Ag/AgCl (as seen in Fig. 4.5)

4.2.3 Apparatus and Method for Spatio-Temporal Resolution of Gradients

The schematic diagram in Fig. 4.1 illustrates a reaction-diffusion system comprising a 2D cell culture (astrocytes or GBM43) surrounded by glucose solution and having three MEA electrodes arranged perpendicularly to the cell culture plane. Each electrode in the MEA operates amperometrically due to the application of a potential that drives the electrooxidation of H_2O_2 generated from oxidation of glucose by the entrapped GOx at the electrode surface and thereby results in an electrical current proportional to the local concentration of glucose. The MEA electrodes were individually addressed by dedicated potentiostats (Reference 600, Gamry Instruments Inc., Warminster, PA) using shared counter and reference electrodes. The counter electrode was a platinum wire of 0.5 mm diameter and the reference electrode was Ag/AgCl (sat'd 3M NaCl), both purchased from BASI Inc. (West Lafayette, IN). Unless stated otherwise, all potentials are referred to the Ag/AgCl (sat'd 3M NaCl) reference electrode, and all experiments were performed at room temperature. The 1D arrangement of the MEA electrodes allows mapping of the concentration profile over a spatial range of 700 μm. The sampling period of each electrode was set at 0.5 s. The measurements were run in a sequence of steps, as follows. Initially, no intentional glucose was in the culture medium. Upon exposure to glucose at t = 0 s, the cells immediately begin uptaking glucose and this uptake generates a transient concentration gradient in the direction perpendicular to the cell culture plane. As it is usual in amperometric measurements, the signals must be conditioned for some time such that the diffusion field around each electrode is reasonably stable. In the present study the conditioning time is 300 s and begins by biasing the electrodes 60 s after glucose exposure. During the conditioning time the MEA chip edge is at 5 mm from the cell surface, and just at the end of this conditioning time (i.e., at t = 360 s) the chip edge is positioned at 30 μm from the cell surface using a XYZ motion control system (Applicable Electronics, New Haven, CT). This movement of the MEA chip

from 5 mm to 30 μm takes 4 s. The relevant data is thus acquired from t = 364 s onwards and the electrode closest to the cell surface (i.e., electrode E1) is located at 110 μm from the cell surface, as illustrated in Fig. 4.1. The amperometric signals measured just prior to t = 360 s at the bulk initial concentration of glucose provided the information to compute the calibration factors for the electrodes, as reported elsewhere. [159, 217]

4.2.4 Astrocyte Cell Culture

Human cerebral cortex astrocytes arrived from ScienCell (Carlsbad, CA) cryopreserved at passage one. Astrocytes were expanded and maintained according to the company's protocol. For each measurement of glucose uptake, passage-three astrocytes (5.0×10^4 cells cm^{-2}) were seeded in 12-well plates (Corning Costar 3515) and incubated for two days in a humidified atmosphere at 37 °C with 5% CO_2. Medium was replaced with fresh astrocyte medium one day after seeding. Glucose uptake rate was measured after two days of incubation. By this time, cultures had grown to approximately 1.2×10^5 cells cm^{-2}. This number was calculated from a growth curve of three human astrocyte cultures (5.0×10^4 cells cm^{-2}) counted each day of incubation for three days. The doubling time was calculated to be 1.547 days. The exponential fit of the cell counts had an $R^2 > 0.99$. Cells were counted by hemocytometer and viability was determined through Trypan Blue Exclusion. Individual cell counts for each culture were acquired immediately following each measurement.

4.2.5 Glioblastoma Cell Culture

Primary patient-derived GBM43 cells were provided by Dr. Jann Sarkaria (Mayo Clinic, Rochester, MN) and have been described prior. [166] Cells were maintained in Dulbecco's Modified Eagle's Medium (DMEM) containing 10% fetal bovine serum in humidified atmosphere at 37 °C with 5% CO_2. Cells were propagated in T75 flasks and fed with growth media every other day. Cells were enzymatically dissociated using

0.25% trypsin/0.5 mmol L^{-1} EDTA solution and passaged every 3 days. For each measurement of glucose uptake rate, propagated GBM43 cells were trypsinized and plated at a density of 10^5 in 1 mL of growth media in 12-well plates (Corning Costar 3515). Glucose uptake rate was measured after the cells had grown to confluency over 3 to 4 days. Cells were counted by hemocytometer and viability was determined through Trypan Blue Exclusion. Individual cell counts for each culture were acquired immediately following each measurement.

4.2.6 Cell Imaging and Preparation for MEA Measurements

Prior to exposing cultures to glucose and measuring uptake rate, cultures were imaged at 100X magnification with ToupView then washed twice with PBS (pH 7.4). The culture wells were then filled with 1 ml of PBS. Next, the culture wells and MEA were put in position for measurement. Finally, 2 ml of PBS with glucose was added, so the resulting glucose concentrations were C_0 = 3, 6, 8, 10 or 15 mM in total volumes o 3 ml. The corresponding surface area and height of the liquid were 3.8 $cm^2$and 0.79 cm, respectively. Following each measurement in glucose solution, cells were imaged again. Appendix shows representative pictures of astrocyte and GBM43 cultures before and after exposure to each C_0 glucose.

4.2.7 Viability Assays

Live/dead assay of astrocyte and GBM43 was used to assess viability of cells after 2 hours of glucose exposure. Cultures were treated in one of four ways: (1) 2 hours in PBS with 5.5 mM glucose, (2) 20 minutes in formalin (negative control), and (3) directly assayed without treatment (positive control). Following treatment, cultures were stained with CellTracker Green (live stain) and propidium iodide (dead stain) (Thermo Fisher Scientific). Images were obtained using confocal fluorescence microscopy with model FV1000 (Olympus). Fig. S-5 in Appendix 1 shows the results.

2 hours in PBS with 5.5 mM glucose had no apparent harmful effect on glioblastoma or astrocyte viability (Fig. S-5(H) in Appendix 1).

4.3 Results

4.3.1 Real Time Acquisition of Transient Glucose Concentrations at Multiple Positions from the Cell Surface

Fig. 4.6 shows representative glucose concentration transients measured in real time at the electrode positions during experiments where in the cell cultures of astrocytes and GBM43 are exposed to C_0 of 3mM and 10mM glucose. Electrodes are labeled as E1 through E3, with E1 and E3 denoting the electrodes nearest to and farthest from the cell surface, respectively. Corresponding results for C_0 of 6, 8, 10 and 15 mM glucose are included in the Appendix. The signals were acquired with sampling period of 0.5 s and were neither filtered nor averaged overtime. The relative values of the concentration amplitudes (E1 $<$ E2 $<$ E3) indicates the presence of a gradient in glucose concentration extending into the bulk solution due to cellular uptake. The recorded concentration transients shown in Fig. 4.6 provide the information required to dynamically map the concentration profile of glucose and determine the corresponding uptake kinetics.

4.3.2 Mapping of the Dynamic Glucose Concentration Profile

Fig. 4.7 shows concentration as a function of distance from the cell surface at selected time points for both astrocytes and GBM43 cells exposed to C_0 of 3mM glucose. Solid symbols are experimental data points obtained from the MEA electrodes (E1-E3) at the indicated time points. The solid red lines represent fits at the corresponding time points, discussed later. Collectively, the data points indicate the evolution of C(z,t) measured over a spatial scale of 700μm and for various time points between 1000 and 8000 s. Although the concentration at each electrode was sampled

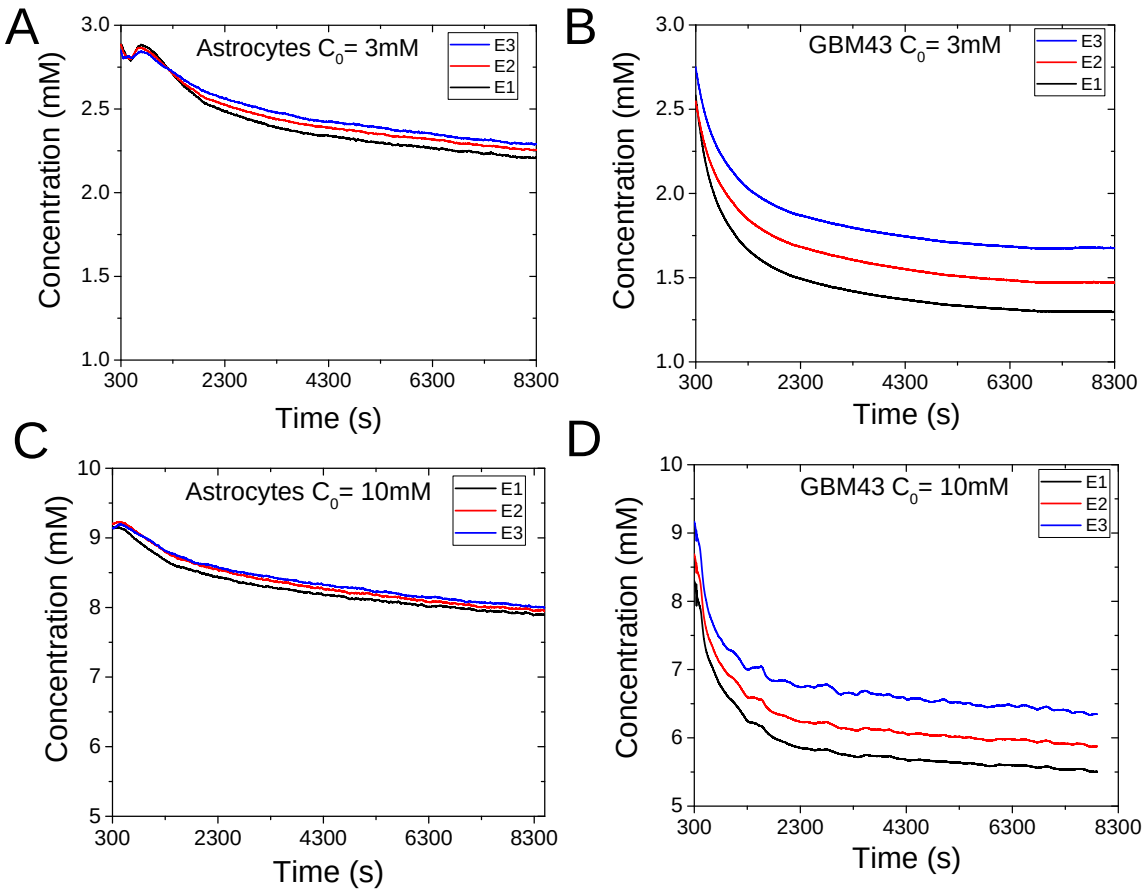

Fig. 4.6. Curves are representative measurements of local concentrations at the positions of the electrodes E1-E3 (located within 700 m from the cell surface) for astrocytes and GBM43 exposed to $C_0 = 3$mM (A and B) and 10mM (C and D) of Glucose. The order in the magnitudes of the signals, E1 < E2 < E3, indicates the presence of a concentration gradient since E1 and E3 are the closest and farthest electrodes from the cell surface, respectively. Measurements were conducted with astrocytes and GBM43 cells at various initial concentrations (3,6,8,10 and 15 mM), as described in text.

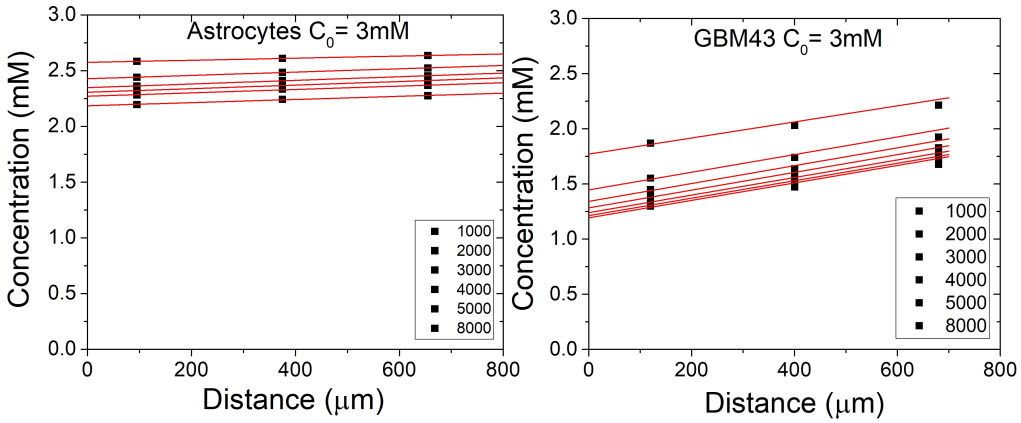

Fig. 4.7. Representative concentration profiles at the indicated timepoints, as measured by the electrodes E1-E3 (symbols) and as obtained from the best fits to a linear model (solid lines) for astrocytes (A) and GBM43 (B) exposed to C_0 of 3mM Glucose. Linear profile fits enable accurate extrapolation of a transient surface concentration and dynamic gradient. For clarity, the profiles are shown at relatively fewer time points as compared to the sampling time of 0.5 s.

every 0.5 s, as shown in Fig. 4.6, C (z,t) is only shown for selected time points for the sake of clarity. Corresponding results for C_0 of 6, 8, 10 and 15mM glucose are included in the Appendix.

A 1D concentration extending into the bulk solution develops because of glucose uptake at the 2D cell surface. Overall, the GBM43 cells exhibit higher glucose uptake rate U_R than the astrocytes since the concentrations near the surface of GBM43 cells are smaller than those of astrocytes. For both cell types a linear profile C(z,t) was observed within the spatial scale over the measurement time (600-8000 s). The linearity of the profile is attributed to relatively low uptake rates of glucose in presence of high analyte concentration. For each time point, surface concentration (C_S) and surface gradient (G_S) can be obtained via extrapolation of the concentration to z=0 and calculation of the corresponding gradient, respectively. Considering the linear C(z,t) observed in the experimental points in Fig. 4.7, a general form linear extrapolation provides accurate values for C_S and G_S.

$$C(z) = A_1(z) + A_2 \tag{4.1}$$

where A_1 and A_2 and A_3 are fitting parameters. Eq. 4.1 was used to fit the experimental concentration versus distance data at timepoints spaced by 100 s. Fig. 4.7 shows the fitted curves (solid redlines) corresponding to the experimental data sets presented in the figure. The fitting was performed at each time point independently, without carrying any information over from prior time points, and the obtained best fits consistently provided $R^2 > 0.97$ at every time point for all the experiments: 30 experiments in total; 15 experiments for each cell type, comprising triplicates of 5 initial concentrations. The consistently high R^2 confirm that the linear regression is enough to extract parameters from the diffusion-reaction system.

4.3.3 Determination of Surface Concentration and Gradients

$C_S(t)$ and $G_S(t)$ can be obtained at every time point from the intercept and the slope respectively from Eq. 4.1,

$$i.e. \left.\frac{\partial C(z,t)}{\partial z}\right|_{z=0} \equiv G_S(t) = A_1 \tag{4.2}$$

$$C(z,t)|_{z=0} \equiv C_S(t) = A_2 \tag{4.3}$$

$$D\left.\frac{\partial C(z,t)}{\partial z}\right|_{z=0} \equiv D \times G_S(t) = F_S(t) \tag{4.4}$$

To minimize variability in cell density between multiple experiments and extract the glucose uptake rate, the surface flux F_S (mol cm^{-2} s^{-1}) in Eq. 4.4, is normalized to the cell density (cell cm^{-2}) to obtain U_R on a per cell basis (mol s^{-1} $cell^{-1}$).

$$D\frac{A}{N}\left.\frac{\partial C(z,t)}{\partial z}\right|_{z=0} \equiv D\frac{A}{N} \times G_S(t) = U_R(t) \tag{4.5}$$

where D = 6×10^{-10} m^2 s^{-1} is the diffusion coefficient of glucose, A is the culture area and N is the number of cells.

The triplicate curves of U_R and C_S for each initial concentration are combined into averaged curves, and these averaged curves are indicated by solid lines in Figs. 4.8 and 4.9, respectively, for astrocytes and GBM43 cells exposed to C_0 of 3, 6, 8, 10 and 15mM glucose. The error bars indicate standard deviation of the averaged curves (n = 3).

As shown in Fig. 4.8, considering the whole spectrum of C_0 from 3 to 15mM, GBM43 show higher glucose uptake as compared to astrocytes. On exposure to higher levels of extracellular glucose (10 and 15 mM), GBM43s uptake glucose at a significantly increased rate ($\sim \times 4$) as compared to the uptake rates at 3,6 and 8mM.

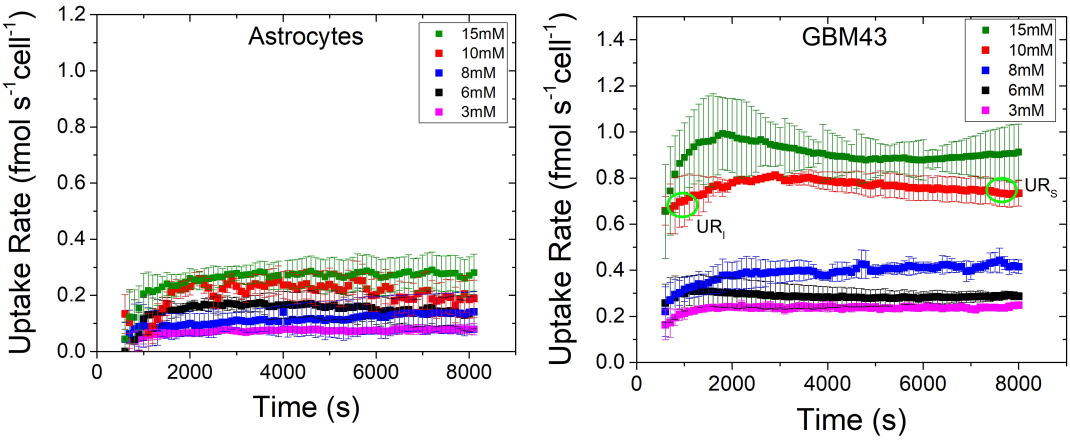

Fig. 4.8. Dynamic glucose uptake rates, U_R, for experiments with the indicated C_0 for astrocytes (A) and GBM43 (B), as extrapolated from the concentration profiles fitted from experimental data. Uptake rate per cell is corresponding surface flux, F_S, computed as the product of gradient and diffusion coefficient of glucose. To minimize variability in cell density between multiple experiments the corresponding flux F_S (mol cm^{-2} s^{-1}) is normalized to the cell density (cell cm^{-2}) to obtain U_R on a per cell basis (mol s^{-1} cell^{-1}). For clarity, data points and error bars are plotted every 100 s. Error bars indicate standard deviation of the mean value from triplicate experiments.

The astrocytes on the other hand show only a moderate increase over the entire spectrum of concentration. Over the measurement time interval, 600-8000 s, the U_R at each C_0 for both cell types shows a modest increase followed by a relatively quick saturation within 1500 s. This transient behavior of U_R is well captured by an exponential fit (solid line) with a time constant (τ). The saturation time, defined as time reach 95% of U_{RS} (3τ), increases from $\sim$(700s and 800s) at 3mM to $\sim$(1300s and 1500s) at 15mM for astrocytes and GBM43 respectively.

Smaller glucose uptake rate implies a lower and slower drop in surface concentration in a reaction-diffusion system, as can be seen Fig. 4.9. Astrocytes show a moderate decrease in surface concentration ($\sim$ 1mM to 2mM) while GBM43s show a higher drop in surface concentration with varying C_0. Moreover, GBM43 exhibit an overlap in surface concentrations when was exposed to C_0 = 8mM (blue curve) and 10mM (red curve) due to a drastic increase in uptake rate by a factor of $\sim$ 2 at 10mM glucose (See Fig. 4.8B). The higher U_R causes increased depletion of the glucose near the vicinity of the cells.

The ample availability of extracellular glucose inferred from the small changes in C_S seen in Fig 4.9 points to a reaction rate limited system, wherein both astrocytes and GBM43 cells kept consuming glucose despite showing changes in morphology during the experiments (see Appendix). Separate live/dead stains (see Appendix) performed on the cells after exposure to glucose indicated high viability of both cell types.

4.3.4 Real time determination of glucose uptake kinetics and extraction of kinetic parameters

The transient behavior of U_R and C_S discussed above captures the effects of cellular kinetics in conjunction with the 1D diffusion profile in the given geometry. As can be seen in Fig. 4.8, the U_{RI} is defined as the initial uptake rate at 600 s and U_{RS} is defined as saturation uptake rate at 8000 s. Fig. 4.10 shows the variation of U_{RS}

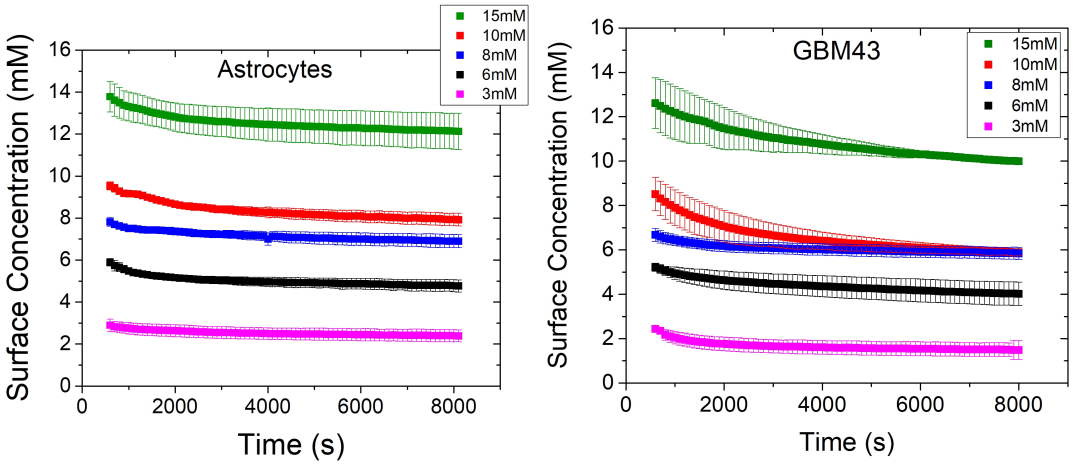

Fig. 4.9. Transient surface concentrations, C_S, for experiments with the indicated C_0 values for astrocytes (A) and GBM43 (B), as extrapolated from the concentration profiles fitted from experimental data. Error bars indicate standard deviation of the mean value from triplicate experiments. For the sake of clarity, data points and error bars are plotted every 100 s as compared to the sampling time of 0.5 s.

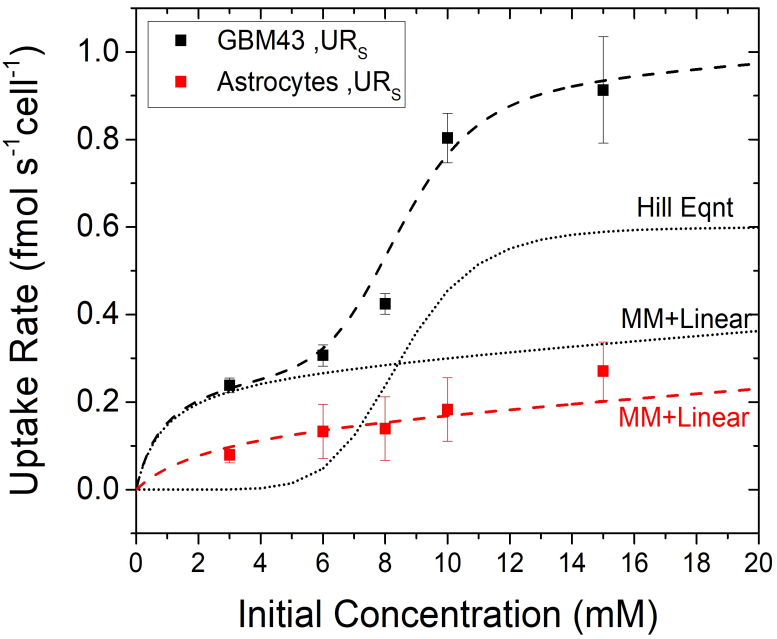

Fig. 4.10. The saturation uptake rate of glucose, U_{RS}, as a function of initial concentration, C_0, for astrocytes (red) and GBM43 (black) as measured experimentally (symbols). Solid symbols indicate the saturation uptake rate measured at 7200s. Error bars indicate standard deviation of the mean value from triplicate experiments. GBM43 demonstrate a combination of linear, Michaelis-Menten (MM) and Hill based allosteric regulation of glucose uptake as can be seen from the best fit of the dashed black line to a Linear + MM + Hill kinetic model. The dotted black lines mark the individual contribution of each mechanism (Linear + MM) and Hill. Whereas, astrocytes show a linear+MM uptake of glucose as seen through the as best fit to a kinetic model (red dashed line).

(solid symbols) versus the initial concentration C_0 for both astrocytes and GBM43. While both GBM43 and astrocyte demonstrate a concentration dependent uptake rate, the GBM43 consume glucose at a higher rate over the entire spectrum of concentration (3-15mM) as compared to astrocytes. The dashed lines passing through the experimental data points in Fig. 4.10 are best fits to Eq. 4.6 (astrocytes) and Eq. 4.7 (GBM43), which describes the dependence of U_{RS} (solid) on C_0 using established kinetic mechanisms, namely simple diffusion via linear and facilitative transport via Michaelis-Menten (MM) [168, 193]. The additional third term in Eq. 4.7 represents the allosteric regulation of glucose consumption or transport in GBM43 via Hill equation for sigmoidal kinetics. The inclusion of the standard deviation of U_R in the data fitting places stronger weighting on data points having the least uncertainty. R^2 for astrocytes and GBM43 cells are 0.997 and 0.996, respectively

$$Astrocytes : U_R(C_0) = [k_{PD} \cdot C_0] + \left[\frac{J_{S1} \cdot C_0}{K_{M1} + C_0}\right] \tag{4.6}$$

$$GBM43 : U_R(C_0) = [k_{PD} \cdot C_0] + \left[\frac{J_{S1} \cdot C_0}{K_{M1} + C_0}\right] + \left[\frac{J_{S2} \cdot (C_0)^n}{(K_{M2})^n + (C_0)^n}\right] \tag{4.7}$$

where K_{PD} is the rate constant for the linear mechanism, J_{S1} is the saturation uptake rate of the MM mechanism and K_{M1} is the MM constant (i.e., concentration at $J_{S1}/2$). Similarly, J_{S2} is the saturation uptake rate of the allosterically regulated MM mechanism, K_{M2} is analogous to MM constant and n is the Hill coefficient indicating the degree of cooperativity. The extracted values of K_{PD}, J_{S1}, k_{M1}, J_{S2}, k_{M2} and n at both initial and saturation time point along with the respective R^2 are presented in Table 4.3.4 for astrocytes and GBM43 cells.

These linear and MM curves quantify the contribution of each mechanism to the measured U_R at any given C_0. The measured rate constant of the linear term representing simple diffusion of glucose across the cell membrane is fairly similar for both cell types. In the physiological glucose concentration range (0–6 mM) the

Table 4.1.
Kinetic parameters extracted from experimental data. Units: K_{PD} - (10^{-12} L s^{-1} $cell^{-1}$), J_{S1} and J_{S2} - (fmol s^{-1} $cell^{-1}$), K_{M1} and K_{M2} - mM

	K_{PD}	J_{S1}	K_{M1}	J_{S2}	K_{M2}	n
Astrocytes	0.0049 ± 0.0005	0.14 ± 0.02	2.4 ± 0.2	–	–	–
GBM43	0.005 ± 0.001	0.27 ± 0.01	0.9 ± 0.1	0.60 ± 0.05	8.5 ± 1	7 ± 2

GBM43 demonstrate a higher affinity for glucose uptake primarily due to the 3x larger J_{S1} and smaller k_{M1}. The low values of $k_{M1} < 3$mM also implies that the measured glucose kinetics in the range (3–6 mM) is observed to be fairly saturated for both cell types. As the concentration increases beyond 6 mM the glucose uptake kinetics in the astrocytes continue to be fairly saturated (the modest increase is attributed to unsaturable simple diffusion across cell membrane). However in GBM43 a sharp increase in the U_R is observed from 6-10 mM which eventually saturates at 15mM. This increase in U_R is attributed to the dominant allosterically regulated MM mechanism with a J_{S2} nearly 5 times as large J_{S1} observed in astrocytes.

The saturation uptake values obtained from the regressions, i.e. $J_{S1} = 0.14 \pm 0.02$ fmol s^{-1} $cell^{-1}$ and 0.27 ± 0.01 fmol s^{-1} $cell^{-1}$ for astrocytes and GBM43 respectively and $J_{S2} = 0.60 \pm 0.05$ fmol s^{-1} $cell^{-1}$ for GBM43,are comparable to results from typical volumetric measurements as discussed in Section 4.4.

The $U_R C_S$ relationships shown in Fig. 4.11 consist of sets of time trajectories, obtained using various U_R values for each cell type (green 15mM, red 10mM, blue 8mM, black 6mM and pink 3mM). Each symbol in every trajectory indicates the time correlated values of U_R versus C_S extracted from experimental data for astrocytes and GBM43. Although each trajectory represents increasing time from right to left (600 to 8000s), as the C_S decreases non-linearly with time (See Fig. 4.9) the representation of time is not linear. Shaded bands surrounding the symbols indicate standard deviation of the mean value of U_R (n = 3). For each cell type, these trajectories can provide insights into the relative effects of cumulative exposure to the analyte, e.g. by comparing the behavior at long exposure times for a large C_0 with that at short time for a smaller C_0.

None of the cell types demonstrate any sets of overlapping/continuous segments as in the case for hydrogen peroxide scavenging reported elsewhere [217]. In astrocytes the uptake rates are small enough such that they do not cause enough depletion near the surface of the cells for any two sets of curves to overlap. However, in GBM43 it is important to note that the segment covering the C_S ranges of $\sim$ (6mM-8mM) shows

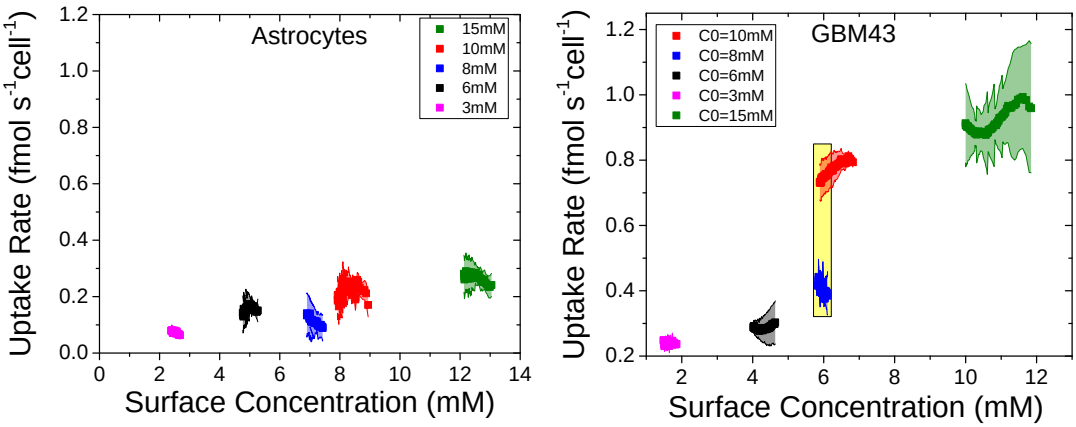

Fig. 4.11. The U_R-C_S relationships consist of sets of time trajectories, obtained using various C_0 values for each cell type (green 15mM, red 10mM, blue 8mM, black 6mM and pink 3mM). Each symbol in every trajectory indicates the time correlated values of U_R versus C_S extracted from the experimental data for astrocytes and GBM43. The shaded bands around each time trajectory indicates the standard deviation from triplicate experiments. The shaded yellow region indicates the hysteretic nature of glucose uptake, wherein despite the same surface concentration being observed, the uptake rate is different and dependent on the intial state i.e. C_0.

two different uptake rates. On exposure to C_0 = 10mM the GBM43 cells consume glucose at twice the rate as compared to C_0= 8mM despite observing the similar range of surface concentrations. Hence it is evident that U_R is not a function C_S but C_S.

4.4 Discussion

Existing glucose assays focus on the use of glucose analogs and/or radiolabels (for e.g. fluorescently tagged 2-NBDG (2-(N-(7-nitrobenz-2-oxa-1,3-diazol-4-yl) amino)-2-deoxyglucose), 2DG (2-deoxyglucose and radio-labeled analog 3H-2DG)) for making an end time point estimate of glucose uptake that can be quantified through detection of accumulated analogs as it is shuttled into a variety of intracellular pathways [53, 210,246]. In this study we have demonstrated the analytical capabilities of a positionable glucose selective MEA to measure extracellular concentration profiles to quantify total glucose uptake kinetics in real time with high temporal resolution. If used in conjunction with powerful tools like the Seahorse extracellular flux (XF) analyzer (Seahorse Bioscience) [2,4,54,247,248] for estimating glycolytic and respiration rates, the MEA and the technique not only enables direct measurement of total glucose uptake by the cells but also simultaneous local surface concentrations.

It is informative to compare the results from the current study with those from prior glucose experiments. In our experiments, the glucose U_{RS} were in the order of the $\sim$ 0.1 fmol s^{-1} $cell^{-1}$ and 0.25 fmol s^{-1} $cell^{-1}$ in physiological range of glucose (3-6mM) for astrocytes and GBM43 respectively. In comparison, reports in literature have quoted uptake rates for astrocytes in the range of 0.05-0.2 fmol s^{-1} $cell^{-1}$ for similar glucose concentration range (3-7mM) (See Table 4.2). *Eloqayli et al.,2011* [277] reported an uptake rate of 0.3 fmol s^{-1} $cell^{-1}$ for C6 glioma cell in 3mM glucose. At higher glucose concentrations (10-15mM) the glucose U_{RS} was measured in the order of the $\sim$ 0.2 fmol s^{-1} $cell^{-1}$ and 1 fmol s^{-1} $cell^{-1}$ in astrocytes and GBM43 respectively. While the increase in U_{RS} for astrocytes is modest, GBM43 cells show

increase by a factor of 4 in the uptake of glucose. This concentration dependent increase in U_R is also comparable to the higher uptake rates reported in the range of 0.84 - 2 fmol s^{-1} $cell^{-1}$ when the measurements were done in the cell media, which typically have higher glucose concentration ∼25mM [207, 278–280]. Note that the U_R quoted from literature are converted into units of fmol s^{-1} $cell^{-1}$ from fmol s^{-1} mg $protein^{-1}$ by assuming protein concentration in the cells [281–284].

Table 4.2.
Estimated glucose Uptake Rates reported in literature. Units: (fmol s^{-1} $cell^{-1}$)

Cells	**Analyte**	**U_R (fmol s^{-1} $cell^{-1}$)**
Average neuronal uptake	Glucose analog	0.1
Astrocytes [285]	Glucose analog	0.05
Astrocytes [286]	Glucose analog	0.1
Astrocytes [287]	D-Glucose	0.1
Astrocytes [277]	D-Glucose	0.2
C6 Glioma [277]	D-Glucose	0.3
C6 Glioma [278]	Glucose analog	2
U87 GBM [207]	D-Glucose	1.5
Glioma [279]	D-Glucose	0.84
Glioma [280]	Glucose analog	1.1

The increased glucose uptake rate of the GBM43 cells as compared to the astrocytes quantifies and contributes to the prevailing hypothesis that cancer cells demonstrate increased glucose metabolism as compared to normal cells [202, 208, 211, 224, 231, 288]. In addition, the concentration dependence of U_R (Fig. 4.8) illustrates the difference between kinetic mechanisms involved in the uptake of glucose for astrocytes and GBM43.

In astrocytes the kinetic uptake of glucose can be explained by MM type high affinity glucose transport mechanisms in combination with a unsaturable diffusion component. Previous reports have shown the presence of GLUT1 transporters in the feet of astrocytes responsible for the primary intake of glucose in the brain due to their proximity to the blood vessels [193, 230, 289–292]. The prevalence of GLUT1 as primary glucose transporter in astrocytes is also confirmed in our experiments. The half-maximal rate concentration for the high affinity glucose mechanism (second term in Eq. 4.6) was measured to be $K_{M1} = 2.4 \pm 0.2$ mM which is comparable to the K_M values of GLUT1 found in literature measured using biochemical assays [193, 196, 289, 291, 293]. Considering the physiological range of glucose (upto 6mM), a high affinity MM kinetic mechanism with $K_{M1} = 0.9 \pm 0.1$ mM was found to be dominant in GBM43. Moreover, the maximum capacity of glucose uptake was measured to be $J_{S1} = 0.27 \pm 0.01$ fmol s^{-1} $cell^{-1}$ which was greater than $J_{S1} = 0.14 \pm 0.02$ fmol s^{-1} $cell^{-1}$ for astrocytes. GLUT3 has been reported to have a $K_M = 1.4$ mM and saturation capacity (V_{max}) 3-5 times greater than GLUT1. While both GLUT1 and GLUT3 are found to be overexpressed in glioblastomas, GLUT3 is shown to be preferentially expressed in brain tumors to survive in glucose poor microenvironments due to its higher glucose affinity and higher capacity [211, 212, 224–227, 229, 230, 294]. Hence, the lower K_{M1} and higher capacity of glucose uptake J_{S1} can be attributed to GLUT3 expression in GBM43.

Beyond the physiological range of glucose (> 6mM), the increase in U_R is modelled well by a sigmoidal fit attributed to a glucose mechanism with apparent $K_{M2} = 8.5 \pm 0.5$ mM and $J_{S2} = 0.60 \pm 0.05$ fmol s^{-1} $cell^{-1}$. Evidence of this non-linear increase in uptake rate in glioblastoma can also be found in previous work by [295] who observed a $\sim 5\times$ increase in the intracellular glucose concentration when the extracellular supply of glucose was elevated from 11mM to 25mM. The S shaped sigmoid clearly points to positive allosteric regulation of glucose uptake in the metabolic pathways of GBM43 cells.

The transient nature of glucose uptake rate as seen in Fig. 4.8 resembles a charging capacitor with a saturation time constant (3τ)). The transient increase and subsequent saturation in glucose uptake rate can be related to the time required to balance intracellular consumption reactions regulated by metabolic processes such as endocytosis of GLUT transporters, gene expressions of metabolic enzymes etc., which have characteristic time scales of minutes [296, 297], with the extracellular glucose uptake. The low measurement times (0.5 s) of the MEA device in contrast with the longer time constants of metabolic processes (minutes) enable the measurement of the resulting transient behavior of glucose uptake rate. Additionally, while the concentration dependence of uptake rate is also observed at early times (U_{RI}- Initial uptake rate after 600s of exposure to C_0 glucose) the maximum capacity of the MM transporter mechanisms (J_{S1} and J_{S2} achieved via kinetic model fits is reduced.

The U_R-C_S relationship shown in Fig. 4.11, contain a set of time trajectories obtained using various C_0 values for each cell type. These trajectories provide insights into the relative effects arising due to differing exposure history of glucose. The hysteretic nature of U_R in GBM43 is evident from the observation of multiple uptake rates at the same surface concentration due to different C_0 = 8mM and 10mM. Critically, this hysteresis stems from the non linear dependence of the reaction rate k_F on the initial extracellular glucose exposure $C_0 = C_S(t=0)$ rather than the instantaneous surface concentration $C_S(t)$ (See Eqs. 4.6 and 4.7). The resulting U_R in turn depends non-linearly on C_0, which can also be seen from the activation of an elevated glucose transport mechanism (as modelled by Hill kinetics in Eq. 4.7) by GBM43 when exposed to a higher C_0 = 10 mM in comparison to C_0 = 8 mM, despite the cells observing a similar instantaneous $C_S(t)$ in both cases. Additionally, the dependence of U_R on C_0 points to the presence of a glucose sensing apparatus in GBM43 which is not only found in brain cells [200, 298, 299] but was also speculated to be in cancer stem cells by *Flavahan et al.,2013* [274] who found elevated levels of GLUT2 in glioblastoma stem cells.Moreover, occurrence of allosteric regulation is also linked to a glucose sensing apparatus in cells [200, 298, 299]. Together, these results

provide with a clear picture of the metabolic reprogramming the GBM43 undergo in comparison to astrocytes. The MEA and the measurement methodology, enables the continuous monitoring of total U_R with high temporal resolution which allows a more quantitative determination of the kinetic parameters in comparison to standard glucose assays. In addition, by simultaneously extracting transient C_S, the kinetic mechanisms were found to hysteretic and dependent on the $C_0 = C_S(t=0)$ while using same measurement methodology with a different MEA on the same set of cells, the hydrogen peroxide U_R was found to be dependent on the instantaneous C_S. Overall the ability to measure U_R, C_S simultaneously as a function of time can also be used as a tool to for distinguishing cellular kinetic mechanisms when used in conjunction with biochemical assays.

4.5 Conclusions

In this chapter, we demonstrate the use of a glucose selective MEA customized for typical 2D culture setups to measure glucose metabolism from normal (human astrocytes) versus cancer (GBM43) cells. The MEA along with the in situ transient calibration technique developed earlier [159, 217] was tuned to provide stable multi-point glucose selective signals over a time span of at least 4hrs, to enable measurement of total glucose uptake from the extracellular media into the 2D culture. At each time point, the concentration profile is fit using an analytical expression for a 1D diffusion/reaction system, allowing extrapolation of the surface concentration and surface gradient. Measurements at various initial concentrations allow determination of the uptake rate over a wide range of surface concentrations. Complementing existing tools like the Seahorse Flux analyzer which measure glycolytic rates (G_R) and respiration rates (R_R), the glucose MEA demonstrated in this study provides a measure of total uptake rate (U_R=G_R+R_R+O_R) which can provide a key insight into other cellular metabolic pathways (O_R) like bio-synthesis. The results show a clear reprogramming of glucose metabolic pathway of GBM43 in comparison to astrocytes.

While both cell types show concentration dependent uptake rates, GBM43 cells have an increased glucose uptake rates as compared to astrocytes over the entire concentration spectrum (0-15mM). The astrocytes glucose uptake over the entire concentration spectrum was well explained by a high affinity MM transporter mechanism, previously attributed to the expression of GLUT1, and an unsaturable passive diffusion component. In comparison, in the physiological range of glucose ($<$ 6mM), GBM43 exhibit a higher affinity and capacity to glucose uptake, attributed primarily to elevated MM type GLUT3 transporter mechanism. Moreover, above ($>$ 6mM) traits of allosteric regulation were observed from a sigmoidal U_R for GBM43. The monitoring of U_R vs C_S in a more natural local environment was used to identify the hysteretic nature of glucose uptake in GBM43, wherein the U_R was dependent on $C_S(t=0)$ i.e. C_0 rather than on instantaneous $C_S(t)$. Collectively, evidence of allosteric regulation along with the possibility of a glucose sensing apparatus in GBM43 warrants further study via biochemical assays. The current study also raises the need to investigate whether metabolic reprogramming observed in the GBM43 cells is a result of culturing of cancer cell lines in high concentration media ($\sim$ 25mM). The capabilities to quantify cumulative exposure effects and uptake rates over a wide range of cell surface concentrations are relevant evaluation of potential therapeutic approaches based on differential uptake by cancerous versus normal cells. In addition to shedding light on mechanistic behavior, the resulting kinetic parameters should be well suited for developing reactiondiffusion models that more accurately describe more complex culture/tissue geometries. Future work also includes extension of the MEA technique to multi-analyte metabolite measurements, e.g. monitoring of both uptake and released analytes in their local diffusion environments.

5. DEMONSTRATION OF SIMULTANEOUS GLUCOSE AND LACTATE GRADIENT MEASUREMENTS

5.1 Introduction

As the focus of this chapter, we consider the cellular uptake of glucose and release of lactate from genetically engineered mouse models of pancreatic ductal adenocarcinoma (PDAC). PDAC is the most common type of pancreatic cancer, comprising of 90% of all exocrine pancreatic cancer [300]. PDAC's extremely dense cellular network leads to a nutrient deficient and hypoxic tumor microenvironment, despite of which increased proliferation, survival and invasion is observed due to the reprogramming of their metabolic and genetic pathways. Genetically engineered mouse models (GEMMs) have been adopted as an approach to understand the metabolism by mimicing the mutations found in human pancreatic cancer [301]. The observation of oncogenic mutations (for e.g KRAS gene) has been linked to upregulation of glucose transporter (GLUT)-1 (increasing glucose uptake) along with other intracellular enzymes like the hexokinase and phosphofructokinase resulting in increased glycolysis and hence the production of lactate. This lactate then acts as a nutrient source for the other cells in the tumor environment [302, 303]. This study proposes the measurement of simultaneous glucose uptake and lactate release from cells isolated from GEMMs with mutations common to human PDAC, such as Kras, p53, and p16.

Previous MEA or wire based platform have reported simultaneous glucose and lactate concentration transient measurements [87, 103, 264–266, 271, 272]. However, in order to extract real time kinetic information, dynamic mapping of the concentration profile near the cell surface is required to enable simultaneous determination of surface concentration (C_S) and uptake rates (U_R) by extrapolation to the cell plane [159, 217]. Hence this chapter focuses on the extension of the enzymatic biosensing strategy

described in the previous chapter to the positionable MEA with customized geometry for the real time,simultaneous measurement of multi-analyte concentration gradients of glucose and lactate near 2D cell cultures.

In addition, the one of the future goals of this study is to enable the integration of a metabolite concentration/gradient measurement system to a Tumor microenvironment on chip (TMOC) with the ability to maintain a microenvironment similar to complex in vivo tumors including geometry, structure, nutrient supply and the chemical diffusion environment (as shown here [304–306]). In the complex spatio-temporal environment of the TMOC quantifying metabolic kinetics of cancer cells requires the optimum measurement and fabrication scheme. By quantifying and providing mechanistic insights into the glucose and lactate metabolism of the pancreatic cancer cells in 2D cell culture, the design and fabrication of microsensors, especially the spatio-temporal resolution, within the TMOC can be optimized. Moreover, while previous works have provided phenomenological insights into the differences between cancer cells cultured in 2D vs 3D environments [304–306], measurement of metabolic kinetics from 2D cell cultures not only acts as point of reference but is also critical in understanding the origin of metabolic differences which may or may not arise due to specific geometry or structural changes.

5.2 Acquisition of Cell Lines

Cells were provided by graduate student Hye-Ran Moon from Dr. Bum Soo Han lab, Purdue University. The description is quoted as is from *Bradney et. al.,2017* [304], "Two different cancer cell genotypes were isolated from genetically engineered mouse models. KPC mice, containing LSL-$Kras^{G12D/+}$, LSL- $Trp_{53}{}^{R172H}$, pdx1Cre alleles gave rise to the KPC-2 tumor cell line. KPC-2 cells were isolated in the lab of Dr. Stephen F. Konieczny at Purdue University. The KIC cell line was established from mice containing $Kras_{G12D}$ allele and an $Ink4a/Arf^{fl/fl}$, and pdx1Cre alleles, which

in turn inactivates p_{16}^{Ink4a}. KIC cells were isolated in the lab of Dr. Murray Korc at Indiana University."

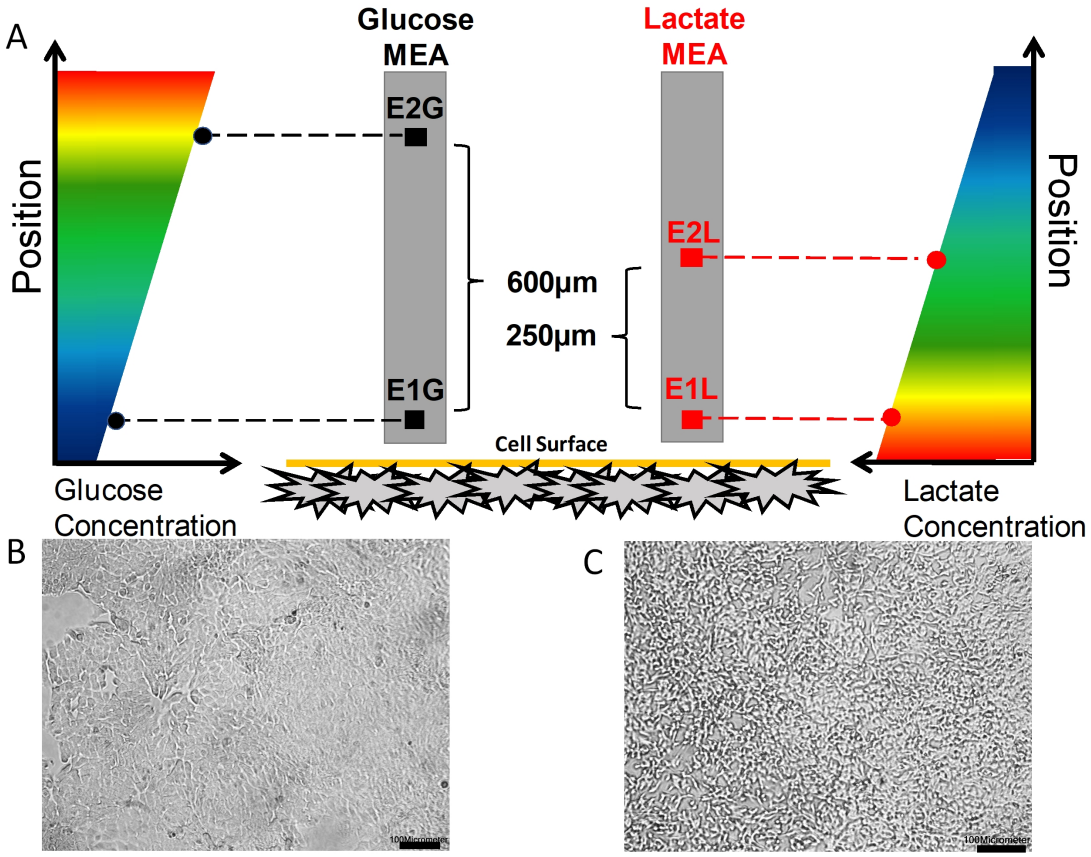

Fig. 5.1. Glucose and Lactate MEAs simultaneously measures transient glucose and lactate concentrations at two positions each near the surface of cells in 2D cell culture. (A) Schematic of the experimental setup (not drawn to scale) illustrating how the glucose and lactate MEA electrodes acquire two spatial data points of the concentration profile near the cell surface. 2 platinum microelectrodes, 100 μm 100 μm each, are arranged in two one-dimensional arrays. The pitch of the glucose and lactate MEAs are 600μm and 250μm respectively. (C) Image of KIC in 2D culture prior to experiment (D) Image of KPC2 in 2D culture prior to experiment. Scale bar is 100μm.

5.3 Cell Culture for Experiments

Both KPC2 and KIC cell lines were initially grown on polystyrene tissue culture treated flasks (Fisher Scientific, Hampton, NH) in HyClone RPMI 1640 medium with L-glutamine (GE Healthcare Life Sciences, Pittsburgh, PA) supplemented with 5% fetal bovine serum (FBS, Gibco, Carlsbad, CA) and 10,000 U/mL Penicillin-Streptomycin (Invitrogen, Carlsbad, CA). For use in experiments, cells were harvested at 70-80% confluence using 0.05% Trypsin-EDTA (Invitrogen, Carlsbad, CA) [304]. The harvested cells were seeded in 12-well plates (Corning Costar 3515) with a density of 10^5 cells/well in 1 mL of growth media and incubated for two days in a humidified atmosphere at 37 °C with 5% CO_2. Medium was replaced every day after seeding. Prior to exposing cultures to glucose and measuring uptake rates, cultures were imaged at 100X magnification with ToupView then washed twice with PBS (pH 7.4). The culture wells were then filled with 1 ml of PBS. Next, the culture wells and MEA were put in position for measurement. Finally, 2 ml of PBS with glucose and lactate was added, so the resulting initial glucose and lactate concentrations were $C_{0,G} = 3$ & 10 mM and $C_{0,L} = 50$ μM & 50 μM respectively in total volumes of 3 ml. The corresponding surface area and height of the liquid were 3.8 cm^2 and 0.79 cm, respectively. Following each measurement in glucose-lactate solution, cells were imaged again.

5.4 MEA Design, Fabrication and Characterization

Two individually addressable 1D MEA arrays, one each for glucose and lactate, were employed for this study for simultaneous gradient measurements. The glucose MEA and lactate MEA were fabricated on separate chips with a spacing of ($\sim$1 cm) between them in order to avoid non-selective adsorption of the selective enzyme and the H_2O_2 crosstalk between the two sets of electrodes. Array 1 with two individually addressable electrodes was used was for measuring glucose uptake with a pitch (ΔX) of 600μm and electrode size of 100 μm. Electrodes are located very close to the bottom edge of the silicon die and are designated E1G and E2G. Relative to the

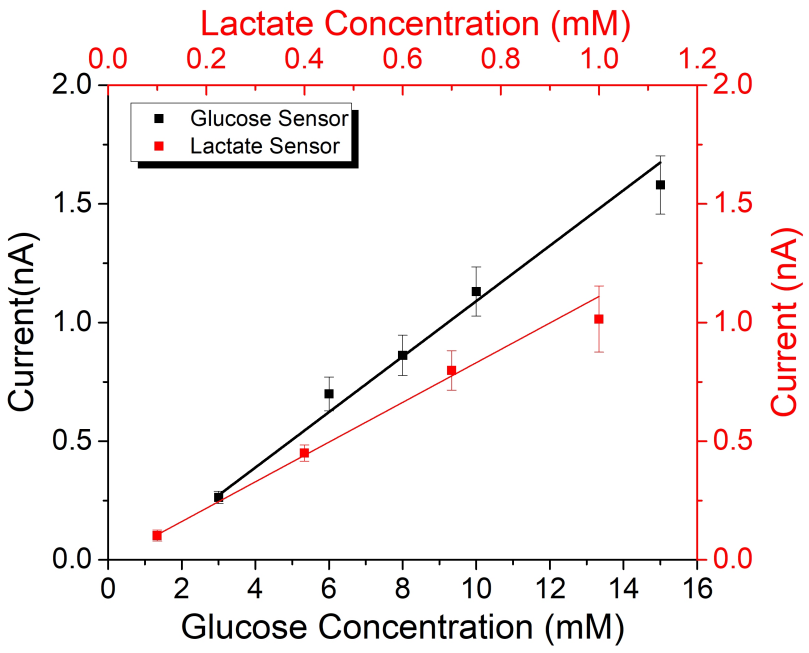

Fig. 5.2. Glucose sensors in MEA 1 have a linear range and sensitivity of 0-15mM and 116 $\pm$ 16 pA mM^{-1}. Lactate sensors in MEA 2 have a linear range and sensitivity of 0-1mM and 1.1 $\pm$ 0.05 nA mM^{-1}.

bottom edge of the die, E1G is the closest and E2G is the farthest electrode. A pitch of 600μm means that the spatial range of the gradient measurements is $\sim$ 700 μm (Fig. 5.1). Array 2 was used was for measuring lactate uptake with a pitch (ΔX) of 250μm and electrode size of 100 μm .Electrodes are located very close to the bottom edge of the silicon die and are designated E1L and E2L. Relative to the bottom edge of the die, E1L is the closest and E2L is the farthest electrode.

In 2D cell cultures, the glucose concentration ranges from 5mM - 25mM and the small glucose uptake rates observed in cells (See Table 4.2) results in shallow concentration gradients. Since only a fraction of the glucose uptaken is expected to be converted to lactate via glycolysis, a smaller pitch for lactate MEA was chosen due to the smaller concentration scale $\sim$ μM and limited release duration resulting in smaller spatial scales of the lactate gradient generated.

The biofunctionalization scheme discussed in Section 4.2.2 was used on each array. The glucose MEA procedure was the same as discussed before, while the only change for the lactate MEA was the enzyme. Lactate Oxidase (LOx) is the primary transducer which oxidizes lactate into pyrvate and H_2O_2.

L-Lactate + O_2 $\longrightarrow$ Pyruvate + H_2O_2

Electro-oxidation of the intermediate H_2O_2 produces the current proportional to the lactate concentration. The bare Pt microelectrodes are nanostructured by electrodeposition of platinum black (Pt-B) to enhance the sensitivity to H_2O_2. LOx is immobilized in a perm-selective layer of poly-O-aminophenol (PoAP) which is electrodeposited on the Pt-B surface. The electroactive polymer layers were deposited one after another using multiple rounds of potential cycling in aqueous enzyme doped monomer solutions. The perm selective layer acts as a deterrent for interferents such as ascorbic acid commonly found in physiological solution [103] . Tuning of the sensitivity was done by controlling the enzyme loading in the perm selective layer. 20 mg/ml was chosen as the optimum enzyme loading concentration based on maximum sensitivity. Ten voltammetry cycles (0-900mV at 50mV/s wrt Ag/AgCl) are applied in the aqueous enzyme doped monomer solution (O- Aminophenol + LOx).

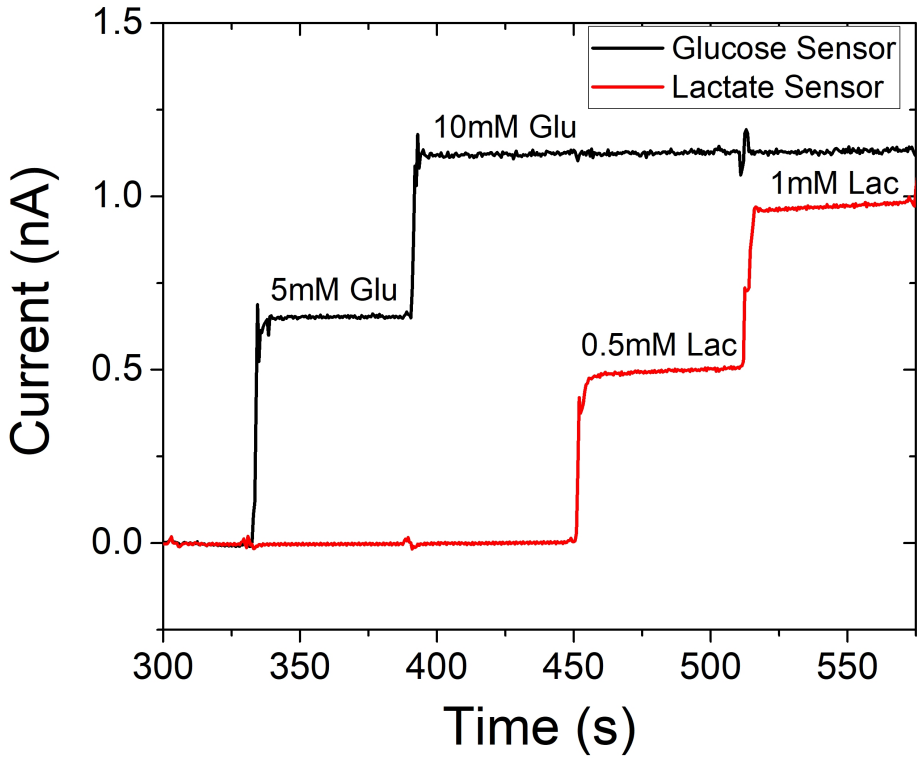

Fig. 5.3. Response of the lactate MEA in presence of glucose and vice versa. A minimum lactate to glucose selectivity of 4000:1 was observed for the lactate MEA. Conversely, minimum glucose to lactate sensitivity of 4000:1 was observed for the glucose MEA.

As before the modified biofunctionalization scheme was supplemented by pre-surface treatment and post-glucose wash to achieve signal stability. Prior to GOx and LOx deposition, the MEAs were were incubated in a solution of 12 mg/ml tris(hydroxymethyl)aminomethane (TRIS) and $\sim$ 1 mg/ml glycine in PBS for 48-60 hours at room temperature. The treatment prevents non-specific adsorption of GOx and LOx on the SU8 passivation layer [276]. Post enzyme deposition, the glucose and lactate wash further removes any loosely attached enzymes to provide a relatively stable signal.

The lactate MEA electrodes were characterized for lactate response by performing amperometry in unstirred solution, as shown in in Fig. 5.2. The average sensitivity of electrodes in the lactate MEA was found to be 1.1 $\pm$ 0.05 nA mM^{-1}. Moreover, as shown in linear range of the lactate sensor was verified to be at least (0-1mM), which is within the concentration range of interest for this study. The effects of the sensitivity variations (electrode-electrode $\sim$ 5% and experiment to experiment $\sim$15%) are minimized via in situ transient calibrations where calibration factors are acquired immediately prior to the measurements near the cell surface. [159, 217]

As shown in Fig. 5.3 selectivity of the glucose and lactate MEA was verified. A resolution of atleast 4000:1 (Glucose MEA response to Glucose:Lactate) and vice versa is observed. The resolution of 4000:1 are due to the signal noise limits rather any discernible crosstalk.

5.5 Apparatus and Method for Spatio-Temporal Resolution of Gradients

The schematic diagram in Fig. 5.1 illustrates a reaction-diffusion system comprising a 2D cell culture (KPC2 or KIC) surrounded by glucose and lactate PBS solution and having two MEAs arranged perpendicularly to the cell culture plane. Each electrode in the glucose MEA operates amperometrically due to the application of a potential that drives the electrooxidation of H_2O_2 generated from oxidation of glucose by the entrapped GOx at the electrode surface and thereby results in an elec-

trical current proportional to the local concentration of glucose. At the same time each electrode in the lactate MEA operates amperometrically due to the application of a potential that drives the electrooxidation of H_2O_2 generated from the oxidation of lactate by the entrapped LOx at the electrode surface and thereby results in an electrical current proportional to the local concentration of lactate.

The MEA electrodes were individually addressed by dedicated potentiostats (Reference 600, Gamry Instruments Inc., Warminster, PA) using shared counter and reference electrodes. The counter electrode was a platinum wire of 0.5 mm diameter and the reference electrode was Ag/AgCl (sat'd 3M NaCl), both purchased from BASI Inc. (West Lafayette, IN). Unless stated otherwise, all potentials are referred to the Ag/AgCl (sat'd 3M NaCl) reference electrode, and all experiments were performed at room temperature.

The 1D arrangement of the glucose MEA electrodes allows mapping of the concentration profile over a spatial range of 600 μm. While the 1D arrangement of the lactate MEA electrodes allows mapping of the concentration profile over a spatial range of 300 μm. The sampling period of each electrode was set at 0.5 s. The measurements were run in a sequence of steps, as follows. Initially, no intentional glucose or lactate was in the culture medium. Upon exposure to glucose and lactate at t = 0 s, the cells immediately begin uptaking glucose and releasing lactate. This uptake and release generates two transient concentration gradient in the direction perpendicular to the cell culture plane, one that of glucose while the other that of lactate.

As it is usual in amperometric measurements, the signals must be conditioned for some time such that the diffusion field around each electrode is reasonably stable. In the present study the conditioning time is 420 s and begins by biasing the electrodes 60 s after glucose and lactate exposure. During the conditioning time the MEA chip edge is at 5 mm from the cell surface, and just at the end of this conditioning time (i.e., at t = 500 s) the chip edge is positioned at 30 μm from the cell surface using a XYZ motion control system (Applicable Electronics, New Haven, CT). This movement of the MEA chip from 5 mm to 30 μm takes 4 s. The relevant data is thus acquired from

t = 500 s onwards and the electrode closest to the cell surface (i.e., electrode E1) is located at 75 μm from the cell surface, as illustrated in Fig. 5.1. The amperometric signals measured just prior to t = 500 s at the bulk initial concentration of glucose and lactate provided the information to compute the calibration factors for the electrodes, as reported elsewhere. [159,217]. For this study only the inital concentration of glucose is varied $C_{0,G}$= 3mM and 10mM, while the $C_{(0}, L)$ is fixed at 50 μM.

5.6 Simultaneous acquisition of multi point transient glucose and lactate concentrations

Fig. 5.4 shows representative glucose concentration transients measured in real time at the electrode positions during experiments where in the cell cultures of KPC2 and KIC are exposed to C_0 of 10mM glucose. Electrodes are labeled as E1G, E2G and E1L and E2L, with E1 and E2 denoting the electrodes nearest to and farthest from the cell surface, respectively. Similar measurements were also made at C_0 of 3 mM glucose. The signals were acquired with sampling period of 0.5 s and were neither filtered nor averaged overtime. The relative values of the concentration amplitudes (E1G < E2G) indicates the presence of a gradient in glucose concentration extending into the bulk solution due to cellular uptake. Similarly, the relative values of the concentration amplitudes (E1L > E2L) indicates the presence of a gradient in lactate concentration extending into the bulk solution due to cellular uptake. The recorded concentration transients shown in Fig. 5.4 provide the information required to dynamically map the concentration profile of glucose and determine the corresponding uptake kinetics. The concentration data acquired from each position is used to map the concentration as a function of distance from the cell surface at selected time points as done in previous chapters. Collectively, the profile indicates the evolution of $C_G(z, t)$ and $C_L(z, t)$ measured over a spatial scales of 600μm and 300μm respectively for various time points between 500 and 5000 s. A 1D concentration extending into the bulk solution develops because of glucose uptake at the 2D cell surface. Simultaneously,

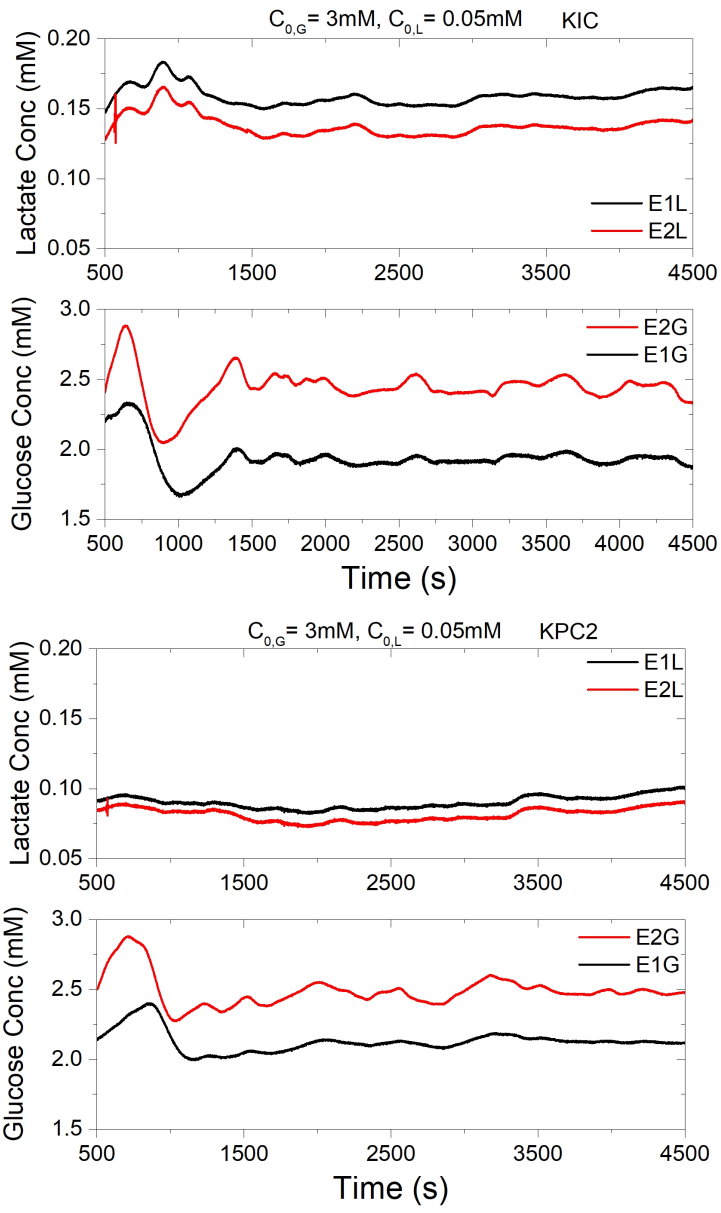

Fig. 5.4. Curves are representative measurements of local concentrations at the positions of the electrodes E1G-E2G (located within 600 m from the cell surface) and E1L-E2L (located within 300 m from the cell surface) for KIC (A and B) and KPC2 (C and D) exposed to $C_{0,G} = 3$mM of Glucose. The order in the magnitudes of the signals, E1G $<$ E2G for glucose and E1L $>$ E2L for lactate indicates the presence of two opposite concentration gradients since E1 and E2 are the closest and farthest electrodes from the cell surface, respectively. Measurements were also conducted with KPC2 and KIC cells at $C_{0,G} = 3$ mM as described in text.

another 1D concentration extending into the bulk solution develops because of lactate release at the 2D cell surface. Extrapolation of the gradient and concentration to the surface of cells enables the determination glucose uptake U_R and lactate release R_R rates.

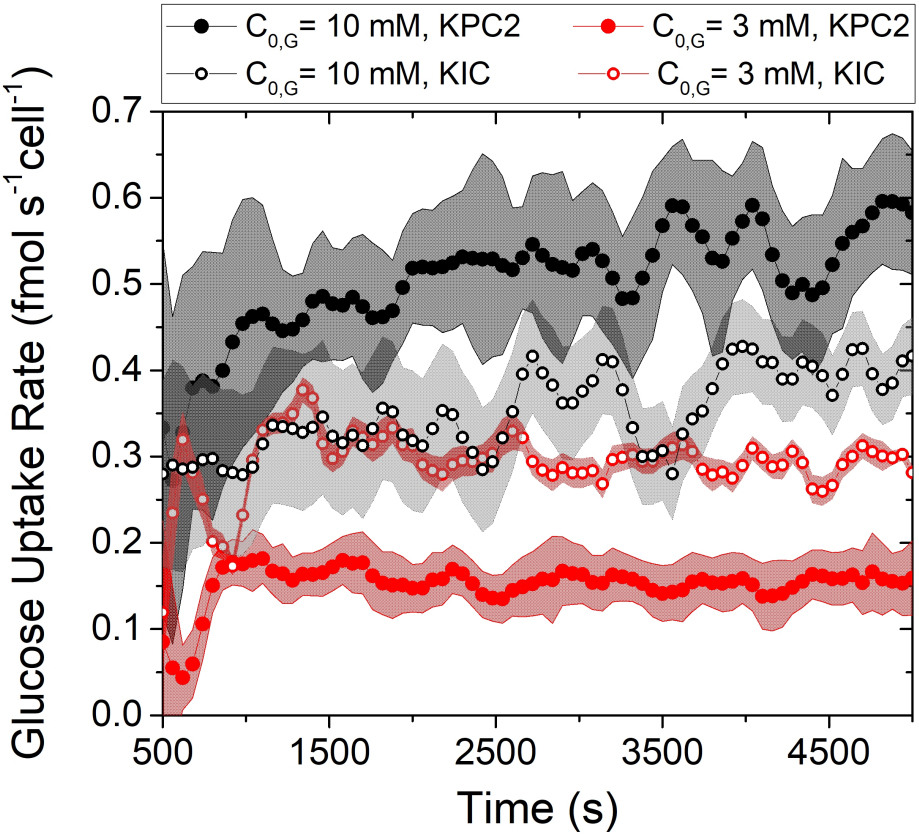

Fig. 5.5. Dynamic glucose uptake rates, U_R, for experiments with the indicated C_0 for KIC and KPC2, as extrapolated from the concentration profiles fitted from experimental data. Uptake rate per cell is corresponding surface flux, F_S, computed as the product of gradient and diffusion coefficient of glucose. To minimize variability in cell density between multiple experiments the corresponding flux F_S (mol cm^{-2} s^{-1}) is normalized to the cell density (cell cm^{-2}) to obtain U_R on a per cell basis (mol s^{-1} cell^{-1}). For clarity, data points and error bars are plotted every 60 s. Shaded error bars indicate standard deviation of the mean value from triplicate experiments.

5.7 Determination of Glucose Uptake and Lactate Release Rates

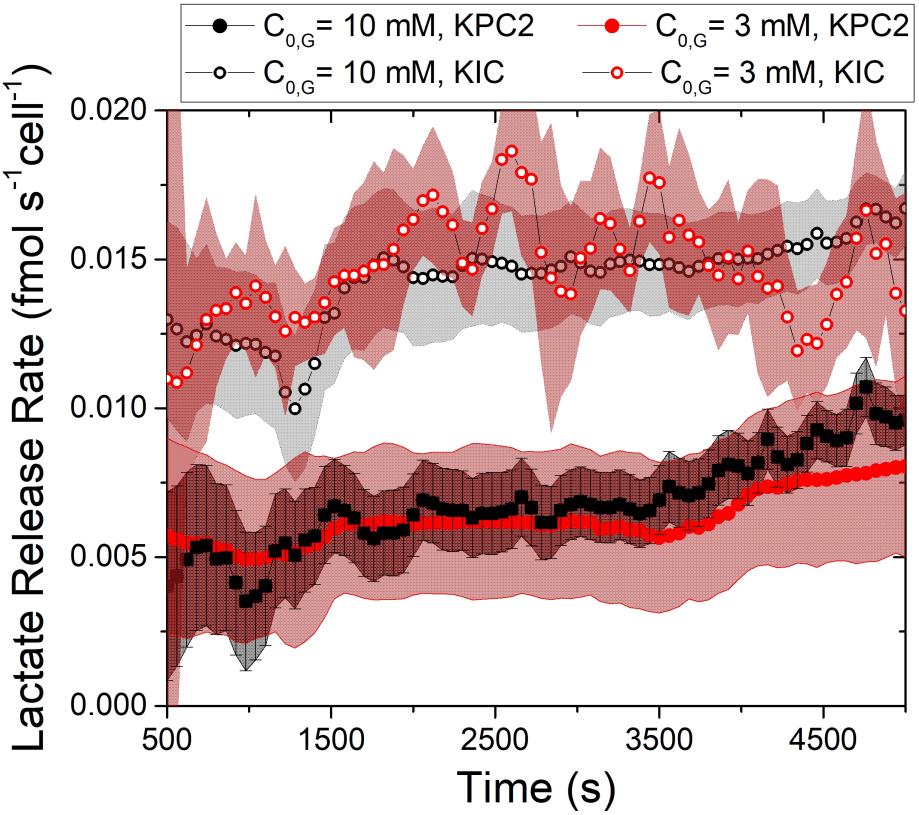

Fig. 5.6. Dynamic lactate release rates, R_R, for experiments with the indicated C_0 for KIC and KPC2, as extrapolated from the concentration profiles fitted from experimental data. Release rate per cell is corresponding surface flux, F_S, computed as the product of gradient and diffusion coefficient of lactate. To minimize variability in cell density between multiple experiments the corresponding flux F_S (mol cm^{-2} s^{-1}) is normalized to the cell density (cell cm^{-2}) to obtain R_R on a per cell basis (mol s^{-1} cell^{-1}). For clarity, data points and error bars are plotted every 60 s. Shaded error bars indicate standard deviation of the mean value from triplicate experiments.

The triplicate curves of glucose U_R for each initial glucose concentration are combined into averaged curves, and these averaged curves are represented in Fig. 5.5. Similarly, the triplicate curves of lactate R_R for each initial glucose concentration are combined into averaged curves, and these averaged curves are represented in Fig. 5.6.

The error bars indicate standard deviation of the averaged curves (n = 3). The Figs. 5.5 and 5.6 show curves for KPC2 and KIC cells exposed to $C_{0,G}$ of 3 and 10mM glucose.

As shown in Fig. 5.5, considering the whole spectrum of C_0 from 3 to 10mM, KPC2 shows an increase in glucose uptake from $C_{0,G}$ of 3 and 10mM. In comparison, KIC cells show the same glucose uptake rate at both $C_{0,G}$. Additionally, the U_R for KPC2 at $C_{0,G}$ = 3mM is lower than the U_R of KIC. However, at 10mM the U_R of KPC2 is significantly higher than that of KIC. Although the lactate R_R does not show any dependence on $C_{0,G}$ for both cell types, KIC shows a higher lactate R_R at both $C_{0,G}$ in comparison to KPC2.(See Fig. 5.6). Finally, lactate release rates for both cell types show a steady increase with time despite the glucose uptake rates being fairly constant with time.

5.8 Estimation of Glycolytic Flux

A reasonable estimate of intracellular glycolytic flux can be provided by measuring glucose uptake and lactate release. Fig. 5.7 shows the saturation glucose uptake rates measured at t = 1 hr for both cell types and the corresponding lactate release rate as a percentage of the total glucose uptake. Only a small percentage of the glucose uptake is released as lactate for both KIC and KPC2 ($\sim$ 1-5%). KIC cells show a higher release of lactate relative to the glucose uptaken ($\sim$ 5%). Interestingly, KPC2 despite showing an increase in glucose uptake at $C_{0,G}$ = 10mM does not seem to utilize that glucose for glycolysis as observed by the relatively small ($\sim$ 1%) of lactate released.

5.9 Conclusions

In this chapter, we demonstrate the extension of the MEA technique to multi-analyte metabolite measurements, i.e. monitoring uptake of glucose and release of lactate in their local diffusion environments. Two 1D MEAs, one selective to glucose and the other to lactate, were customized for typical 2D culture setups and used to

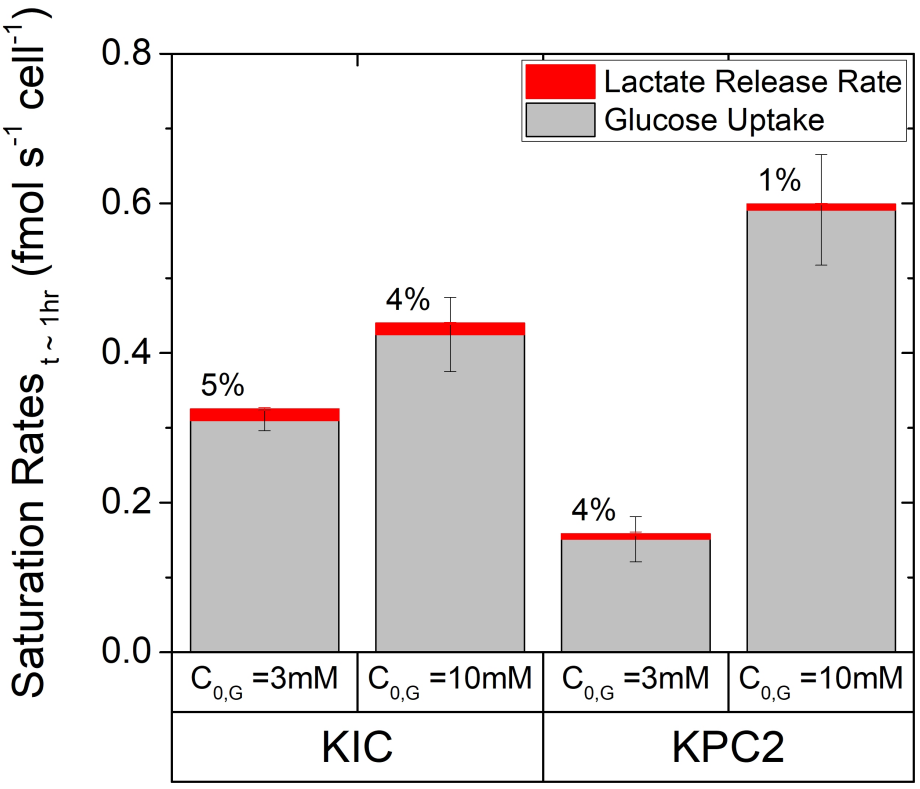

Fig. 5.7. Estimate of the glycolytic flux measured by the ratio of lactate release rate vs. glucose uptake rate. The saturation uptake and release rates shown were measured 1 hour after the exposure to $C_{0,G} = 3$ and 10mM. KIC cells utilize a higher percentage of glucose uptaken for glycolysis because of the relatively higher (5%) lactate release.

simultaneously measure glucose and lactate metabolism from genetically engineered mouse models of pancreatic cancer. The MEAs along with the in situ transient calibration technique developed earlier was tuned to measure simultaneous glucose and lactate gradients generated from the cell surface over a time span of 1hr, to enable determination of total glucose uptake rates and lactate release rates from and to the extracellular media respectively. The results show that KPC2 demonstrate a concentration dependent glucose uptake which increases with increasing glucose exposure. KIC does not exhibit a concentration dependent uptake rate, but shows a higher glucose uptake rate than KPC2 at 3mM of glucose exposure. However, at both the exposed glucose concentrations (3mM and 10mM) KIC demonstrate a higher lactate release rate than KPC2. While the estimated glycolytic flux for both cell types is small, KIC do show an increased glycolytic flux (5% of total glucose uptake) as compared to KPC2. The increased glycolysis may correspond to the the respective behavior of corresponding GEMMs wherein it was observed that KIC was more aggressive than KPC-2 in vitro [304].

6. SUMMARY OF CONTRIBUTIONS AND SUGGESTED FUTURE WORK

In the preceding chapters, we have successfully demonstrated the development of electrochemical microelectrode arrays (MEAs) as a tool for real time extracellular metabolite monitoring from 2D cell cultures. The MEA tool and associated measurement techniques enable the determination of cellular kinetics via the measurement of local or surface concentrations and fluxes. Previously demonstrated biofunctionalization schemes were tuned and adapted for MEAs of various sizes, spatial scales and geometries in order to measure multiple metabolites like glucose and lactate and metabolic by-products like hydrogen peroxide. The MEA was used in various physiological and non-physiological scenarios to map concentration profiles by accurately measuring the concentration transients and associated gradients. According to the results of this work, the following conclusions can be made:

1. A simple and cost effective process for fabrication of an on chip MEA was designed to address 2D culture setups. Various silicon based MEAs were fabricated with varying spatial scales (30 μm to 700 μm), inter-electrode spacing (15 μm to 600 μm) and electrode sizes (5 μm to 100 μm) to address the transient spatial scale of the relevant concentration gradient. Individually addressable amperometric electrodes with shared a reference and counter electrode were utilized to extract multi-point concentration transients with a high temporal resolution of 10 ms. The packaging of the MEA was optimized for a "positionable" approach to address standard 2D cell cultures in order to allow for off chip culture of the cells with appropriate physiological conditions important for proper growth and development. Moreover, positioning allowed us to not only

address different spatial scales of multifarious gradients but also develop a new calibration methodology.

2. For the determination of absolute concentrations with enough accuracy so as to determine gradients based on concentration differences between closely spaced electrodes, the sensitivity variability in amperometric MEAs was reduced via a novel in-situ transient calibration scheme. Using the customized MEAs and the in-situ transient calibration technique we demonstrated the measurement of transient gradients of H_2O_2 generated from an active surface that controllably induces transient gradients (analog) upon excitation. The reliability of the measurements was verified by comparing the experimental data with reaction diffusion simulations in comparable geometries. The results of this analysis indicate that the in situ transient calibration, developed here, minimizes the effects of sensitivity variability to such an extent that accurate determination of local absolute concentrations is possible. Measurements demonstrated include transient gradients caused by sub-second uptake events (using sampling time and measurement time of 10 ms, spatial range of 70 μm, and spatial resolution of 35 μm) and hourly uptake events (using sampling time and measurement time of 0.5 s, spatial range of 600 μm, and spatial resolution of 140 μm) through continuous H_2O_2 uptake by the analog. Additionally, extrapolation of surface concentration and gradient from the measured concentration profile enabled the determination of surface kinetic rates of the analog.

3. We demonstrate the use of the positionable MEA along with the in-situ calibration technique customized for typical 2D culture setups, to measure dynamic H_2O_2 concentration profiles from normal (human astrocytes) versus astrocyte derived cancer (GBM43) cells. The MEA provides multi-point concentration data with a sampling period of 0.5 s. At each time point, the concentration data is fit using an analytical expression for a 1D diffusion/reaction system, allowing extrapolation of the surface concentration and surface gradient. Real

time determination of cellular parameters i.e, uptake rate (U_R) and their dependence on the local or surface concentration (C_S) enabled the quantification of cellular uptake kinetics and provided mechanistic insights of H_2O_2 scavenging. Both cell types show surface concentration dependent H_2O_2 uptake rates, i.e., non-linear kinetics. The results show that GBM43 cells have increased H_2O_2 uptake rates as compared to astrocytes primarily due to an elevated linear scavenging mechanism, which has previously been attributed to catalase. The Michaelis-Menten components are comparable for the two cell types for H_2O_2 concentrations within the 0–100 μM range. Additionally, the continuous monitoring of U_R vs C_S is used to used to quantify transient and cumulative exposure effects. In the current experiment, the uptake rate primarily depends on the instantaneous H_2O_2 surface concentration for both astrocytes and GBM43, albeit a minor tail-off observed in the uptake rate of GBM43 cells after cumulative exposure to high concentrations of H_2O_2. The capabilities to quantify cumulative exposure effects and uptake rates over a wide range of cell surface concentrations are relevant for evaluation of potential therapeutic approaches based on catalase dominant uptake of H_2O_2 by cancerous GBM43.

4. A glucose selective positionable MEA was realized by applying existing enzymatic bio-functionalization schemes appended with pre/post surface treatment methods in order to achieve stable glucose signals for atleast 4 hours. We demonstrate the use of the glucose selective MEA to measure glucose metabolism from normal (human astrocytes) versus cancer (GBM43) cells. The MEA, with a higher spatial scale of 700μm and a spatial resolution of 280 μm, was used to measure multi-point glucose selective signals over a time span of 2hrs, to enable measurement of total glucose uptake from the extracellular media into the 2D cell culture. The results show a clear reprogramming of the glucose metabolic pathway of GBM43 in comparison to astrocytes. While both cell types show concentration dependent uptake rates, GBM43 has an increased glucose uptake rate as compared to astrocytes over the entire concentration spectrum (0-

15mM). The astrocytes glucose uptake over the entire concentration spectrum was well explained by a high affinity MM transporter mechanism, previously attributed to the expression of GLUT1, and an unsaturable passive diffusion component. In comparison, in the physiological range of glucose (< 6mM), GBM43 exhibit a higher affinity and capacity to glucose uptake, attributed primarily to elevated MM type GLUT3 transporter expressions. Moreover, above (> 6mM) traits of allosteric regulation were observed from a sigmoidal glucose U_R for GBM43. The monitoring of U_R vs C_S in the natural chemical micro-environment was used to identify the hysteretic nature of glucose uptake in GBM43, wherein the U_R was dependent on $C_S(t=0)$ i.e. C_0 rather than on instantaneous $C_S(t)$. Complementing existing tools like the Seahorse Flux analyzer which measure glycolytic rates (G_R) and respiration rates (R_R), the glucose MEA demonstrated in this study provides a measure of total uptake rate ($U_R=G_R+R_R+O_R$) which can provide a key insight into other cellular metabolic pathways (O_R) like bio-synthesis. GBM43s enhanced glucose metabolism over a wide range of glucose concentrations and its dependence on the in vitro culture conditions (availability of glucose) can potentially be of interest for therapeutic approaches based on targeting the differential nutrient uptake by cancer cells.

5. We demonstrate the extension of the MEA technique to simultaneous multi-analyte metabolite measurements, i.e. monitoring uptake of glucose and release of lactate in their local diffusion environments. Two 1D MEAs, one selective to glucose and the other to lactate, were customized for typical 2D culture setups and used to simultaneously measure glucose and lactate metabolism from genetically engineered mouse models of pancreatic cancer. The MEAs measured simultaneous glucose and lactate gradients generated from the cell surface over a time span of 1hr, to enable determination of total glucose uptake rates and lactate release rates from and to the extracellular media respectively. The results show that KPC2 cells with *KRAS and p53* mutations demonstrate a concentration dependent glucose uptake which increases with increasing glucose exposure.

KIC cells with *KRAS and p16* mutations does not exhibit a concentration dependent uptake rate, but shows a higher glucose uptake rate than KPC2 at 3mM of glucose exposure and a lower uptake rate than KPC2 at 10mM of glucose exposure. Additionally, at both the exposed glucose concentrations (3mM and 10mM) KIC demonstrate a higher lactate release rate than KPC2. While the estimated glycolytic flux for both cell types is small, KIC do show an increased glycolytic flux (5% of total glucose uptake) as compared to KPC2. The increased glycolysis corresponds to the the respective behavior of the GEMMs wherein it was observed that KIC was more aggressive than KPC-2 in vivo.

Future work could focus on scaling and packaging of the MEA platform to simultaneously address multiple culture wells and plates. Further investigation can also be conducted to explore many interesting aspects of the cellular kinetics measured using the MEA tool.

1. We are currently working on complementing the results of glucose metabolism from GBM43 cells by measuring glycolytic rates (G_R) and respiration rates (R_R) from Seahorse Flux Analyzer system. Since the glucose MEA demonstrated in this study provides a measure of total uptake rate (U_R=G_R+R_R+O_R), the fate of the upregulated glucose uptake in GBM43 can be quantified. Additionally, we propose further investigation into the positive allosteric regulation of glucose uptake at higher concentrations by studying the enzymatic expressions of the tightly regulated pathways of glucose breakdown in GBM43 (like hexokinase etc). Finally, the effects of high glucose culture media in which GBM43 is grown on the metabolic reprogramming observed in GBM43 cells have to be investigated.

2. We are currently working on supplementing the results observed with the genetically modified mouse models of pancreatic cancer cell lines with the study of glucose inhibitor CPI-613. CPI-613, is being investigated in clinical studies as a therapy designed to target mitochondrial enzymes (TCA cycle) that

are involved in cancer metabolism. Further investigation will be conducted to study the effect of the inhibitor dose on the glucose uptake and lactate release observed. Moreover, we propose the use of the metabolic results demonstrated as a guide for the design of a metabolite monitoring system in an on chip tumor micro-environment.

3. From the standpoint of the MEA device, a two pronged approach to improve the device performance is proposed. Firstly, characterization of cells in a complex media with other chemical stimulants and/or inhibitors is desirable. The current work focuses on the use first generation enzymatic biosensors for glucose and lactate detection. The current scheme provides good selectivity to the analyte of interest with fast response times in a limited media comprising of phosphate buffer and a few energy substrates like glucose lactate and glutamine. An enzyme deposition scheme with multiple layers and low electrode potentials maybe adopted for use in complex media, however a trade off between the electrode response time and selectivity would be required.

4. Secondly, to achieve a high throughput measurement system for metabolic profiling of multiple wells in a cell plate, the MEA must be packaged with multichannel potentiostats and a rudimentary motion system into an integrated system.

REFERENCES

REFERENCES

[1] Y. Zhao, E. B. Butler, and M. Tan, "Targeting cellular metabolism to improve cancer therapeutics," *Cell death & disease*, vol. 4, no. 3, p. e532, 2013.

[2] M. Pelletier, L. K. Billingham, M. Ramaswamy, and R. M. Siegel, "Extracellular flux analysis to monitor glycolytic rates and mitochondrial oxygen consumption," in *Methods in enzymology*. Elsevier, 2014, vol. 542, pp. 125–149.

[3] D. Bavli, S. Prill, E. Ezra, G. Levy, M. Cohen, M. Vinken, J. Vanfleteren, M. Jaeger, and Y. Nahmias, "Real-time monitoring of metabolic function in liver-on-chip microdevices tracks the dynamics of mitochondrial dysfunction," *Proceedings of the National Academy of Sciences*, vol. 113, no. 16, pp. E2231–E2240, 2016.

[4] S. A. Mookerjee and M. D. Brand, "Measurement and analysis of extracellular acid production to determine glycolytic rate," *JoVE (Journal of Visualized Experiments)*, no. 106, p. e53464, 2015.

[5] L. Hertz, Y. Chen, and H. S. Waagepetersen, "Effects of ketone bodies in alzheimer's disease in relation to neural hypometabolism, β-amyloid toxicity, and astrocyte function," *Journal of neurochemistry*, vol. 134, no. 1, pp. 7–20, 2015.

[6] M. G. Vander Heiden, L. C. Cantley, and C. B. Thompson, "Understanding the warburg effect: the metabolic requirements of cell proliferation," *science*, vol. 324, no. 5930, pp. 1029–1033, 2009.

[7] D. R. Wise and C. B. Thompson, "Glutamine addiction: a new therapeutic target in cancer," *Trends in biochemical sciences*, vol. 35, no. 8, pp. 427–433, 2010.

[8] F. P. Kuhajda, "Fatty acid synthase and cancer: new application of an old pathway," *Cancer research*, vol. 66, no. 12, pp. 5977–5980, 2006.

[9] Y. J. Lee, A. Cho, B. C. Cho, M. Yun, S. K. Kim, J. Chang, J. W. Moon, I. K. Park, H. J. Choi, and J.-H. Kim, "High tumor metabolic activity as measured by fluorodeoxyglucose positron emission tomography is associated with poor prognosis in limited and extensive stage small-cell lung cancer," *Clinical cancer research*, vol. 15, no. 7, pp. 2426–2432, 2009.

[10] U. E. Martinez-Outschoorn, M. Prisco, A. Ertel, A. Tsirigos, Z. Lin, S. Pavlides, C. Wang, N. Flomenberg, E. S. Knudsen, A. Howell *et al.*, "Ketones and lactate increase cancer cell stemness, driving recurrence, metastasis and poor clinical outcome in breast cancer: achieving personalized medicine via metabologenomics," *Cell cycle*, vol. 10, no. 8, pp. 1271–1286, 2011.

[11] R. J. DeBerardinis, N. Sayed, D. Ditsworth, and C. B. Thompson, "Brick by brick: metabolism and tumor cell growth," *Current opinion in genetics & development*, vol. 18, no. 1, pp. 54–61, 2008.

[12] M. G. Vander Heiden, "Targeting cancer metabolism: a therapeutic window opens," *Nature reviews Drug discovery*, vol. 10, no. 9, p. 671, 2011.

[13] T. Soga, "Cancer metabolism: key players in metabolic reprogramming," *Cancer science*, vol. 104, no. 3, pp. 275–281, 2013.

[14] C. C. Winterbourn, "Reconciling the chemistry and biology of reactive oxygen species," *Nature chemical biology*, vol. 4, no. 5, p. 278, 2008.

[15] A. C. von Eschenbach, "A vision for the national cancer program in the united states," *Nature Reviews Cancer*, vol. 4, no. 10, p. 820, 2004.

[16] H. J. Forman, "Use and abuse of exogenous h2o2 in studies of signal transduction," *Free Radical Biology and Medicine*, vol. 42, no. 7, pp. 926–932, 2007.

[17] B. C. Dickinson and C. J. Chang, "Chemistry and biology of reactive oxygen species in signaling or stress responses," *Nature chemical biology*, vol. 7, no. 8, p. 504, 2011.

[18] H. S. Marinho, C. Real, L. Cyrne, H. Soares, and F. Antunes, "Hydrogen peroxide sensing, signaling and regulation of transcription factors," *Redox Biology*, vol. 2, pp. 535 – 562, 2014. [Online]. Available: http://www.sciencedirect.com/science/article/pii/S2213231714000457

[19] F. Antunes and P. M. Brito, "Quantitative biology of hydrogen peroxide signaling," *Redox biology*, vol. 13, pp. 1–7, 2017.

[20] H. Link, D. Christodoulou, and U. Sauer, "Advancing metabolic models with kinetic information," *Current opinion in biotechnology*, vol. 29, pp. 8–14, 2014.

[21] R. Benfeitas, M. Uhlen, J. Nielsen, and A. Mardinoglu, "New challenges to study heterogeneity in cancer redox metabolism," *Frontiers in cell and developmental biology*, vol. 5, p. 65, 2017.

[22] B. Thorens and M. Mueckler, "Glucose transporters in the 21st century," *American Journal of Physiology-Endocrinology and Metabolism*, vol. 298, no. 2, pp. E141–E145, 2009.

[23] M. Mueckler and B. Thorens, "The slc2 (glut) family of membrane transporters," *Molecular aspects of medicine*, vol. 34, no. 2-3, pp. 121–138, 2013.

[24] A. P. Halestrap, "The monocarboxylate transporter familystructure and functional characterization," *IUBMB life*, vol. 64, no. 1, pp. 1–9, 2012.

[25] K. Takata, T. Matsuzaki, and Y. Tajika, "Aquaporins: water channel proteins of the cell membrane," *Progress in histochemistry and cytochemistry*, vol. 39, no. 1, pp. 1–83, 2004.

[26] G. P. Bienert, J. K. Schjoerring, and T. P. Jahn, "Membrane transport of hydrogen peroxide," *Biochimica et Biophysica Acta (BBA) - Biomembranes*, vol. 1758, no. 8, pp. 994–1003, aug 2006. [Online]. Available: http://www.sciencedirect.com/science/article/pii/S0005273606000472

[27] G. P. Bienert, A. L. Møller, K. A. Kristiansen, A. Schulz, I. M. Møller, J. K. Schjoerring, and T. P. Jahn, "Specific aquaporins facilitate the diffusion of hydrogen peroxide across membranes," *Journal of Biological Chemistry*, vol. 282, no. 2, pp. 1183–1192, 2007.

[28] L. Pellerin and P. J. Magistretti, "Glutamate uptake into astrocytes stimulates aerobic glycolysis: a mechanism coupling neuronal activity to glucose utilization," *Proceedings of the National Academy of Sciences*, vol. 91, no. 22, pp. 10 625–10 629, 1994.

[29] J. P. Meeks and S. Mennerick, "Feeding hungry neurons: Astrocytes deliver food for thought," *Neuron*, vol. 37, no. 2, pp. 187 – 189, 2003. [Online]. Available: http://www.sciencedirect.com/science/article/pii/S0896627303000278

[30] A. Suzuki, S. A. Stern, O. Bozdagi, G. W. Huntley, R. H. Walker, P. J. Magistretti, and C. M. Alberini, "Astrocyte-neuron lactate transport is required for long-term memory formation," *Cell*, vol. 144, no. 5, pp. 810–823, 2011.

[31] I. Allaman, M. Belanger, and P. J. Magistretti, "Astrocyte–neuron metabolic relationships: for better and for worse," *Trends in neurosciences*, vol. 34, no. 2, pp. 76–87, 2011.

[32] M. Bélanger, I. Allaman, and P. J. Magistretti, "Brain energy metabolism: focus on astrocyte-neuron metabolic cooperation," *Cell metabolism*, vol. 14, no. 6, pp. 724–738, 2011.

[33] L. A. Newman, D. L. Korol, and P. E. Gold, "Lactate produced by glycogenolysis in astrocytes regulates memory processing," *PloS one*, vol. 6, no. 12, p. e28427, 2011.

[34] P. Mchler, M. Wyss, M. Elsayed, J. Stobart, R. Gutierrez, A. vonFaber Castell, V. Kaelin, M. Zuend, A. SanMartn, I. Romero-Gmez, F. Baeza-Lehnert, S. Lengacher, B. Schneider, P. Aebischer, P. Magistretti, L. Barros, and B. Weber, "Invivo evidence for a lactate gradient from astrocytes to neurons," *Cell Metabolism*, vol. 23, no. 1, pp. 94 – 102, 2016. [Online]. Available: http://www.sciencedirect.com/science/article/pii/S1550413115005264

[35] M. Kapałczyńska, T. Kolenda, W. Przybyła, M. Zajaczkowska, A. Teresiak, V. Filas, M. Ibbs, R. Bliźniak, Ł. Łuczewski, and K. Lamperska, "2d and 3d cell cultures–a comparison of different types of cancer cell cultures," *Archives of medical science: AMS*, vol. 14, no. 4, p. 910, 2018.

[36] A. L. Paguirigan and D. J. Beebe, "Microfluidics meet cell biology: bridging the gap by validation and application of microscale techniques for cell biological assays," *BioEssays*, vol. 30, no. 9, pp. 811–821, 2008.

[37] H. Yu, I. Meyvantsson, I. A. Shkel, and D. J. Beebe, "Diffusion dependent cell behavior in microenvironments," *Lab on a Chip*, vol. 5, no. 10, pp. 1089–1095, 2005.

[38] F. Guo, J. B. French, P. Li, H. Zhao, C. Y. Chan, J. R. Fick, S. J. Benkovic, and T. J. Huang, "Probing cell–cell communication with microfluidic devices," *Lab on a Chip*, vol. 13, no. 16, pp. 3152–3162, 2013.

[39] B. P. Dranka, G. A. Benavides, A. R. Diers, S. Giordano, B. R. Zelickson, C. Reily, L. Zou, J. C. Chatham, B. G. Hill, J. Zhang *et al.*, "Assessing bioenergetic function in response to oxidative stress by metabolic profiling," *Free Radical Biology and Medicine*, vol. 51, no. 9, pp. 1621–1635, 2011.

[40] S. Desagher, J. Glowinski, and J. Premont, "Astrocytes protect neurons from hydrogen peroxide toxicity," *Journal of Neuroscience*, vol. 16, no. 8, pp. 2553–2562, 1996.

[41] X. Liu, M. M. Ramsey, X. Chen, D. Koley, M. Whiteley, and A. J. Bard, "Real-time mapping of a hydrogen peroxide concentration profile across a polymicrobial bacterial biofilm using scanning electrochemical microscopy," *PNAS*, vol. 108, no. 7, pp. 2668–2673, feb 2011. [Online]. Available: http://www.pnas.org/content/108/7/2668

[42] B. A. Wagner, J. R. Witmer, T. J. van't Erve, and G. R. Buettner, "An assay for the rate of removal of extracellular hydrogen peroxide by cells," *Redox Biology*, vol. 1, no. 1, pp. 210–217, 2013. [Online]. Available: http://www.sciencedirect.com/science/article/pii/S2213231713000323

[43] A. Bagulho, F. Vilas-Boas, A. Pena, C. Peneda, F. C. Santos, A. Jerónimo, R. F. M. de Almeida, and C. Real, "The extracellular matrix modulates {H}2O2 degradation and redox signaling in endothelial cells," *Redox Biology*, vol. 6, pp. 454–460, dec 2015. [Online]. Available: http://www.sciencedirect.com/science/article/pii/S2213231715001172

[44] H. S. Marinho, L. Cyrne, E. Cadenas, and F. Antunes, "H2o2 delivery to cells: steady-state versus bolus addition," *Methods Enzymol*, vol. 526, pp. 159–173, 2013.

[45] D. Ellison, A. Mugler, M. D. Brennan, S. H. Lee, R. J. Huebner, E. R. Shamir, L. A. Woo, J. Kim, P. Amar, I. Nemenman, A. J. Ewald, and A. Levchenko, "Cell-cell communication enhances the capacity of cell ensembles to sense shallow gradients during morphogenesis," *Proc Natl Acad Sci U S A*, vol. 113, no. 6, pp. E679–E688, feb 2016. [Online]. Available: http://www.ncbi.nlm.nih.gov/pmc/articles/PMC4760786/

[46] "Consequences of relative cellular positioning on quorum sensing and bacterial cell-to-cell communication," *FEMS Microbiology Letters*, vol. 292, no. 2, pp. 149–161, mar 2009. [Online]. Available: http://onlinelibrary.wiley.com/doi/10.1111/j.1574-6968.2008.01478.x/abstract

[47] B. J. Kim and M. Wu, "Microfluidics for mammalian cell chemotaxis," *Annals of Biomedical Engineering*, vol. 40, no. 6, pp. 1316–1327, 2012.

[48] T. M. Keenan and A. Folch, "Biomolecular gradients in cell culture systems," *Lab Chip*, vol. 8, no. 1, pp. 34–57, dec 2007. [Online]. Available: http://pubs.rsc.org/en/content/articlelanding/2008/lc/b711887b

[49] S. Kim, H. J. Kim, and N. L. Jeon, "Biological applications of microfluidic gradient devices," *Integrative Biology*, vol. 2, no. 11-12, pp. 584–603, 2010.

[50] G. E. Derfus, D. Abramzon, M. Tung, D. Chang, R. Kiss, and A. Amanullah, "Cell culture monitoring via an auto-sampler and an integrated multi-functional off-line analyzer," *Biotechnology progress*, vol. 26, no. 1, pp. 284–292, 2010.

[51] L. Dekker and K. M. Polizzi, "Sense and sensitivity in bioprocessingdetecting cellular metabolites with biosensors," *Current opinion in chemical biology*, vol. 40, pp. 31–36, 2017.

[52] G. J. van der Windt, C.-H. Chang, and E. L. Pearce, "Measuring bioenergetics in t cells using a seahorse extracellular flux analyzer," *Current protocols in immunology*, vol. 113, no. 1, pp. 3–16, 2016.

[53] T. TeSlaa and M. A. Teitell, "Techniques to monitor glycolysis," in *Methods in enzymology*. Elsevier, 2014, vol. 542, pp. 91–114.

[54] J. Traba, P. Miozzo, B. Akkaya, S. K. Pierce, and M. Akkaya, "An optimized protocol to analyze glycolysis and mitochondrial respiration in lymphocytes," *JoVE (Journal of Visualized Experiments)*, no. 117, p. e54918, 2016.

[55] L. S. P. Winer and M. Wu, "Rapid analysis of glycolytic and oxidative substrate flux of cancer cells in a microplate," *PloS one*, vol. 9, no. 10, p. e109916, 2014.

[56] M. B. de Moura and B. Van Houten, "Bioenergetic analysis of intact mammalian cells using the seahorse xf24 extracellular flux analyzer and a luciferase atp assay," in *Molecular Toxicology Protocols*. Springer, 2014, pp. 589–602.

[57] A. C. Michael and L. Borland, *Electrochemical methods for neuroscience*. CRC Press, 2006.

[58] E. McLamore, J. Shi, D. Jaroch, J. Claussen, A. Uchida, Y. Jiang, W. Zhang, S. Donkin, M. Banks, K. Buhman, D. Teegarden, J. Rickus, and D. Porterfield, "A self referencing platinum nanoparticle decorated enzyme-based microbiosensor for real time measurement of physiological glucose transport," *Biosensors and Bioelectronics*, vol. 26, no. 5, pp. 2237 – 2245, 2011. [Online]. Available: http://www.sciencedirect.com/science/article/pii/S095656631000655X

[59] L. M. Kauri, S.-K. Jung, and R. T. Kennedy, "Direct measurement of glucose gradients and mass transport within islets of langerhans," *Biochemical and biophysical research communications*, vol. 304, no. 2, pp. 371–377, 2003.

[60] J. Galceran, J. Monné, J. Puy, and H. P. van Leeuwen, "The impact of the transient uptake flux on bioaccumulation: Linear adsorption and first-order internalisation coupled with spherical semi-infinite mass transport," *Marine chemistry*, vol. 85, no. 1, pp. 89–102, 2004.

[61] E. S. McLamore, S. Mohanty, J. Shi, J. Claussen, S. S. Jedlicka, J. L. Rickus, and D. M. Porterfield, "A self-referencing glutamate biosensor for measuring real time neuronal glutamate flux," *Journal of Neuroscience Methods*, vol. 189, no. 1, pp. 14–22, may 2010. [Online]. Available: http://www.sciencedirect.com/science/article/pii/S0165027010001196

[62] D. M. Porterfield, "Measuring metabolism and biophysical flux in the tissue, cellular and sub-cellular domains: {Recent} developments in self-referencing amperometry for physiological sensing," *Biosensors and Bioelectronics*, vol. 22, no. 7, pp. 1186–1196, feb 2007. [Online]. Available: http://www.sciencedirect.com/science/article/pii/S0956566306002740

[63] Q. Wu, M. E. Reith, R. M. Wightman, K. T. Kawagoe, and P. A. Garris, "Determination of release and uptake parameters from electrically evoked dopamine dynamics measured by real-time voltammetry," *Journal of neuroscience methods*, vol. 112, no. 2, pp. 119–133, 2001.

[64] C. F. Ng, F. Q. Schafer, G. R. Buettner, and V. Rodgers, "The rate of cellular hydrogen peroxide removal shows dependency on gsh: mathematical insight into in vivo h2o2 and gpx concentrations," *Free radical research*, vol. 41, no. 11, pp. 1201–1211, 2007.

[65] S. H. Walters, I. M. Taylor, Z. Shu, and A. C. Michael, "A novel restricted diffusion model of evoked dopamine," *ACS chemical neuroscience*, vol. 5, no. 9, pp. 776–783, 2014.

[66] A. I. Oleinick, C. Amatore, M. Guille, S. Arbault, O. V. Klymenko, and I. Svir, "Modelling release of nitric oxide in a slice of rat's brain: describing stimulated functional hyperemia with diffusion-reaction equations," *Mathematical Medicine and Biology*, vol. 23, no. 1, pp. 27–44, 2006.

[67] L. F. Jaffe and R. Nuccitelli, "An {Ultrasensitive} {Vibrating} {Probe} for {Measuring} {Steady} {Extracellular} {Currents}," *J Cell Biol*, vol. 63, no. 2, pp. 614–628, nov 1974. [Online]. Available: http://jcb.rupress.org/content/63/2/614

[68] W. M. Kühtreiber and L. F. Jaffe, "Detection of extracellular calcium gradients with a calcium-specific vibrating electrode." *The Journal of cell biology*, vol. 110, no. 5, pp. 1565–1573, 1990.

[69] S.-K. Jung, J. R. Trimarchi, R. H. Sanger, and P. J. Smith, "Development and application of a self-referencing glucose microsensor for the measurement of glucose consumption by pancreatic β-cells," *Analytical chemistry*, vol. 73, no. 15, pp. 3759–3767, 2001.

[70] J. Shi, E. S. McLamore, D. Jaroch, J. C. Claussen, R. G. Mirmira, J. L. Rickus, and D. M. Porterfield, "Oscillatory glucose flux in ins 1 pancreatic β cells: A self-referencing microbiosensor study," *Analytical biochemistry*, vol. 411, no. 2, pp. 185–193, 2011.

[71] N. Baltes, L. Thouin, C. Amatore, and J. Heinze, "Imaging {Concentration} {Profiles} of {Redox}-{Active} {Species} with {Nanometric} {Amperometric} {Probes}: {Effect} of {Natural} {Convection} on {Transport} at {Microdisk} {Electrodes}," *Angewandte Chemie International Edition*, vol. 43, no. 11, pp. 1431–1435, mar 2004. [Online]. Available: http://onlinelibrary.wiley.com/doi/10.1002/anie.200352662/abstract

[72] R. Chen, K. Hu, Y. Yu, M. V. Mirkin, and S. Amemiya, "Focused-ion-beam-milled carbon nanoelectrodes for scanning electrochemical microscopy," *Journal of The Electrochemical Society*, vol. 163, no. 4, pp. H3032–H3037, 2016.

[73] T. Sun, Y. Yu, B. J. Zacher, and M. V. Mirkin, "Scanning electrochemical microscopy of individual catalytic nanoparticles," *Angewandte Chemie International Edition*, vol. 53, no. 51, pp. 14 120–14 123, 2014.

[74] S. Amemiya, A. J. Bard, F.-R. F. Fan, M. V. Mirkin, and P. R. Unwin, "Scanning electrochemical microscopy," *Annu. Rev. Anal. Chem.*, vol. 1, pp. 95–131, 2008.

[75] P. Sun, F. O. Laforge, and M. V. Mirkin, "Scanning electrochemical microscopy in the 21st century," *Physical Chemistry Chemical Physics*, vol. 9, no. 7, pp. 802–823, 2007.

[76] S. M. Oja, Y. Fan, C. M. Armstrong, P. Defnet, and B. Zhang, "Nanoscale electrochemistry revisited," *Analytical Chemistry*, vol. 88, no. 1, pp. 414–430, 2016, pMID: 26630546. [Online]. Available: http://dx.doi.org/10.1021/acs.analchem.5b04542

[77] C. Amatore, A. Chovin, P. Garrigue, L. Servant, N. Sojic, S. Szunerits, and L. Thouin, "Remote {Fluorescence} {Imaging} of {Dynamic} {Concentration} {Profiles} with {Micrometer} {Resolution} {Using} a {Coherent} {Optical} {Fiber} {Bundle}," *Analytical Chemistry*, vol. 76, no. 24, pp. 7202–7210, dec 2004. [Online]. Available: http://pubs.acs.org/doi/abs/10.1021/ac049017g

[78] S. G. Rhee, T.-S. Chang, W. Jeong, and D. Kang, "Methods for detection and measurement of hydrogen peroxide inside and outside of cells," *Molecules and cells*, vol. 29, no. 6, pp. 539–549, 2010.

[79] C. Amatore, S. Szunerits, L. Thouin, and J.-S. Warkocz, "The real meaning of {Nernst}'s steady diffusion layer concept under non-forced hydrodynamic conditions. {A} simple model based on {Levich}'s seminal view of convection," *Journal of Electroanalytical Chemistry*, vol. 500, no. 12, pp. 62–70, mar 2001. [Online]. Available: http://www.sciencedirect.com/science/article/pii/S0022072800003788

[80] ——, "Mapping concentration profiles within the diffusion layer of an electrode: part iii. steady-state and time-dependent profiles via amperometric measurements with an ultramicroelectrode probe," *Electrochemistry communications*, vol. 2, no. 5, pp. 353–358, 2000.

[81] R. C. Engstrom, M. Weber, D. J. Wunder, R. Burgess, and S. Winquist, "Measurements within the diffusion layer using a microelectrode probe," *Anal. Chem.*, vol. 58, no. 4, pp. 844–848, apr 1986. [Online]. Available: http://pubs.acs.org/doi/abs/10.1021/ac00295a044

[82] P. Niethammer, C. Grabher, A. T. Look, and T. J. Mitchison, "A tissue-scale gradient of hydrogen peroxide mediates rapid wound detection in zebrafish," *Nature*, vol. 459, no. 7249, pp. 996–999, jun 2009. [Online]. Available: http://www.nature.com/nature/journal/v459/n7249/full/nature08119.html

[83] K. Y. Inoue, M. Matsudaira, R. Kubo, M. Nakano, S. Yoshida, S. Matsuzaki, A. Suda, R. Kunikata, T. Kimura, R. Tsurumi *et al.*, "Lsi-based amperometric sensor for bio-imaging and multi-point biosensing," *Lab on a Chip*, vol. 12, no. 18, pp. 3481–3490, 2012.

[84] J. B. Wydallis, R. M. Feeny, W. Wilson, T. Kern, T. Chen, S. Tobet, M. M. Reynolds, and C. S. Henry, "Spatiotemporal norepinephrine mapping using a high-density {CMOS} microelectrode array," *Lab Chip*, vol. 15, no. 20, pp. 4075–4082, sep 2015. [Online]. Available: http://pubs.rsc.org/en/content/articlelanding/2015/lc/c5lc00778j

[85] B. N. Kim, A. D. Herbst, S. J. Kim, B. A. Minch, and M. Lindau, "Parallel recording of neurotransmitters release from chromaffin cells using a 1010 {CMOS} {IC} potentiostat array with on-chip working electrodes," *Biosensors and Bioelectronics*, vol. 41, pp. 736–744, mar 2013. [Online]. Available: http://www.sciencedirect.com/science/article/pii/S0956566312006641

[86] J. Rothe, O. Frey, A. Stettler, Y. Chen, and A. Hierlemann, "Fully integrated cmos microsystem for electrochemical measurements on 32× 32 working electrodes at 90 frames per second," *Analytical chemistry*, vol. 86, no. 13, pp. 6425–6432, 2014.

[87] H. Meyer, H. Drewer, B. Gruendig, K. Cammann, R. Kakerow, Y. Manoli, W. Mokwa, and M. Rospert, "Two-dimensional imaging of o2, h2o2, and glucose distributions by an array of 400 individually addressable microelectrodes," *Analytical Chemistry*, vol. 67, no. 7, pp. 1164–1170, 1995.

[88] J. Wang, R. Trouillon, J. Dunevall, and A. G. Ewing, "Spatial resolution of single-cell exocytosis by microwell-based individually addressable thin film ultramicroelectrode arrays," *Analytical chemistry*, vol. 86, no. 9, pp. 4515–4520, 2014.

[89] J. Wigström, J. Dunevall, N. Najafinobar, J. Lovrić, J. Wang, A. G. Ewing, and A.-S. Cans, "Lithographic microfabrication of a 16-electrode array on a probe tip for high spatial resolution electrochemical localization of exocytosis," *Analytical chemistry*, vol. 88, no. 4, pp. 2080–2087, 2016.

[90] J. Yan, V. A. Pedrosa, J. Enomoto, A. L. Simonian, and A. Revzin, "Electrochemical biosensors for on-chip detection of oxidative stress from immune cells," *Biomicrofluidics*, vol. 5, no. 3, p. 032008, 2011.

[91] M. Şen, K. Ino, K. Y. Inoue, T. Arai, T. Nishijo, A. Suda, R. Kunikata, H. Shiku, and T. Matsue, "Lsi-based amperometric sensor for real-time monitoring of embryoid bodies," *Biosensors and Bioelectronics*, vol. 48, pp. 12–18, 2013.

[92] J. Wang, R. Trouillon, Y. Lin, M. I. Svensson, and A. G. Ewing, "Individually addressable thin-film ultramicroelectrode array for spatial measurements of single vesicle release," *Analytical chemistry*, vol. 85, no. 11, pp. 5600–5608, 2013.

[93] H. Abe, K. Ino, C.-Z. Li, Y. Kanno, K. Y. Inoue, A. Suda, R. Kunikata, M. Matsudaira, Y. Takahashi, H. Shiku *et al.*, "Electrochemical imaging of dopamine release from three-dimensional-cultured pc12 cells using large-scale integration-based amperometric sensors," *Analytical chemistry*, vol. 87, no. 12, pp. 6364–6370, 2015.

[94] C. Amatore, J. Delacotte, M. Guille-Collignon, and F. Lemaître, "Vesicular exocytosis and microdevices–microelectrode arrays," *Analyst*, vol. 140, no. 11, pp. 3687–3695, 2015.

[95] F. Picollo, A. Battiato, E. Bernardi, A. Marcantoni, A. Pasquarelli, E. Carbone, P. Olivero, and V. Carabelli, "Microelectrode arrays of diamond-insulated graphitic channels for real-time detection of exocytotic events from cultured chromaffin cells and slices of adrenal glands," *Analytical chemistry*, vol. 88, no. 15, pp. 7493–7499, 2016.

[96] J. Rothe, M. Lewandowska, F. Heer, O. Frey, and A. Hierlemann, "Multi-target electrochemical biosensing enabled by integrated cmos electronics," *Journal of Micromechanics and Microengineering*, vol. 21, no. 5, p. 054010, 2011.

[97] Y. Zhang and G. S. Wilson, "Electrochemical oxidation of h2o2 on pt and pt+ ir electrodes in physiological buffer and its applicability to h2o2-based biosensors," *Journal of Electroanalytical Chemistry*, vol. 345, no. 1-2, pp. 253–271, 1993.

[98] S. A. Evans, J. M. Elliott, L. M. Andrews, P. N. Bartlett, P. J. Doyle, and G. Denuault, "Detection of hydrogen peroxide at mesoporous platinum microelectrodes," *Analytical Chemistry*, vol. 74, no. 6, pp. 1322–1326, 2002.

[99] S. R. Belding, E. I. Rogers, and R. G. Compton, "Potential step chronoamperometry at microdisc electrodes: effect of finite electrode kinetics," *The Journal of Physical Chemistry C*, vol. 113, no. 10, pp. 4202–4207, 2009.

[100] N. G. Poulos, J. R. Hall, and M. C. Leopold, "Functional layer-by-layer design of xerogel-based first-generation amperometric glucose biosensors," *Langmuir*, vol. 31, no. 4, pp. 1547–1555, 2015.

[101] C. F. Lourenço, A. Ledo, J. Laranjinha, G. A. Gerhardt, and R. M. Barbosa, "Microelectrode array biosensor for high-resolution measurements of extracellular glucose in the brain," *Sensors and Actuators B: Chemical*, vol. 237, pp. 298–307, 2016.

[102] Gamry, "Electrode experiments: Gamry potentiostat 4-probe instrument," https://www.gamry.com/application-notes/electrodes-cells/two-three-and-four-electrode-experiments/, (Accessed on 09/28/2017).

[103] R. Madangopal, M. Stensberg, M. Porterfield, J. Rickus, and N. Pulliam, "Directed enzyme deposition via electroactive polymer-based nanomaterials for multi-analyte amperometric biosensors," in *2012 IEEE Sensors*, Oct 2012, pp. 1–4.

[104] D. M. H. Kern, "The {Polarography} and {Standard} {Potential} of the {Oxygen}-{Hydrogen} {Peroxide} {Couple}," *J. Am. Chem. Soc.*, vol. 76, no. 16, pp. 4208–4214, aug 1954. [Online]. Available: http://dx.doi.org/10.1021/ja01645a059

[105] J. Hasegawa, S. Uno, and K. Nakazato, "Amperometric electrochemical sensor array for on-chip simultaneous imaging: Circuit and microelectrode design considerations," *Japanese Journal of Applied Physics*, vol. 50, no. 4S, p. 04DL03, 2011. [Online]. Available: http://stacks.iop.org/1347-4065/50/i=4S/a=04DL03

[106] T. Kuno, K. Niitsu, and K. Nakazato, "Amperometric electrochemical sensor array for on-chip simultaneous imaging," *Japanese Journal of Applied Physics*, vol. 53, no. 4S, p. 04EL01, 2014. [Online]. Available: http://stacks.iop.org/1347-4065/53/i=4S/a=04EL01

[107] A. J. Bard, F. R. F. Fan, J. Kwak, and O. Lev, "Scanning electrochemical microscopy. {Introduction} and principles," *Anal. Chem.*, vol. 61, no. 2, pp. 132–138, jan 1989. [Online]. Available: http://pubs.acs.org/doi/abs/10.1021/ac00177a011

[108] P. R. Nair and M. A. Alam, "A compact analytical formalism for current transients in electrochemical systems," *Analyst*, vol. 138, pp. 525–538, 2013. [Online]. Available: http://dx.doi.org/10.1039/C2AN35346F

[109] C. Amatore, S. Arbault, D. Bruce, P. de Oliveira, M. Erard, and M. Vuillaume, "Analysis of individual biochemical events based on artificial synapses using ultramicroelectrodes: cellular oxidative burst," *Faraday Discuss.*, vol. 116, no. 0, pp. 319–333, jan 2000. [Online]. Available: http://pubs.rsc.org/en/content/articlelanding/2000/fd/b001448f

[110] C. Amatore, S. Arbault, D. Bruce, P. De Oliveira, M. Erard, N. Sojic, and M. Vuillaume, "Nitrogen monoxide and oxidative stress: composition and intensity of cellular oxidative bursts cocktail. a study through artificial electrochemical synapses on single human fibroblasts," *Analusis*, vol. 28, no. 6, pp. 506–517, 2000.

[111] C. Amatore, S. Arbault, C. Bouton, K. Coffi, J.-C. Drapier, H. Ghandour, and Y. Tong, "Monitoring in real time with a microelectrode the release of reactive oxygen and nitrogen species by a single macrophage stimulated by its membrane mechanical depolarization," *ChemBioChem*, vol. 7, no. 4, pp. 653–661, 2006.

[112] V. Folmer, N. Pedroso, A. C. Matias, S. C. Lopes, F. Antunes, L. Cyrne, and H. S. Marinho, "H 2 o 2 induces rapid biophysical and permeability changes in the plasma membrane of saccharomyces cerevisiae," *Biochimica et Biophysica Acta (BBA)-Biomembranes*, vol. 1778, no. 4, pp. 1141–1147, 2008.

[113] D. Erudaitius, A. Huang, S. Kazmi, G. R. Buettner, and V. G. Rodgers, "Peroxiporin expression is an important factor for cancer cell susceptibility to therapeutic h2o2: Implications for pharmacological ascorbate therapy," *PloS one*, vol. 12, no. 1, p. e0170442, 2017.

[114] D. Suazo-Dávila, J. Rivera-Meléndez, J. Koehne, M. Meyyappan, and C. R. Cabrera, "Surface analysis and electrochemistry of a robust carbon-nanofiber-based electrode platform h2o2 sensor," *Applied Surface Science*, vol. 384, no. Supplement C, pp. 251 – 257, 2016. [Online]. Available: http://www.sciencedirect.com/science/article/pii/S0169433216310339

[115] B. I. Rosario-Castro, E. J. Contés-de Jesús, M. Lebrón-Colón, M. A. Meador, M. A. Scibioh, and C. R. Cabrera, "Single-wall carbon nanotube chemical attachment at platinum electrodes," *Applied Surface Science*, vol. 257, no. 2, pp. 340–353, 2010.

[116] B. K. Day, F. Pomerleau, J. J. Burmeister, P. Huettl, and G. A. Gerhardt, "Microelectrode array studies of basal and potassium-evoked release of l-glutamate in the anesthetized rat brain," *Journal of Neurochemistry*, vol. 96, no. 6, pp. 1626–1635, 2006.

[117] L. Fenno, O. Yizhar, and K. Deisseroth, "The development and application of optogenetics," *Annual review of neuroscience*, vol. 34, pp. 389–412, 2011.

[118] S. Hoffman, B. Rzigalinski, K. Willoughby, and E. Ellis, "Astrocytes generate isoprostanes in response to trauma or oxygen radicals," *Journal of neurotrauma*, vol. 17, no. 5, pp. 415–420, 2000.

[119] X. Liu and J. L. Zweier, "A real-time electrochemical technique for measurement of cellular hydrogen peroxide generation and consumption: evaluation in human polymorphonuclear leukocytes," *Free Radical Biology and Medicine*, vol. 31, no. 7, pp. 894–901, 2001.

[120] A. L. Hogerton and M. T. Bowser, "Monitoring neurochemical release from astrocytes using in vitro microdialysis coupled with high-speed capillary electrophoresis," *Analytical chemistry*, vol. 85, no. 19, pp. 9070–9077, 2013.

[121] M. Spanos, J. Gras-Najjar, J. M. Letchworth, A. L. Sanford, J. V. Toups, and L. A. Sombers, "Quantitation of hydrogen peroxide fluctuations and their modulation of dopamine dynamics in the rat dorsal striatum using fast-scan cyclic voltammetry," *ACS chemical neuroscience*, vol. 4, no. 5, pp. 782–789, 2013.

[122] H. Sies, "Hydrogen peroxide as a central redox signaling molecule in physiological oxidative stress: Oxidative eustress," *Redox Biology*, vol. 11, pp. 613 – 619, 2017.

[123] P. Nair and M. Alam, "Performance limits of nanobiosensors," *Applied physics letters*, vol. 88, no. 23, p. 233120, 2006.

[124] A. J. Bard, L. R. Faulkner *et al.*, *Fundamentals and applications*. Wiley New York, 2001, vol. 2.

[125] L. Rajendran, "Modelling of reaction–diffusion processes: the theory of catalytic electrode processes at hemispheroidal ultramicroelectrodes," *Electrochemistry communications*, vol. 2, no. 10, pp. 679–684, 2000.

[126] S. Loghambal and L. Rajendran, "Mathematical modeling of diffusion and kinetics in amperometric immobilized enzyme electrodes," *Electrochimica Acta*, vol. 55, no. 18, pp. 5230–5238, 2010.

[127] B. Chance, H. Sies, and A. Boveris, "Hydroperoxide metabolism in mammalian organs." *Physiological reviews*, vol. 59, no. 3, pp. 527–605, 1979.

[128] J. R. Stone and S. Yang, "Hydrogen peroxide: a signaling messenger," *Antioxidants & redox signaling*, vol. 8, no. 3-4, pp. 243–270, 2006.

[129] M. Gülden, A. Jess, J. Kammann, E. Maser, and H. Seibert, "Cytotoxic potency of h2o2 in cell cultures: impact of cell concentration and exposure time," *Free Radical Biology and Medicine*, vol. 49, no. 8, pp. 1298–1305, 2010.

[130] C. Röhl, E. Armbrust, E. Herbst, A. Jess, M. Gülden, E. Maser, G. Rimbach, and C. Bösch-Saadatmandi, "Mechanisms involved in the modulation of astroglial resistance to oxidative stress induced by activated microglia: antioxidative systems, peroxide elimination, radical generation, lipid peroxidation," *Neurotoxicity research*, vol. 17, no. 4, pp. 317–331, 2010.

[131] K. J. Barnham, C. L. Masters, and A. I. Bush, "Neurodegenerative diseases and oxidative stress," *Nature reviews Drug discovery*, vol. 3, no. 3, p. 205, 2004.

[132] L. C. Seaver and J. A. Imlay, "Hydrogen {Peroxide} {Fluxes} and {Compartmentalization} inside {Growing} {Escherichia} coli," *J. Bacteriol.*, vol. 183, no. 24, pp. 7182–7189, dec 2001. [Online]. Available: http://jb.asm.org/content/183/24/7182

[133] L. E. Tomalin, A. M. Day, Z. E. Underwood, G. R. Smith, P. Dalle Pezze, C. Rallis, W. Patel, B. C. Dickinson, J. Bähler, T. F. Brewer *et al.*, "Increasing extracellular h2o2 produces a bi-phasic response in intracellular h2o2, with peroxiredoxin hyperoxidation only triggered once the cellular h2o2-buffering capacity is overwhelmed," *Free Radical Biology and Medicine*, vol. 95, pp. 333–348, 2016.

[134] S. Desagher, J. Glowinski, and J. Prémont, "Pyruvate protects neurons against hydrogen peroxide-induced toxicity," *Journal of Neuroscience*, vol. 17, no. 23, pp. 9060–9067, 1997.

[135] F. Antunes and E. Cadenas, "Estimation of {H}2O2 gradients across biomembranes," *FEBS Letters*, vol. 475, no. 2, pp. 121–126, jun 2000. [Online]. Available: http://www.sciencedirect.com/science/article/pii/S0014579300016380

[136] R. Dringen, P. G. Pawlowski, and J. Hirrlinger, "Peroxide detoxification by brain cells," *Journal of neuroscience research*, vol. 79, no. 1-2, pp. 157–165, 2005.

[137] B. K. Huang and H. D. Sikes, "Quantifying intracellular hydrogen peroxide perturbations in terms of concentration," *Redox biology*, vol. 2, pp. 955–962, 2014.

[138] C. M. Doskey, V. Buranasudja, B. A. Wagner, J. G. Wilkes, J. Du, J. J. Cullen, and G. R. Buettner, "Tumor cells have decreased ability to metabolize h2o2: Implications for pharmacological ascorbate in cancer therapy," *Redox biology*, vol. 10, pp. 274–284, 2016.

[139] N. Makino, Y. Mochizuki, S. Bannai, and Y. Sugita, "Kinetic studies on the removal of extracellular hydrogen peroxide by cultured fibroblasts." *Journal of Biological Chemistry*, vol. 269, no. 2, pp. 1020–1025, 1994.

[140] K. Sasaki, S. Bannai, and N. Makino, "Kinetics of hydrogen peroxide elimination by human umbilical vein endothelial cells in culture," *Biochimica et Biophysica Acta (BBA)-General Subjects*, vol. 1380, no. 2, pp. 275–288, 1998.

[141] K. Hashida, Y. Sakakura, and N. Makino, "Kinetic studies on the hydrogen peroxide elimination by cultured pc12 cells: rate limitation by glucose-6-phosphate dehydrogenase," *Biochimica et Biophysica Acta (BBA)-General Subjects*, vol. 1572, no. 1, pp. 85–90, 2002.

[142] N. Makino, K. Sasaki, K. Hashida, and Y. Sakakura, "A metabolic model describing the h2o2 elimination by mammalian cells including h2o2 permeation through cytoplasmic and peroxisomal membranes: comparison with experimental data," *Biochimica et Biophysica Acta (BBA)-General Subjects*, vol. 1673, no. 3, pp. 149–159, 2004.

[143] N. Makino, T. Mise, and J.-i. Sagara, "Kinetics of hydrogen peroxide elimination by astrocytes and c6 glioma cells: analysis based on a mathematical model," *Biochimica et Biophysica Acta (BBA)-General Subjects*, vol. 1780, no. 6, pp. 927–936, 2008.

[144] L. Sokoloff, M. Reivich, C. Kennedy, M. Des Rosiers, C. S. Patlak, K. e. a. Pettigrew, O. Sakurada, and M. Shinohara, "The [14c] deoxyglucose method for the measurement of local cerebral glucose utilization: theory, procedure, and normal values in the conscious and anesthetized albino rat," *Journal of neurochemistry*, vol. 28, no. 5, pp. 897–916, 1977.

[145] Y. Chen, N. E. Vartiainen, W. Ying, P. H. Chan, J. Koistinaho, and R. A. Swanson, "Astrocytes protect neurons from nitric oxide toxicity by a glutathione-dependent mechanism," *Journal of neurochemistry*, vol. 77, no. 6, pp. 1601–1610, 2001.

[146] A. Y. Shih, D. A. Johnson, G. Wong, A. D. Kraft, L. Jiang, H. Erb, J. A. Johnson, and T. H. Murphy, "Coordinate regulation of glutathione biosynthesis and release by nrf2-expressing glia potently protects neurons from oxidative stress," *Journal of Neuroscience*, vol. 23, no. 8, pp. 3394–3406, 2003.

[147] Y. Jiang and L. Uhrbom, "On the origin of glioma," *Upsala journal of medical sciences*, vol. 117, no. 2, pp. 113–121, 2012.

[148] M. C. Papadopoulos and A. S. Verkman, "Aquaporin water channels in the nervous system," *Nature Reviews Neuroscience*, vol. 14, no. 4, p. 265, 2013.

[149] A. Salazar-Ramiro, D. Ramírez-Ortega, V. Pérez de la Cruz, N. Y. Hérnandez-Pedro, D. F. González-Esquivel, J. Sotelo, and B. Pineda, "Role of redox status in development of glioblastoma," *Frontiers in immunology*, vol. 7, p. 156, 2016.

[150] M. Rinaldi, M. Caffo, L. Minutoli, H. Marini, R. V. Abbritti, F. Squadrito, V. Trichilo, A. Valenti, V. Barresi, D. Altavilla, M. Passalacqua, and G. Caruso, "Ros and brain gliomas: An overview of potential and innovative therapeutic strategies," *International Journal of Molecular Sciences*, vol. 17, no. 6, p. 984, 2016. [Online]. Available: http://www.mdpi.com/1422-0067/17/6/984

[151] D. Trachootham, J. Alexandre, and P. Huang, "Targeting cancer cells by ros-mediated mechanisms: a radical therapeutic approach?" *Nature Reviews Drug Discovery*, vol. 8, pp. 579–591, 2009.

[152] C. M. Cabello, G. Wondrak *et al.*, "Experimental therapeutics: targeting the redox achilles heel of cancer." *Current opinion in investigational drugs (London, England: 2000)*, vol. 8, no. 12, pp. 1022–1037, 2007.

[153] S. Rodic and M. D. Vincent, "Reactive oxygen species (ros) are a key determinant of cancer's metabolic phenotype," *International Journal of Cancer*, vol. 142, no. 3, pp. 440–448, 2018. [Online]. Available: https://onlinelibrary.wiley.com/doi/abs/10.1002/ijc.31069

[154] H. Guo, H. Aleyasin, B. C. Dickinson, R. E. Haskew-Layton, and R. R. Ratan, "Recent advances in hydrogen peroxide imaging for biological applications," *Cell & Bioscience*, vol. 4, no. 1, p. 64, Oct 2014. [Online]. Available: https://doi.org/10.1186/2045-3701-4-64

[155] M. B. Grisham, "Methods to detect hydrogen peroxide in living cells: Possibilities and pitfalls," *Comparative Biochemistry and Physiology Part A: Molecular & Integrative Physiology*, vol. 165, no. 4, pp. 429 – 438, 2013, first International Conference on Oxidative Stress in Aquatic Ecosystems. [Online]. Available: http://www.sciencedirect.com/science/article/pii/S1095643313000330

[156] P. Lefrancois, V. S. R. Vajrala, I. B. Arredondo, B. Goudeau, T. Doneux, L. Bouffier, and S. Arbault, "Direct oxidative pathway from amplex red to resorufin revealed by in situ confocal imaging," *Phys. Chem. Chem. Phys.*, vol. 18, pp. 25 817–25 822, 2016. [Online]. Available: http://dx.doi.org/10.1039/C6CP04438G

[157] S.-Y. Liu, Y.-P. Chen, F. Fang, J. Xu, G.-P. Sheng, H.-Q. Yu, G. Liu, and Y.-C. Tian, "Measurement of dissolved oxygen and its diffusivity in aerobic granules using a lithographically-fabricated microelectrode array," *Environmental Science & Technology*, vol. 43, no. 4, pp. 1160–1165, 2009. [Online]. Available: https://doi.org/10.1021/es802662e

[158] W. Tedjo, J. Nejad, R. Feeny, L. Yang, C. Henry, T. Stuart, and T. Chen, "Electrochemical biosensor system using a cmos microelectrode array provides high spatially and temporally resolved images," *Biosensors and Bioelectronics*, vol. 114, pp. 78–88, 2018.

[159] S. V. Sridharan, J. F. Rivera, J. K. Nolan, M. A. Alam, J. L. Rickus, and D. B. Janes, "On-chip microelectrode array and in situ transient calibration for measurement of transient concentration gradients near surfaces of 2d cell cultures," *Sensors and Actuators B: Chemical*, vol. 260, pp. 519 – 528, 2018. [Online]. Available: http://www.sciencedirect.com/science/article/pii/S0925400517325303

[160] M. G. Sullivan, H. Utomo, P. J. Fagan, and M. D. Ward, "Automated electrochemical analysis with combinatorial electrode arrays," *Analytical Chemistry*, vol. 71, no. 19, pp. 4369–4375, 1999, pMID: 21662862. [Online]. Available: https://doi.org/10.1021/ac990331y

[161] X. Xu, S. Zhang, H. Chen, and J. Kong, "Integration of electrochemistry in micro-total analysis systems for biochemical assays: Recent developments," *Talanta*, vol. 80, no. 1, pp. 8 – 18, 2009. [Online]. Available: http://www.sciencedirect.com/science/article/pii/S0039914009004615

[162] J. R. Liddell, C. Zwingmann, M. M. Schmidt, A. Thiessen, D. Leibfritz, S. R. Robinson, and R. Dringen, "Sustained hydrogen peroxide stress decreases lactate production by cultured astrocytes," *Journal of neuroscience research*, vol. 87, no. 12, pp. 2696–2708, 2009.

[163] T. P. Szatrowski and C. F. Nathan, "Production of large amounts of hydrogen peroxide by human tumor cells," *Cancer Research*, vol. 51, no. 3, pp. 794–798, 1991. [Online]. Available: http://cancerres.aacrjournals.org/content/51/3/794

[164] U. E. Martinez-Outschoorn, Z. Lin, C. Trimmer, N. Flomenberg, C. Wang, S. Pavlides, R. G. Pestell, A. Howell, F. Sotgia, and M. P. Lisanti, "Cancer cells metabolically" fertilize" the tumor microenvironment with hydrogen peroxide, driving the warburg effect: implications for pet imaging of human tumors," *Cell cycle*, vol. 10, no. 15, pp. 2504–2520, 2011.

[165] D. Yan, H. Cui, W. Zhu, A. Talbot, L. G. Zhang, J. H. Sherman, and M. Keidar, "The strong cell-based hydrogen peroxide generation triggered by cold atmospheric plasma," *Scientific reports*, vol. 7, no. 1, p. 10831, 2017.

[166] B. L. Carlson, J. L. Pokorny, M. A. Schroeder, and J. N. Sarkaria, "Establishment, maintenance, and in vitro and in vivo applications of primary human glioblastoma multiforme (gbm) xenograft models for translational biology studies and drug discovery," *Current protocols in pharmacology*, pp. 14–16, 2011.

[167] A. J. Bard and L. R. Faulkner, *Electrochemical Methods: Fundamentals and Applications*. Wiley, 2000. [Online]. Available: https://books.google.com/books?id=kv56QgAACAAJ

[168] L. Michaelis and M. L. Menten, "The kinetics of the inversion effect," *Biochem. Z*, vol. 49, pp. 333–369, 1913.

[169] K. A. Johnson and R. S. Goody, "The original michaelis constant: translation of the 1913 michaelis–menten paper," *Biochemistry*, vol. 50, no. 39, pp. 8264–8269, 2011.

[170] R. Dringen and B. Hamprecht, "Involvement of glutathione peroxidase and catalase in the disposal of exogenous hydrogen peroxide by cultured astroglial cells," *Brain research*, vol. 759, no. 1, pp. 67–75, 1997.

[171] R. Dringen, L. Kussmaul, and B. Hamprecht, "Detoxification of exogenous hydrogen peroxide and organic hydroperoxides by cultured astroglial cells assessed by microtiter plate assay," *Brain Research Protocols*, vol. 2, no. 3, pp. 223–228, 1998.

[172] R. Dringen, L. Kussmaul, J. M. Gutterer, J. Hirrlinger, and B. Hamprecht, "The glutathione system of peroxide detoxification is less efficient in neurons than in astroglial cells," *Journal of neurochemistry*, vol. 72, no. 6, pp. 2523–2530, 1999.

[173] J. R. Liddell, S. R. Robinson, and R. Dringen, "Endogenous glutathione and catalase protect cultured rat astrocytes from the iron-mediated toxicity of hydrogen peroxide," *Neuroscience letters*, vol. 364, no. 3, pp. 164–167, 2004.

[174] R. Dringen, "Metabolism and functions of glutathione in brain," *Progress in neurobiology*, vol. 62, no. 6, pp. 649–671, 2000.

[175] R. Dringen, J. M. Gutterer, and J. Hirrlinger, "Glutathione metabolism in brain," *The FEBS Journal*, vol. 267, no. 16, pp. 4912–4916, 2000.

[176] R. Dringen, M. Brandmann, M. C. Hohnholt, and E.-M. Blumrich, "Glutathione-dependent detoxification processes in astrocytes," *Neurochemical research*, vol. 40, no. 12, pp. 2570–2582, 2015.

[177] B. Grobben, P. De Deyn, and H. Slegers, "Rat c6 glioma as experimental model system for the study of glioblastoma growth and invasion," *Cell and Tissue Research*, vol. 310, no. 3, pp. 257–270, Dec 2002. [Online]. Available: https://doi.org/10.1007/s00441-002-0651-7

[178] S. Doblas, T. He, D. Saunders, J. Pearson, J. Hoyle, N. Smith, M. Lerner, and R. A. Towner, "Glioma morphology and tumor-induced vascular alterations revealed in seven rodent glioma models by in vivo magnetic resonance imaging and angiography," *Journal of Magnetic Resonance Imaging*, vol. 32, no. 2, pp. 267–275, 2010.

[179] A. Gieryng, D. Pszczolkowska, K. Bocian, M. Dabrowski, W. D. Rajan, M. Kloss, J. Mieczkowski, and B. Kaminska, "Immune microenvironment of experimental rat c6 gliomas resembles human glioblastomas," *Scientific reports*, vol. 7, no. 1, p. 17556, 2017.

[180] I. Dokic, C. Hartmann, C. Herold-Mende, and A. Régnier-Vigouroux, "Glutathione peroxidase 1 activity dictates the sensitivity of glioblastoma cells to oxidative stress," *Glia*, vol. 60, no. 11, pp. 1785–1800, 2012. [Online]. Available: https://onlinelibrary.wiley.com/doi/abs/10.1002/glia.22397

[181] M. C. Sobotta, A. G. Barata, U. Schmidt, S. Mueller, G. Millonig, and T. P. Dick, "Exposing cells to h2o2: a quantitative comparison between continuous low-dose and one-time high-dose treatments," *Free Radical Biology and Medicine*, vol. 60, pp. 325–335, 2013.

[182] M. C. Regier, E. T. Alarid, and D. J. Beebe, "Progress towards understanding heterotypic interactions in multi-culture models of breast cancer," *Integrative Biology*, vol. 8, no. 6, pp. 684–692, 2016.

[183] L. Kim, Y.-C. Toh, J. Voldman, and H. Yu, "A practical guide to microfluidic perfusion culture of adherent mammalian cells," *Lab on a Chip*, vol. 7, no. 6, pp. 681–694, 2007.

[184] F. Meiners, I. Plettenberg, J. Witt, B. Vaske, A. Lesch, I. Brand, and G. Wittstock, "Local control of protein binding and cell adhesion by patterned organic thin films," *Analytical and bioanalytical chemistry*, vol. 405, no. 11, pp. 3673–3691, 2013.

[185] S. B. Hall, E. A. Khudaish, and A. L. Hart, "Electrochemical oxidation of hydrogen peroxide at platinum electrodes. part 1. an adsorption-controlled mechanism," *Electrochimica Acta*, vol. 43, no. 5-6, pp. 579–588, 1998.

[186] ——, "Electrochemical oxidation of hydrogen peroxide at platinum electrodes. part ii: effect of potential," *Electrochimica Acta*, vol. 43, no. 14-15, pp. 2015–2024, 1998.

[187] ——, "Electrochemical oxidation of hydrogen peroxide at platinum electrodes. part iii: Effect of temperature," *Electrochimica Acta*, vol. 44, no. 14, pp. 2455–2462, 1999.

[188] ——, "Electrochemical oxidation of hydrogen peroxide at platinum electrodes. part iv: phosphate buffer dependence," *Electrochimica Acta*, vol. 44, no. 25, pp. 4573–4582, 1999.

[189] ——, "Electrochemical oxidation of hydrogen peroxide at platinum electrodes. part v: inhibition by chloride," *Electrochimica Acta*, vol. 45, no. 21, pp. 3573–3579, 2000.

[190] D. Rolfe and G. C. Brown, "Cellular energy utilization and molecular origin of standard metabolic rate in mammals," *Physiological reviews*, vol. 77, no. 3, pp. 731–758, 1997.

[191] J. R. Wisniewski, A. Gizak, and D. Rakus, "Integrating proteomics and enzyme kinetics reveals tissue-specific types of the glycolytic and gluconeogenic pathways," *Journal of proteome research*, vol. 14, no. 8, pp. 3263–3273, 2015.

[192] L. Pellerin and P. J. Magistretti, "How to balance the brain energy budget while spending glucose differently," *The Journal of physiology*, vol. 546, no. 2, pp. 325–325, 2003.

[193] S. J. Vannucci, F. Maher, and I. A. Simpson, "Glucose transporter proteins in brain: delivery of glucose to neurons and glia," *Glia*, vol. 21, no. 1, pp. 2–21, 1997.

[194] K. Adekola, S. T. Rosen, and M. Shanmugam, "Glucose transporters in cancer metabolism," *Current opinion in oncology*, vol. 24, no. 6, p. 650, 2012.

[195] P.-B. Ancey, C. Contat, and E. Meylan, "Glucose transporters in cancer–from tumor cells to the tumor microenvironment," *The FEBS journal*, vol. 285, no. 16, pp. 2926–2943, 2018.

[196] F.-Q. Zhao and A. F. Keating, "Functional properties and genomics of glucose transporters," *Current genomics*, vol. 8, no. 2, pp. 113–128, 2007.

[197] B. C. Mulukutla, S. Khan, A. Lange, and W.-S. Hu, "Glucose metabolism in mammalian cell culture: new insights for tweaking vintage pathways," *Trends in biotechnology*, vol. 28, no. 9, pp. 476–484, 2010.

[198] R. C. Vannucci and S. J. Vannucci, "Glucose metabolism in the developing brain," in *Seminars in perinatology*, vol. 24, no. 2. Elsevier, 2000, pp. 107–115.

[199] A. L. McCall, "Chapter 22 - glucose transport," in *Stress: Physiology, Biochemistry, and Pathology*, G. Fink, Ed. Academic Press, 2019, pp. 293 – 307. [Online]. Available: http://www.sciencedirect.com/science/article/pii/B9780128131466000229

[200] N. Marty, M. Dallaporta, and B. Thorens, "Brain glucose sensing, counter-regulation, and energy homeostasis," *Physiology*, vol. 22, no. 4, pp. 241–251, 2007.

[201] R. J. DeBerardinis, J. J. Lum, G. Hatzivassiliou, and C. B. Thompson, "The biology of cancer: Metabolic reprogramming fuels cell growth and proliferation," *Cell Metabolism*, vol. 7, no. 1, pp. 11 – 20, 2008. [Online]. Available: http://www.sciencedirect.com/science/article/pii/S1550413107002951

[202] R. A. Cairns, I. S. Harris, and T. W. Mak, "Regulation of cancer cell metabolism," *Nature Reviews Cancer*, vol. 11, no. 2, p. 85, 2011.

[203] K. Duan, Z.-j. Liu, S.-q. Hu, H.-y. Huo, Z.-r. Xu, J.-f. Ruan, Y. Sun, L.-p. Dai, C.-b. Yan, W. Xiong *et al.*, "Lactic acid induces lactate transport and glycolysis/oxphos interconversion in glioblastoma," *Biochemical and biophysical research communications*, vol. 503, no. 2, pp. 888–894, 2018.

[204] F. Galeffi and D. A Turner, "Exploiting metabolic differences in glioma therapy," *Current drug discovery technologies*, vol. 9, no. 4, pp. 280–293, 2012.

[205] A. Tabernero, J. M. Medina, and C. Giaume, "Glucose metabolism and proliferation in glia: role of astrocytic gap junctions," *Journal of neurochemistry*, vol. 99, no. 4, pp. 1049–1061, 2006.

[206] S. Agnihotri and G. Zadeh, "Metabolic reprogramming in glioblastoma: the influence of cancer metabolism on epigenetics and unanswered questions," *Neuro-oncology*, vol. 18, no. 2, pp. 160–172, 2015.

[207] E. Poteet, G. R. Choudhury, A. Winters, W. Li, M.-G. Ryou, R. Liu, L. Tang, A. Ghorpade, Y. Wen, F. Yuan *et al.*, "Reversing the warburg effect as a treatment for glioblastoma," *Journal of Biological Chemistry*, vol. 288, no. 13, pp. 9153–9164, 2013.

[208] J. Galarraga, D. J. Loreck, J. F. Graham, R. L. DeLaPaz, B. Smith, D. Hallgren, and C. Cummins, "Glucose metabolism in human gliomas: Correspondence ofin situ andin vitro metabolic rates and altered energy metabolism," *Metabolic brain disease*, vol. 1, no. 4, pp. 279–291, 1986.

[209] J. Flöter, I. Kaymak, and A. Schulze, "Regulation of metabolic activity by p53," *Metabolites*, vol. 7, no. 2, p. 21, 2017.

[210] M. K. Ediriweera, K. H. Tennekoon, and S. R. Samarakoon, "In vitro assays and techniques utilized in anticancer drug discovery," *Journal of Applied Toxicology*, vol. 39, no. 1, pp. 38–71, 2019.

[211] C. M. Labak, P. Y. Wang, R. Arora, M. R. Guda, S. Asuthkar, A. J. Tsung, and K. K. Velpula, "Glucose transport: meeting the metabolic demands of cancer, and applications in glioblastoma treatment," *American journal of cancer research*, vol. 6, no. 8, p. 1599, 2016.

[212] T. Nishioka, Y. Oda, Y. Seino, T. Yamamoto, N. Inagaki, H. Yano, H. Imura, R. Shigemoto, and H. Kikuchi, "Distribution of the glucose transporters in human brain tumors," *Cancer research*, vol. 52, no. 14, pp. 3972–3979, 1992.

[213] K. Shibuya, M. Okada, S. Suzuki, M. Seino, S. Seino, H. Takeda, and C. Kitanaka, "Targeting the facilitative glucose transporter glut1 inhibits the self-renewal and tumor-initiating capacity of cancer stem cells," *Oncotarget*, vol. 6, no. 2, p. 651, 2015.

[214] G. I. Bell, T. Kayano, J. B. Buse, C. F. Burant, J. Takeda, D. Lin, H. Fukumoto, and S. Seino, "Molecular biology of mammalian glucose transporters," *Diabetes care*, vol. 13, no. 3, pp. 198–208, 1990.

[215] A. M. Navale and A. N. Paranjape, "Glucose transporters: physiological and pathological roles," *Biophysical reviews*, vol. 8, no. 1, pp. 5–9, 2016.

[216] R. A. Medina and G. I. Owen, "Glucose transporters: expression, regulation and cancer," *Biological research*, vol. 35, no. 1, pp. 9–26, 2002.

[217] J. F. Rivera, S. V. Sridharan, J. K. Nolan, S. A. Miloro, M. A. Alam, J. L. Rickus, and D. B. Janes, "Real-time characterization of uptake kinetics of glioblastoma vs. astrocytes in 2d cell culture using microelectrode array," *Analyst*, vol. 143, no. 20, pp. 4954–4966, 2018.

[218] N. Hay, "Reprogramming glucose metabolism in cancer: can it be exploited for cancer therapy?" *Nature Reviews Cancer*, vol. 16, no. 10, p. 635, 2016.

[219] C. V. Dang, A. Le, and P. Gao, "Myc-induced cancer cell energy metabolism and therapeutic opportunities," *Clinical cancer research*, vol. 15, no. 21, pp. 6479–6483, 2009.

[220] A. Wolf, S. Agnihotri, and A. Guha, "Targeting metabolic remodeling in glioblastoma multiforme," *Oncotarget*, vol. 1, no. 7, p. 552, 2010.

[221] I. Nakano, "Therapeutic potential of targeting glucose metabolism in glioma stem cells," 2014.

[222] R. B. Hamanaka and N. S. Chandel, "Targeting glucose metabolism for cancer therapy," *Journal of Experimental Medicine*, vol. 209, no. 2, pp. 211–215, 2012.

[223] U. E. Martinez-Outschoorn, M. Peiris-Pages, R. G. Pestell, F. Sotgia, and M. P. Lisanti, "Cancer metabolism: a therapeutic perspective," *Nature reviews Clinical oncology*, vol. 14, no. 1, p. 11, 2017.

[224] W. A. Flavahan, Q. Wu, M. Hitomi, N. Rahim, Y. Kim, A. E. Sloan, R. J. Weil, I. Nakano, J. N. Sarkaria, B. W. Stringer *et al.*, "Brain tumor initiating cells adapt to restricted nutrition through preferential glucose uptake," *Nature neuroscience*, vol. 16, no. 10, p. 1373, 2013.

[225] R. Kuang, A. Jahangiri, S. Mascharak, A. Nguyen, A. Chandra, P. M. Flanigan, G. Yagnik, J. R. Wagner, M. De Lay, D. Carrera *et al.*, "Glut3 upregulation promotes metabolic reprogramming associated with antiangiogenic therapy resistance," *JCI insight*, vol. 2, no. 2, 2017.

[226] R. J. Boado, K. L. Black, and W. M. Pardridge, "Gene expression of glut3 and glut1 glucose transporters in human brain tumors," *Molecular brain research*, vol. 27, no. 1, pp. 51–57, 1994.

[227] É. Cosset, S. Ilmjärv, V. Dutoit, K. Elliott, T. von Schalscha, M. F. Camargo, A. Reiss, T. Moroishi, L. Seguin, G. Gomez *et al.*, "Glut3 addiction is a druggable vulnerability for a molecularly defined subpopulation of glioblastoma," *Cancer Cell*, vol. 32, no. 6, pp. 856–868, 2017.

[228] C. Zheng, K. Yang, M. Zhang, M. Zou, E. Bai, Q. Ma, and R. Xu, "Specific protein 1 depletion attenuates glucose uptake and proliferation of human glioma cells by regulating glut3 expression," *Oncology letters*, vol. 12, no. 1, pp. 125–131, 2016.

[229] Y. Liu, Y.-m. Li, R.-f. Tian, W.-p. Liu, Z. Fei, Q.-f. Long, X.-a. Wang, and X. Zhang, "The expression and significance of hif-1α and glut-3 in glioma," *Brain research*, vol. 1304, pp. 149–154, 2009.

[230] S. Nagamatsu, H. Sawa, A. Wakizaka, and T. Hoshino, "Expression of facilitative glucose transporter isoforms in human brain tumors," *Journal of Neurochemistry*, vol. 61, no. 6, pp. 2048–2053, 1993. [Online]. Available: https://onlinelibrary.wiley.com/doi/abs/10.1111/j.1471-4159.1993.tb07441.x

[231] S. Abbadi, J. J. Rodarte, A. Abutaleb, E. Lavell, C. L. Smith, W. Ruff, J. Schiller, A. Olivi, A. Levchenko, H. Guerrero-Cazares *et al.*, "Glucose-6–phosphatase is a key metabolic regulator of glioblastoma invasion," *Molecular Cancer Research*, vol. 12, no. 11, pp. 1547–1559, 2014.

[232] A. Herling, M. König, S. Bulik, and H.-G. Holzhütter, "Enzymatic features of the glucose metabolism in tumor cells," *The FEBS journal*, vol. 278, no. 14, pp. 2436–2459, 2011.

[233] J. E. Dominguez, J. F. Graham, C. Cummins, D. J. Loreck, J. Galarraga, J. Van der Feen, R. DeLaPaz, and B. H. Smith, "Enzymes of glucose metabolism in cultured human gliomas: neoplasia is accompanied by altered hexokinase, phosphofructokinase, and glucose-6-phosphate dehydrogenase levels," *Metabolic brain disease*, vol. 2, no. 1, pp. 17–30, 1987.

[234] D. J. Loreck, J. Galarraga, J. Van der Feen, J. M. Phang, B. H. Smith, and C. Cummins, "Regulation of the pentose phosphate pathway in human astrocytes and gliomas," *Metabolic brain disease*, vol. 2, no. 1, pp. 31–46, 1987.

[235] J. B. Alavi, A. Alavi, J. Chawluk, M. Kushner, J. Powe, W. Hickey, and M. Reivich, "Positron emission tomography in patients with glioma a predictor of prognosis," *Cancer*, vol. 62, no. 6, pp. 1074–1078, 1988.

[236] R. J. Gillies, I. Robey, and R. A. Gatenby, "Causes and consequences of increased glucose metabolism of cancers," *Journal of Nuclear Medicine*, vol. 49, no. Suppl 2, pp. 24S–42S, 2008. [Online]. Available: http://jnm.snmjournals.org/content/49/Suppl_2/24S.abstract

[237] N. J. Patronas, G. D. Chiro, C. Kufta, D. Bairamian, P. L. Kornblith, R. Simon, and S. M. Larson, "Prediction of survival in glioma patients by means of positron emission tomography," *Journal of Neurosurgery*, vol. 62, no. 6, pp. 816 – 822, 1985. [Online]. Available: https://thejns.org/view/journals/j-neurosurg/62/6/article-p816.xml

[238] R. J. DeBerardinis, A. Mancuso, E. Daikhin, I. Nissim, M. Yudkoff, S. Wehrli, and C. B. Thompson, "Beyond aerobic glycolysis: Transformed cells can engage in glutamine metabolism that exceeds the requirement for protein and nucleotide synthesis," *Proceedings of the National Academy of Sciences*, vol. 104, no. 49, pp. 19 345–19 350, 2007. [Online]. Available: https://www.pnas.org/content/104/49/19345

[239] A. Wolf, S. Agnihotri, J. Micallef, J. Mukherjee, N. Sabha, R. Cairns, C. Hawkins, and A. Guha, "Hexokinase 2 is a key mediator of aerobic glycolysis and promotes tumor growth in human glioblastoma multiforme," *Journal of Experimental Medicine*, vol. 208, no. 2, pp. 313–326, 2011. [Online]. Available: http://jem.rupress.org/content/208/2/313

[240] E. Vlashi, C. Lagadec, L. Vergnes, T. Matsutani, K. Masui, M. Poulou, R. Popescu, L. Della Donna, P. Evers, C. Dekmezian, K. Reue, H. Christofk, P. S. Mischel, and F. Pajonk, "Metabolic state of glioma stem cells and nontumorigenic cells," *Proceedings of the National Academy of Sciences*, vol. 108, no. 38, pp. 16 062–16 067, 2011. [Online]. Available: https://www.pnas.org/content/108/38/16062

[241] P. Gupta, K. Jagavelu, and D. P. Mishra, "Inhibition of nadph oxidase-4 potentiates 2-deoxy-d-glucose-induced suppression of glycolysis, migration, and invasion in glioblastoma cells: Role of the akt/hif1/hk-2 signaling axis," *Antioxidants & Redox Signaling*, vol. 23, no. 8, pp. 665–681, 2015, pMID: 25891245. [Online]. Available: https://doi.org/10.1089/ars.2014.5973

[242] J. B. McGillen, C. J. Kelly, A. Martnez-Gonzlez, N. K. Martin, E. A. Gaffney, P. K. Maini, and V. M. Prez-Garca, "Glucoselactate metabolic cooperation in cancer: Insights from a spatial mathematical

model and implications for targeted therapy," *Journal of Theoretical Biology*, vol. 361, pp. 190 – 203, 2014. [Online]. Available: http://www.sciencedirect.com/science/article/pii/S0022519314005578

[243] M. Wu, A. Neilson, A. L. Swift, R. Moran, J. Tamagnine, D. Parslow, S. Armistead, K. Lemire, J. Orrell, J. Teich, S. Chomicz, and D. A. Ferrick, "Multiparameter metabolic analysis reveals a close link between attenuated mitochondrial bioenergetic function and enhanced glycolysis dependency in human tumor cells," *American Journal of Physiology-Cell Physiology*, vol. 292, no. 1, pp. C125–C136, 2007, pMID: 16971499. [Online]. Available: https://doi.org/10.1152/ajpcell.00247.2006

[244] S. Shibao, N. Minami, N. Koike, N. Fukui, K. Yoshida, H. Saya, and O. Sampetrean, "Metabolic heterogeneity and plasticity of glioma stem cells in a mouse glioblastoma model," *Neuro-Oncology*, vol. 20, no. 3, pp. 343–354, 09 2017. [Online]. Available: https://doi.org/10.1093/neuonc/nox170

[245] I. Saga, S. Shibao, J. Okubo, S. Osuka, Y. Kobayashi, S. Yamada, S. Fujita, K. Urakami, M. Kusuhara, K. Yoshida, H. Saya, and O. Sampetrean, "Integrated analysis identifies different metabolic signatures for tumor-initiating cells in a murine glioblastoma model," *Neuro-Oncology*, vol. 16, no. 8, pp. 1048–1056, 05 2014. [Online]. Available: https://doi.org/10.1093/neuonc/nou096

[246] N. Yamamoto, M. Ueda-Wakagi, T. Sato, K. Kawasaki, K. Sawada, K. Kawabata, M. Akagawa, and H. Ashida, "Measurement of glucose uptake in cultured cells," *Current protocols in pharmacology*, vol. 71, 2015.

[247] G. J. van der Windt, C.-H. Chang, and E. L. Pearce, "Measuring bioenergetics in t cells using a seahorse extracellular flux analyzer," *Current Protocols in Immunology*, vol. 113, no. 1, pp. 3.16B.1–3.16B.14, 2016. [Online]. Available: https://currentprotocols.onlinelibrary.wiley.com/doi/abs/10.1002/0471142735.im0316bs113

[248] M. B. de Moura and B. Van Houten, *Bioenergetic Analysis of Intact Mammalian Cells Using the Seahorse XF24 Extracellular Flux Analyzer and a Luciferase ATP Assay.* Totowa, NJ: Humana Press, 2014, pp. 589–602. [Online]. Available: https://doi.org/10.1007/978-1-62703-739-6_40

[249] J. Wang, "Electrochemical glucose biosensors," *Chemical Reviews*, vol. 108, no. 2, pp. 814–825, 2008, pMID: 18154363. [Online]. Available: https://doi.org/10.1021/cr068123a

[250] G. S. Wilson and M. A. Johnson, "In-vivo electrochemistry: What can we learn about living systems?" *Chemical Reviews*, vol. 108, no. 7, pp. 2462–2481, 2008, pMID: 18558752. [Online]. Available: https://doi.org/10.1021/cr068082i

[251] D. L. Robinson, A. Hermans, A. T. Seipel, and R. M. Wightman, "Monitoring rapid chemical communication in the brain," *Chemical Reviews*, vol. 108, no. 7, pp. 2554–2584, 2008, pMID: 18576692.

[252] S. Vaddiraju, D. J. Burgess, I. Tomazos, F. C. Jain, and F. Papadimitrakopoulos, "Technologies for continuous glucose monitoring: Current problems and future promises," *Journal of Diabetes Science and Technology*, vol. 4, no. 6, pp. 1540–1562, 2010, pMID: 21129353.

[253] J. Shi, E. S. McLamore, and D. M. Porterfield, "Nanomaterial based self-referencing microbiosensors for cell and tissue physiology research," *Biosensors and Bioelectronics*, vol. 40, no. 1, pp. 127 – 134, 2013, selected Papers from the World Congress on Biosensors.

[254] E. S. McLamore and D. M. Porterfield, "Non-invasive tools for measuring metabolism and biophysical analyte transport: self-referencing physiological sensing," *Chem. Soc. Rev.*, vol. 40, pp. 5308–5320, 2011. [Online]. Available: http://dx.doi.org/10.1039/C0CS00173B

[255] R.-I. Stefan, J. F. van Staden, and H. Y. Aboul-Enein, "Electrochemical sensor arrays," *Critical Reviews in Analytical Chemistry*, vol. 29, no. 2, pp. 133–153, 1999, pMID: 29364707.

[256] J. L. Hammond, N. Formisano, P. Estrela, S. Carrara, and J. Tkac, "Electrochemical biosensors and nanobiosensors," *Essays In Biochemistry*, vol. 60, no. 1, pp. 69–80, 2016. [Online]. Available: http://essays.biochemistry.org/content/60/1/69

[257] J. J. Burmeister and G. A. Gerhardt, "Self-referencing ceramic-based multisite microelectrodes for the detection and elimination of interferences from the measurement of l-glutamate and other analytes," *Analytical Chemistry*, vol. 73, no. 5, pp. 1037–1042, 2001, pMID: 11289414. [Online]. Available: https://doi.org/10.1021/ac0010429

[258] J. J. Burmeister, K. Moxon, and G. A. Gerhardt, "Ceramic-based multisite microelectrodes for electrochemical recordings," *Analytical Chemistry*, vol. 72, no. 1, pp. 187–192, 2000, pMID: 10655652. [Online]. Available: https://doi.org/10.1021/ac9907991

[259] J. J. Burmeister, F. Pomerleau, M. Palmer, B. K. Day, P. Huettl, and G. A. Gerhardt, "Improved ceramic-based multisite microelectrode for rapid measurements of l-glutamate in the cns," *Journal of Neuroscience Methods*, vol. 119, no. 2, pp. 163 – 171, 2002. [Online]. Available: http://www.sciencedirect.com/science/article/pii/S0165027002001723

[260] C. Loureno, A. Ledo, G. A. Gerhardt, J. Laranjinha, and R. Barbosa, "Neurometabolic and electrophysiological changes during cortical spreading depolarization: Multimodal approach based on a lactate-glucose dual microbiosensor arrays," *Scientific Reports*, vol. 7, 12 2017.

[261] "Microelectrode array biosensor for high-resolution measurements of extracellular glucose in the brain," *Sensors and Actuators B: Chemical*, vol. 237, pp. 298 – 307, 2016. [Online]. Available: http://www.sciencedirect.com/science/article/pii/S0925400516309352

[262] W. Wei, Y. Song, W. Shi, N. Lin, T. Jiang, and X. Cai, "A high sensitivity mea probe for measuring real time rat brain glucose flux," *Biosensors and Bioelectronics*, vol. 55, pp. 66 – 71, 2014. [Online]. Available: http://www.sciencedirect.com/science/article/pii/S0956566313008385

[263] W. Wei, Y. Song, L. Wang, S. Zhang, J. Luo, S. Xu, and X. Cai, "An implantable microelectrode array for simultaneous l-glutamate and electrophysiological recordings in vivo," *Microsystems &Amp; Nanoengineering*,

vol. 1, pp. 15 002 EP –, May 2015, article. [Online]. Available: https://doi.org/10.1038/micronano.2015.2

[264] J. Olivo, L. Foglia, M. A. Casulli, C. Boero, S. Carrara, and G. De Micheli, "Glucose and lactate monitoring in cell cultures with a wireless android interface," in *2014 IEEE Biomedical Circuits and Systems Conference (BioCAS) Proceedings*, Oct 2014, pp. 400–403.

[265] C. Boero, S. Carrara, G. Vecchio, L. Calza, and G. Micheli, "Highly sensitive carbon nanotube-based sensing for lactate and glucose monitoring in cell culture," *IEEE Transactions on NanoBioscience*, vol. 10, no. 1, pp. 59–67, March 2011.

[266] C. Boero, J. Olivo, G. De Micheli, and S. Carrara, "New approaches for carbon nanotubes-based biosensors and their application to cell culture monitoring," vol. 6, no. 5, pp. 479–485, 2012.

[267] I. A. Ges and F. Baudenbacher, "Enzyme-coated microelectrodes to monitor lactate production in a nanoliter microfluidic cell culture device," *Biosensors and Bioelectronics*, vol. 26, no. 2, pp. 828 – 833, 2010. [Online]. Available: http://www.sciencedirect.com/science/article/pii/S0956566310002988

[268] I. Ges and F. Baudenbacher, "Enzyme electrodes to monitor glucose consumption of single cardiac myocytes in sub-nanoliter volumes," *Biosensors and Bioelectronics*, vol. 25, pp. 1019–1024, 01 2010.

[269] R. Pemberton, T. Cox, R. Tuffin, G. Drago, J. Griffiths, R. Pittson, G. Johnson, J. Xu, I. Sage, R. Davies, S. Jackson, G. Kenna, R. Luxton, and J. Hart, "Fabrication and evaluation of a micro(bio)sensor array chip for multiple parallel measurements of important cell biomarkers," *Sensors (Basel, Switzerland)*, vol. 14, pp. 20 519–20 532, 10 2014.

[270] P. J. S. Smith, R. H. Sanger, and M. Messerli, *Principles, Development and Applications of Self-Referencing Electrochemical Microelectrodes to the Determination of Fluxes at Cell Membranes*, 01 2007.

[271] C. F. Lourenço, A. Ledo, G. A. Gerhardt, J. Laranjinha, and R. M. Barbosa, "Neurometabolic and electrophysiological changes during cortical spreading depolarization: multimodal approach based on a lactate-glucose dual microbiosensor arrays," *Scientific Reports*, vol. 7, no. 1, p. 6764, 2017.

[272] A. Cavallini, C. Baj-Rossi, S. Ghoreishizadeh, G. De Micheli, and S. Carrara, "Design, fabrication, and test of a sensor array for perspective biosensing in chronic pathologies," in *2012 IEEE Biomedical Circuits and Systems Conference (BioCAS)*, Nov 2012, pp. 124–127.

[273] F. Maher, S. Vannucci, and I. Simpson, "Glucose transporter proteins in brain," *FASEB journal : official publication of the Federation of American Societies for Experimental Biology*, vol. 8, pp. 1003–11, 11 1994.

[274] W. A. Flavahan, "Glioma stem cells adapt to restricted nutrition through preferential glucose uptake," Ph.D. dissertation, Case Western Reserve University School of Graduate Studies, 2013. [Online]. Available: http://rave.ohiolink.edu/etdc/view?acc_num=case1384252748

[275] A. Bronisz, E. A. Chiocca, and J. Godlewski, "Response to energy depletion: mir-451/ampk loop," *Oncotarget*, vol. 6, no. 20, pp. 17 851–17 852, Jun 2015, 26257001[pmid]. [Online]. Available: https://www.ncbi.nlm.nih.gov/pubmed/26257001

[276] N. Thomas, I. Lhdesmki, and B. Parviz, "Direct immobilization of enzymes on common photoresists," in *2011 IEEE 24th International Conference on Micro Electro Mechanical Systems*, Jan 2011, pp. 233–236.

[277] H. Eloqayli, T. M. Melø, A. Haukvik, and U. Sonnewald, "[2,4-13c]β-hydroxybutyrate metabolism in astrocytes and c6 glioblastoma cells," *Neurochemical Research*, vol. 36, no. 8, pp. 1566–1573, Aug 2011. [Online]. Available: https://doi.org/10.1007/s11064-011-0485-3

[278] W.-L. Yeh, C.-J. Lin, and W.-M. Fu, "Enhancement of glucose transporter expression of brain endothelial cells by vascular endothelial growth factor derived from glioma exposed to hypoxia," *Molecular Pharmacology*, vol. 73, no. 1, pp. 170–177, 2008. [Online]. Available: http://molpharm.aspetjournals.org/content/73/1/170

[279] V. Miranda-Gonçalves, S. Granja, O. Martinho, M. Honavar, M. Pojo, B. M. Costa, M. M. Pires, C. Pinheiro, M. Cordeiro, G. Bebiano, P. Costa, R. M. Reis, and F. Baltazar, "Hypoxia-mediated upregulation of mct1 expression supports the glycolytic phenotype of glioblastomas," *Oncotarget*, vol. 7, no. 29, pp. 46 335–46 353, Jun 2016. [Online]. Available: https://www.ncbi.nlm.nih.gov/pubmed/27331625

[280] Y. Zhou, Y. Zhou, T. Shingu, L. Feng, Z. Chen, M. Ogasawara, M. J. Keating, S. Kondo, and P. Huang, "Metabolic alterations in highly tumorigenic glioblastoma cells: Preference for hypoxia and high dependency on glycolysis," *Journal of Biological Chemistry*, vol. 286, no. 37, pp. 32 843–32 853, 2011. [Online]. Available: http://www.jbc.org/content/286/37/32843.abstract

[281] K. M. Carroll, D. M. Simpson, C. E. Eyers, C. G. Knight, P. Brownridge, W. B. Dunn, C. L. Winder, K. Lanthaler, P. Pir, N. Malys, D. B. Kell, S. G. Oliver, S. J. Gaskell, and R. J. Beynon, "Absolute quantification of the glycolytic pathway in yeast:," *Molecular & Cellular Proteomics*, vol. 10, no. 12, 2011. [Online]. Available: https://www.mcponline.org/content/10/12/M111.007633

[282] R. Milo, "What is the total number of protein molecules per cell volume? a call to rethink some published values," *BioEssays*, vol. 35, no. 12, pp. 1050–1055. [Online]. Available: https://onlinelibrary.wiley.com/doi/abs/10.1002/bies.201300066

[283] A. B. Fulton, "How crowded is the cytoplasm?" *Cell*, vol. 30, no. 2, pp. 345–347, Sep 1982. [Online]. Available: https://doi.org/10.1016/0092-8674(82)90231-8

[284] A. P. Minton, "The influence of macromolecular crowding and macromolecular confinement on biochemical reactions in physiological media," *Journal of Biological Chemistry*, vol. 276, no. 14, pp. 10 577–10 580, 2001. [Online]. Available: http://www.jbc.org/content/276/14/10577.short

[285] N. Yu, J.-L. Martin, N. Stella, and P. J. Magistretti, "Arachidonic acid stimulates glucose uptake in cerebral cortical astrocytes." *Proceedings of the National Academy of Sciences*, vol. 90, no. 9, pp. 4042–4046, 1993.

[286] L. Pellerin and P. J. Magistretti, "Excitatory amino acids stimulate aerobic glycolysis in astrocytes via an activation of the na+/k+ atpase," *Developmental neuroscience*, vol. 18, no. 5-6, pp. 336–342, 1996.

[287] M. Lopes-Cardozo, O. M. Larsson, and A. Schousboe, "Acetoacetate and glucose as lipid precursors and energy substrates in primary cultures of astrocytes and neurons from mouse cerebral cortex," *Journal of neurochemistry*, vol. 46, no. 3, pp. 773–778, 1986.

[288] I. Marin-Valencia, C. Yang, T. Mashimo, S. Cho, H. Baek, X.-L. Yang, K. Rajagopalan, M. Maddie, V. Vemireddy, Z. Zhao, L. Cai, L. Good, B. Tu, K. Hatanpaa, B. Mickey, J. Mats, J. Pascual, E. Maher, C. Malloy, R. DeBerardinis, and R. Bachoo, "Analysis of tumor metabolism reveals mitochondrial glucose oxidation in genetically diverse human glioblastomas in the mouse brain invivo," *Cell Metabolism*, vol. 15, no. 6, pp. 827 – 837, 2012. [Online]. Available: http://www.sciencedirect.com/science/article/pii/S1550413112001945

[289] S. Morgello, R. R. Uson, E. J. Schwartz, and R. S. Haber, "The human blood-brain barrier glucose transporter (glut1) is a glucose transporter of gray matter astrocytes," *Glia*, vol. 14, no. 1, pp. 43–54, 1995. [Online]. Available: https://onlinelibrary.wiley.com/doi/abs/10.1002/glia.440140107

[290] A. Allen and C. Messier, "Plastic changes in the astrocyte glut1 glucose transporter and beta-tubulin microtubule protein following voluntary exercise in mice," *Behavioural Brain Research*, vol. 240, pp. 95 – 102, 2013. [Online]. Available: http://www.sciencedirect.com/science/article/pii/S0166432812007541

[291] A. M. Fernandez, E. Hernandez-Garzón, P. Perez-Domper, A. Perez-Alvarez, S. Mederos, T. Matsui, A. Santi, A. Trueba-Saiz, L. García-Guerra, J. Pose-Utrilla, J. Fielitz, E. N. Olson, R. Fernandez de la Rosa, L. Garcia Garcia, M. A. Pozo, T. Iglesias, A. Araque, H. Soya, G. Perea, E. D. Martin, and I. Torres Aleman, "Insulin regulates astrocytic glucose handling through cooperation with igf-i," *Diabetes*, vol. 66, no. 1, pp. 64–74, 2017. [Online]. Available: https://diabetes.diabetesjournals.org/content/66/1/64

[292] R. Leino, D. Gerhart, A. van Bueren, A. McCall, and L. Drewes, "Ultrastructural localization of glut 1 and glut 3 glucose transporters in rat brain," *Journal of Neuroscience Research*, vol. 49, no. 5, pp. 617–626, 1997.

[293] M. Uldry, M. Ibberson, M. Hosokawa, and B. Thorens, "Glut2 is a high affinity glucosamine transporter," *FEBS Letters*, vol. 524, no. 1-3, pp. 199–203, 2002.

[294] C. J. Libby, A. N. Tran, S. E. Scott, C. Griguer, and A. B. Hjelmeland, "The pro-tumorigenic effects of metabolic alterations in glioblastoma including brain tumor initiating cells," *Biochimica et Biophysica Acta (BBA) - Reviews on Cancer*, vol. 1869, no. 2, pp. 175 – 188, 2018. [Online]. Available: http://www.sciencedirect.com/science/article/pii/S0304419X17301658

[295] H. Oppermann, Y. Ding, J. Sharma, M. Berndt Paetz, J. Meixensberger, F. Gaunitz, and C. Birkemeyer, "Metabolic response of glioblastoma cells associated with glucose withdrawal and pyruvate substitution as revealed by gc-ms," *Nutrition & metabolism*, vol. 13, pp. 70–70, Oct 2016, 27777605[pmid]. [Online]. Available: https://www.ncbi.nlm.nih.gov/pubmed/27777605

[296] M. Shamir, Y. Bar-On, R. Phillips, and R. Milo, "Snapshot: timescales in cell biology," *Cell*, vol. 164, no. 6, pp. 1302–1302, 2016.

[297] P. A. HELLIWELL, M. RICHARDSON, J. AFFLECK, and G. L. KELLETT, "Stimulation of fructose transport across the intestinal brush-border membrane by pma is mediated by glut2 and dynamically regulated by protein kinase c," *Biochemical Journal*, vol. 350, no. 1, pp. 149–154, 2000.

[298] A. J. López-Gambero, F. Martínez, K. Salazar, M. Cifuentes, and F. Nualart, "Brain glucose-sensing mechanism and energy homeostasis," *Molecular Neurobiology*, vol. 56, no. 2, pp. 769–796, Feb 2019. [Online]. Available: https://doi.org/10.1007/s12035-018-1099-4

[299] B. Thorens, "Brain glucose sensing and neural regulation of insulin and glucagon secretion," *Diabetes, Obesity and Metabolism*, vol. 13, no. s1, pp. 82–88, 2011.

[300] A. Adamska, A. Domenichini, and M. Falasca, "Pancreatic ductal adenocarcinoma: current and evolving therapies," *International journal of molecular sciences*, vol. 18, no. 7, p. 1338, 2017.

[301] H. Ijichi, "Genetically-engineered mouse models for pancreatic cancer: Advances and current limitations," *World journal of clinical oncology*, vol. 2, no. 5, p. 195, 2011.

[302] A. Daemen, D. Peterson, N. Sahu, R. McCord, X. Du, B. Liu, K. Kowanetz, R. Hong, J. Moffat, M. Gao *et al.*, "Metabolite profiling stratifies pancreatic ductal adenocarcinomas into subtypes with distinct sensitivities to metabolic inhibitors," *Proceedings of the National Academy of Sciences*, vol. 112, no. 32, pp. E4410–E4417, 2015.

[303] R. Cohen, C. Neuzillet, A. Tijeras-Raballand, S. Faivre, A. de Gramont, and E. Raymond, "Targeting cancer cell metabolism in pancreatic adenocarcinoma," *Oncotarget*, vol. 6, no. 19, p. 16832, 2015.

[304] M. J. Bradney, "Development of an 0rw1s34rfesdcfkexd09rt2in vitro1rw1s34rfesdcfkexd09rt2 model for pancreatic ductal adenocarcinoma," Ph.D. dissertation, 2017, copyright - Database copyright ProQuest LLC; ProQuest does not claim copyright in the individual underlying works; Last updated - 2018-01-09. [Online]. Available: https://search-proquest-com.ezproxy.lib.purdue.edu/docview/1975367057?accountid=13360

[305] B. Han, C. Qu, K. Park, S. F. Konieczny, and M. Korc, "Recapitulation of complex transport and action of drugs at the tumor microenvironment using tumor-microenvironment-on-chip," *Cancer letters*, vol. 380, no. 1, pp. 319–329, 2016.

[306] B. Kwak, K. Park, and B. Han, "Tumor-microenvironment-on-chip : Simulation of complex transport around tumor," 2013.

APPENDIX

Control experiments

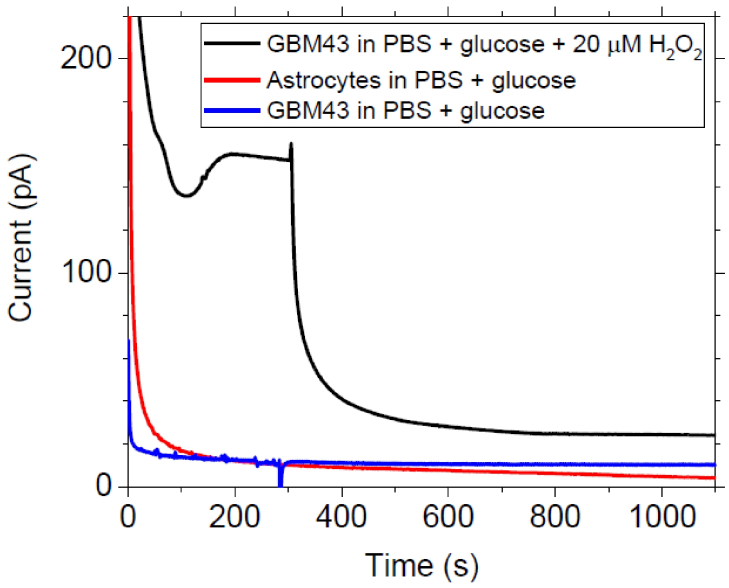

Fig. 1. Control experiments were performed to detect cellular secretion using the same experimental setup and timeline as in the measurements of H2O2 uptake kinetics. The amperometric signals measured for astrocytes (red) and GBM43 cells (blue) exposed to 5.5 mM glucose in PBS (without H2O2) were smaller than the smallest measured signal during H2O2 exposure, as indicated by the response (black) for GBM43 cells exposed to 20 μM H2O2 in the same measurement medium. This observation indicates that the response due to release of analytes by the cells (if any) is below the magnitude of the signals measured during H2O2 exposure.

Sensitivities to glucose, lactate and H2O2 are calculated as the ratio of the change in current (ΔI) to the change in concentration (ΔC): ΔI/ΔC (glucose) = 35.4 pA/5.5 mM = 6 pA/mM ΔI/ΔC (lactate) = 183.4 pA/11 mM = 16 pA/mM ΔI/ΔC (H2O2) = 728.8 pA/0.1 mM = 7288 pA/mM The selectivity to H2O2 is calculated as the sensitivity ratio of H2O2 to glucose and lactate: Selectivity of H2O2 relative to glucose = 1130 Selectivity of H2O2 relative to lactate = 437 From the literature, rat astrocytes exposed to a sustained concentration of 50 μM H2O2 for 2 hours exhibited changes in glucose uptake and lactate release, from 1.28 to 1.05 μmol (mg protein)$^{-1}$

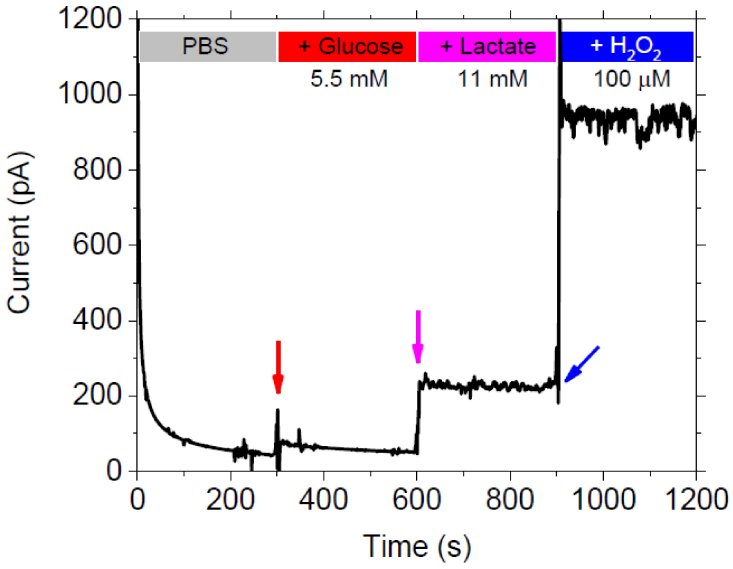

Fig. 2. Response of representative platinum electrode in the MEA to step changes in concentration of glucose, lactate and H2O2. Arrows indicate the time at which each compound is introduced into the solution. The solution is homogenized by stirring using a magnetic bar. The noise level observed in the signal is due to the stirring of the solution. Homogenized concentrations are indicated at the top of the plot.

h^{-1} for glucose uptake and from 2.40 to 1.50 μmol (mg protein)$^{-1}$ h^{-1} for lactate release [162]. This result indicates that H2O2 induced negative changes of 0.23 μmol (mg protein)$^{-1}$ h^{-1} in glucose uptake and 0.9 μmol (mg protein)$^{-1}$ h^{-1} in lactate release, which correspond to 8.3 and 32.5 amol s^{-1} $cell^{-1}$, respectively. Although these changes in the rates are in the same order as the smallest H2O2 uptake rate measured in our experiments, 8 amol s^{-1} $cell^{-1}$ as obtained for astrocytes exposed to 20 μM H2O2, the selectivity of H2O2 relative to glucose (1130) and lactate (437) indicates that their impact on the H2O2 signals is minimal.

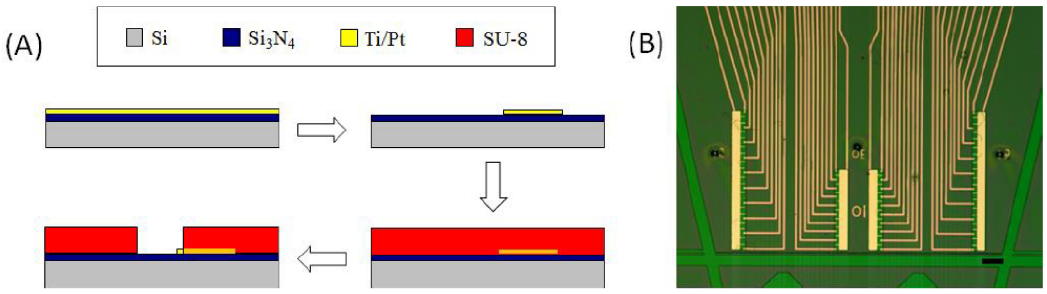

Fig. 3. Cross sections (A) and photograph of the MEA chip (B). Scale bar is 100 μm. On silicon substrate, 300 nm silicon nitride was deposited by low pressure chemical vapor deposition (LPCVD). Titanium/platinum (10 nm/100 nm) were deposited by electron-beam evaporation, followed by photo-lithographical patterning and lift-off processing to define the electrodes and lead traces. SU-8 photoresist (0.5 μm thick) was spin-coated and then photolithographically patterned to expose the electrodes and contact pads. Finally, the wafer was diced, and the dies were wire-bonded to printed circuit boards (PCBs).

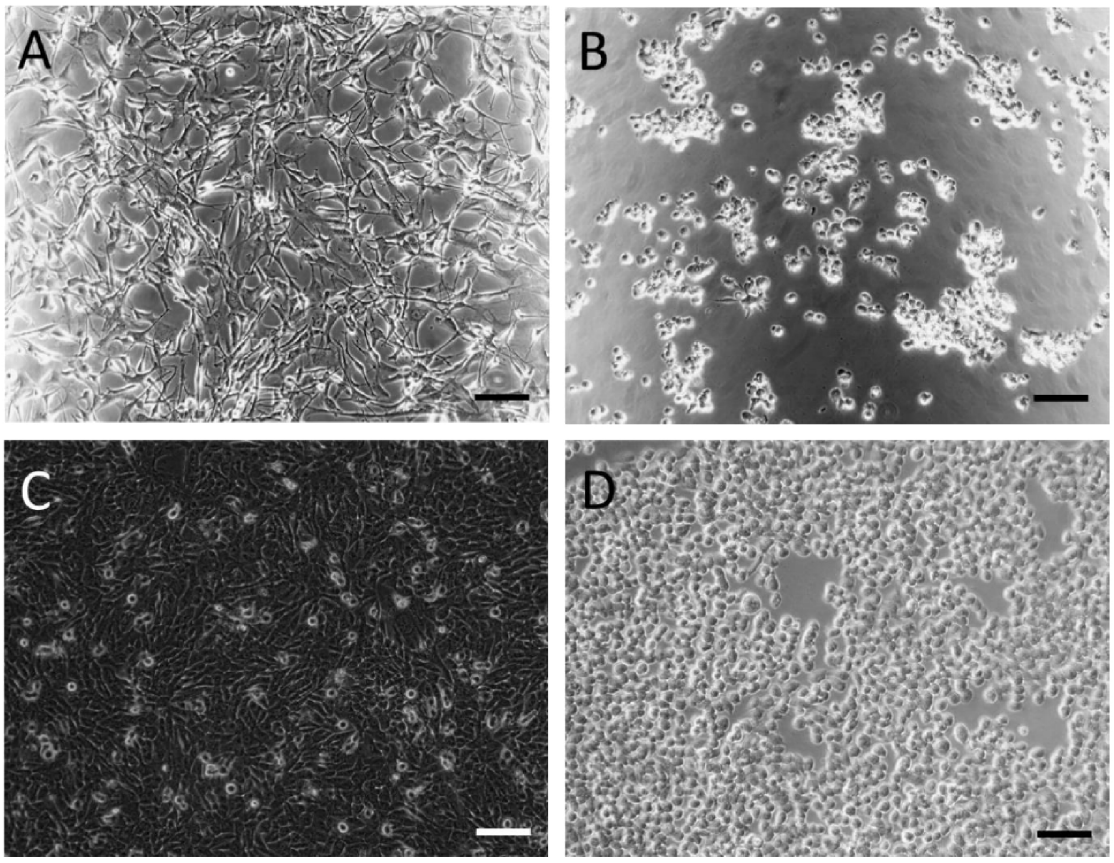

Fig. 4. Representative pictures of human astrocyte (A-B) and GBM43 (C-D) cultures. (A, C) before treatment with 500 μM H2O2 and measurement with MEA for approximately 2 h. (B, D) after the treatment. Scale bars are 100 μm. Both cell types lose adherence and change morphology after the treatment; however, as shown in Fig. 5, the cells are highly viable.

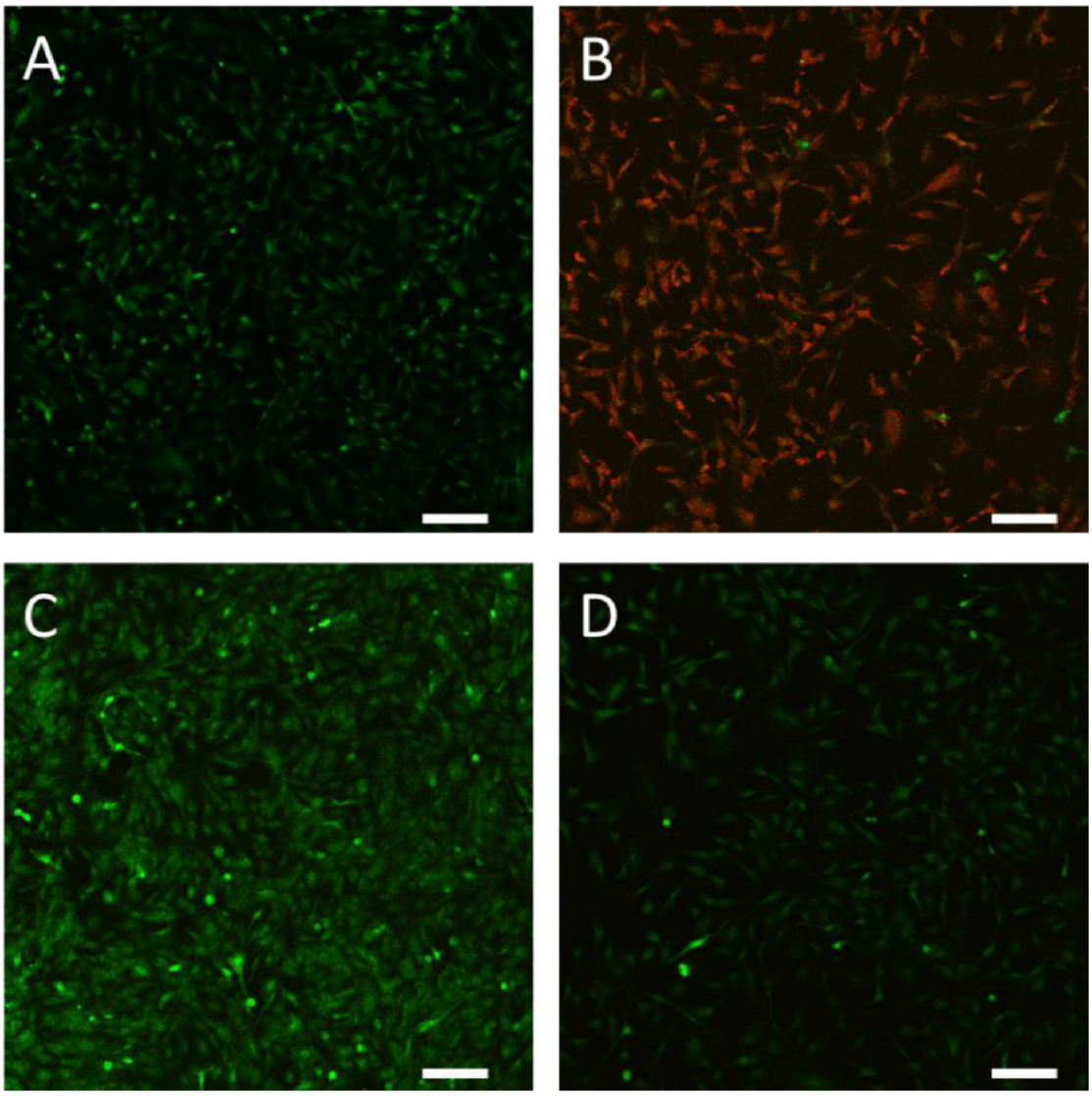

Fig. 5. Live/dead assays for astrocytes (A-D) and GBM43 (E-H in next page) cultures. (A) positive control (no treatment). (B) negative control (fixed with formalin for 20 minutes). (C) incubated for 2 h in PBS (pH 7.4) + 5.5 mM glucose. (D) incubated for 2 h in PBS + 5.5 mM glucose + 500 μM H2O2. Cell viability determined by CellTracker Green (live) and propidium iodide (red, dead) labeling. Scale bars are 100 μm. (Continue on next page).Two hours in H2O2 caused a fraction of astrocytes to lose adherence and thus being washed away during the live/dead assay, which would explain the apparent reduction in cell confluence in (D) compared to (C). However, the astrocytes that remained adhered were viable.

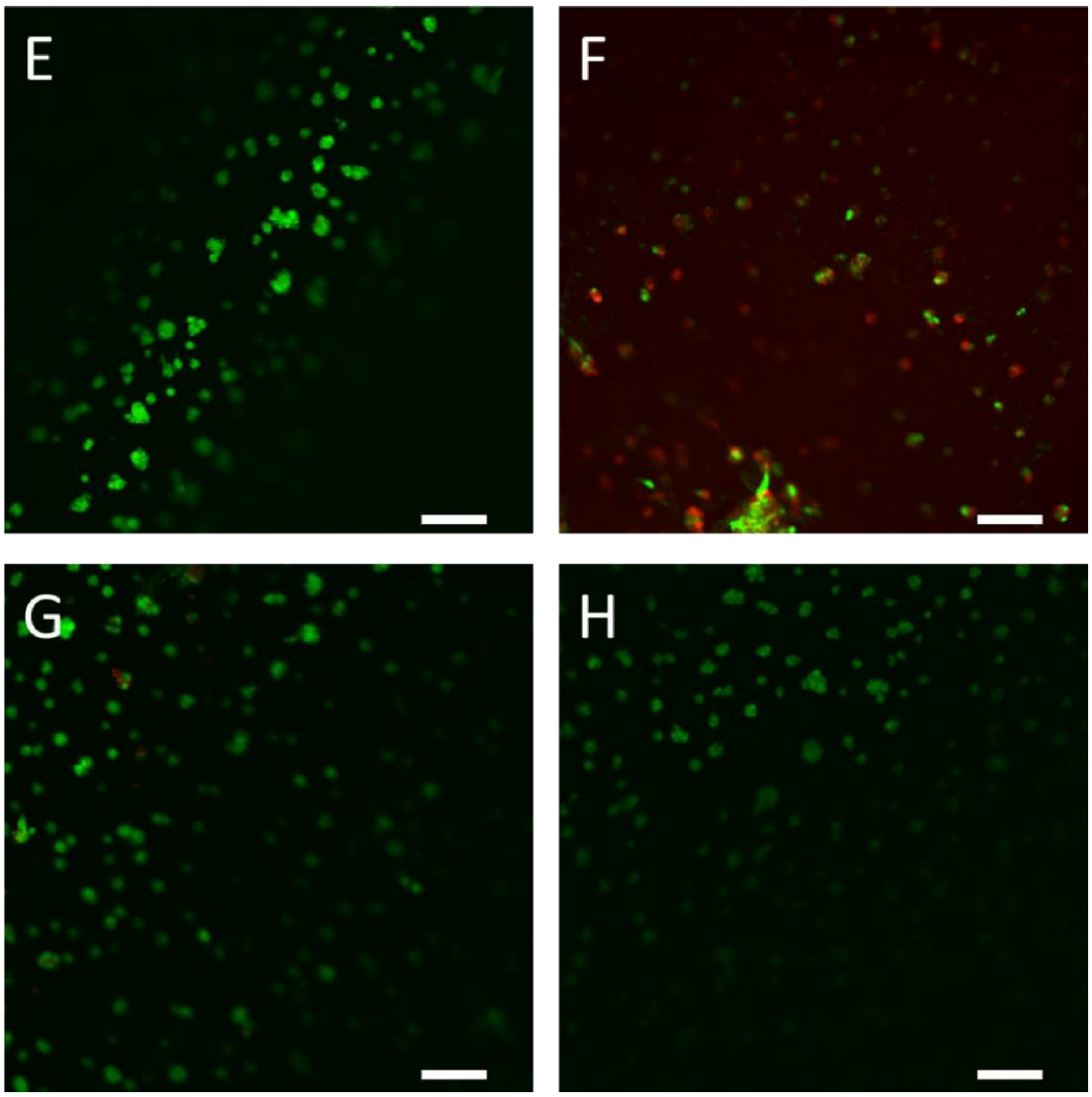

Fig. 6. (Continued from previous Fig. 5) Live/dead assays for astrocytes (A-D in previous page) and GBM43 (E-H) cultures. (E) positive control (no treatment). (F) negative control (fixed with formalin for 20 minutes). (G) incubated for 2 h in PBS (pH 7.4) + 5.5 mM glucose. (H) incubated for 2 h in PBS + 5.5 mM glucose + 500 μM H2O2. Cell viability determined by CellTracker Green (live) and propidium iodide (red, dead) labeling. Scale bars are 100 μm. Despite losing adherence, two hours in 500 μM H2O2 had no apparent harmful effect on GBM43 cells viability (H).

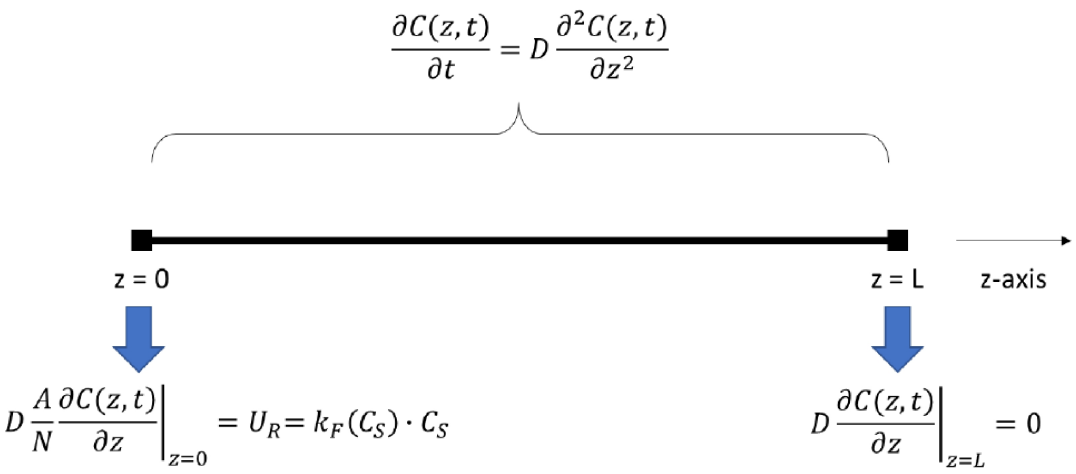

Fig. 7. Simulation geometry and boundary conditions. The surface of the cells is defined as the plane z = 0, wherein the boundary condition is set to U_R. The interface air/solution is defined as the plane z = L, wherein the boundary condition is set to zero flux. The initial condition, C(z,0) for 0 z L, is set to C_0 where C_0 = 20, 60, 100, 200, 300 or 500 μM.

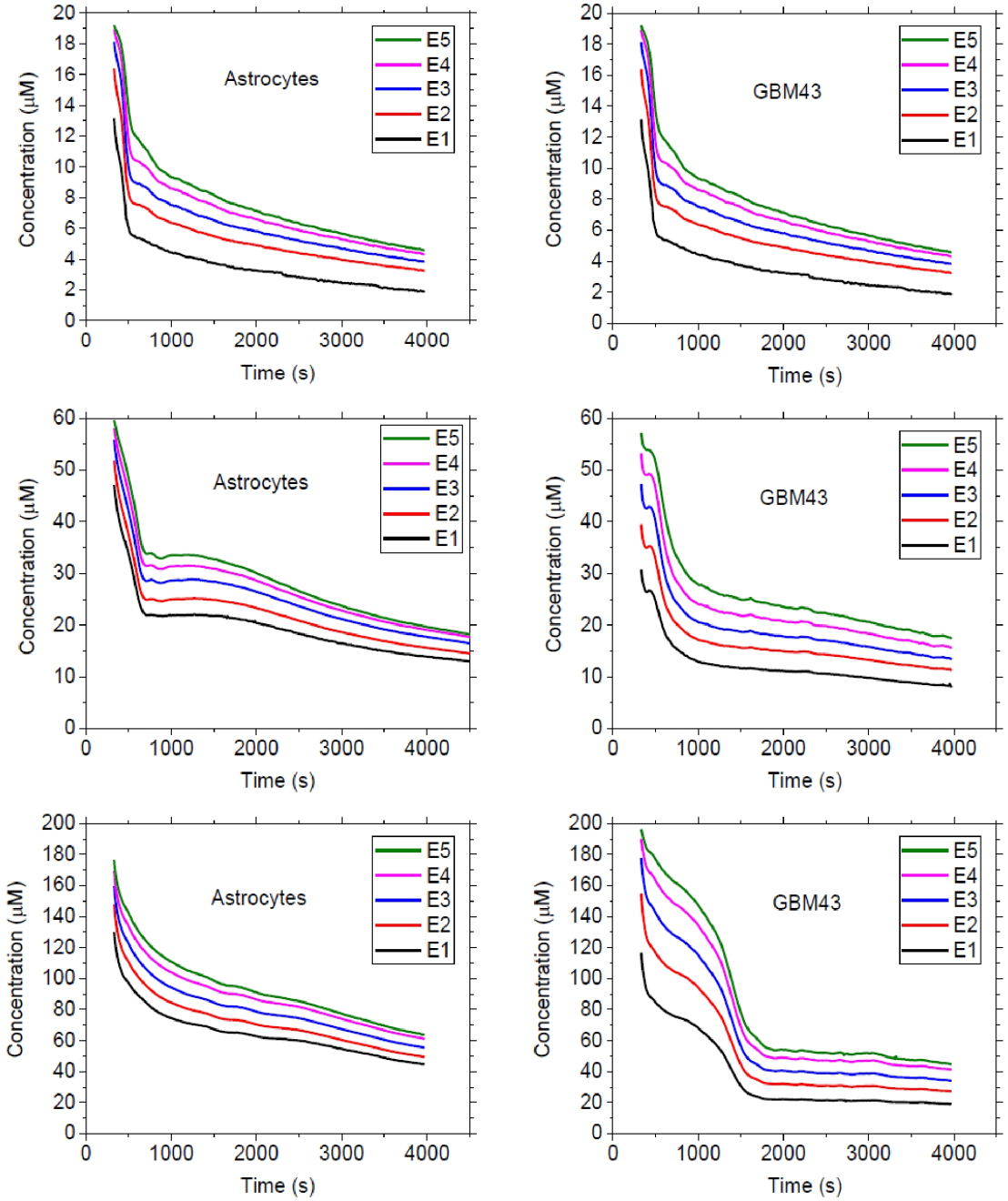

Fig. 8. Representative concentration transients measured in real time at the electrode positions during experiments wherein the cell cultures of astrocytes and GBM43 are exposed to C_0 of 20, 60, 200, 300 and 500 μM H2O2. (Continue in next page).

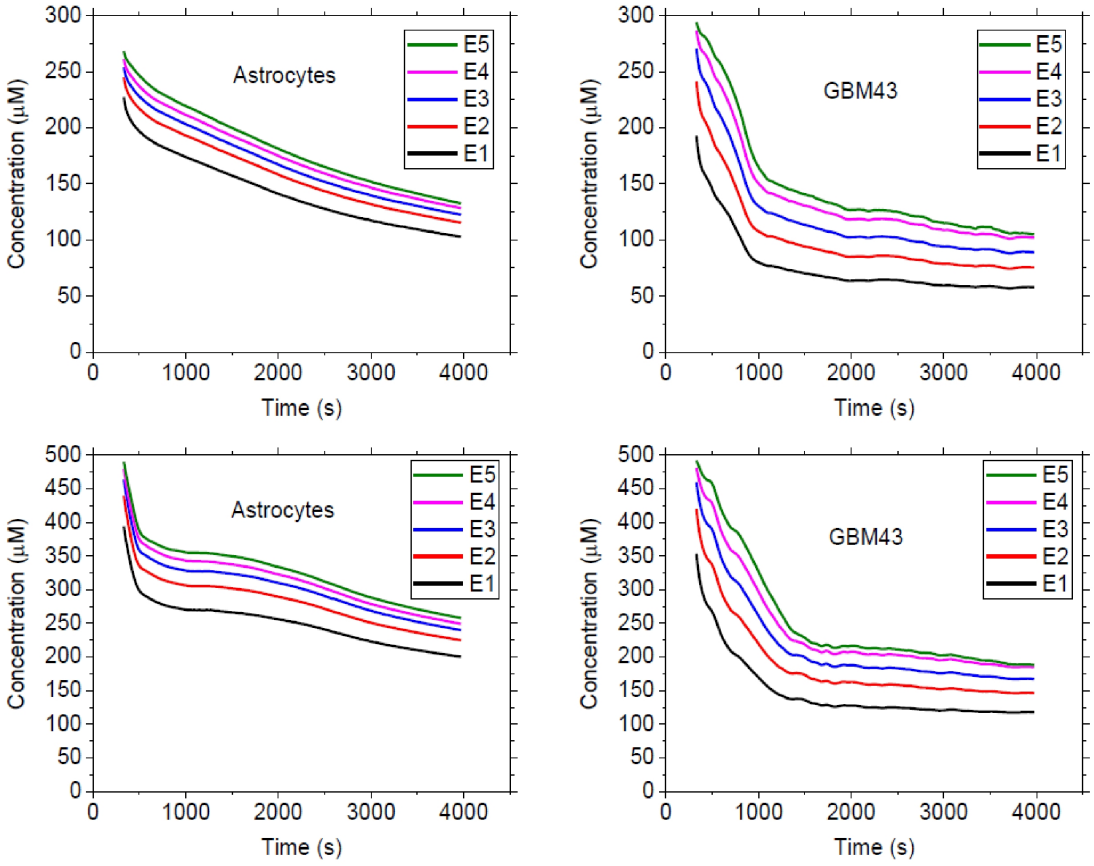

Fig. 9. (Continued from previous page) Representative concentration transients measured in real time at the electrode positions during experiments wherein the cell cultures of astrocytes and GBM43 are exposed to C_0 of 20, 60, 200, 300 and 500 μM H2O2.

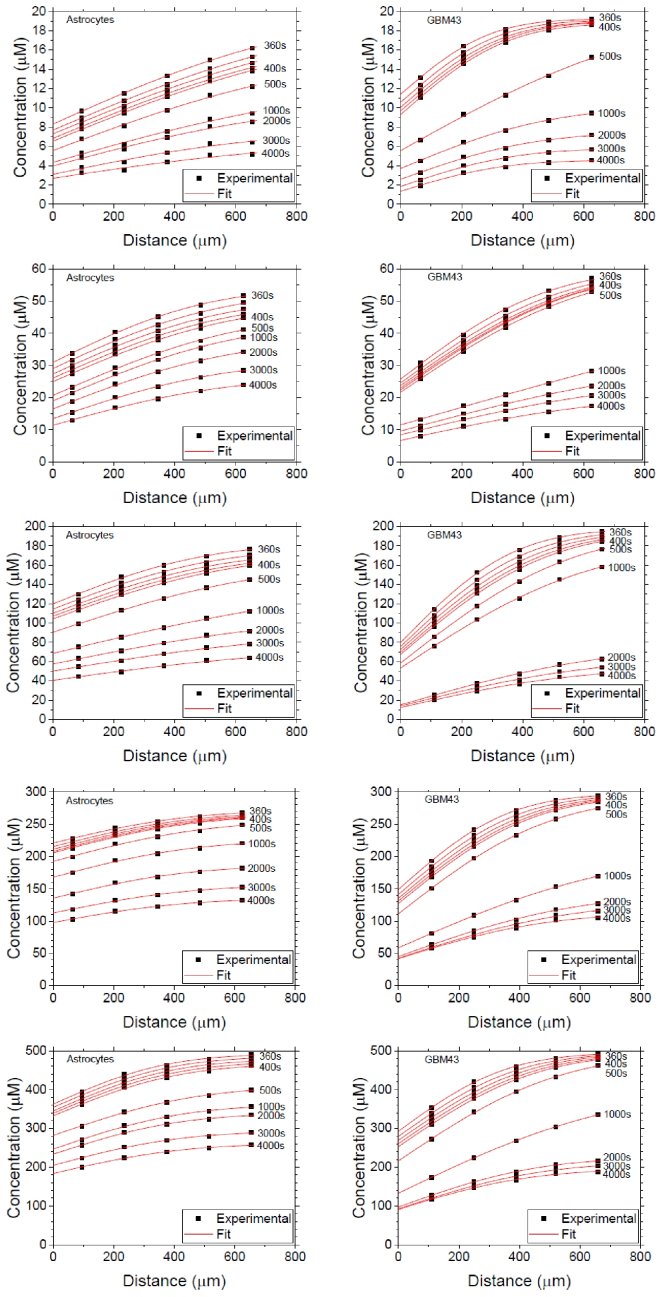

Fig. 10. Representative concentration as a function of distance from the cell surface at the indicated time points for both astrocytes and GBM43 cells exposed to C0 of 20, 60, 200, 300 and 500 μM H2O2. (Continue in next page).

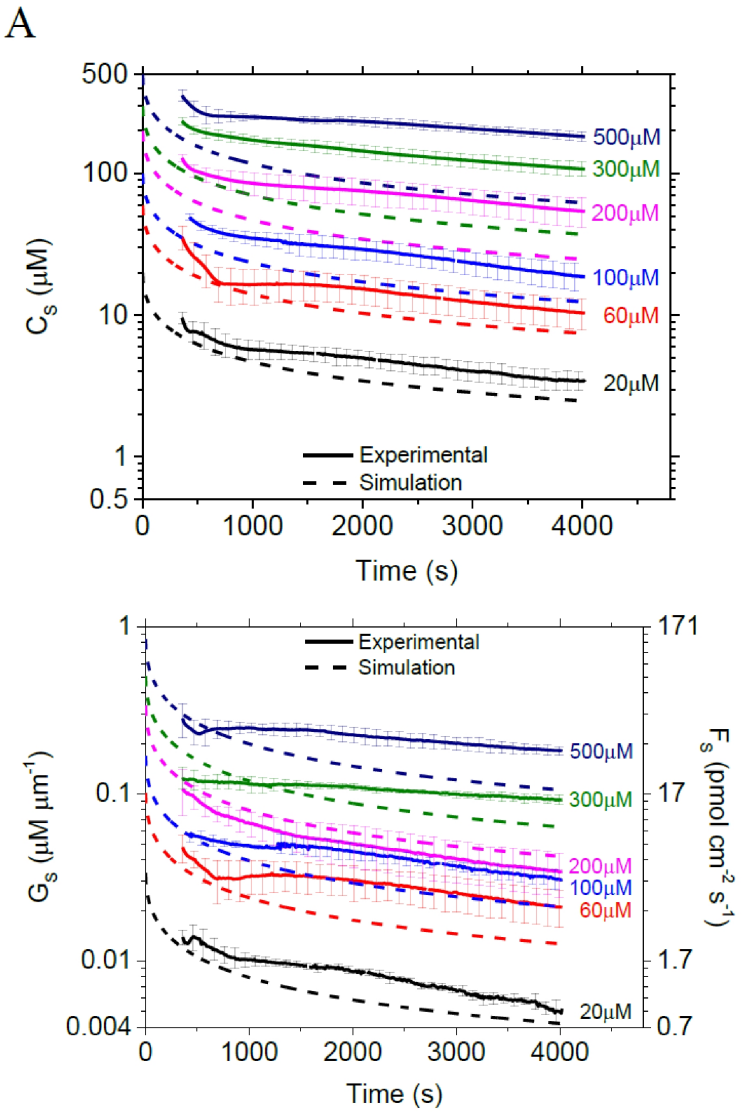

Fig. 11. Simulation results using constant k_F extracted from linear regressions of the experimental data within 020 μM H2O2. (A) Astrocytes, using k_F of 2.63 $\times$ 10-12 L s^{-1} cell^{-1}. (B)GBM43, using k_F of 4.2 $\times$ 10^{-12} L s^{-1} cell^{-1}. (Continue in next page).

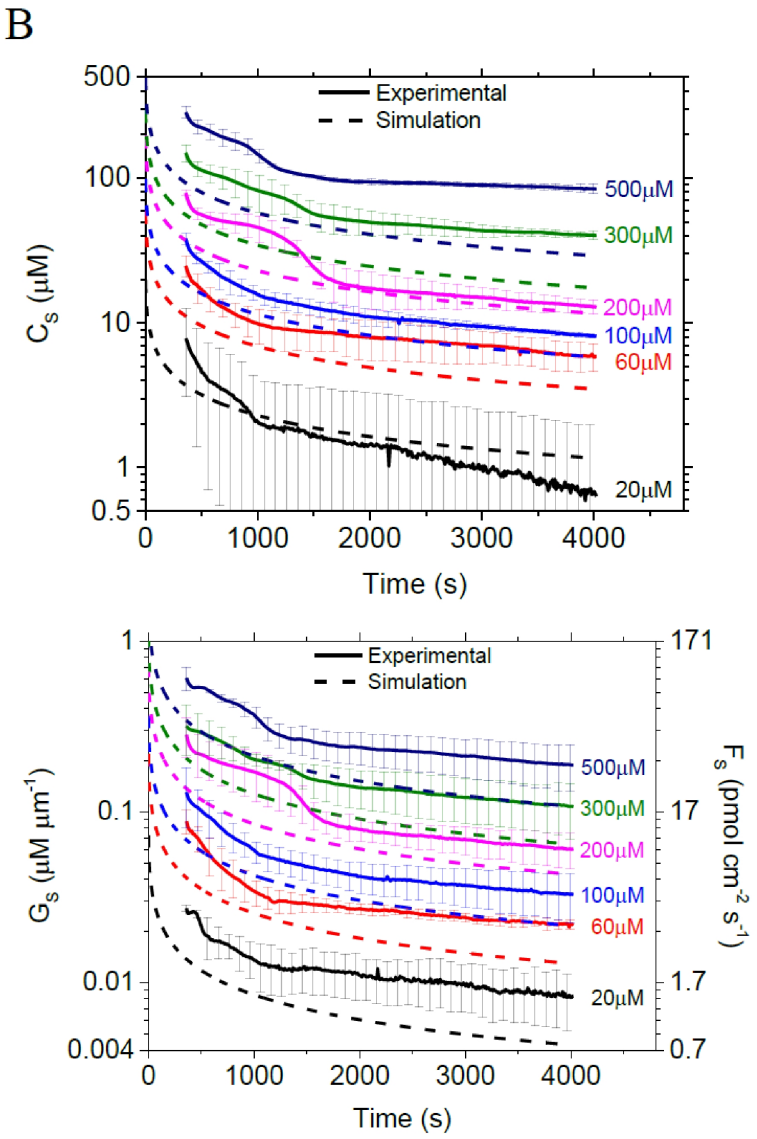

Fig. 12. (Continued) Simulation results using constant k_F extracted from linear regressions of the experimental data within 020 μM H2O2. (A) Astrocytes, using k_F of 2.63 $\times$ 10-12 L s^{-1} cell^{-1}. (B)GBM43, using k_F of 4.2 $\times$ 10^{-12} L s^{-1} cell^{-1}.

VITA

VITA

Siddarth V. Sridharan

svyaghra@purdue.edu | 765-409-8762 | LinkedIn: svyaghra

2060 Country Squire Ct, Apt 105, West Lafayette, IN-47906

Research Interests

Micro/nano biosensor arrays, electrochemical microelectrode arrays, optical sensors, bio-reactors for measuring extracellular metabolites, cellular kinetics, metabolism etc. Numerical simulations of reaction-diffusion models in order to improve the design and performance of sensor arrays.

Education

- **PhD (+ MS) in electrical engineering (Microelectronics and Nanotechnology)**
  Advisor: Dr. David Janes
  Purdue University, USA (AUG 2012- JUN 2019)
  Major GPA: 3.73/4
- **Bachelor of Technology in Electronics and Communication Engineering**
  SRM University, India (2008-2010,2012)
  Special Student Program, Massachusetts Institute of Technology, USA (2010-2011)
  Major GPA: 9.2/10

Academic Experience

- **Research Assistant**

  Advisor: Dr. David Janes

  Dept. Of Electrical Engineering, Purdue University 2014-2018

  Electrochemical biosensor arrays based multi-analyte system used for measurement of bio analyte flux and mapping concentration profiles to quantify cellular metabolism and kinetics.

- **Instructor**

  ECE 207 Electronic Measurement Techniques. (Rating 4.9/5)

  Dept. Of Electrical Engineering, Purdue University (2018-present).

- **Graduate Teaching Assistant**

  Course: ECE 557 Integrated Circuit and MEMS fabrication. (Rating 4.9/5)

  Dept. Of Electrical Engineering, Purdue University 2013-2017.

- **Graduate Assistant - Instructional Design Assistant**

  MIIT, Dept. Of Veterinary Medicine, Purdue University 2013.

Courses

- Biosensors: Fundamentals and Applications (BME 521)
- Fundamentals of MEMS and Micro-Integrated Systems (BME 581/ECE 526)
- Introduction to Biophysics (Phys 570)
- Principles of Electronic Nanobiosensors
- Fundamentals of Nanoelectronics (ECE 595)
- Integrated Circuit and MEMS fabrication (ECE 557)
- Numerical Analysis (MA 514)
- Advanced Mathematics for engineers and physicists

- Semiconductor Material and Device Characterization (ECE 658)
- Electronic Transport in Semiconductors (ECE 656)
- Solid State Devices I (ECE 606)
- Advanced VLSI devices (ECE 612)
- Electromagnetic Field Theory (ECE 604)

Major Publications and Conference Proceedings

- NSF Nano-biosensing Award Abstract 1403582: NSF:1403582
- Siddarth Sridharan, Jose Rivera, James Nolan, Muhammad Alam, Jenna Rickus and David Janes. "On-chip microelectrode array and in situ transient calibration for measurement of transient concentration gradients near surfaces of 2Dcell cultures," Sensors and Actuators B: Chemical, v.260, 2018, p. 519. doi:doi
- Jose F. Rivera, Siddarth V. Sridharan, James K. Nolan, Stephen A. Miloro, Muhammad A. Alam, Jenna L. Rickus, and David B. Janes. "Real-Time Characterization of Uptake Kinetics of Glioblastoma vs. Astrocytes in 2D Cell Culture Using Microelectrode Array," Analyst, v.143, 2018, p. 4954. DOI:doi
- Siddarth V. Sridharan; Jose F. Rivera; Xin Jin; David B. Janes ; Jenna L. Rickus ; Muhammad A. Alam. "Electrochemical micro-electrode arrays for measurement of transient concentration gradients of hydrogen peroxide," 2016 74th Annual Device Research Conference (DRC), 2016. doi:doi
- Rivera, J. F., Sridharan S. V., Janes, D. B., Rickus J. L., 2015. 57th Electronic Materials Conference.
- James Nolan, Jose F. Rivera, Siddarth V. Sridharan, Leyla Kahyaoglu, Rajtarun Madangopal, Bruce Hope, David Janes, Jenna Rickus, Bio-functionalization and modeling of microsensors for on chip single cell extracellular flux and intracellular biocatalysis, Biosensors 2016, 2527 May 2016, Gothenburg, Sweden.

- Siddarth V. Sridharan, Jose F. Rivera, Xin Jin, David B. Janes, Jenna L. Rickus and Muhammad A. Alam, Electrochemical Micro-Electrode Arrays for Measurement of Transient Concentration Gradients of Hydrogen Peroxide, DRC 2016.
- Siddarth V. Sridharan, Jose F. Rivera, James Nolan, David B. Janes and Jenna L. Rickus, Surface Functionalization approaches for Quantitative Sensing of Bioanalytes using Amperometric Micro-Electrode Arrays, 59th Electronic Materials Conference.
- Jose F. Rivera, Siddarth V. Sridharan, James Nolan, David B. Janes and Jenna L. Rickus, Implications of using high reaction rate amperometric micro-electrode array for measurement of local concentration variations of bioanalytes, 59th Electronic Materials Conference.
- United Nations and European Space Agency Conference on Small Satellites In Graz, Austria, 2010 Presentation on Design of Ground Station for a nanosatellite: SRMSAT